

UNIVERSITE LIBRE DE BRUXELLES
FACULTE DES SCIENCES

BINARY INTRUDERS AMONG
PECULIAR RED GIANT STARS

Sophie Van Eck
September 1999

Thesis submitted
for the degree of
Docteur en Sciences

A ma famille

Remerciements

Ces dernières années passées à l’Institut d’Astronomie et d’Astrophysique, d’abord pour mon travail de fin d’études, puis pour ma thèse, furent extrêmement enrichissantes. On y trouve un cadre de travail très motivant, et surtout une chaleureuse ambiance qui permet de se consacrer à un travail de recherche de manière optimale. Je voudrais en remercier particulièrement le Professeur Marcel Arnould, Directeur de l’Institut, qui m’a permis de passer ces années de thèse dans des conditions idéales, et s’est toujours montré d’une aide attentive et précieuse face à mes interrogations et sollicitations.

Il est d’usage de remercier son directeur de thèse pour les nombreuses discussions stimulantes et les critiques toujours constructives prodiguées avec une disponibilité constante durant le doctorat. Je m’en voudrais d’en rester là, car le rôle d’Alain Jorissen dans ce travail fut autrement marquant. Je voudrais par exemple évoquer comment, tout au long de ces quatre années, il m’a encouragée à aller au bout de mes idées, quand bien même il ne les partageait pas, pour me laisser parvenir à une compréhension personnelle des choses, pour que j’en vienne de moi-même à réaliser le mieux-fondé de ses suggestions suite à la prise en compte d’éléments dont je n’avais d’abord pas entièrement saisi la pertinence.

Je voudrais également exprimer ma gratitude à tous les autres membres de l’Institut, en particulier à Yves Busegnies et à Stéphane Goriely pour les éclairages intéressants qu’ils ont apportés sur divers points de ce travail, ainsi qu’à Guy Paulus pour une relecture bénéfique de l’introduction et pour son aide “logicielle” permanente, et à Marc Rayet pour son soutien informatique sans faille et sa compréhension envers les appétits à jamais inassouvis en “espace disque” des observateurs. Je remercie enfin Dimitri Pourbaix pour ses astuces informatiques d’une radicale efficacité, ainsi que Abdallah Mamdouh, Sami Dib, Carmen Angulo et Yvette Levasseur pour leur bonne humeur permanente.

Plusieurs résultats de ce travail dépendent directement d’observations obtenues grâce à l’Observatoire de Genève et à la généreuse coopération d’observateurs anonymes que je remercie ici. J’en suis extrêmement reconnaissante au Professeur Burki et au Dr. Burnet, ainsi qu’à toute l’équipe CORAVEL. Je tiens à remercier particulièrement le Professeur Mayor pour m’avoir permis d’effectuer un séjour de 4 mois à l’Observatoire de Genève, ainsi

que pour son hospitalité chaleureuse et ses conseils durant ce séjour. Je remercie également Stéphane Udry pour son aide toujours efficace et souriante dans la gestion des orbites CORAVEL.

Je voudrais enfin remercier mes parents pour avoir éveillé et toujours encouragé mon goût pour l'astronomie, ainsi que pour leur soutien constant durant toutes ces années. Merci aussi à Anne et Nikita pour leurs conseils judicieux. Merci enfin à Rodrigo de partager et d'embellir ma vie.

Acknowledgements

The completion of this project greatly benefitted from advices and contributions provided throughout the course of the work. I am very grateful to Drs. Catchpole and Feast for sending their *JHKL* data on the Henize sample. Dr. Rousseeuw is warmly acknowledged for sharing with me his expertise (and software) in multivariate classification.

Very little information was available on the Henize sample of S stars at the beginning of this work, since it was never published by Henize. I am grateful to the many people who provided me with information concerning this survey; particular thanks are due to Drs R. Wing, J. Wray and T. Lloyd Evans for their precious help. Finally, it is a pleasure to acknowledge Vance Henize for having found me through the internet, and for having sent to me his late father's unpublished star lists and working notes.

Contents

Preface	1
1 Peculiar red giant stars	3
1.1 Single star evolution	3
1.1.1 Brief sketch of stellar evolution	3
1.1.2 Stellar evolution of low- and intermediate-mass single stars	6
1.1.3 Observational counterparts	15
1.1.4 Problems	20
1.2 Stellar evolution of double stars	20
1.2.1 Binary interaction	20
1.2.2 A binary evolutionary sequence	21
1.3 Some families of red giant stars	25
1.3.1 Barium stars	26
1.3.2 S stars	27
1.3.3 Carbon stars	36
1.3.4 Yellow symbiotic stars	38
1.4 Testing the binary scenario	38
1.4.1 Candidate progenitors of peculiar red giant stars	38
1.4.2 Frequencies of extrinsic stars	40
1.4.3 Remaining issues	42
2 Orbital elements	45
2.1 Introduction	45
2.2 The stellar samples	45
2.2.1 Strong barium stars	46
2.2.2 Mild barium stars	46
2.2.3 Non-variable S Stars	47
2.2.4 Mira S stars	47
2.2.5 SC and Tc-poor C stars	47
2.2.6 CH stars	47
2.3 The radial-velocity jitter	48
2.4 Binary frequency	49
2.4.1 Strong barium stars	49
2.4.2 Mild barium stars	51

2.4.3	S stars	51
2.4.4	Tc-poor carbon stars	52
2.5	Incompleteness study	53
2.5.1	General principles	53
2.5.2	Detection rates for specific P , e and Q distributions . . .	54
2.5.3	Discussion	56
2.6	The $(e, \log P)$ diagram	58
2.7	Period distributions	62
2.8	Barium intensity and orbital period	63
2.9	The mass-function distributions	65
2.9.1	Barium and CH stars	65
2.9.2	S stars	68
2.10	Mild vs. strong barium stars	69
2.11	RLOF	74
2.12	Link between Ba and S stars	76
2.13	Conclusions	77
3	The HIPPARCOS HR diagram of S stars	95
3.1	Introduction	95
3.2	HIPPARCOS S stars	96
3.3	Colours and bolometric magnitudes	103
3.3.1	Colours	103
3.3.2	Bolometric magnitudes	104
3.4	The HR diagram of S stars	105
3.4.1	Uncertainties	105
3.4.2	Statistical biases	108
3.4.3	Comparison with theoretical RGB and AGB evolutionary tracks	111
3.4.4	Comparison with S and carbon stars in external systems .	114
3.5	Infrared excess	118
3.6	Conclusions	119
4	The Henize sample of S stars	121
5	The technetium dichotomy	125
5.1	Introduction	125
5.2	Observations and reduction	126
5.2.1	Instrumental set-up	126
5.2.2	Stellar samples	127
5.2.3	Data reduction and S/N ratio	127
5.3	Analysis	132
5.3.1	Fit of the technetium blends	132
5.3.2	Misclassified and SC stars	138
5.4	Discussion	141
5.4.1	The technetium dichotomy	141
5.4.2	M stars with $60\mu\text{m}$ excess and symbiotic stars	145

5.5	Conclusion	145
6	More observational characteristics	147
6.1	Introduction	147
6.2	Radial velocities of S stars	147
6.2.1	CORAVEL monitoring of the Henize sample	147
6.2.2	Binarity in the Henize sample	148
6.2.3	The CORAVEL parameter Sb	148
6.3	Geneva photometry	152
6.3.1	Rejected measurements	152
6.3.2	Average colours and standard deviation	154
6.3.3	Dereddening	154
6.3.4	Colour-colour diagram	155
6.3.5	Symbiotic stars	157
6.4	JHKL photometry	160
6.5	IRAS photometry	160
6.6	Low-resolution spectroscopy	161
6.6.1	Observations and reductions	161
6.6.2	Construction of band-strength indices	162
6.6.3	Misclassified stars	162
6.6.4	ZrO and TiO band strengths of S stars	165
6.6.5	Na D index and SC stars	166
6.7	Conclusion	169
7	Properties of Henize S stars	171
7.1	Multivariate classification	171
7.1.1	The problem	171
7.1.2	The clustering algorithm	172
7.1.3	Classification parameters	174
7.1.4	Clustering analysis: results	175
7.1.5	Testing the validity of the cluster assignments	177
7.2	Radial-velocity variations in the Henize sample	180
7.3	Galactic distribution	181
7.3.1	Extrapolation to the complete sphere	181
7.3.2	Estimates of bolometric magnitudes	182
7.3.3	Distances	182
7.3.4	Distribution on the galactic plane	183
7.3.5	Galactic scale heights	185
7.4	Relative frequencies	188
7.4.1	Magnitude-limited sample	188
7.4.2	Volume-limited sample	188
7.4.3	The Henize survey as compared to other surveys	189
7.5	Conclusion	192
	Summary and conclusions	193

A Library of Tc spectra	197
B The Henize sample: data	221
References	239
Bibliography	253

List of Figures

1.1	Main evolutionary phases	4
1.2	Schematic HR diagram	9
1.3	Surface abundances of Zr and Tc	18
1.4	Binary scenario	22
2.1	Radial velocity jitter versus Sb	50
2.2	Iso-probabilities for binarity detection	55
2.3	Standard deviation of the radial velocity	58
2.4	$(e, \log P)$ diagram	60
2.5	Period distributions	61
2.6	Synthetic and observed mass function distributions	67
2.7	Mass ratio distributions	68
2.8	Mass function distributions	69
2.9	Schematic predictions of the wind-accretion scenario	73
3.1	The spectrum of HIC 42650	102
3.2	HR diagram for S stars	106
3.3	Distribution of the relative error σ_π/π	107
3.4	The uncertainty on M_{bol} due to the uncertainty on the parallax	108
3.5	Evaluation of statistical biases impact	110
3.6	HR diagram of S stars: location of the RGB	112
3.7	HR diagram of S stars: location of the EAGB	113
3.8	HR diagram of S stars: comparison with S stars belonging to external systems	116
3.9	HR diagram of S stars: infrared excess	118
5.1	Tc spectra in the 4262Å region	134
5.2	Tc spectra in the 4238Å region	135
5.3	Artificial broadening of Tc-poor spectra at 4238 Å	136
5.4	Artificial broadening of Tc-poor spectra at 4262 Å	137
5.5	Tc spectra in the 4262Å region for SC stars	139
5.6	Frequency histograms of the wavelength of the X_{4262} Tc spectral feature	142
5.7	The wavelength of the X_{4262} Tc feature versus the wavelength of the X_{4238} Tc feature	143

6.1	Orbits for 5 Henize S stars	150
6.2	Examples of CORAVEL cross-correlation dips	151
6.3	Histogram of the CORAVEL cc-dip widths for the Henize S stars	152
6.4	Dereddened $(U - B), (B - V)$ color-color diagram of Henize S stars (average measurements)	156
6.5	Dereddened $(U - B), (B - V)$ color-color diagram of symbiotic Henize S stars (individual measurements)	158
6.6	High-resolution spectra of 4 Henize S stars at H_α	159
6.7	The IRAS colour-colour diagram of Henize S stars	161
6.8	ZrO index versus TiO index of Henize S stars	164
6.9	Na D line index of Henize S stars	167
6.10	LaO index and Na D line index of Henize S stars	168
7.1	Schematic illustration of clustering	174
7.2	Average values and standard deviation of the clustering parameters	178
7.3	$\sigma(V_r)$ histogram for Henize S stars	180
7.4	Azimuthal projection of the Henize sample of S stars	181
7.5	Projection of the Henize S stars on the galactic plane	185
7.6	Density distribution perpendicular to the galactic plane for intrinsic and extrinsic Henize S stars	186
7.7	The galactic latitude distribution for S stars from various surveys	190
7.8	Comparison of the TiO and ZrO band-strength for Henize and MacConnell S stars	191
A.1	Tc-rich spectra at 4238.191 Å	198
A.2	Tc-rich spectra at 4262.270 Å	199
A.3	Tc-rich spectra at 4238.191 Å	200
A.4	Tc-rich spectra at 4262.270 Å	201
A.5	Tc-rich spectra at 4238.191 Å	202
A.6	Tc-rich spectra at 4262.270 Å	203
A.7	Tc-rich spectra at 4238.191 Å	204
A.8	Tc-rich spectra at 4262.270 Å	205
A.9	Tc-poor spectra at 4238.191 Å	206
A.10	Tc-poor spectra at 4262.270 Å	207
A.11	Tc-poor spectra at 4238.191 Å	208
A.12	Tc-poor spectra at 4262.270 Å	209
A.13	Tc-poor spectra at 4238.191 Å	210
A.14	Tc-poor spectra at 4262.270 Å	211
A.15	Tc-poor spectra at 4238.191 Å	212
A.16	Tc-poor spectra at 4262.270 Å	213
A.17	Tc-poor spectra at 4238.191 Å	214
A.18	Tc-poor spectra at 4262.270 Å	215
A.19	Tc-poor spectra at 4238.191 Å	216
A.20	Tc-poor spectra at 4262.270 Å	217
A.21	Spectra of SC stars at 4238.191 Å	218
A.22	Spectra of SC stars at 4262.270 Å	219

List of Tables

1.1	Stars misclassified as S	29
1.1	Stars misclassified as S (continued)	30
1.1	Stars misclassified as S (continued)	31
1.2	Observational data collected on the Henize sample of S stars	43
2.1	Comparison of the simulated and observed binary detection rates	56
2.2	Summary of the distinctive features of the period distributions of mild and strong barium stars	62
2.3	Normal giants in barium-like binary systems	64
2.4	Average masses \overline{M}_1 of the giant star in various PRG families	66
2.5	Orbital elements for mild barium stars	79
2.5	Orbital elements for mild barium stars (continued)	80
2.6	Suspected binary mild barium stars	81
2.7	Mild barium stars with no evidence of binary motion	82
2.8	Supergiants misclassified as mild barium stars	83
2.9	Orbital elements for strong barium stars	84
2.9	Orbital elements for strong barium stars (continued)	85
2.10	Strong barium stars with no evidence for binary motion	86
2.11	Orbital elements of S stars	87
2.11	Orbital elements of S stars (continued)	88
2.12	Non-binary (misclassified?) S stars	89
2.13	S stars with radial-velocity jitter	90
2.14	Mira S stars	91
2.15	SC Stars	92
2.16	Tc-poor carbon stars	93
2.17	References to Tables 2.5–2.16	94
3.1	HIPPARCOS S stars: identifications and parallaxes	98
3.1	HIPPARCOS S stars: identifications and parallaxes (continued)	99
3.2	HIPPARCOS S stars: photometry	100
3.2	HIPPARCOS S stars: photometry (continued)	101
5.1	Tc observations for non-Henize stars	128
5.2	Tc observations for Henize stars	129
5.2	Tc observations for Henize stars (continued)	130

5.2	Tc observations for Henize stars (continued)	131
5.3	Percentages of neutral and ionized technetium	144
6.1	Orbital elements for Henize S stars	149
6.2	Definition of band-strength indices	163
6.3	Observational data collected on the Henize sample, their discrim- inating power and their limitations	170
7.1	Clusters average properties	179
7.2	Exponential scale heights z_0 for extrinsic and intrinsic Henize S stars	184
B.1	CORAVEL data	223
B.1	CORAVEL data (continued)	224
B.1	CORAVEL data (continued)	225
B.1	CORAVEL data (continued)	226
B.2	Geneva photometric data	227
B.2	Geneva photometric data (continued)	228
B.2	Geneva photometric data (continued)	229
B.2	Geneva photometric data (continued)	230
B.3	Infrared photometric data	231
B.3	Infrared photometric data (continued)	232
B.3	Infrared photometric data (continued)	233
B.3	Infrared photometric data (continued)	234
B.4	Spectroscopic data and clustering results	235
B.4	Spectroscopic data and clustering results (continued)	236
B.4	Spectroscopic data and clustering results (continued)	237
B.4	Spectroscopic data and clustering results (continued)	238

Preface

The AGB phase (where AGB stands for *Asymptotic Giant Branch*) represents the final evolutionary phase for the vast majority (> 95%) of stars – including our sun – in the universe. AGB stars are important because they satisfactorily meet the model conditions for a rich nucleosynthesis to occur in their interiors. Moreover they lose 50% to 90% of their initial mass in the interstellar medium; hence they are significant contributors to the chemical enrichment of galaxies. Given their high luminosities, they also constitute useful old population probes of galactic structure and dynamics.

Because AGB stars are efficient producers of carbon and heavy elements (elements heavier than iron), all stars observed to exhibit carbon and heavy-element overabundances were traditionally assigned to the AGB phase.

However, an increasing number of arguments recently suggested that the AGB family is overgrown with intruders, i.e., stars that have many observational characteristics of AGB stars but that are definitely not AGB stars. Among the intruder families, barium giants are probably the less talented, for they were easily unmasked some 30 years ago. They are intruders because, unlike AGB stars, they do not produce their heavy elements by themselves, but accreted them in the past from a closeby, now extinguished, companion AGB star.

They are however betrayed by their much too high temperatures and too low luminosities compared to genuine AGB stars – indeed, barium stars need not be as evolved (as cold and luminous) giants as AGB stars, because they do not have to be efficient producers of heavy elements.

Another significant number of intruders lie among the S star family. But S intruders are much more difficult to unmask; in fact, they still widely abuse astronomers, because in addition to the heavy element overabundances, they also mimic quite closely the luminosities and temperatures of AGB stars. An additional entanglement arises from the fact that some S stars are true AGB stars (they are called *intrinsic* S stars), while some are binary intruders like barium stars (they are named *extrinsic*). Both groups are however indistinguishable on the basis of low-resolution spectra commonly used for classification purposes. Hence, all these S stars were historically assigned to the same “S” spectral class.

Yet it is of key importance to distinguish the AGB stars from their binary masqueraders, because the latter may otherwise strongly bias some of the properties derived for AGB stars. For instance, the number ratio of AGB versus non-AGB giant stars, and the deduced respective durations of these phases, will be totally in error if intruders have not been correctly removed from the studied sample. Moreover, the very study of the intruder properties yields invaluable constraints, for example on giant star radii.

This work aims at testing the binary scenario proposed to account for the intruders, and at better characterizing barium stars and the two kinds of S stars (extrinsic and intrinsic). First, the AGB evolution and the taxonomy of red giant stars will be briefly presented. The binarity of barium and S stars will then be examined, thanks to a decade-long radial-velocity monitoring in collaboration with the Geneva Observatory. The recent HIPPARCOS parallaxes will allow to derive more accurate luminosities for the two kinds of S stars. Finally, the binary scenario will be tested on a homogeneous, well-defined sample of 205 S stars, thanks to a five-years large-scale observing program including radial-velocity measurements, photometry, and low- and high-resolution spectroscopy, thus allowing to derive the frequency and properties of intruders among the S star family, and to better characterize genuine AGB S stars.

Chapter 1

Peculiar red giant stars

The purpose of this introduction is to provide an outline of the general context concerning peculiar red giant stars. In fact, the zoo of peculiar red giant stars is so diverse and complex that only some well-defined evolutionary sequences and a limited number of stellar classes will be considered. The evolution of single low- and intermediate-mass stars is sketched in Sect. 1.1. Given the failures of the single star framework to explain observational characteristics of some stellar classes, the binary scenario that is potentially able to solve these contradictions is presented in Sect. 1.2. Sect. 1.3 then depicts various peculiar red giant star families and the way some of them at least are believed to fit within the binary framework. This binary scenario gives rise to many observational tests; some have already been performed and are discussed in Sect. 1.4. However many important issues remain that ought to be examined. The present work aims at studying some of these issues on the basis of large-scale stellar samples. The reader interested in the general organization of the present work is thus invited to jump directly to Sect. 1.4.3.

1.1 Single star evolution

1.1.1 Brief sketch of single star evolution as a function of initial mass

The life of a star is a succession of thermonuclear burning stages and gravitational contraction phases. Fig. 1.1 presents a broad schematic view of the main thermonuclear burning steps of single solar-metallicity stars. The emphasis is on the main structural changes rather than on a quantitative estimate of each of the relevant limiting masses, still subject to large uncertainties. The quoted masses refer to *main-sequence* masses (different from *actual* masses, since stars lose mass as they evolve). Evolution of binary stars, where mass transfer between the components of the binary system may play a key role, is not considered for the moment.

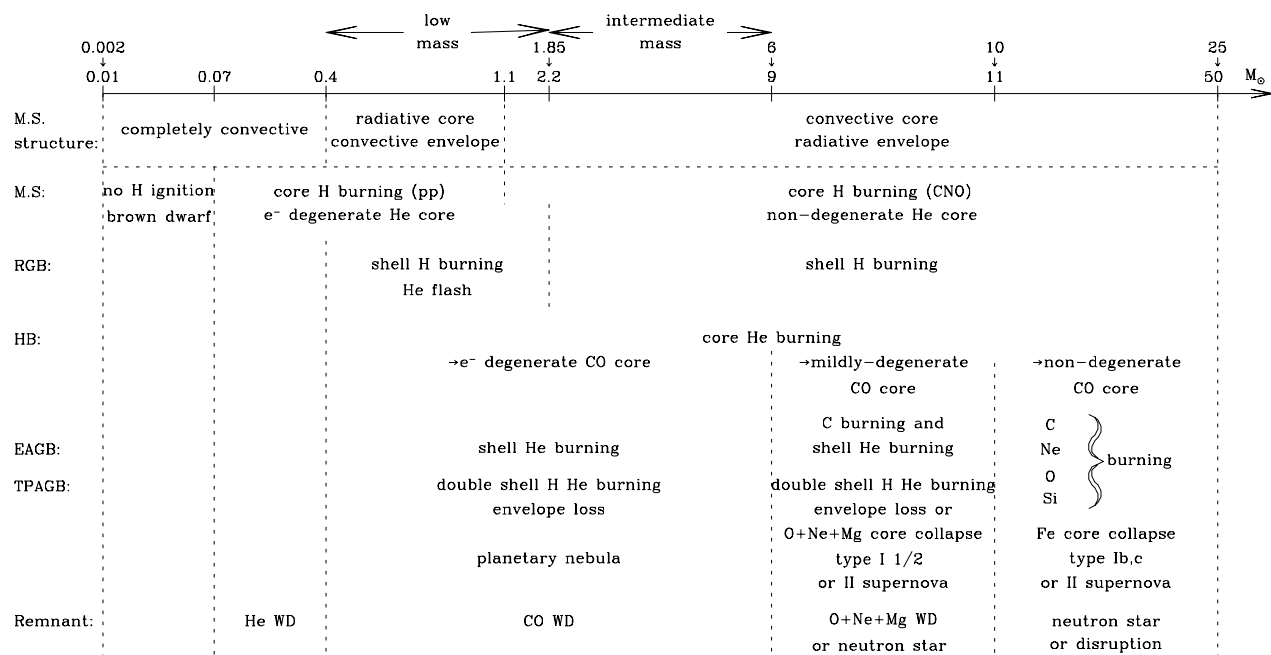


Figure 1.1: Main evolutionary phases as a function of the initial stellar mass

Stars with masses $0.01M_{\odot} \lesssim M \lesssim 0.07M_{\odot}$ (Mayor 1997) never reach central temperatures high enough to ignite hydrogen and stay *brown dwarfs* during their whole life.

Stars more massive than $\sim 0.07M_{\odot}$ (Chabrier & Baraffe 1997) experience core hydrogen burning. Hydrogen burning proceeds via the *pp-chain* if the temperature is lower than $\sim 20 \times 10^6 \text{K}$ (i.e. for stars less massive than $\sim 1.1M_{\odot}$), and via the *CNO cycle* at higher temperatures (i.e. in the core of main-sequence stars if $M \gtrsim 1.1M_{\odot}$, and in hydrogen-burning shells). When the cold CNO cycle is active in central regions of main-sequence stars, convection develops in the core due to the steep temperature dependence of the energetics of the CNO reactions.

For stars less massive than $\sim 0.4M_{\odot}$, the evolution stops at this stage, thus leaving a helium white dwarf. Since the main-sequence lifetime is larger than the age of the universe for $M \lesssim 0.8\text{-}0.9M_{\odot}$, helium white dwarfs are academic objects, in the sense that they are not yet observable¹. Hence the only observable single stars having evolved off the main sequence have masses larger than $\sim 0.8M_{\odot}$.

All stars more massive than $0.4M_{\odot}$ further evolve as giant stars while burning hydrogen in a shell on the *Red Giant Branch* (RGB).

In stars less massive than $1.85\text{-}2.2M_{\odot}$ (Maeder & Meynet 1989), the helium core resulting from hydrogen burning will be electron degenerate and an explosive helium ignition (*helium flash*) will occur at the top of the RGB. Such stars are called *low-mass stars*.

Following the RGB, stars burn helium first in their core, then in a shell on the *Asymptotic Giant Branch* (AGB), thereby growing their degenerate CO core. In stars less massive than $6\text{-}9M_{\odot}$ (this large uncertainty is mainly due to a poor knowledge of mass loss on the giant branches and to shortcomings in the convection prescriptions), mass loss prevents the core from growing to the Chandrasekhar limit mass ($\sim 1.4M_{\odot}$, the maximum mass that can be supported by electron degeneracy) and terminates the AGB. Such stars (having ignited helium non-degenerately and developing an electron-degenerate CO core without carbon ignition) are called *intermediate-mass stars*.

Low- and intermediate-mass stars eject the remainder of their envelope at the top of the AGB; they become post-AGB and planetary nebulae stars and finish their lives as white dwarfs devoid of any nuclear sources.

Stars more massive than $11M_{\odot}$ go through all nuclear burning phases (H, He, C, Ne, O, and Si-burning; note that they ignite carbon at the center of their non-degenerate CO core) and become supernovae; their core of iron-peak elements then collapses to become a neutron star or, if $M \gtrsim 25\text{-}50M_{\odot}$ (Maeder & Meynet 1989), a black hole.

Stars with $6\text{-}9M_{\odot} \lesssim M \lesssim 11M_{\odot}$ constitute difficult intermediate cases; only recently have some models been attempted [Nomoto (1987) and the series of papers by Iben, Ritossa and García-Berro (1996, 1997, 1999)]. Contrarily to stars with $M \gtrsim 11M_{\odot}$, carbon is ignited off-center in a (mildly) degenerate en-

¹except if they belong to binary systems where a companion may have stripped their formerly hydrogen-rich envelope

vironment. If mass loss has not reduced the mass of the star below the Chandrasekhar limit before carbon ignition, a thermal runaway cannot be avoided and these stars may explode as type I 1/2 supernovae (Iben & Renzini 1983). However, it seems that at least some of the $6-11M_{\odot}$ stars manage to become *super AGB stars*, with O-Ne cores, experiencing first He-burning in a shell, then H-He burning in two shells and thermal instabilities (thermal pulses). Their final state might be neon-oxygen white dwarfs if mass loss is sufficient, or core collapse leading to a type II supernova and a neutron star, or an O-deflagration leading to disruption.

1.1.2 Stellar evolution of low- and intermediate-mass single stars

A qualitative picture (e.g. Lattanzio 1995) of the main phases of evolution of low- and intermediate-mass stars (i.e., with $0.9 \lesssim M \lesssim 6 - 8M_{\odot}$ on the main sequence) is sketched in the following.

From birth to main sequence

A star's life begins with the gravitational collapse (on a free-fall time-scale, typically on the order of a few times 10^5 years) of an interstellar molecular cloud. Interestingly, observations show that large clouds do not form isolated stars: it appears that stars frequently (or even preferentially) tend to form in groups, ranging from binary star systems to clusters that contain hundreds of thousands of members. The collapsing cloud is segmented by the process of *fragmentation*, i.e. local collapse of some parts of the cloud under their own gravity – whether the fragmentation occurs prior to, or during collapse, or if it acts on a disk composed of infalling material, is poorly known.

Later, the evolution of the protostar is controlled by the rate at which it can thermally adjust to the collapse (Kelvin-Helmholtz time scale): this is the pre-main-sequence phase [see e.g. Bernasconi (1996)]. To give an idea, a $1M_{\odot}$ star requires on the order of 10^7 years to contract quasi-statically to its main-sequence structure.

The main-sequence is the location in the Hertzsprung-Russell (HR) diagram (Fig. 1.2) where stars convert hydrogen into helium in their core. Their evolution is governed by the time scale of nuclear reactions ($\sim 9 \times 10^9$ years for the Sun, $\sim 9 \times 10^7$ years for a $5M_{\odot}$ star; Charbonnel et al. 1996; Landolt & Börnstein 1982), which explains that approximately 80% to 90% of all stars in the solar neighbourhood are observed to be main-sequence stars.

The red giant branch and the horizontal branch

Once hydrogen burning is completed at the center of the star, it may still continue (if the star is more massive than $\sim 0.4M_{\odot}$) in a thin peripheral shell surrounding the central helium core. During this stage the star leaves the main

sequence and rapidly crosses the Hertzsprung gap in the HR diagram. It expands and its outer layers become convective. As the star reaches the Hayashi limit, convection extends deeply inward (in mass) from the surface, and the star, still becoming redder and brighter, ascends the *red giant branch* (RGB) in the HR diagram. The convective envelope deepens and penetrates into the region where partial H-burning has occurred previously. This material is still mostly hydrogen, but with added helium together with the products of CN cycling, primarily ^{14}N (that roughly doubles at the expense of ^{12}C which drops by about 30%) and ^{13}C , while ^{16}O is preserved at essentially its initial abundance. These products are mixed to the surface; hence the surface ratio $^{12}\text{C}/^{13}\text{C}$ is predicted to drop from its initial value of ~ 90 to lie between 18 (for intermediate-mass stars) and 26 (for low-mass stars). This phase is known as the *first dredge-up*.

In order to explain the lower observed values of the $^{12}\text{C}/^{13}\text{C}$ ratio ($3 \lesssim ^{12}\text{C}/^{13}\text{C} \lesssim 25$), some non-convective extra-mixing referred to as *cool bottom processing* has been speculated to occur in low-mass stars and to transport material between a zone close to the hydrogen-burning shell and the (relatively cool) bottom of the convective envelope (Boothroyd et al. 1995); hence more ^{13}C will be brought to the surface and the resulting $^{12}\text{C}/^{13}\text{C}$ ratio may reach values as low as ~ 11 . The extra-mixing origin is usually supposed to be rotation-induced and/or shear-induced turbulence.

Low-mass stars may spend as much as 20% of their life as red giants, while for intermediate-mass stars this phase lasts generally less than 7% of their lifetime.

As the star ascends the giant branch the helium core continues to contract and heat. If the star is less massive than $1.8 - 2.2M_{\odot}$, the helium core will be electron degenerate. Eventually the helium combustion starts at the (off-center) point of maximum temperature. Since temperature and density are decoupled, the triple- α ignition of helium is explosive, being referred to as the (core) *helium flash*. Following this, the star quickly moves in the HR diagram to the clump, also called, when dealing with low-mass stars, the *horizontal branch*, where it burns helium hydrostatically in a convective core and hydrogen in a thin shell. This is the second longest phase in the life of a star: $\sim 1.2 \times 10^8$ years for a solar-metallicity $1M_{\odot}$ star (Charbonnel et al. 1996).

The only difference for intermediate-mass stars ($1.8 - 2.2 \lesssim M \lesssim 6 - 8M_{\odot}$) is that helium ignition occurs under non-degenerate conditions in the center; hence no runaway situation, such as the core helium flash for low-mass stars, is encountered.

The asymptotic giant branch

- *The early asymptotic giant branch*

When the central helium is exhausted, the star starts burning helium in a thin shell surrounding a degenerate carbon-oxygen core and ascends the giant branch for the second time. This phase is referred to as the *asymptotic giant branch* or AGB because, for low-mass stars, the evolutionary track in the HR

diagram is very close to (but slightly to the blue of) the low-mass red giant branch.

The structural readjustment to helium-shell burning results in a strong expansion of the star, and for stars with masses greater than $\sim 4M_{\odot}$, the hydrogen shell is temporarily extinguished as the star begins its ascent on the AGB. The inner edge of the convective envelope is thus free to penetrate the extinct hydrogen shell, and to mix to the surface the products of complete hydrogen burning. This episode, termed the *second dredge-up*, will further reduce the ^{12}C abundance, enhance the ^{14}N abundance, and reduce slightly the ^{16}O abundance. More details on surface abundance changes observed following the dredge-up episodes may be found in Smith & Lambert (1990).

Following this, the hydrogen shell is re-ignited. At this stage the structure is qualitatively similar for all masses (e.g. Blöcker 1999): (i) a very concentrated CO core (~ 0.5 to $1M_{\odot}$, but the radial extent of its edge is only $\sim 10^{-4}$ of that of the stellar surface); this core is in fact a very hot white dwarf which grows in mass by accreting nuclear-processed matter from the burning shells; (ii) a thin layer ($\sim 10^{-2}M_{\odot}$) occupied by the helium and hydrogen burning shells, and (iii) the extended hydrogen envelope.

The thin helium burning shell becomes thermally unstable and experiences periodic outbursts called *thermal pulses*, during which it liberates on a short time scale hundreds to millions times the energy provided by the hydrogen-burning shell. Hence the remaining of the evolution on the AGB is referred to as the *thermally-pulsing asymptotic giant branch* (or TPAGB), and the former evolution on the AGB as the *early asymptotic giant branch* (or EAGB). To give an idea, the EAGB lasts for about 50×10^6 years, and the TPAGB some 2×10^6 years for $1\text{-}3M_{\odot}$ stars (Blöcker 1995).

- *The thermal pulses*

Thermal pulses were first discovered in AGB models of low-mass Population II stars by Schwarzschild & Härm (1965) and in AGB models of intermediate-mass Population I stars by Weigert (1966). They are often dubbed *helium shell flashes*, despite the fact that their physical origin is completely different (they are explained by the classical gas law) than that leading to the core helium flash (which is produced under degenerate conditions at the top of the RGB and only for low-mass stars). The instability is a consequence of the high temperature sensitivity of the rate of helium burning combined with the thinness of the shell in which it occurs. The following paragraphs rely heavily on Forestini (1991).

When energy is dumped into a shell within a star, this shell expands and thus lifts the above layers upward. Being pushed farther away from the center of the star, those layers will have a decreasing weight. Since the pressure in the considered shells is directly caused – in hydrostatic equilibrium – by the weight of the surmounting layers, the pressure will drop. Now if the shell in question is thin (like the burning shells in low- and intermediate-mass stars), it can undergo a substantial expansion with a large fractional drop in density, but only lift the overlying layers by a small fraction of their radial distance to the center. Consequently, the pressure drop within the shell will be small compared

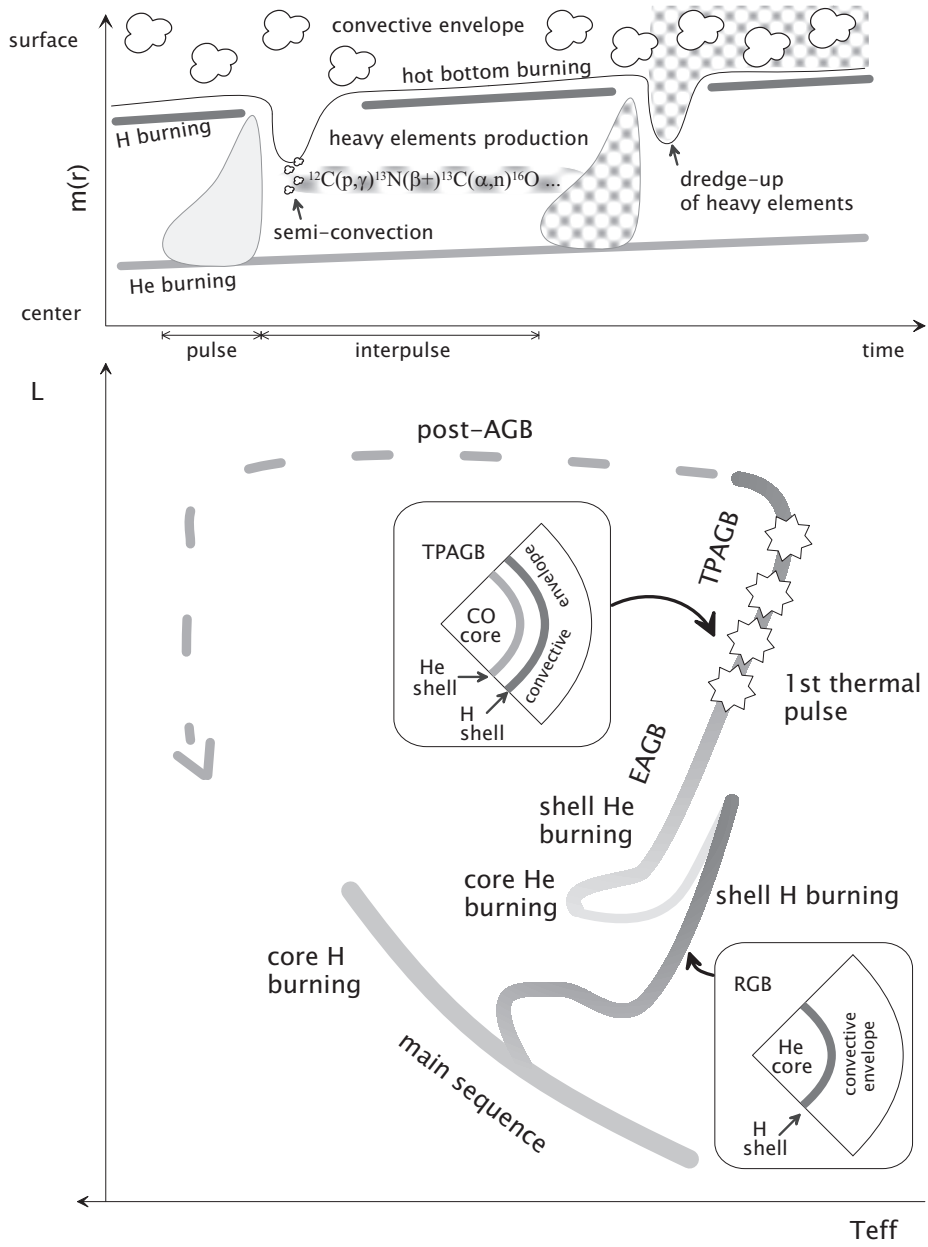


Figure 1.2: Schematic Hertzsprung-Russell diagram (bottom) and nucleosynthesis during the thermal pulses (top)

to the density drop. Then, according to the classical gas law, the temperature will actually rise. If this shell contains a substantial source of nuclear energy whose production rate is very sensitive to temperature, the rise in temperature will cause a further energy gain. Provided the shell has a high enough optical thickness, the energy loss will be smaller than the gain.

Hence an energy gain leads to a thermal runaway in a shell that is (1) sufficiently thin that perturbations in it do not affect the hydrostatic structure of the star, and (2) optically thick enough that it does not lose easily the excess thermal energy. This instability becomes a *thermal pulse* if it is strong enough to require a convective transport of the energy in the helium shell (i.e. if the convective gradient exceeds the adiabatic gradient)².

Therefore the thermally-pulsing AGB may be seen as a succession of four phases (e.g. Lattanzio 1995), and this cycle goes on till the end of the AGB, when mass loss has removed almost all of the star envelope.

1. *the quiescent helium-hydrogen double-shell burning* : the structure is basically that of an EAGB star. Almost all of the surface luminosity is provided by the hydrogen shell. This phase lasts for 10^4 to 10^5 years, depending on the core mass (the smaller the core mass, the longer the phase). In stars more massive than $\sim 4M_{\odot}$, the convective envelope is deep enough to reach temperatures where non-negligible hydrogen-burning can take place: this phenomenon has been given the colourful name of *hot bottom burning* (e.g. Lattanzio et al. 1997). The processed matter is immediately convected to the stellar surface.
2. *the thermal-pulse phase* : the thermal instability develops in the helium-burning shell, producing a convective zone that extends from the helium shell almost to the hydrogen-shell and that lasts for about 200 years. This convective zone comprises helium and ^{12}C ; it comes very close to the now-extinguished hydrogen-burning shell (although without penetrating it).
3. *the hydrogen-off phase* : the helium shell dies down and the convection is shut-off. The energy released previously drives a substantial expansion, pushing the hydrogen-shell to such low temperatures and densities that it is extinguished. A phase of slow helium burning starts, that will last a few thousand years.
4. *dredge-up phase* : in response to the cooling of the outer layers, the convective envelope extends inward. After a (not precisely known) number of pulses, it will manage to penetrate into the formerly convective tongue (developed during the pulse), where the composition has been modified due

²If the runaway is not strong enough to lead to the rise of convection, one generally speaks of a *micro-pulse*. Sometimes, the beginning of the TPAGB is defined as the epoch at which the luminosity produced by the helium-burning shell during a flash exceeds *for the first time* that produced by the hydrogen-burning shell, instead of the epoch at which a convective tongue first develops in the helium-burning shell (sometimes called the first *major* thermal pulse)

to helium burning. This results in freshly produced ^4He , ^{12}C and heavy elements (see below) being mixed to the surface by envelope convection [Iben & Renzini 1983; Sackmann & Boothroyd 1991; see also Mowlavi 1999]. The star contracts back and the hydrogen-shell is re-ignited, re-starting at step 1.

- *Nucleosynthesis on the TPAGB*

Many observations have demonstrated that low-mass AGB stars are enriched with carbon and specific heavy elements (like Sr, Y, Zr, Tc, Ba), implying that such elements have been synthesized in the interiors of the stars and dredged up to the stellar surface.

▷ carbon: The repeated operation of the thermal pulse cycle is responsible for the periodic addition of carbon to the stellar surface. If enough dredge-ups have time to occur before the stellar envelope is entirely stripped, an AGB star whose initial surface C/O ratio is less than 1, will change into a *carbon star*, with $\text{C/O} > 1$.

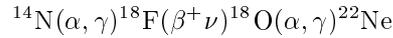
▷ heavy elements: In AGB stars, the heavy elements observed to be overabundant are known to be produced by the nucleosynthetic *s-process* (where “s” stands for *slow*; see e.g. Arnould 1991; Arnould & Takahashi 1999). The s-process is a neutron-capture process starting on iron seed nuclei that occurs if the neutron flux is weak enough for the β -decay time scale to be (generally) shorter than the neutron-capture time scale: in other words unstable nuclei have time to β -decay before capturing a neutron. The s-process is therefore able to synthesize only those nuclides close to the valley of nuclear stability (Burbidge et al. 1957). In fact it imprints a very clear signature on its product nuclei, in the form of overabundance peaks, one around Sr, another around Ba, a third one around Pb, which are precisely those observed in AGB stars (Smith and Lambert 1985, 1990). These peaks reflect underlying nuclear properties: magic nuclei with closed neutron shells (with $N=50$, 82 and 126 neutrons) have very small neutron-capture cross sections and constitute bottlenecks along the s-process nuclear path. Hence, these magic nuclei (like ^{88}Sr , ^{89}Y , ^{90}Zr , ^{138}Ba , ^{139}La , ^{140}Ce) are piling up and the corresponding elements are indeed observed to be overabundant.

A distinction is made between *light-s* elements (Sr, Y, Zr) and *heavy-s* elements (Ba, La, Nd): the ratio of the *heavy-s* to *light-s* ($[hs/l_s]$) is a sensitive function of the total neutron irradiation, the neutron exposure, because high neutron exposures will cause the first bottleneck ($N=50$) to be bypassed and nuclides will thus accumulate at the second bottleneck.

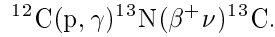
Technetium (Tc) is a particularly interesting element, because all its isotopes are radioactive. ^{99}Tc , the only technetium isotope produced by s-processing, has a half-life of $\sim 213\,000$ years in the laboratory; this is short compared to the AGB lifetime. Although some objections have been raised concerning the presence of technetium during the whole TPAGB phase (see discussion in

Chap. 5), observations tend to demonstrate that from some point on the AGB, technetium is always present in those stars. Hence technetium plays a key diagnostic role in identifying recent s-processing stars, serving as a marker of TPAGB stars.

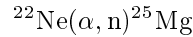
▷ **The neutron source:** Observations of s-process overabundances in AGB stars demand that a neutron source operates before or during the AGB stage. The thermal pulses have been soon recognised as a promising site for s-process nucleosynthesis, since they consist of repeated hydrogen and helium burning phases, producing respectively abundant ^{14}N and ^{12}C . At the start of helium burning, ^{14}N gives rise to



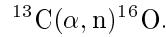
and in the presence of protons, ^{12}C reacts according to:



The ^{13}C and ^{22}Ne nuclei produced are the most important source of neutrons in hydrostatic stellar conditions, through the reactions



and



In low-mass stars, the ^{22}Ne neutron source is marginally activated because of too low temperatures, and neutrons are believed to be produced through the alternative and much faster reaction $^{13}\text{C}(\alpha, \text{n})^{16}\text{O}$.

Unfortunately, the amount of ^{13}C left behind by the CNO cycling in the hydrogen-burning shell turns out to be far too low to drive the synthesis of the s-elements. The following *ad hoc* assumption has to be made: some kind of extra mixing must take place at the bottom of the convective envelope during the dredge-up phase, so that “just the right quantity” of protons from the envelope is mixed into the inter-shell region rich in newly synthesized ^{12}C . At hydrogen re-ignition (during the subsequent inter-pulse phase), protons are captured by ^{12}C to form ^{13}C which will later produce the necessary neutrons (if the amount of mixed hydrogen is too low, too few neutrons will be released, but if it is too high, all the ^{13}C will further burn into ^{14}N before producing any neutrons). Such partial mixing at the base of the convective envelope might arise from overshoot below the convective region (Herwig et al. 1997) and/or rotationally induced mixing (Langer et al. 1999).

The ^{13}C pocket is usually believed to sit in the star and wait until the next thermal pulse. Then, it will be engulfed in the flash-driven convective tongue, where the temperatures are high enough to release the neutrons: the s-processing will solely occur in this convective zone.

However, recent computations (Straniero et al. 1995; Mowlavi et al. 1995) show that the inter-pulse is long enough to produce sufficiently high temperatures in the inter-shell so as to release neutrons and to make s-processing already in the inter-shell during the inter-pulse. During the next thermal pulse, the s-process elements will be mixed in the convective flash-driven zone [in advanced pulses a second small neutron burst may be induced by the ^{22}Ne source; Gallino et al. 1998]. Later, during the following dredge-up phase, the convective envelope will come down to gather matter enriched in s-process elements up to the surface of the star.

There are several observational hints that the neutron source is indeed ^{13}C . In particular, if the neutron source is $^{13}\text{C}(\alpha, n)^{16}\text{O}$, the s-process efficiency is expected to increase with decreasing metallicity (Clayton 1988): indeed, the number of neutrons available per seed iron nucleus is larger at lower metallicities. Observations seem to confirm this tendency [increase of $[s/\text{Fe}]$ with decreasing $[\text{Fe}/\text{H}]$ (Feltzing & Gustafsson 1998); increase of the ratio *heavy-s* to *light-s* ($[hs/ls]$) with decreasing $[\text{Fe}/\text{H}]$ in Ba stars and CH subgiants and giants (Luck & Bond 1991; Vanture 1992c)].

▷ Hot bottom burning: In stars more massive than $\sim 4M_{\odot}$, the *hot bottom burning* is also responsible for changes in stellar surface abundances. In particular, Li abundances and C/O ratio are affected:

- ^7Li overabundances are plausibly explained via the Cameron-Fowler beryllium transport (Cameron & Fowler 1971; Sackmann & Boothroyd 1992), though this mechanism requires fine-tuning: on the one hand, a long enough ^3He processing through $^3\text{He}(\alpha, \gamma)^7\text{Be}$ must occur in order to produce significant amounts of ^7Be ; but on the other hand, the ^7Be must be quickly removed from hot layers by convection, in order to avoid destruction by the $^7\text{Be}(p, \alpha)^4\text{He}$ reaction (most efficient at temperatures $> 2.5 \times 10^6\text{K}$). Once lifted to cooler layers, ^7Be captures an electron to form ^7Li . This scenario is in good agreement with observations of galactic (Abia et al. 1993) and Magellanic Clouds (Smith et al. 1995) Li-rich AGB stars. Note that the Li-rich phase is only temporary, since at some time the limited amount of seed nuclei ^3He (left over from the early main sequence evolution) will be exhausted.
- C/O and $^{12}\text{C}/^{13}\text{C}$ decrease: the ^{12}C dredged-up will be processed by hot bottom burning into ^{14}N via the CNO cycle, hence the C/O ratio decreases; this will necessarily involve the production of some ^{13}C ; hence the surface ratio $^{12}\text{C}/^{13}\text{C}$ drops to its CNO equilibrium value of ~ 3 . This latter point is fortunate because it solves the so-called “carbon star mystery” (Iben 1981) raised at a time when current models (thermal pulses and dredge-up of carbon) predicted that the most evolved, and thus the most luminous AGB stars, had to be the most carbon-rich; but intriguingly, observations showed at that time a lack of carbon stars among the brightest stars of the Magellanic Clouds. This contradiction is solved with

hot bottom burning, which predicts a maximum luminosity of $M_{\text{bol}}=-6.4$ for carbon stars (Boothroyd et al. 1993), as stars more luminous will have burnt enough carbon to reduce C/O to less than unity.

Interestingly, hot bottom burning is predicted to be more efficient in low-metallicity stars (because of higher temperatures at the base of the convective envelope). This is consistent with the fact that in our Galaxy, the majority of Li-rich stars are carbon stars (C/O > 1), while in the Magellanic Clouds, they are S stars (hence with C/O < 1). Note also that if mass loss decreases the hydrogen envelope mass sufficiently, hot bottom burning is quenched and stars may become carbon stars again with low $^{12}\text{C}/^{13}\text{C}$ ratio (Frost et al. 1998). This is consistent with recent findings of obscured carbon stars (Kastner et al. 1993; van Loon et al. 1998); in the Magellanic Clouds, their luminosities reach $M_{\text{bol}}=-6.8$.

- *Conclusion:* In summary, the thermally-pulsing AGB evolution is a complex interplay between thermal pulses, dredge-up, hot bottom burning and mass loss, that is far from being well understood. The similarity between dynamic, thermal and nuclear burning time-scales during the TPAGB prevents many usual approximations from being used, not to mention stellar pulsations (on a much shorter time-scale, ~ 500 days) that are not currently included in models.

From the asymptotic giant branch to the white dwarf stage

In order to form a planetary nebula of typically a few tenths of a solar mass within $\sim 10^4$ years, a heavy mass loss (i.e., a *superwind* of $\sim 10^{-5}M_{\odot}/\text{year}$, Renzini 1981) is required at the tip of the AGB. The asymptotic giant branch evolution is terminated when the mass of the envelope decreases below $\sim 0.01M_{\odot}$. At this stage stars evolve off the AGB toward higher temperatures through a plateau phase at constant luminosity. They are called *post-AGB stars* or equivalently *proto-planetary nebulae*. In this transition phase, the central stars may take very different aspects including those of (high galactic latitude) intermediate-type supergiants, R CrB, RV Tau, or [WC] stars. This transition phase is believed to be short with respect to the previous TPAGB phase: typically 10^3 to 10^4 years.

During the descent of the white dwarf cooling track some stars are believed to experience a final helium shell flash and to make a second appearance as AGB stars. The lifetime of such “born-again” giants is however short (typically 100-1000 years). Sakurai’s object, as well as FG Sge may be examples of these stars.

Interestingly, many post-AGB stars appear to be binaries, but this might be due to an observational bias, since binaries display a prolonged infra-red lifetime due to the presence of hot dust presumably trapped in a stable circumbinary disc (Van Winckel 1999). At least, the binary nature of the extremely iron-deficient post-AGB stars (that may reach $[\text{Fe}/\text{H}]=-4.8$) is well established (Van Winckel et al. 1999). In these stars, the good correlation between the chemical deficiencies of the photosphere and the condensation temperature of the

corresponding elements is a hint that the observed chemical patterns are due to *depletion in refractory elements*: in a gas-dust mixture, the elements with a lower condensation temperature remain in the gas phase while the others (the refractory elements, i.e. elements with a high dust condensation temperature) more easily condense to the dust particles. During AGB evolution, dust condensates in a circumstellar shell; it is then blown away by radiation pressure. When the outflow stops, “cleaned” material (depleted in refractory elements) – possibly located in a circumbinary disk – may be partially re-accreted by the star, which will thus show a lack of refractory elements. Because s-process elements have high dust condensation temperatures, they are depleted as well; hence it is hard to trace the dredge-ups history in these objects. Whether the same (or the complementary) chemical fractionation alters as well the composition of the matter accreted by the companion is currently unknown; it is however an important issue, since the polluted companion may in turn evolve and exhibit anomalous abundance patterns (see Sect. 1.2).

The orbital periods of binary post-AGB stars may be as short as 116 days, and their orbits are not circularized. It is not clear how the progenitor AGB stars can avoid a cataclysmic evolution (common envelope phase, spiral-in) with so short orbital periods (see however discussion in Sect. 2.11).

When stars reach high enough effective temperatures to ionise the circumstellar (or circumbinary) material they become planetary nebulae. When the nebula is dispersed, they appear as white dwarfs. Central stars of planetary nebulae have indeed been identified as immediate progenitors of white dwarfs. Single white dwarfs in the solar neighbourhood present the interesting property that their mass distribution is strongly peaked around $0.6 \pm 0.2 M_{\odot}$ (Weidemann 1990).

1.1.3 Observational counterparts

For each of the main evolutionary phases outlined above, observational counterparts ought to be found in order to check and better constrain theory. This is often a hard task because some evolutionary phases have very short lifetimes or because they lack unambiguous observational signatures.

Main sequence

Low- and intermediate-mass stars that are currently on the main sequence have effective temperatures in the range 3700-18000K; as such they are classified as M0-1 to B3-5 dwarf stars (Landolt & Börnstein 1982).

RGB and EAGB

As stars reach the giant stage, their effective temperature decreases and they are classified as G ($T_{\text{eff}}=4800\text{-}5900\text{K}$), then K ($T_{\text{eff}}=3800\text{-}4800\text{K}$) giants. Only the lower mass stars ($M \lesssim 1.7 M_{\odot}$ according to Schaller et al. 1992) manage to reach

low enough temperatures on the RGB in order to exhibit TiO bands, and to be classified as M giants ($T_{\text{eff}}=3200\text{-}3800\text{K}$). The observed abundances for normal G, K and M giants are similar, and are in fair agreement with the predictions of the first dredge-up (Smith & Lambert 1990).

However, it is not clear that all G and K stars are less evolved than M stars. Indeed, when stars evolve from the tip of the red giant branch to the clump their temperature re-increases; therefore stars regress along the spectral type sequence, becoming late-G or early-K stars again. K stars may actually be found among stars ascending the RGB or in the clump and on the EAGB, and M stars among stars near the RGB tip, on the early-AGB and possibly on the TPAGB. The infrared properties of M stars agree with this hypothesis (Habing 1987; Jorissen et al. 1993).

TPAGB

- *The M-S-C sequence*

The many dredge-ups occurring on the TPAGB periodically add s-process- and C-rich matter to the stellar surface. While $\text{C}/\text{O} < 1$, the star is not seen as a carbon star, because the formation of the stable CO molecule does not exhaust all the oxygen supply: enough oxygen remains available in order to form the oxide bands characteristic of M stars. However, because of the s-process enrichment, ZrO bands become apparent and the star is therefore classified in the MS or S family. Detailed spectroscopic abundances have confirmed the M-S-C sequence³: these stars indeed share a common relation of increasing s-process enhancement with increasing ^{12}C (Smith & Lambert 1990): $\text{C}/\text{O} \sim 0.4$ for M stars, ~ 0.5 for MS stars, ~ 0.6 for S stars (Smith & Lambert 1990), $\sim 0.98 - 1.0$ for SC stars (Keenan & Boeshaar 1980) and $\sim 1.01 - 1.5$ in C stars (Lambert et al. 1986) even if each group shows considerable scatter. The S stars mass loss rates were found to be comparable to those of AGB M stars (Jura 1988) and C stars (Bieging & Latter 1994). Moreover, there is direct evidence for the intermediate status of S stars in their location between the M and C stars in the field (e.g. Knapik et al. 1999) and on the upper giant branches of intermediate age clusters in the Magellanic Clouds (e.g. Bessell et al. 1983; Lloyd Evans 1984).

Hence, single stars are currently believed to evolve among the M-MS-S-SC-C sequence. However the details of this evolutionary sequence have been lively debated with the discovery of carbon stars surrounded by circumstellar shells containing silicate-type dust (usually a signature of oxygen-rich stars) rather than carbon-rich dust (Willems & De Jong 1986; Little-Marenin 1986; Little-Marenin et al. 1988; Kwok & Chan 1993). Willems & De Jong (1986) and De Jong (1989) argued that these stars are observed in a brief transient evolutionary stage ($\lesssim 10$ years) after conversion from a M to a C star, during which mass loss effectively ceases and the circumstellar envelope, produced while the star was still oxygen-rich, coasts outward.

³more precisely, the M-S-N sequence, since most of the hotter carbon stars of type R are not believed to belong to this evolutionary path, see Sect. 1.3.3

Several alternative binary models have been proposed (Little-Marenin et al. 1988; Le Bertre et al. 1990; Lloyd Evans 1990; Barnbaum et al. 1991); however it is not clear whether the binary system should contain (i) a carbon giant and an oxygen-rich giant or (ii) a carbon giant and a dwarf companion, with oxygen-rich matter, ejected by the previously oxygen-rich giant, trapped within the binary system. There are also some evidences that these silicate carbon stars are in fact J-type carbon stars (i.e., they are ^{13}C -rich), which may be an important clue to understand their status (Lloyd Evans 1990; Lloyd Evans 1991; Lambert et al. 1990).

Hence the adequation of the M-S-C sequence for all AGB stars is still subject to some uncertainties.

Another uncertainty concerns the detectability of various s-process elements. In principle, once dredge-ups have started, all the stars should display s-process elements. Yet it is worth noting that all the s-process elements (i) are not produced in equal amounts, and (ii) do not become detectable at the same abundance level. For example, if the ZrO bands do not become observable at the same time as the Tc lines, one could expect to observe, on the TPAGB, *technetium-poor S stars* or *Tc-rich M stars*.

The predicted surface abundances of Zr and Tc are plotted in Fig. 1.3 (Goriely 1999) as a function of the number of thermal pulses for two different stellar masses at solar metallicity. The ratio of the semi-convective mass with respect to the pulse mass is chosen as $\lambda_{SC} = 0.1$, while the ratio of the dredged-up mass with respect to the pulse mass is taken as $\lambda_{DU} = 0.05$.

The following observational detection thresholds have been adopted and drawn with horizontal lines on Fig. 1.3: Vanture et al. (1991) find that M stars without Tc have $\log[N(\text{Tc})/N(\text{Ti})] < -4.8$. The Tc detection threshold has thus been set at $\log[N(\text{Tc})/N(\text{Ti})] = -5$. A Zr overabundance of 0.2 dex corresponds to barely detectable Zr enhancements and has been adopted as a transition value between M and S stars ($\log[N(\text{Zr})/N(\text{Ti})] = -2.2$).

With this choice of detection thresholds and model parameters, a $1.5M_{\odot}$ star exhibits zirconium *after* showing technetium (the situation for the $3M_{\odot}$ star is less clear-cut because of the strong dilution of s-process elements in its more massive atmosphere). This would explain the puzzling Tc-rich M stars: Sanner (1978), Little-Marenin & Little (1979) and Little et al. (1987) found 37 Tc-rich M stars (among which 11 “certainly” Tc-rich, and the rest “probably” Tc-rich), versus 127 Tc-poor M stars (among which 58 “certainly” Tc-poor, and the rest with “doubtful” Tc). These Tc-rich M stars are predominantly found among Mira variables with periods exceeding 300 days. The zirconium abundances derived for Tc-rich M stars are on average (slightly) higher than that of Tc-poor M stars and similar to that of Tc-rich MS stars (Vanture et al. 1991); hence some of these stars may well be intermediates between M and MS-S stars, and will possibly all turn as weakly s-process enhanced stars as abundances determinations gain precision.

This picture is, however, oversimplified, and there is actually some room for variations:

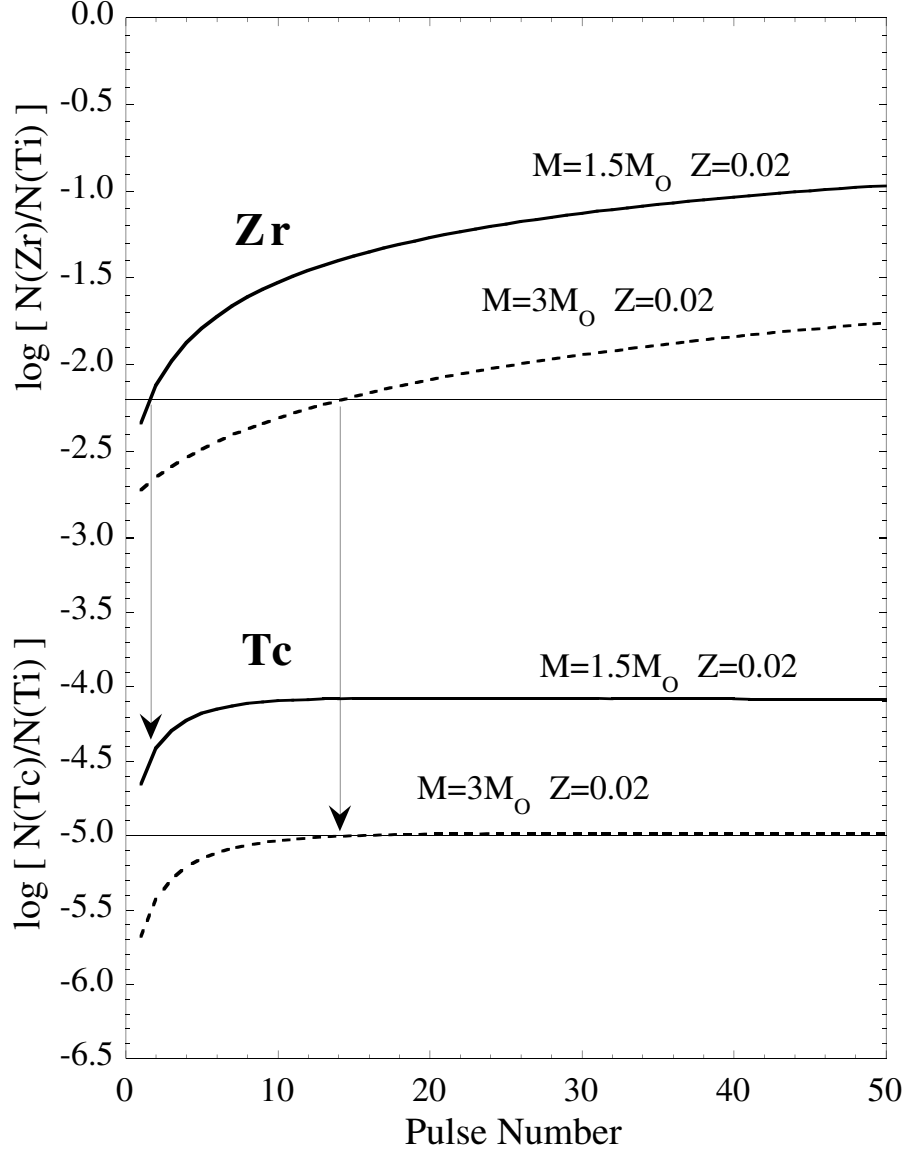


Figure 1.3: Evolution of the surface abundances of zirconium and technetium (normalized to Ti) as a function of the pulse number (Goriely 1999). The solid horizontal lines at $\log[N(\text{Tc})/N(\text{Ti})] = -5$ and $\log[N(\text{Zr})/N(\text{Ti})] = -2.2$ roughly correspond to the detection thresholds for technetium and for enhanced zirconium, respectively

- the adopted Zr and Tc detection thresholds contain some degree of arbitrariness; in particular, Tc abundance determinations suffer from large uncertainties;
- the model parameters λ_{SC} and λ_{DU} are of major importance for deriving the Tc and Zr surface abundance curves in Fig. 1.3, but they are poorly known;
- another implicit hypothesis in the above scheme is that a dredge-up occurs after every pulse (i.e., every $\sim 1 - 3 \times 10^5$ yr). However, Busso et al. (1992) argued that if stars experience dredge-up only rarely (every 8-10 pulses) some TPAGB stars without technetium should be observed, because the time delay between the dredge-up events will be long enough for Tc to decay below detectable levels;
- finally, the temperature dependence of the Tc half-life must be considered: the high temperatures encountered during thermal pulses strongly shorten the effective half-life of ^{99}Tc ($t_{1/2} \sim 1$ yr at $\sim 3 \times 10^8$ K, Cosner et al. 1984). However the large neutron densities at these high temperatures more than compensate the reduction of ^{99}Tc life-time (Mathews et al. 1986) and enable a substantial technetium production. Third dredge-up episodes then carry technetium to the envelope, where it decays steadily at its terrestrial rate of $t_{1/2} = 2.13 \times 10^5$ yr. Starting from an abundance corresponding to the maximum observed one, technetium should remain detectable during $1.0 - 1.5 \times 10^6$ yr (Smith & Lambert 1988).

Nevertheless, Straniero et al. (1995) advocated that the s-process nucleosynthesis mainly occurs during the interpulse. When technetium is engulfed in the subsequent thermal pulse, it will decay at a fast rate because of the high temperature, and will not be replenished if there is no neutron source operating within the pulse itself. The conclusion that s-process enriched TPAGB stars should necessarily exhibit technetium would then be challenged. However, recent calculations (Goriely 1999) show that the temperatures encountered inside a thermal pulse are not high enough everywhere in the pulse and during enough time in order to destroy technetium significantly.

Given these uncertainties, the aim of Fig. 1.3 is mainly to stress that the M-S-C evolutionary sequence probably leaves room to explain some Tc-rich M stars; similarly, the existence of Tc-poor S stars belonging to this very same evolutionary channel (supposing then that ZrO becomes detectable *before* Tc) cannot a priori be excluded. For these latter stars however, a more likely scenario will be presented in Sect. 1.2 and further confirmed in the main part of this work.

- *Metallicity dependence*

Since a lower amount of dredged-up carbon is needed to achieve C>O in low-metallicity stars, the ratio of C to M giants is expected and observed to increase as metallicity decreases (e.g., Groenewegen 1999). Moreover, the dependence

of the giant branch temperature on metallicity (hotter if more metal-poor), may lead to a smaller number of M stars in metal-poor environments, because they will rather show off as K stars. This will further strengthen the trend of increasing C/M stars ratio with decreasing metallicity.

As far as S stars are concerned, column density calculations predict that the hotter stars will need larger abundance enhancements to make ZrO detectable (Piccirillo 1980). All these arguments suggest that S stars are probably less numerous in a metal-poor environment.

1.1.4 Problems

This scenario however faced a problem with the discovery of a class of stars that could fit in none of its predicted evolutionary phases: barium stars are a small group of G-K giants with definite overabundances in s-process elements, but much too low luminosities to be located on the thermally-pulsing AGB (Scalo 1976). Hence their overabundance patterns could not be understood by dredge-up of self-produced s-elements, and defied explanation for many years, until the contradiction was solved by invoking a binary scenario.

1.2 Stellar evolution of low- and intermediate-mass double stars

In the following we consider a system composed of a red giant (dubbed the *primary*) and a compact (main sequence or white dwarf) companion (the *secondary*).

1.2.1 Binary interaction

To what extent can binarity influence the evolution of low- and intermediate-mass giants as described in Sect. 1.1.2? In fact, *close binaries* are defined as binary systems in which some significant interaction – other than simple gravitational attraction between point masses – takes place. If the orbital semi-major axis becomes sufficiently small with respect to the stellar radii, either because of the expansion of a star (due to its own evolution) or by orbital contraction due to angular momentum losses, then interaction will occur. The interaction may be radiative, as in the heating of the surface of one component by the hot companion, or it may be tidal, distorting both components through the combination of gravitational and centrifugal effects.

The possible interactions are:

- **rotational synchronization and orbital circularization:** because of tidal effects on the envelope of the giant star, the rotational period of the extended star locks on the orbital period and the eccentricity of the system decreases.

• **mass transfer:** The mass transfer modalities depend on the size of the Roche lobe. In the Roche approximation it is assumed that (i) two stars rotate about their center of mass in a circular orbit, (ii) the gravitational fields of the two stars can be described by those of two point masses, (iii) the stars are in synchronous rotation with the orbital motion. The precise form of the resulting potential was first discussed by Roche. It can be shown that the isobars coincide with equipotential surfaces, hence the shape of the binary components will be that of the Roche equipotential surfaces. Close to each star, the potential is dominated by the gravitational potential of that star, thus the equipotential surfaces are almost spherical. Moving farther from a stellar center, two effects become important: (i) the tidal effect of the companion, which causes an elongation in the direction of the companion, and (ii) flattening by the centrifugal force. Consequently, the equipotential surfaces are distorted and almost pear-shaped in a way that their largest dimension is along the line of center (e.g. Livio et al. 1992). The equipotential surface passing through the point where the Roche potential vanishes along the line of centers ($= L_1$, the inner Lagrangian point) is defined as the *Roche lobe*. The critical *Roche radius*⁴ is defined as the radius of a sphere that has the same volume as the Roche lobe. The importance of the Roche lobe lies in the fact that stars that fill their Roche lobe start to transfer mass through the inner Lagrangian point L_1 to their companion.

The binary star nomenclature depends on the degree to which one or both components fill their Roche lobe: binaries are named *detached* if neither component fills its Roche lobe, and *semi-detached* or *contact* if respectively one or the two component(s) are filling their Roche lobe.

In detached systems, mass transfer can occur through wind accretion (Boffin & Jorissen 1988), while semi-detached systems experience Roche-lobe overflow (RLOF). When a star fills its Roche lobe, an infall of gas occurs towards the secondary star. Because of the angular momentum of this gas, it cannot fall directly onto the star and forms an accretion disc inside the Roche lobe. As this process is ongoing, more and more gas gets ejected into the ring and friction causes the gas to lose angular momentum, allowing the matter in the disc to spiral down and to be accreted onto the secondary.

1.2.2 A binary evolutionary sequence

The evolution of two low- or intermediate-mass stars belonging to a binary system is illustrated in Fig. 1.4 (Jorissen 1999; Jorissen & Van Eck 1999). Only the situation leading to the formation of stars polluted in carbon and s-process elements is considered⁵.

⁴Several approximations are available in the literature for the Roche radius (around star 1) as a function of the orbital separation A and the mass ratio $q = M_1/M_2$. For example, Eggleton (1983) derives:

$$R_{LR} = A \times \frac{0.49q^{2/3}}{0.6q^{2/3} + \ln(1 + q^{1/3})}$$

⁵This is of course a very restricted view of the binary star evolution problem, that involves a wealth of exotic evolutionary paths leading, e.g., to Algol stars, cataclysmic variables, helium

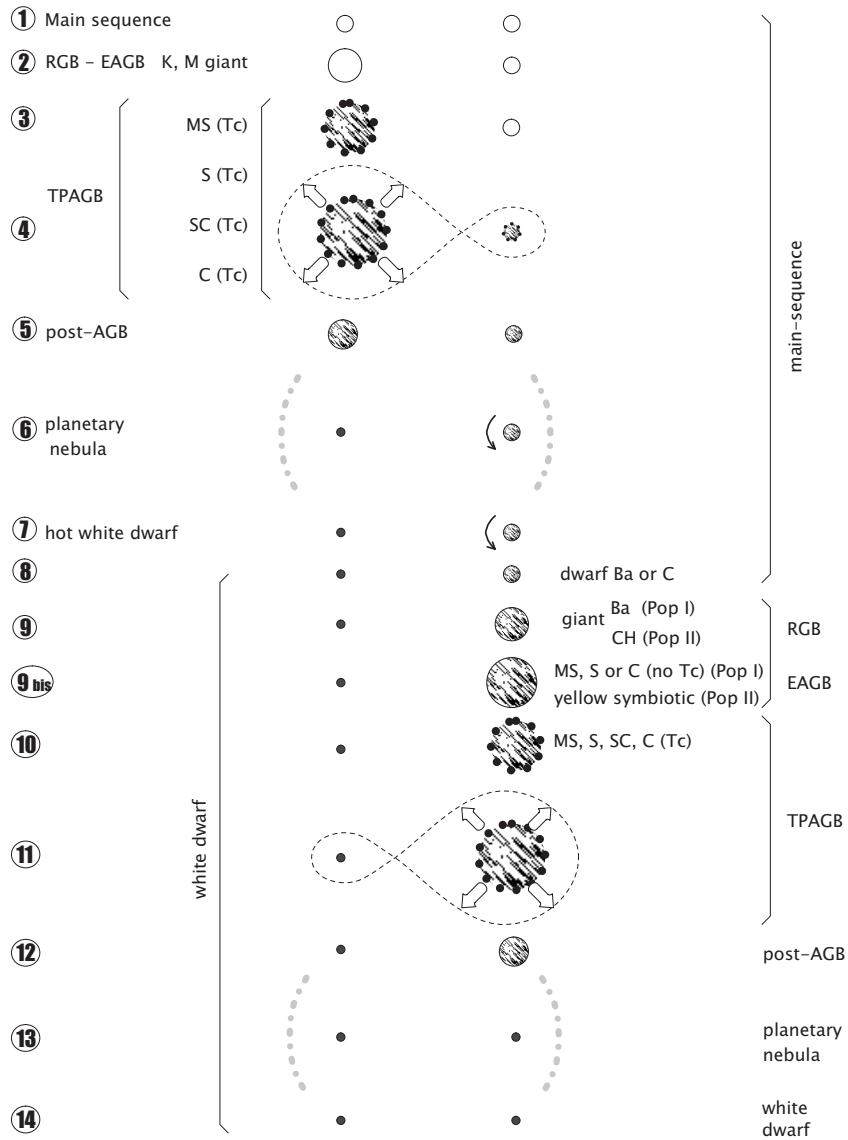


Figure 1.4: Binary evolution involving two low- or intermediate-mass stars. Modifications in the orbital elements are not represented; it is supposed that no cataclysmic outcome – e.g. merging of the components – interrupts the evolution before the final white dwarf pair state. Stars with excess carbon and s-process elements at their surface are filled with grey clouds, and stars that show Tc have a thick dotted border. The numbers refer to explanations in the text

In the left column of Fig. 1.4 are represented the spectral families not requiring binarity, whereas the right column identifies classes of peculiar stars requiring binarity. The successive evolutionary phases are now briefly presented, as well as their observational counterparts; Sect. 1.3 will provide more detailed information on each family of peculiar red giants.

- **Phase 1: Binary main sequence stars:** this starting point is known to be a common one, since many binaries are found among main-sequence field stars (Duquennoy & Mayor 1991; Fischer & Marcy 1992).

It is worth a brief digression concerning the frequency of multiple systems in unevolved stars. In the Taurus-Auriga association (the most extensively surveyed star-forming region), a lower limit of 51% is quoted (Mathieu 1994). The binary rate among main-sequence stars amounts to $\sim 2/3$ for main-sequence G stars (Duquennoy & Mayor 1991), $\sim 45\%$ for main-sequence K stars (Mayor et al. 1992) and to $\sim 40\%$ for main-sequence M stars (Fischer & Marcy 1992). However, when extrapolation is made to compare the same range of orbital separations, the frequency of pre-main-sequence binaries and higher-order systems may be in excess (by a factor 2-4) of that found among field main-sequence stars. To explain the possible overabundance of pre-main-sequence binaries, one may invoke time evolution of the semi-major axis of the system, including possible cases of disruption. In an alternative scenario, the bulk of the field population is to be formed in dense stellar clusters (e.g. Lada et al. 1991; Kroupa 1995) where binaries are easily disrupted, and are later dispersed into the field; the similar binary frequency found in the Trapezium cluster core and among main-sequence field stars is compatible with this hypothesis (Petr et al. 1998).

However large uncertainties still exist, both because of small sample sizes and incompleteness problems, and because different observational techniques are used for the detection of pre-main-sequence and main-sequence binaries, therefore implying different detection biases.

- **Phase 2: Normal giant + main sequence star:** The more massive star (the primary) leaves first the main sequence and may be observed as a binary normal giant while being a RGB, core-helium burning or early-AGB giant. Observational counterparts are the field binary giants listed in Boffin et al. (1993), and the open clusters binary giants of Mermilliod (1996), though the main-sequence nature of their companion is not guaranteed in all cases.

- **Phase 3: TPAGB star + main sequence star:** The binarity of TPAGB stars is very difficult to detect because such evolved stars have a turbulent atmosphere. The S star π^1 Gru is however known to be the primary of a wide (~ 400 AU) binary system, whose secondary is a solar-mass main-sequence star (Feast 1953; Proust et al. 1981; Ake & Johnson 1992). T Sgr also enters this class (Culver & Ianna 1975). Recently the orbital motion of a dozen of Mira and semi-regular variables has been detected (Hinkle et al. 1999). Many more additional candidates may come from MACHO observations that

stars, binary pulsars, black hole binaries, Thorne-Żytkow objects, type Ia supernovae, etc. For a larger overview of binary star evolution, see Iben (1991)

possibly discovered numerous ($\sim 25\%$ of AGB stars) semi-detached AGB Miras in the Large Magellanic Cloud (Wood et al. 1999). Depending on their Roche geometry, their s-process overabundances and on the nature of their compact companion, such binary Miras either belong to this phase, phase 4, 10 or 11.

• **Phase 4: TPAGB star + main sequence star + mass-transfer:**

At this phase, the companion accretes s-process- and carbon-enriched matter lost by the TPAGB star. Some symbiotic systems may be in that situation: they indeed consist of a mass-losing red giant, a compact companion (generally a main-sequence or a white dwarf star), a nebula surrounding the system and an accretion disk surrounding the secondary. Since not all symbiotics are filling their Roche lobe, mass transfer may also occur through wind accretion. Hence some of them (the TPAGB symbiotics) constitute observational counterparts of either phase 4 or 11, depending on the nature of their companion.

• **Phase 5: Post-AGB star + main-sequence star:**

Binarity is a widespread phenomenon among post-AGB stars (Van Winckel 1992, 1995, 1998a, 1999abc; Waters et al. 1993; Pollard et al. 1996; Hrivnak 1999), but their mass functions⁶ do not always allow to distinguish between a main sequence and a white dwarf companion, hence they may belong to either phase 5 or 12.

• **Phase 6: Binary nucleus of planetary nebulae: Abell 35 system:**

Abell 35 systems are planetary nebulae with wide binary nuclei, consisting of an extremely hot, hence young, white dwarf and a late-type (G-K) rapidly rotating dwarf, probably spun-up by a previous accretion event.

• **Phase 7: Hot white dwarf + rapidly rotating s-process-enriched main-sequence star: WIRRing stars:** Here are probably located the recently-discovered WIRRing stars (*Wind-Induced Rapidly Rotating*); they consist of a rapidly rotating, s-process-enriched K dwarf with a hot white dwarf companion.

• **Phase 8: Main-sequence s-process- and carbon-enriched star + white dwarf companion:** At this stage the white dwarf has become cool enough to be very difficult to detect; and the binary system is observed as a main sequence star showing carbon and s-process overabundances (no technetium, because it had enough time to decay). Such binary main-sequence s-process-enriched stars have been identified as *dwarf barium stars* and as the *CH subgiants*. Main-sequence carbon-enriched stars are also observed as *dwarf*

⁶Observations of a single-lined spectroscopic binary system readily provide the radial velocity semi-amplitude K , the period P and the eccentricity e of the orbit, hence the *mass function*, where the stellar masses (M_1 and M_2) and the inclination (i) of the orbit with respect to the line of sight appear in an inseparable combination (K and P in km s^{-1} and days, respectively):

$$f(M) = \frac{[M_2 \sin(i)]^3}{(M_1 + M_2)^2} = 1.036 \times 10^{-7} K^3 P (1 - e^2)^{3/2} (M_\odot)$$

carbon stars; a dozen are known. Dwarf S stars might also exist, though none has been identified yet.

• **Phase 9 and 9bis: s-process- and carbon-enriched giant stars + white dwarf companion:** Depending on their effective temperature, the observational counterparts of this evolutionary phase show off differently:

- ▷ G-K giants enriched in s-process elements will be classified as *barium stars*; they are technetium-poor, because Tc had time to decay since the mass transfer event (phase 9);
- ▷ M giants enriched in s-process elements will be classified as *S stars*, because ZrO molecular bands will be able to form and to be observed in these cooler stars (phase 9bis);
- ▷ Whether stars in this evolutionary phase can be observed as *carbon stars* is not yet firmly demonstrated, though it is very likely;
- ▷ *Yellow symbiotics* also enter this category, since they belong to interacting binary systems composed of a G-K giant with s-process overabundances and a white dwarf.

• **Phase 10: TPAGB star + white dwarf:** As for phase 3, binarity is very difficult to detect in TPAGB stars. A possible case is the non-conformist Tc-rich S star σ^1 Ori known to have a white dwarf companion (Ake & Johnson 1988). Some among the binary long-period variables of Hinkle et al. (1999) and Wood et al. (1999) may also enter this category.

• **Phase 11: TPAGB star + white dwarf + mass-transfer:** Here are found the TPAGB symbiotic stars with a white dwarf companion.

• **Phase 12: Post-AGB star + white dwarf:** Some of the post-AGB binaries (Van Winckel 1999) may enter this category.

• **Phase 14: Double degenerates:** Binary systems composed of two white dwarfs have been discovered only recently (Saffer et al. 1988, 1998) although they are believed to be extremely common (roughly 10% of all white dwarfs; Maxted & Marsh 1999); they are predicted (and observed) to be very short periods (1.5 hours \lesssim P \lesssim 1 week), probably because of the consequences of the previous mass transfer events.

1.3 Some families of red giant stars

A brief description of various stellar families of cool stars, some of them presumably involved in the binary scenario, is given below, with special emphasis on the techniques used to expose the binary stars that mimic single TPAGB giants.

1.3.1 Barium stars

Barium stars were first identified by Bidelman & Keenan (1951) as G-K giant stars with abnormally strong lines of Ba II and Sr II as well as strong CH G bands, and sometimes strong CN and C₂ bands.

Since Warner (1965), a visual estimate of the Ba II $\lambda 4554$ line strength is used to characterise the abundance peculiarity, on a scale from 1 to 5. Later on, Keenan & Pitts (1980) introduced *semi-barium stars* (or *marginal barium stars*) with Ba indices between 0.1 and 0.9. However, these indices do not provide a robust appreciation of the chemical peculiarities involved, mainly because the Ba II $\lambda 4554$ line is somewhat sensitive to stellar luminosity; therefore, normal bright giants have often been misclassified as marginal barium stars (Smith & Lambert 1987; McWilliam 1990). Keenan & McNeil (1989), aware of this problem, decided to drop the barium stars indices below 0.3 from their subsequent spectral classification.

Abundance studies (e.g. Burbidge et al. 1957; Lambert 1985) have shown that these strong lines are not solely caused by luminosity effects but by real overabundances of heavy elements. In addition to barium and strontium, other heavy elements are also enhanced, principally Y, Zr, La, Ce, Pr, Nd and Sm. Furthermore, there is clearly a real range of overabundances among barium stars (e.g. see the spectrophotometric work of Williams 1975); therefore barium stars are customarily divided between *strong barium stars* (Ba 1 to 2-2.5) and *mild barium stars* (Ba 2.5 to 5).

Interestingly, the two groups seem to have different mean ages and luminosities (Catchpole et al. 1977; Mennessier et al. 1997): mild barium stars would have kinematic properties similar to those of early F stars, and would be younger and more luminous on average than strong barium stars.

In fact a third group of stars, the *metal deficient barium stars* (or *weak-lined barium stars*) has been reported (MacConnell et al. 1972; Catchpole et al. 1977; Yamashita & Norimoto 1981); it is not clear whether they are transition objects between the Population I barium stars and their Population II analogs (the CH stars, see Sect. 1.3.3), or whether they are truly Population II objects but with $C/O < 1$ (unlike CH stars).

As already noted, it was soon recognised (Scalo 1976) that barium stars, despite their s-process enhancements, were too warm and of too low a luminosity to be on the thermally-pulsing AGB. This has been further confirmed with HIPPARCOS parallaxes (Bergeat & Knapik 1997; Mennessier et al. 1997): barium stars clearly concentrate between $M_v \sim 3$ and -1.5 [which corresponds roughly to $M_{bol} \sim 2.4$ and -2.2 with bolometric corrections taken from Landolt & Börnstein (1982)]. This is clearly too low a luminosity as compared to the predicted thermal pulse luminosities ($M_{bol} \sim -4$ for $1.2M_{\odot}$ star, Boothroyd & Sackmann 1988).

The discovery that many barium stars belong to binary systems (McClure et al. 1980; McClure 1983; McClure & Woodsworth 1990) solved the problem of their s-process overabundances: when the current WD companion of the

barium star was a thermally-pulsing AGB star, it transferred s-process- and C-rich material onto its companion, which may now be observed as a barium or CH star (phase 9 of Fig. 1.4).

Several studies have attempted to detect the UV radiation of the white dwarf companion of barium stars, but only in very few cases firm detections (ζ Cap, ζ Cyg, HD 165141, 56 Peg, χ^1 Cet)⁷ or possible detections (ν^2 Cas, HD 65699) could be established (Schindler et al. 1982; Dominy & Lambert 1983; Böhm-Vitense et al. 1984; Böhm-Vitense & Johnson 1985; Fekel et al. 1993). The paucity of systems with confirmed white dwarf companions – as compared for example to companion detections for dwarf carbon stars, see Sect. 1.4.1 – probably results from the much larger distances of giant stars.

Barium stars are not expected to show technetium, because this s-element had enough time to decay since the mass transfer event. Tc I was searched but not found in barium stars (Burbidge & Burbidge 1957; Warner 1965; Boesgaard & Fesen 1974). In fact, technetium is expected to be primarily ionized in these relatively hot giants (see Table 5.3); hence Tc II was also searched for in the UV spectral region with IUE (Little-Marenin & Little 1987), with negative results.

1.3.2 S stars

Spectroscopy

The S class was originally defined by Merrill (1922), to designate a group of curious red stars which did not fit well into either class M (TiO stars) or classes R and N (carbon stars); hence the resulting class was somewhat heterogeneous (e.g. some barium stars were called 'S'). The original prototypes of the class were π^1 Gru and the two long-period variables R And and R Cyg. Keenan (1954) clarified the situation by accepting only as S stars those exhibiting ZrO bands. Hence the spectra of S stars resemble those of M stars but with disappearing bands of TiO and additional bands of ZrO and sometimes LaO. If the ZrO bands are weak or can be seen only at dispersion higher than 100-200Å/mm at H_γ , the star is called *MS*. *Pure S stars* are those S stars where the TiO bands (characteristic of M stars) are not visible any more. Lines of s-process⁸ elements like Y, Sr, Zr, Ba and La are also enhanced in S stars.

The classification rules for S stars have regularly changed with time. Keenan (1954) devised a two-parameter system [Sx,y with x and y temperature and abundance (ZrO) indices, respectively] based upon the relative intensity of the TiO and ZrO bands. The abundance class has often been taken as indicating the “S-ness” of a star: S stars are referred to as “weak”, “mild”, “intermediate” or “strong” for increasing abundance classes. In a later work, Keenan & McNeil (1976) changed slightly the procedure using a temperature index and two separate estimates of the strength of ZrO and TiO bands on a scale from 0 (very

⁷Moreover, the reality of the heavy-element overabundances has been questioned in the case of 56 Peg (Luck 1977) and χ^1 Cet (Fekel et al. 1993)

⁸an accident of nomenclature, since the *slow* neutron capture process was unknown when the S spectral type was introduced

weak) to 5 (very strong), hence eliminating the abundance parameter. Some other notations are found in the literature; for example MacConnell's classification (MacConnell 1979) uses simply a $Sm * n$ format, where m is the TiO band strength, and n the ZrO band strength.

All these classification rules are successful in isolating S stars from other late-type stars, but are inadequate in establishing temperature and abundance classes. As shown by early molecular-equilibrium calculations (Scalo & Ross 1976; Piccirillo 1980), the prime cause for this failure is the large effect of a star's C/O ratio on its molecular band strengths; for example this classification cannot properly handle SC stars. This criticism was voiced among others by Ake (1979), who proposed a solution using the strength of the Na D lines, commonly used in carbon stars, as well as the ZrO and TiO intensities, in defining the temperature index. He also devised an abundance index based upon the strengths of ZrO, TiO and YO, and presumably related to the C/O ratio. Keenan & Boeshaar (1980) rediscussed the problem once more and adopted a new classification Sx/y , where the temperature index (mainly based on TiO, ZrO and LaO band strengths) is quoted before the slanting line, and the C/O index (based on TiO, ZrO, YO bands strengths and Na D lines) after.

In fact, a definite classification of S stars should probably await dedicated model atmospheres in order to properly disentangle the effects of C/O, s-process enhancements and temperature.

S star catalogues

S stars are rare: among the 9110 stars of the Bright Star Catalogue (Hoffleit & Jaschek 1991), 518 (=5.7%) are M or S giants, among which only 10 (=2%) are of type S.

The currently most extensive catalogue of S stars is the *General Catalogue of Galactic S Stars, 2nd edition* (GCGSS, Stephenson 1984) with 1347 objects (it updated the 1976 *General Catalogue of S stars* that listed 741 stars). Moreover, Table 2 of the *General catalogue of cool C stars, 2nd edition* (Stephenson 1989) lists a number of S (or MS or SC) stars previously misclassified as C stars, and about 75 new S stars were also reported by Stephenson (1990); hence some 1435 S stars are known to date. The GCGSS unfortunately contains several stars misclassified as S, as listed in Table 1.1, mostly communicated by Jorissen (1998, priv. comm.). Many are M supergiants (because of the confusion of strong CN bands close to 7910Å with LaO bands, Lloyd Evans & Catchpole 1989), some are M giants, other are M dwarfs (probably because at low plate resolution CaH λ 6385 falls close to ZrO λ 6474).

Chemical peculiarities

The presence of ZrO bands has often been considered as a direct consequence of molecular equilibrium in the special circumstances where the atmospheric C/O ratio is within 10% of unity (e.g. Scalo & Ross 1976). However, Piccirillo (1977)

Table 1.1: Stars misclassified as S. In column 1, S90-nn refers to the list of Stephenson (1990). In column 2, the WO number refers to the Westerlund & Olander (1978) sample. Stars tagged ‘Stephenson M stars’ by Smith & Lambert (1990) are included as well, and are denoted by ‘Ste M’ in column 3

GCGSS	Name	revised Sp. Typ.	Ref.
22	HD 6409 = BD+18°145	M?	Smith & Lambert (1988)
25	YZ Cet	dM5.5e	Stephenson (1986); MacConnell (1997)
149	NO Aur	M2Iab	Bidelman (1998, priv. comm.)
247	HD 262427	?	Jorissen et al. (1998)
341	TT CMa	M8–10	Lloyd Evans & Little-Marenin (1999)
359	Hen 22	K3-5III	this work
382	NZ Gem	M3 II-III	Keenan & McNeil (1989)
500	HR 3296	M3- III	Keenan & McNeil (1989)
539	WO7	M1.5	Lloyd Evans & Catchpole (1989)
544	HIC 42650	early M dwarf	Van Eck et al. (1998)
566	+06°2063	Ste M	Smith & Lambert (1990)
569	WO9	M1.5	Lloyd Evans & Catchpole (1989)
648	WO15	M4	Lloyd Evans & Catchpole (1989)
722	HD 96360	Ste M	Smith & Lambert (1990)
726	WO22	M2-	Lloyd Evans & Catchpole (1989)
738	WO25	M5.5	Lloyd Evans & Catchpole (1989)
771	WO28	M2.5	Lloyd Evans & Catchpole (1989)
776	WO31	M3	Lloyd Evans & Catchpole (1989)
780	LTT 13336	M3V	Stephenson (1986); MacConnell (1997)
796	HR 4755	M3-IIIa	Keenan & McNeil (1989)
805	WO34	M2	Lloyd Evans & Catchpole (1989)

Table 1.1: (continued)

GCGSS	Name	revised Sp. Typ.	Ref.
806	WO35	M2	Lloyd Evans & Catchpole (1989)
828	WO39	M2	Lloyd Evans & Catchpole (1989)
847	WO40	M2+	Lloyd Evans & Catchpole (1989)
868	WO44	M3:	Lloyd Evans & Catchpole (1989)
871	WO46	M2	Lloyd Evans & Catchpole (1989)
873	Hen 154	G8III	this work
875	LTT 14486	M2V	Stephenson (1986); MacConnell (1997)
886	WO48	C	Meadows et al. (1987)
888	WO49	M2	Lloyd Evans & Catchpole (1989)
890	WO50	M2.5	Lloyd Evans & Catchpole (1989)
893	WO52	early type?	Lloyd Evans & Catchpole (1989)
897	WO53	M3	Lloyd Evans & Catchpole (1989)
905	WO55	M5-6	Lloyd Evans & Little-Marenin (1999)
919 ^a	WO58	early type?	Lloyd Evans & Catchpole (1989)
	PK 332-0.2	misclassified PN; Me?	Acker et al. (1987)
924	WO60	M4	Lloyd Evans & Catchpole (1989)
925	WO61	M3	Lloyd Evans & Catchpole (1989)
933	WO63	M2	Lloyd Evans & Catchpole (1989)
934	WO64	M2	Lloyd Evans & Catchpole (1989)
937	HD 150922 = $-13^{\circ}4495$	Ste M	Smith & Lambert (1990)
942	WO65	M2.5	Lloyd Evans & Catchpole (1989)
943	Hen 169	carbon	reclassified in Rybski's thesis (Stephenson 1984)
944	WO66	M1.5	Lloyd Evans & Catchpole (1989)
951	WO68	M1.5	Lloyd Evans & Catchpole (1989)

Table 1.1: (continued)

GCGSS	Name	revised Sp. Typ.	Ref.
952	WO69	M3:	Lloyd Evans & Catchpole (1989)
956	WO70	M3	Lloyd Evans & Catchpole (1989)
957	WO71	M5	Lloyd Evans & Catchpole (1989)
1031	HD 167539 = +16°3426	Ste M	Smith & Lambert (1990)
1034		M1-3	Lloyd Evans & Little-Marenin (1999)
1146		M8-10	Lloyd Evans & Little-Marenin (1999)
1178	HD 189581	Ste M	Smith & Lambert (1990)
1237		MV	MacConnell (1997)
1259	V1959 Cyg	M3	Lloyd Evans & Little-Marenin (1999)
1271	+22°4385	?	Jorissen et al. (1998)
1292			MacConnell (1999, priv. comm.)
1301	HD 214285 = BD−11°5880	M?	Smith & Lambert (1988)
1314	-	M4I	Winfrey et al. (1994)
1322	57 Peg	M4+IIIa	Bidelman (1998, priv. comm.)
S90-41	-	M8III	Winfrey et al. (1994)
-	HR 4088 = DE Leo	M	Lambert et al. (1995)
-	HR 7442	M	Lambert et al. (1995)

Notes: a. Star GCGSS 919 has various conflicting spectral classifications: it found its way into the catalogue of S stars from the Westerlund & Olander (1978) survey, but was later dismissed as S star by Lloyd Evans & Catchpole (1989), who proposed an early spectral type instead. It was also classified as a planetary nebula under the identification PK 332-0.2. Acker et al. (1987) do not confirm this classification and quotes two earlier spectral assignments as Me. An unpublished low-resolution (450-800 nm) spectrum obtained by the author in January 1997 at ESO with the Boller & Chivens spectrograph on the 1.52m-telescope reveals a perfect continuum with no visible spectral features except for a very broad and strong H α emission line obliterated on its blue side. It is thus very likely that this star has a variable spectrum. The various spectral classifications received over the years make it a good candidate symbiotic star. It certainly deserves a close monitoring.

has shown that the above statement is only valid for stars with $T_{\text{eff}} < 3000\text{K}$. At higher temperature, the mere presence of ZrO attests a real Zr enhancement.

As far as TiO is concerned, the reduced strength of TiO in the spectra of S stars, as compared to M stars, is a direct indication of C/O values greater than the solar value of 0.6 (Piccirillo 1977). Hence the absence of S stars with strong TiO *and* strong ZrO indicates that there is no substantial s-process enhancements in stars with solar C/O. Piccirillo thus concludes that S stars are characterised by a reduced supply of free oxygen *and* an enhanced supply of s-process elements.

Subsequent detailed abundance analyses (e.g., Smith & Lambert 1990) have shown that the overabundance pattern for the elements heavier than Fe bears the signature of the s-process nucleosynthesis (Käppeler et al. 1989).

Dichotomy

Because their spectra can have some common features with either those of M or C stars (as proved by the very existence of the MS and SC spectroscopic classes), and because they bridge an abundance gap between oxygen and carbon stars, all the S stars were traditionally considered as transition objects between normal M giants and carbon stars on the AGB (Sect. 1.1.3).

However, some early studies already pointed at a possible dichotomy in the S star family: Keenan (1954) noted from motions and galactic distribution considerations that there was a considerable dispersion in absolute magnitudes of S stars. Takayanagi (1960) distinguished Mira S stars (with $M_v \approx -3$) from non-variable and small-amplitude variable S stars (with $M_v \approx 0$). Yorke & Wing (1979) found a similar dichotomy, with $M_v \approx -1.5$ to -2 and $M_v = -1$ for Mira and non-Mira S stars, respectively. Hence evidences for a possible dichotomy inside the S family was suspected quite early⁹.

Surveys for technetium in S stars (Little-Marenin & Little 1979) later revealed that not all S stars exhibit Tc lines. A breakthrough in our understanding of the evolutionary status of S stars came with the realization that Tc-poor S stars could be the cooler analogs of barium stars, a suspicion first explicated by Iben & Renzini (1983), and later confirmed by additional technetium observations (Little et al. 1987; Smith & Lambert 1988): the binary scenario (Fig. 1.4) predicts that there should exist *two kinds* of S stars:

- ▷ S stars in phase 3 (*bona fide* TPAGB stars); they are called *intrinsic S stars*
- ▷ S stars in phase 9bis (binary masqueraders); they are called *extrinsic S stars*. By extension, all the stars that owe their chemical peculiarities to a mass transfer rather than to self-nucleosynthesis are called *extrinsic*.

Hence Tc-rich S stars can still be identified with genuine TPAGB stars dredging-up to the surface their home-made s-process elements (including Tc),

⁹The S stars “seem to be a mixture of two subgroups of stars with different space distribution” (Mavridis 1971)

but Tc-poor S stars emerge from a totally different evolutionary history, owing their chemical peculiarities to the accretion of s-process-rich matter from their companion (formerly a TPAGB star, now an undetected white dwarf). As barium stars, they are technetium-poor, because enough time has elapsed for the technetium to decay since the mass transfer event.

In fact, the dichotomy noted in the early days (Keenan 1954; Takayanagi 1960), although solely based on photometric variability properties, bore some resemblance with the technetium dichotomy (Tc-poor stars being predominantly non-variable, and Mira S stars Tc-rich); however, the non-variable group was most probably polluted by many Tc-rich, intrinsic stars.

(Interacting) binaries

Subsequent radial velocity surveys (Jorissen & Mayor 1988; Brown et al. 1990; Jorissen & Mayor 1992) have clearly detected a high percentage of binaries among Tc-poor stars, as it is the case among barium stars. When observed with the IUE satellite, many Tc-poor S stars exhibit a hot UV continuum that can be attributed to a white dwarf companion (Johnson et al. 1993). Furthermore, several Tc-poor S stars like HD 35155 and HR 1105, as well as the mild barium star 56 Peg, exhibit a UV spectrum typical of interacting binary systems. The UV emission lines are probably associated with hot gas flows resulting from the accretion of the red giant wind by the white dwarf companion. Moreover, Tc-poor stars systematically exhibit the high excitation He λ 10830 line, like symbiotic stars but unlike Tc-rich stars or normal giants (Brown et al. 1990). Like in symbiotic systems, X-rays have been detected in the Tc-poor S stars HR 363 and HD 35155, as well as in the barium star HD 165141 (Jorissen et al. 1996).

Mass loss

Because they are located on the TPAGB, intrinsic S stars are supposed to suffer from a severe mass loss and thus to present evidence for circumstellar dust, contrarily to extrinsic S stars. Such evidence is provided by IRAS photometry, maser emission and CO circumstellar emission detection. However, several studies (Jura 1988; Chen & Kwok 1993; Bieging & Latter 1994; Sahai & Liechti 1995) do not really take into account the S star dichotomy (though testing the AGB evolutionary M-S-C sequence requires stellar samples devoid of any extrinsic components). Hence the results of Jorissen & Knapp (1998) are preferentially reported here (but see also Jorissen et al. 1993; Groenewegen 1993; Chen et al. 1998): the S stars are located in well-defined groups in the IRAS colour-colour diagram ([12]-[25], [25]-[60]), a partition reminiscent of, albeit not identical to, the one described by van der Veen & Habing (1988). The main results are the following:

- All Tc-poor S stars are non- or weakly- variable stars with undetectable circumstellar shells, thus suffering only a moderate mass loss ($< 2 \times 10^{-8} M_{\odot}/\text{yr}$).

Binarity does not increase their mass loss rates; however, the few binary *intrinsic* S stars are among the stars with the largest mass loss rates in the sample of Jorissen & Knapp (1998). Hence, binarity seems to influence mass loss in *evolved* stars, which may be of importance when designing mass transfer models.

- Tc-rich S stars may be divided into various subclasses:

(1) a few Tc-rich stars have undetectable circumstellar shells and thus have very low mass loss rates, similar to those of extrinsic S stars; these S stars have weak chemical peculiarities, barely distinguishable from normal giants;

(2) S stars with tenuous oxygen-rich circumstellar shells, fed by a small mass loss rate of a few $10^{-7}M_{\odot}/\text{yr}$; these are short-period ($P \sim 100$ to 150 days) semi-regular variables or short-period ($P < 500\text{d}$) Mira variables; they have weak chemical peculiarities;

(3) S stars with dense oxygen-rich circumstellar shells, with mass loss rates ranging from a few $10^{-8}M_{\odot}/\text{yr}$ to a few $10^{-5}M_{\odot}/\text{yr}$; they are predominantly long-period ($P > 300\text{d}$) Mira variables (see also Jura 1988) and have strong chemical peculiarities;

(4) S stars with strong chemical peculiarities (often classified as SC in the optical), with moderate mass loss rates of a few $10^{-8}M_{\odot}/\text{yr}$ to a few $10^{-7}M_{\odot}/\text{yr}$ with small wind velocities; they are mostly semi-regular (with periods ranging for 60 to 360 days) or irregular variables, with a few short-period ($P < 370$ days) Miras, and they are reminiscent of carbon stars;

(5) a few S stars have very extended IR shells, probably detached from their parent star, and cover a wide range in wind velocities and in mass loss rates, from a few $10^{-7}M_{\odot}/\text{yr}$ to several $10^{-6}M_{\odot}/\text{yr}$. They are often SC or CS stars.

Hence it is noteworthy that among the S family, the onset of a significant mass loss rate is concomitant with detectable overabundances imputable to the third dredge-up events.

Galactic distribution

Because S stars are relatively rare and because of their weird spectra, their galactic distribution still suffers from large uncertainties.

There has been a long “spiral arms” tradition: in the first study ever of the galactic distribution of S stars, Keenan (1954) found that S stars (excluding long-period variables) fall along spiral arms (as mapped by Morgan et al. 1953) whereas the long-period variables projected on the galactic plane only showed a random scatter. Nassau & Blanco (1954), though emphasizing the small size of their data sample (31 stars), suggested that the S star distribution was dissimilar to that of N stars, and that they appeared in groups which in some cases agreed in position with previously known concentrations of OB stars. Later, Takayanagi (1960) basically reached the same conclusions as Keenan.

As reported by Yorke & Wing (1979), many subsequent studies confirmed the spiral-arm nature of S stars or their coincidence with OB associations, simply because most of the early searches for S stars were carried out in the galactic plane. This situation prevailed until Henize reported briefly (1964, IAU Symposium No 24) on his survey covering the entire sky south of $\delta = -25^{\circ}$ (hence all

galactic latitudes). Going against main-stream beliefs, he noted (i) a substantial number of high latitude S stars, (ii) a much greater resemblance between S stars and the disk population late-M stars, than with young Population I objects in the spiral arms, and (iii) no significant difference between the surface distribution of variable and non-variable S stars.

Using more than 700 S stars (including the Henize sample), Yorke & Wing confirmed in a landmark paper (1979) the absence of correlation between the S star distribution and either OB associations or spiral arms; on the contrary, S stars were found to have the same age (or mixture of ages) as the normal red giants of types G, K and M. The derived scale heights were $z=230$ pc (if $M_v = -1.6$) for Mira S stars and $z=200$ pc for non-Mira S stars. Unfortunately the technetium dichotomy of S stars was unknown at that time, and here again, their non-Mira class is a mixture of intrinsic and extrinsic S stars. Similarly, Lloyd Evans & Catchpole (1989) studied the Westerlund-Olander sample of S stars (selected from the strength of the LaO bands, and thus strongly biased toward cooler, probably intrinsic, more extreme S stars) and concluded that the galactic distribution of S stars was not significantly different from that of carbon stars in the same field.

However, one cannot totally exclude that at least some S stars may belong to a much younger population, since e.g. the stars TT9 and TT12=WO23 seem to be physically associated with young clusters in the η Car complex and have high masses (Catchpole & Feast 1976).

The S star subgroups derived from infrared colours confirmed the presence of different galactic distributions: for example Jorissen et al. (1993) have shown that the mean intrinsic (according to IRAS colours: $[12]-[25] > -1.3$) S stars galactic latitude is 5° , whereas it is 12° if $[12]-[25] < -1.3$, i.e. for a mixture of extrinsic and intrinsic S stars (as it is for M giants). Interestingly, despite different magnitude distributions, M giants with $[12]-[25] > -1.3$ or < -1.3 appear to have *identical* galactic latitude distributions, in contrast to the situation prevailing for S stars. This further supports the idea that, unlike M giants, S giants are composed of two distinct stellar families.

Globular clusters

Curiously, there is only one galactic globular cluster known to have barium and S stars: ω Centauri (Lloyd Evans 1983b). This is undoubtedly a clue regarding the s-process nucleosynthesis or efficiency as a function of metallicity. ω Cen is the most massive globular cluster associated with the Galaxy. Whereas stars in most metal-poor globular clusters exhibit a single metallicity indicating a single, common formation or enrichment event, ω Centauri is unique in showing a wide spread of metallicity among the red giants, an evidence of a continuous self-enrichment of the cluster. The S stars of ω Centauri are fainter than normal TPAGB stars, which would point toward a binary explanation; however, the binary frequency of chemically peculiar stars was found to be unexpectedly low (out of 32 Ba, CH and S stars, only 2 (CH) binaries uncovered, Mayor et al. 1996). Either these stars were indeed enriched in the past by mass transfer

in soft binary systems which have been later dynamically disrupted, or they may represent the top of the range of metal abundance in ω Cen and thus have *primordial* abundance anomalies (Lloyd Evans 1983b; Vanture et al. 1994): a third formation channel for peculiar red giants may exist there.

1.3.3 Carbon stars

Carbon stars have been known for well over a century; they exhibit strong C_2 , CN and CH bands and no metallic oxide bands. They were soon separated in groups R and N (Pickering 1908). N stars exhibit a very strong depression in the violet part of their spectrum, while R stars have warmer temperatures. However, since the coolest R stars were very difficult to distinguish from the hottest N stars, Keenan & Morgan (1941) attempted to arrange all the carbon stars in one temperature sequence, ignoring the R and N dichotomy: this was the C_{x,y} system, where x is expected to be a temperature index while y is a C_2 strength index. This lumping of type N and R groups into the single C classification might have been a “regressive step” (Eggen 1972a), since it became gradually apparent that the early-R type and the N type described two different stellar types. The most relevant differences between early-R and N stars are that N stars have s-process overabundances, whereas early-R stars do not, and early-R stars have a low $^{12}C/^{13}C$ ratio, unlike N stars.

Therefore, a revision of the Morgan-Keenan system has been established by Keenan (1993), where the author divides carbon stars into a C-R sequence, a C-N sequence and a C-H sequence.

Technetium has been searched in carbon stars (Merrill 1955; Peery 1971; Little-Marenin & Little 1987; Smith & Wallerstein 1983), despite the extreme faintness of carbon stars in the region of the strong blue resonance lines of technetium (below 4300Å). Frequencies of 75% of carbon stars being Tc-rich are sometimes quoted but are subject to large uncertainties. As expected since they lack s-process enhancement, J stars (the ^{13}C -rich cool carbon stars) were found to be Tc-poor, but then a significant fraction of Tc-poor carbon stars remains; they may be the *extrinsic* carbon stars, i.e., analogs of S stars but with $C/O > 1$. This remains to be proven by a radial-velocity monitoring.

The galactic distribution of carbon stars (mainly of N stars, because they are the most easily detected in infra-red surveys) has been thoroughly studied (Dean 1976; Claussen et al. 1987; Kerschbaum & Hron 1992; Guglielmo et al. 1998) and is characterized by a scale height of ~ 200 pc.

N stars

They have temperatures comparable to normal giants of spectral type M3 or later; many are variable. Both their s-process enhancements (Utsumi 1985; Lambert et al. 1986) and their HIPPARCOS absolute magnitudes (Wallerstein & Knapp 1998) are compatible with their TPAGB status, except for the few which do not have s-process enhancements and which are also J stars (e.g. Lloyd Evans 1986).

Early R stars

While the later R stars are indistinguishable from the earlier N stars, the early R stars (R0-R3) form a distinct class of (predominantly) non-variable stars that are not losing mass. They are solar-metallicity carbon stars with temperatures corresponding to those of normal G and K giants ($4200 \lesssim T_{\text{eff}} \lesssim 5000\text{K}$, Dominy 1984). They have no technetium; in fact, unlike in N, S, Ba, CH, subgiant CH and dwarf carbon stars, no s-process enhancement at all could be detected (Dominy 1984). Too faint to be on the AGB, they rather lie near the barium and CH stars in the HR diagram (Scalo 1976; Alksnis et al. 1998). They might be related to the cooler J stars. The absence of any evidence of binary motion after a ~ 16 -year radial-velocity monitoring of 22 R stars (whereas the rate of spectroscopic binaries among normal late-type giants is $\sim 20\%$) led McClure (1997b) to suggest that early R stars might once have been binaries that have now coalesced (however such a coalescence is predicted to spin up the accreting star, which does not appear to be the case).

J stars

J type stars are characterized by strong isotopic bands of carbon; since their $^{12}\text{C}/^{13}\text{C}$ ratio is often low (3-9, whereas most N stars have $^{12}\text{C}/^{13}\text{C} > 20$, Utsumi 1985; Dominy 1985), they might be hot bottom burning stars. Some of them are the silicate carbon stars described in Sect. 1.1.3, and are possibly members of binary systems.

CH stars

The CH class is a rather ill-defined class of stars that are seen in dwarf spheroidal galaxies, in the galactic globular cluster ω Cen, and in the galactic halo. They were mostly classified as early-R stars before they were recognised as a separate class by Keenan (1942), who defined them as having strong CH bands, strong Swan bands of C_2 (indicating $\text{C}/\text{O} > 1$), strong resonance lines of Ba II and Sr II, strong H lines, weak lines of the iron-group elements and high radial velocities. The chief distinguishing feature between CH and R stars is the presence of s-elements overabundances in the former. Moreover CH giants have metallicities lower than $[\text{Fe}/\text{H}] = -1$, consistent with abundances in Population II stars (Vanture 1992a; Vanture 1992b; Vanture 1992c). All CH stars in the field are spectroscopic binaries (McClure 1984b; McClure & Woodsworth 1990). Provided that their companion is a white dwarf of $0.6M_{\odot}$, the CH stars have masses near $0.8 \pm 0.1M_{\odot}$ (McClure & Woodsworth 1990). They are thus believed to be the Population II equivalent of barium stars.

Yet a different situation arises in the LMC, where the luminous and blue CH stars discovered by Hartwick & Cowley (1988, 1991) presumably belong to a much younger population than the bulk of the LMC carbon stars (Suntzeff et al. 1993), and thus could be in a totally different evolutionary phase than galactic CH stars.

There are also a few low-velocity ($\lesssim 60 \text{ km s}^{-1}$) CH stars with disk-like motions, which Yamashita (1975) has classified as *CH-like* stars. They appear to have much larger masses than the classical red-giant CH stars, and at least some of them show no evidence of binarity (Vanture & Wallerstein 1999). Whether they really represent a separate class of stars from the early R stars is still uncertain.

1.3.4 Yellow symbiotic stars

Symbiotic systems consist of a late-type giant and a hot companion, a white dwarf in most cases, exhibiting nebular lines in their spectra (e.g. Kenyon 1986). Yellow symbiotics involve a G or K giant and are often halo objects (Schmid & Nussbaumer 1993). Abundance analyses have revealed their s-process enhancements and low-metallicity (e.g. UKS-Ce1 and S32: Schmid 1994; AG Dra: Smith et al. 1996; BD-21°3873: Smith et al. 1997). These yellow symbiotics are probably evolving on the upper RGB or on the E-AGB, thus being the Population II counterparts of the extrinsic S stars. Low-metallicity G-K giants are known to be more luminous (by about 2 magnitudes) than their solar-metallicity counterparts (Smith et al. 1996); since mass loss is known to increase with luminosity among giant stars, it has been argued (Jorissen 1997) that Population II giants have larger mass loss rates than the Population I stars of the same temperature; they will consequently, as shown by Nussbaumer & Vogel (1987), exhibit more easily a symbiotic activity.

1.4 Testing the binary scenario

While the binary scenario described in Sect. 1.2 leads to an attractive explanation of the chemical peculiarities encountered in several families of stars, it certainly needs to be strengthened and refined. Fortunately it provides several predictions which may be observationally tested.

1.4.1 Candidate progenitors of peculiar red giant stars

An important prediction of the binary scenario is the existence of polluted dwarf stars. In fact, several classes of main-sequence stars have been identified as possible progenitors of barium and extrinsic S stars. However the boundary between these classes is often fuzzy; in fact all these various families are probably manifestations of the barium syndrome in populations of various ages and with various levels of carbon pollution in their atmosphere.

Dwarf barium stars

In phase 4 of Fig. 1.4, the accreting star is supposed to be still a main sequence star. This situation is clearly supported by timescale considerations, and further confirmed by observations: the cooling times of the discovered companion white dwarfs of S stars are so long that mass transfer must have occurred early in the

life of the S star, certainly while it was still on the main sequence (Johnson et al. 1993). Moreover, the cross section for wind accretion is independent of the geometric radius of the star according to the Bondi-Hoyle formula, hence dwarf accretors are not at a disadvantage with regard to giant accretors. Considerations on the mass of the giant barium stars suggest that the bulk of dwarf barium stars should populate the main sequence from spectral types \sim A2 to \sim G0. In fact dwarf barium stars long remained elusive, until it was recognised that the subgiant CH stars and the F Sr λ 4077 dwarfs had the proper abundance anomalies, gravities and galactic frequencies to be identified with the long-sought Ba dwarfs.

- CH subgiants: They were discovered by Bond (1974) as F and G-type stars with weak metallic lines but enhanced features of CH and of s-process elements (Sr II). Their spectral features are very similar to those of CH-like stars, with the exception that the C₂ bands are generally absent in subgiant CH stars, indicating that C/O < 1 in their atmospheres.

Most are moderately metal-deficient ($[\text{Fe}/\text{H}] = -0.1$ to -0.8) and have s-process enhancements similar to barium stars (but lower than the classical CH stars). At least some of them were shown to lie on the main sequence, and this was plainly confirmed by HIPPARCOS measurements (Luck & Bond 1982; Luck & Bond 1991; Tomkin et al. 1989; North et al. 1994; Mennessier et al. 1997).

They belong to an old disk (mostly low-velocity) population and, despite their name, the subgiant CH are the progenitors of barium stars rather than the halo CH stars themselves: the abundance patterns of barium giants are consistent with those of CH subgiants, provided that the material now observed in the atmospheres of the CH subgiants is convectively mixed in the star's envelope as it ascends the red giant branch to become barium giants (Luck & Bond 1982; Tomkin et al. 1989; Luck & Bond 1991; Smith et al. 1993).

- F Sr λ 4077 stars: CH subgiants overlap with stars referred to as “F Sr λ 4077” (North & Duquennoy 1991; North et al. 1994). The latter, previously classified by Bidelman (1985a) as having a ‘strong Sr λ 4077’ line within a FV spectrum, constitute an inhomogeneous group; however, half of them were identified by North et al. (1994) as dwarf barium stars, mainly because of s-process and carbon enhancements.

As expected, a large fraction of binaries (about 90%) has been found among CH subgiants and barium dwarfs; moreover they have similar mass functions and orbital elements as barium stars (McClure 1997a; North et al. 1999). The suspected WD companions to these dwarf barium stars however appear to be too cool to be detectable with the IUE satellite (Bond 1984; North & Lanz 1991).

- WIRring stars: On the contrary, it is the presence of a hot WD companion to the rapidly-rotating, magnetically active K dwarf 2RE J0357+283 that led Jeffries & Stevens (1996) to suspect it might be a dwarf barium star. A subsequent spectroscopic analysis (Jeffries & Smalley 1996) confirmed this early

suspicion. This star is the first example of the new class of WIRRing (‘Wind-Induced Rapidly Rotating’) stars (Kellett et al. 1995; Jeffries et al. 1996; Jeffries & Stevens 1996), that have been spun up by wind accretion, as predicted by SPH simulations (Theuns et al. 1996): accretion of the slow, massive wind from the AGB progenitor of the white dwarf by the K star in a detached configuration, is able to transfer both mass and angular momentum, thus spinning up the K star (Jeffries & Stevens 1996)¹⁰.

Dwarf carbon stars

Because main-sequence stars do not produce carbon on their own, it had been widely assumed that the faint carbon stars were more distant examples of the classical bright giant carbon stars. However, roughly a dozen carbon stars with high parallaxes or proper motions have been recently discovered (Liebert et al. 1979; Green et al. 1991; Green et al. 1992; Warren et al. 1993; Heber et al. 1993; Green et al. 1994; Liebert et al. 1994).

Hence these dwarf carbon stars must have been polluted. In fact, at least two of them have a hot white dwarf companion (Heber et al. 1993; Liebert et al. 1994). Green & Margon (1994) found that barium is enhanced in all six dwarf carbon stars they have analysed.

Interestingly, the dwarf carbon star G77-61 has an extreme metal deficiency of -5.6 dex (Gass et al. 1988), far greater than for any ordinary halo dwarf or giant, but reminding the binary post-AGB stars depleted in refractory elements (Sect. 1.1.2). This similarity reinforces the evolutionary link between binary post-AGB stars and binary dwarf peculiar stars. New discoveries of dwarf carbon stars are expected due to an on-going dedicated survey (MacConnell 1997).

Dwarf S stars?

Dwarf S stars are predicted to exist [see Fig. 2c of De Kool & Green (1995)], but none is known. Model atmospheres are currently too poorly developed to predict in detail their spectral characteristics.

1.4.2 Frequencies of extrinsic stars

A direct check of the binary scenario may be performed by comparing the frequency of dwarf barium, barium and extrinsic S stars with respect to their respective normal (i.e., non-polluted) analogs.

- **dwarf barium stars:** From their survey of ~ 200 slightly evolved F dwarfs, Tomkin et al. (1989) discovered 2 barium dwarfs, and thus derive a rough frequency of 1% barium stars among F dwarfs. Edvardsson et al. (1993) find 6 dwarf barium stars among 200 F stars, or 3%, but their binary nature

¹⁰however, WIRRing stars do not need to be dwarfs: the giant barium star HD 165141, known to have a hot WD companion (Fekel et al. 1993), is another member of that class (Jorissen et al. 1996)

remains to be proven. North & Duquennoy (1991) find a frequency of 0.5 to 1.0% Ba dwarfs among FV stars.

- **barium stars:** MacConnell et al. (1972) estimated that Ba stars were 1% as abundant as normal G and K giants in the vicinity of the sun. From a 200 stars sample, Williams (1975) derived a frequency of barium stars among G-K giants of 1 to 4 %. Bidelman (1985b) obtained a frequency between 0.5 and 1%.

- **S stars:** The following estimates are performed on samples restricted to $\delta < -25^\circ$, because this portion of the sky has been uniformly covered by S stars surveys. The Michigan Spectral Survey (Houk 1975, 1978, 1982, 1988) lists 2930 M giants south of $\delta = -25^\circ$ (excluding luminosity classes I, II and V, but keeping the stars with no indication concerning their luminosity class; hence the number of genuine M giants may be somewhat smaller). Down to $B = 9.5$, the slope of the $d \log N/dV$ amounts to 0.6, as expected for an infinite and uniform distribution of stars (e.g., Mihalas & Binney 1987), hence the Michigan Spectral Survey is probably complete for M stars down to $B = 9.5$; 725 M stars are found up to this limiting magnitude. Adopting a typical $B - V$ value for S stars ($B - V = 1.5$), the limiting magnitude of $B = 9.5$ translates into $V = 8$; the GCGSS catalogue of Stephenson (1984), complete to $V \approx 10$, comprises 17 S stars brighter than $V = 8$ and south of $\delta = -25^\circ$. Among these, 2 are misclassified as S stars (CSS 500 and 796, see Table 1.1). The resulting frequency of S stars among M giants is $\sim 2\%$.

- **extrinsic vs. intrinsic S stars:** Very few estimates of the respective frequencies of extrinsic vs. intrinsic S stars are quoted in the literature. Little et al. (1987) found 71% of Tc-rich S stars and 29% Tc-poor S stars; however these numbers have not been corrected for the selection biases present in their sample and, therefore, do not represent the true frequency of these stars in the solar neighbourhood. Separating extrinsic and intrinsic S stars on the basis of their visual and infrared photometry, Groenewegen (1993) derives that in a magnitude-limited sample of S stars, 50% to 70% are extrinsic S stars. Jorissen et al. (1993) find that about 90% of all S stars in a volume-limited sample have no IR excess and therefore are extrinsic S stars. Other estimates derived from various studies (e.g. Smith & Lambert 1988; Brown et al. 1990) are regularly quoted, though all of them suffer from large uncertainties, because they never refer to well-defined, complete S stars samples. Hence a reliable determination of the frequencies of extrinsic and intrinsic S stars in an homogeneous stellar sample is still missing; deriving such an estimate is in fact one of the aim of this work.

Anticipating the result that roughly one S star out of two is extrinsic, then 1% of extrinsic S stars are found among normal giants, a ratio in good agreement with the previous estimates of dwarf barium stars among normal main-sequence stars, and of giant barium stars among normal G-K giants.

Therefore, the binary scenario is at least not contradicted by these very rough estimates of the respective proportions of barium and S stars.

1.4.3 Remaining issues

The very existence of dwarf extrinsic stars, and the fact that their estimated proportion (among normal dwarfs) compares well with corresponding proportions of giant extrinsic stars (among normal giants), tend to strengthen the binary scenario; however there still remains unsolved issues and important predictions that ought to be checked on large-scale stellar samples rather than on isolated objects.

All barium stars and extrinsic S stars should be binaries. McClure & Woodsworth (1990) examined the binarity of 20 barium stars. The present work will extend their results to about 70 barium stars and 30 Tc-poor S stars, from data obtained after a 10-years radial velocity monitoring in collaboration with the Geneva Observatory. The suspected evolutionary link between barium and extrinsic S stars will be discussed.

The exact way by which the matter is transferred from the AGB star onto its companion – either by wind accretion in a detached binary, or by Roche lobe overflow (RLOF) in a semi-detached binary – is still a matter of debate, and will be discussed in Chap. 2.

The companion of (dwarf and giant) barium stars should always be a white dwarf. Direct and indirect methods are available for determining the nature of the companion: (1) searching for the ultraviolet light of the companion directly; (2) deriving the mass of the companion from radial velocity measurements. The first method has been used thanks to several years of IUE observations (Johnson et al. 1993) and leads to the conclusion that Tc-poor S and MS stars tend to have white dwarfs companions, while Tc-rich stars do not. The second method has been applied by McClure & Woodsworth (1990) on their restricted sample of barium and CH stars, and will be used on a much larger sample of barium and S stars in the present work.

Having a white dwarf companion is certainly a *necessary* condition for a barium star or a Tc-poor S star, but not a *sufficient* one: binary systems consisting of a normal red giant *and* a white dwarf companion are indeed observed. The additional parameters thus required to turn a star into a barium star will be discussed.

These issues, relating to the binarity of barium and extrinsic S stars, will be examined in Chap. 2.

The binary scenario predicts that two kinds of S stars should exist. In fact, technetium is expected to be the only conspicuous spectroscopic difference to distinguish extrinsic S stars from their intrinsic analogs. Both classes were therefore completely confused until recently; in fact, the extrinsic scenario is still widely ignored. The present work will attempt to better delineate the specificities of both families.

First, extrinsic S stars are expected to be less evolved, hotter and less luminous than intrinsic S stars. Thanks to the new parallaxes provided by the HIPPARCOS satellite, the luminosities of extrinsic and intrinsic S stars will be derived, and compared to that of similar stars in external galaxies (Chap. 3).

Second, a systematic study of a well-defined sample of S stars covering all galactic latitudes and separating intrinsic S stars from their extrinsic analogs is still lacking. A study of the magnitude-limited Henize sample of 205 S stars scanning all galactic latitudes up to the galactic pole (see Chap. 4) has been performed and is presented in this work; the observational material collected for this purpose is summarized in Table 1.2; it will be described in more details in Chap. 5 and 6.

Table 1.2: Observational material collected on the Henize sample of 205 S stars

Observation	Aim
(1) 5-year radial velocity monitoring	⇒ detection of binary stars
(2) 5-year photometric monitoring in the <i>UBV</i> Geneva photometric system, as well as <i>JHKL</i> photometry	⇒ estimate of photometric variability; estimate of apparent magnitudes; identification of specific classes of stars (symbiotic, SC)
(3) 70 high-resolution spectra around 4250Å	⇒ determination of Tc content
(4) 30 high-resolution spectra around H $_{\alpha}$	⇒ detection of symbiotic stars
(5) 160 low-resolution spectra	⇒ spectral classification

Apart from the wealth of information provided by each data type alone, multivariate classification techniques will be applied on the whole data set in order to guarantee a classification as objective as possible. Once the extrinsic and intrinsic S stars will be properly unmasked, a statistical characterization of each family (proportion, galactic scale height, average colours, ...) will be attempted (Chap. 7).

These issues go beyond the “simple” problem of stellar classification, because intrinsic S stars represent an evolutionary phase of great importance in order to understand the production of heavy elements in stellar interiors and their spreading in the interstellar medium; any unnoticed extrinsic contribution will inevitably skew all the derived properties. For example, the third dredge-up luminosity threshold (commonly measured as the minimum luminosity of S stars) or the evolutionary timescales of TPAGB stars can be strongly in error if the considered star samples are polluted by non-AGB, mass-transfer S stars. Unmasking the extrinsic masqueraders is a crucial step in our global understanding of stellar evolution.

Chapter 2

Orbital elements of barium and Tc-poor S stars

Sometime look for double stars

K. G. Henize, private notes on S stars, ~1961

2.1 Introduction

The present chapter contains an extensive analysis of the orbital elements of barium stars, since the new orbits [presented in Udry et al. (1998a,b)] considerably enlarge the database, from the 17 orbits from McClure & Woodsworth (1990) to more than 50 now. The binary evolution channels relevant for barium stars will be confronted with our new data, with special emphasis on the $(e, \log P)$ diagram. The number of available orbits is now large enough to perform a meaningful comparison of the period and mass-function distributions of strong and mild barium stars.

As far as S stars are concerned, their evolutionary link with barium stars is discussed in the light of the 25 new S stars orbits now available, and appears to be fully confirmed. Finally, we present some suggestions to solve the dilemma (see Chap. 1) about the mass transfer mode that operated in barium and extrinsic S stars.

2.2 The stellar samples

Radial-velocity monitoring of several samples of chemically-peculiar red giants (PRG) has been performed by the team of McClure at the Dominion Astrophysical Observatory (DAO, Canada) and by the CORAVEL team on the Swiss 1-m telescope at Haute-Provence Observatory (France) and on the Danish 1.54-m telescope at the European Southern Observatory (La Silla, Chile), with the aim

of deriving their binary frequencies. A detailed description of the CORAVEL data, along with the new orbits, is given in Udry et al. (1998a,b); see Baranne et al. (1979) for a description of the CORAVEL spectro-velocimeter.

A brief description of these samples, on which the present study relies, is given below, with special emphasis on their statistical significance.

2.2.1 Barium stars with strong anomalies

The CORAVEL and DAO samples taken together contain *all 34 known barium stars with strong anomalies* [i.e. Ba4 or Ba5 on the scale defined by Warner (1965)] from the list of Lü et al. (1983). The binary frequency derived for this complete sample in Sect. 2.4 thus allows us to address the question of whether binarity is a necessary condition to form a strong barium star. Three stars with a Ba3 index monitored by McClure were included as well in this sample of strong barium stars.

2.2.2 Barium stars with mild anomalies

The CORAVEL and DAO samples taken together include 40 stars with a mild barium anomaly [Ba<1, Ba1 and Ba2 on the scale of Warner (1965)]. The CORAVEL sample is a random selection of 33 Ba<1, Ba1 and a few Ba2 stars from the list of Lü et al. (1983). Although this sample is by no means complete, it provides a good comparison to the sample of strong barium stars described above, for investigating the correlation between the orbital elements and the intensity of the chemical anomaly.

Because orbital elements for barium stars are spread in the literature, Tables 2.5 and 2.9 collect all orbital elements available for mild and strong barium stars, respectively. The number in column ‘Ref.’ of these tables refers to the papers where the complete set of orbital elements for the considered star can be found (see Tab. 2.17). Fekel et al. (1993) report preliminary orbital elements for the mild barium star HD 165141; the lower limit on the orbital period quoted in Table 2.5 is derived from their more accurate KPNO data. For the sake of completeness, a note identifies stars with an orbital or acceleration solution in the Hipparcos Double and Multiple Systems Annex (ESA 1997).

For several barium stars monitored by McClure, a few CORAVEL measurements have been obtained to improve the DAO orbit, since these measurements significantly increase the time span of the monitoring. These updated orbits are listed in Tables 2.5 and 2.9 under the reference number 0. A zero-point correction of -0.46 km s^{-1} has been applied to the DAO measurements, as derived from the average difference in systemic velocity for the 3 stars (HD 46407, HD 131670 and HD 223617) for which independent DAO and CORAVEL orbits are available.

Several barium stars have very long periods, exceeding the time span of the monitoring. In those cases, whenever possible, a preliminary orbit was nevertheless derived by fixing one of the orbital parameters (usually the period). Those cases can be readily identified in Tables 2.5 and 2.9 by the fact that there

is no uncertainty given for the fixed parameter [see Udry et al. (1998a) for more details].

2.2.3 Non-variable S Stars

Besides the orbit obtained for the S star HR 1105 (=HD 22649) by Griffin (1984), our CORAVEL monitoring of a sample of 56 S stars is the primary source for investigating the binary frequency among S stars. This sample includes 36 bright, northern S stars from the *General Catalogue of Galactic S Stars* (GCGSS; Stephenson 1984) with no variable star designation, neither in the *General Catalogue of Variable Stars* (Kholopov et al. 1985) nor in the *New Catalogue of Suspected Variable Stars* (Kukarkin et al. 1982). The criterion of photometric stability has been adopted to avoid the confusion introduced by the envelope pulsations masking the radial-velocity variations due to orbital motion. Such a selection criterion clearly introduces a strong bias against intrinsically bright S stars, which is of importance when deriving the binary frequency among S stars (see the discussion in Sect. 2.4.3).

Our samples include the border case HD 121447, sometimes classified as a Ba5 star and sometimes as an S star; in the analysis of the orbits presented in the next sections, this star has been included among *both* barium and S stars.

Table 2.11 presents all 25 orbits available for S stars, collected from the papers referred to in column ‘Ref.’ (see Table 2.17). The orbits of Jorissen & Mayor (1992) have been updated with a few new measurements and listed in Table 2.11 with reference number 0 in column ‘Ref’.

2.2.4 Mira S stars

A sample of 13 Mira S stars has also been monitored with CORAVEL, in order not to restrict the search for binaries to low-luminosity S stars (see Table 2.14 and Sect. 2.2.3). However, the envelope pulsations of Mira stars will undoubtedly hamper that search [see Sect. 2.3 and Udry et al. (1998a) for a detailed discussion].

2.2.5 SC and Tc-poor carbon stars

A sample of 7 SC and CS stars has been monitored as well with CORAVEL (Table 2.15), along with the 3 carbon stars lacking Tc from the list of Little et al. (1987, see Table 2.16).

2.2.6 CH stars

Orbits of CH stars are provided by McClure & Woodsworth (1990), and are not repeated here.

2.3 The radial-velocity jitter: a new diagnostic

The standard deviation of the $O - C$ residuals for some of the orbits computed by Udry et al. (1998ab) is clearly larger than expected from the error $\bar{\epsilon}_1$ on one measurement (Tables 2.5, 2.9 and 2.11). Figure 2.1 shows that there is a tendency for the largest $O - C$ residuals to be found in the systems with the largest macroturbulence, as measured by the CORAVEL index Sb . The significance of this correlation is discussed in this section.

The CORAVEL spectrovelocimeter (Baranne et al. 1979) measures the stellar radial velocity by cross-correlating the stellar spectrum with a mask reproducing about 1500 lines of neutral and ionized iron-group species from the spectrum of Arcturus (K1III). The cross-correlation dip (cc-dip) of minor planets (reflecting the sun light), corrected for the solar rotational velocity and photospheric turbulence, allows the determination of an ‘instrumental profile’ σ_0 . That parameter corresponds to the sigma of a gaussian function fitted to the cc-dip of a hypothetical star without rotation and turbulence. An estimator of the stellar macroturbulence can then be derived from the observed width σ of the stellar cc-dip as $Sb = (\sigma^2 - \sigma_0^2)^{1/2}$.

The Sb parameter is expected to increase with luminosity, as does macroturbulence (e.g. Gray 1988). This prediction will be confirmed from the luminosities derived in Chap. 3 from HIPPARCOS parallaxes for 23 S stars in common with the present sample. A least-square fit to these data yields the relation

$$M_{\text{bol}} = -1.60 - 0.37 Sb, \quad (2.1)$$

valid for $3 \leq Sb \leq 9 \text{ km s}^{-1}$. Since bright giants also exhibit large velocity jitters probably associated with envelope pulsations (e.g. Mayor et al. 1984), a correlation between Sb and the radial velocity jitter must indeed be expected, as observed on Fig. 2.1. Orbits with a large jitter tend to be associated with giants having large Sb indices. This trend is especially clear among binary S stars, and continues in fact among non-binary S stars (the jitter being then simply the standard deviation of the radial-velocity measurements). Binary (‘extrinsic’) and non-binary (‘intrinsic’) S stars actually form a continuous sequence in the (Sb , jitter) diagram of Fig. 2.1, the transition between extrinsic and intrinsic S stars occurring around $Sb = 5 \text{ km s}^{-1}$. Intrinsic S stars, with their larger Sb indices ($\gtrsim 5 \text{ km s}^{-1}$), may thus be expected to be more luminous than extrinsic S stars [$3 \lesssim Sb (\text{km s}^{-1}) \lesssim 5$]¹. Extrinsic S stars are in turn more luminous than barium stars, with the border case HD 121447 (K7IIIBa5 or S0; Keenan 1950, Ake 1979) having $Sb = 2.8 \text{ km s}^{-1}$, intermediate between Ba and S stars. HD 60197 (K3Ba5) and BD-14°2678 (K0Ba1.5) are two other barium stars with especially large Sb indices, suggestive of a luminosity larger than average for barium stars, though there is no information available in the literature to confirm that suggestion.

¹The binary S star HDE 332077, with $Sb = 10.3 \text{ km s}^{-1}$, is outlying in that respect, as in many others (see Sect. 2.9.2)

Not represented (because accurate ϵ_1 values are lacking) are the two remarkable mild barium stars HD 77247 ($Sb = 5.8 \text{ km s}^{-1}$) and HD 204075 ($Sb = 4.9 \text{ km s}^{-1}$) observed at DAO. The latter is indeed known to be a bright giant, with $M_v = -1.67$ (Bergeat & Knapik 1997), thus confirming the fact that Sb is a good luminosity indicator for red giants.

The large velocity jitter observed in Mira S stars is a consequence of their complex and variable cc-dips (Barbier et al. 1988; see also Udry et al. 1998a). In some cases however (like AA Cyg and R Hya), the cc-dips are featureless, broad and very stable. These stars with a comparatively smaller jitter are located on the lower boundary of the region occupied by intrinsic S stars in Fig. 2.1.

2.4 Binary frequency

2.4.1 Strong barium stars

According to Tables 2.9 and 2.10, the frequency of binaries among barium stars with strong Ba indices (Ba3, Ba4 or Ba5) is 35/37, the only stars with constant radial-velocities being HD 19014 and HD 65854. Before coming to a conclusion as to whether binarity is or is not a necessary condition to produce a PRG star, one needs first to assess the barium nature of the constant stars and second, to evaluate the efficiency with which binary stars can be detected with our particular protocol of observations. The latter question is discussed in Sect. 2.5.

The case of HD 19014 deserves some comments, as its radial velocity appears definitely variable (Table 2.10) though with no clear evidence for binary motion. Its only distinctive property is its rather large Sb index of 2.5 km s^{-1} (Fig. 2.1), suggesting a luminosity larger than average for barium stars. With a radial-velocity standard deviation of 0.5 km s^{-1} , HD 19014 falls right on the (Sb , jitter) correlation observed in Fig. 2.1, leaving no room for variations due to binary motion.

In the absence of any abundance analysis available for HD 19014, the photometric index $\Delta(38 - 41)$, correlated with the level of chemical peculiarities in barium stars (Jorissen et al. 1998), may be used instead. As shown in Jorissen et al. (1998), HD 19014 appears to have rather weak peculiarities, and furthermore lies in between the loci of normal giants and Ib supergiants with respect to this photometric index, suggesting that the strong barium lines are more likely due to a high luminosity (as inferred from the large Sb index) than to an abundance effect.

HD 65854 is the other strong barium star with no evidence for binary motion (McClure & Woodsworth 1990). Začs (1994) performed a detailed abundance analysis of that star, confirming its barium nature.

Finally, it has to be noted that BD+38°118 is a triple hierarchical system, with a period ratio $P(ab + c)/P(a + b) = 13$ (Table 2.5). At this stage, it is not entirely clear whether the inner pair $a + b$ or the outer pair $ab + c$ is the one responsible for the barium syndrome. Based on the position of the two pairs in the (e , $\log P$) diagram, it is argued in Sect. 2.6 that the barium syndrome is

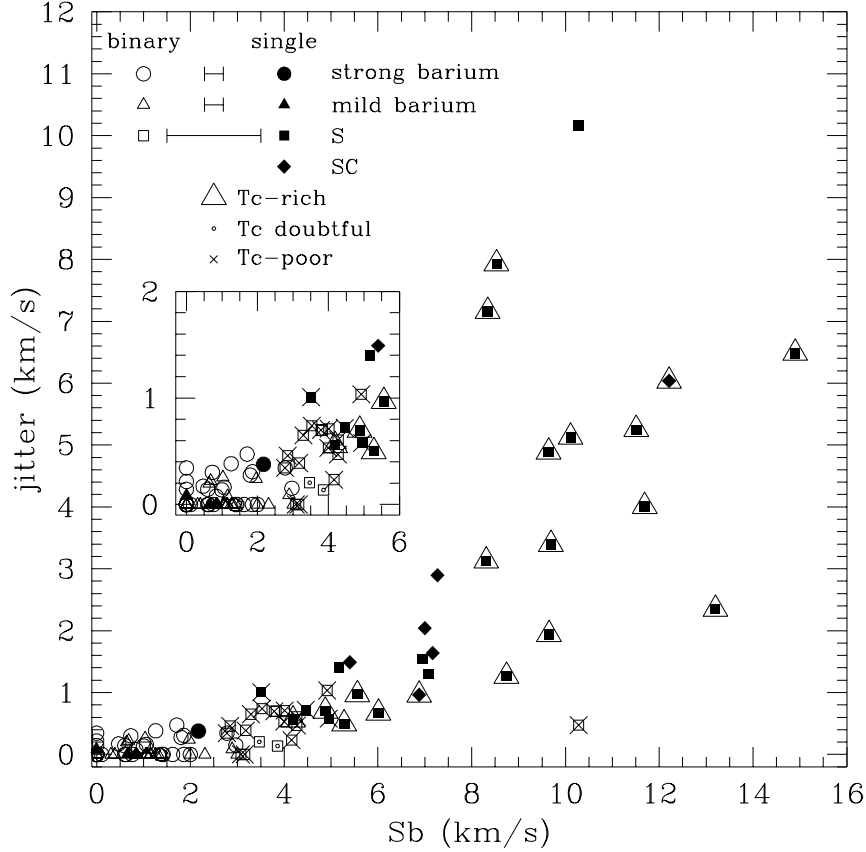


Figure 2.1: The jitter $(\sigma^2 - \bar{\epsilon}_1^2)^{1/2}$ (where $\bar{\epsilon}_1$ is the average uncertainty on one measurement, and σ is the standard deviation of the radial-velocity measurements for non-binary stars, and of the $O - C$ residuals around the computed orbit for binary stars) as a function of the CORAVEL index Sb (see text). Stars with a cc-dip narrower than the instrumental profile have been assigned $Sb = 0$. Similarly, the jitter has been set to 0 if $\sigma \leq \bar{\epsilon}_1$. Data are from Tables 2.5–2.15. Typical error bars on Sb are displayed in the upper left corner. The suspectedly misclassified S stars HD 262427 and BD+22°4385 (Table 2.12) have not been plotted. The inset is a zoom of the lower left corner

more likely to be associated with the wider pair than with the closer one.

2.4.2 Mild barium stars

The risk of misclassifying a supergiant as a mild barium star is high, since luminosity also strengthens the very lines of Ba II and Sr II that are often used to identify barium stars (Keenan & Wilson 1977; Smith & Lambert 1987). Excluding the two supergiants obviously misclassified as mild barium stars and listed in Table 2.8, the frequency of binary stars among barium stars with mild Ba indices (Ba<1, Ba1 and Ba2) is at least 34/40 (= 85%; Table 2.5), and possibly 37/40 (= 93%) when including the suspected small-amplitude binaries HD 18182 and HD 183915 (Table 2.6), as well as 56 Peg, an interacting binary system (Schindler et al. 1982). HD 130255 has not been included in the previous statistics, since it has been shown to be a subgiant CH star rather than a barium star (Lambert et al. 1993).

Detailed abundance analyses are available for two among the three constant stars (HD 50843, HD 95345 = 58 Leo and HD 119185). Sneden et al. (1981) find an average overabundance (with respect to solar) of 0.23 dex for the s-process elements in HD 95345. A similar result is obtained by McWilliam (1990). The $\Delta(38 - 41)$ index of Jorissen et al. (1998) is compatible with such a small overabundance level. Zács et al. (1997) find overabundance levels up to 0.4 dex for s-process elements in HD 119185. No detailed analysis is available for HD 50843, but its $\Delta(38 - 41)$ index is comparable to that of HD 119185 (Jorissen et al. 1998), so that s-process overabundances similar to those of HD 119185 may be expected for HD 50843. In summary, all three stars appear to be truly mild barium stars despite the absence of radial-velocity variations.

2.4.3 S stars

The results of the radial velocity monitoring of S stars are presented in Tables 2.11–2.15, which have been subdivided in the following way: 2.11: S stars for which an orbit or a lower limit on the orbital period is available; 2.12: S stars with no radial-velocity variations; 2.13: S stars with radial-velocity variations but no clear evidence for orbital motion; 2.14: Mira S stars; 2.15: SC stars.

This partition is motivated by the fact that S stars generally exhibit some radial-velocity jitter very likely due to envelope pulsation, that complicates the search for binaries. This is especially true for Mira S stars and SC stars [see Sect. 2.3, Fig. 2.1 and the detailed discussion in Udry et al. (1998a)]. In these conditions, binary stars are extremely difficult to find among the stars listed in Tables 2.14 and 2.15. Among these, S UMa may perhaps be binary, but more measurements are needed before a definite statement can be made. The two CS stars with the broadest *cc*-dips ($Sb > 10 \text{ km s}^{-1}$), R CMi and RZ Peg, exhibit radial-velocity variations mimicking an orbital motion. These variations are however most probably due to envelope pulsations, since their period is identical to the period of the light variations (see Udry et al. 1998a). An orbital

solution has been found for BD−08°1900, but the binary nature of that star is questionable for several reasons, as discussed by Udry et al. (1998a).

The stars listed in Table 2.13 exhibit radial-velocity variations that cannot satisfactorily be fitted by an orbital solution despite the fact that their jitter is moderate when compared to that of Mira S stars or SC stars.

An interesting difference may be noticed between the S stars with moderate jitter listed in Table 2.13 and the binary S stars of Table 2.11: as already shown in Sect. 2.3 and Fig. 2.1, binary S stars are restricted to the range $2.8 \lesssim Sb \text{ (km s}^{-1} \text{)} \lesssim 5$, whereas Mira, SC and non-binary S stars generally have $Sb \gtrsim 4.5 \text{ km s}^{-1}$ (BD−21°2601, with $Sb = 3.4 \text{ km s}^{-1}$, is the only exception but since it lacks Tc, it is likely *not* an intrinsic S star). In Sect. 2.3, it was argued that this separation reflects a difference in the average luminosities of these two groups of S stars (Eq. 2.1), as will be confirmed in Chap. 3. The data presented in Tables 2.11–2.15 thus largely confirm the binary paradigm, since all Tc-poor S stars (with the only exceptions of HD 189581 and BD−21°2601) are binary stars. The presence of Tc-rich S stars among the binary stars, although allowed in principle, is limited to HD 63733, HD 170970 and o^1 Ori. As argued by Jorissen et al. (1993), the presence of Tc in the former two stars is even questionable, since they fall on the boundary between Tc-rich and Tc-poor stars according to the criterion of Smith & Lambert (1988, see also Fig. 5.6). The absence of infrared excesses (Jorissen et al. 1993) and their small Sb indices (Fig. 2.1, where HD 63733 and HD 170970 are flagged as ‘Tc doubtful’) lend support to their extrinsic nature. o^1 Ori is a very special case, as it shares the properties of extrinsic (in having a WD companion; Ake & Johnson 1988) and intrinsic (in having Tc) S stars. It may be an extrinsic S stars starting its ascent on the thermally-pulsing AGB (phase 10 of Fig. 1.4).

Finally, it should be noted that two S stars with constant radial velocities (Table 2.12) were found. The absence of any detectable jitter and their small Sb index are, however, quite unusual for S stars. We therefore suspect that these stars may have been misclassified as S stars. This suspicion appears justified at least for HD 262427, which is listed as S? in the discovery paper of Perraud (1959).

2.4.4 Tc-poor carbon stars

In their extensive study of Tc in late-type stars, Little et al. (1987) list only 3 carbon stars lacking Tc lines (X Cnc, SS Vir and UU Aur). They might possibly be the analogs of the extrinsic, Tc-poor S stars. If so, they should be binary stars. The results of their CORAVEL monitoring is presented in Table 2.16, with no clear evidence for binary motion, except perhaps in the case of X Cnc. The large jitter exhibited by these stars (especially SS Vir) is reminiscent of the situation encountered for SC stars, and like them, the Tc-poor C stars have large $B - V$ indices (≥ 3.0).

2.5 Incompleteness study

2.5.1 General principles

In order to evaluate the real frequency of binary stars within a given stellar sample, it is of key importance to properly evaluate the efficiency with which binary systems can be detected. That detection efficiency not only depends upon *internal* factors set by the protocol of observations (internal velocity error, sampling and time span of the observations), but also upon *external* factors related to the orbital properties of the binary systems [through the distributions of periods P , eccentricities e , and ratios $Q = M_2^3/(M_1 + M_2)^2$], or to their orientation with respect to the line of sight (through the inclinations i and longitudes of periastron ω), or with respect to the time sampling (through the epochs T of passage at periastron).

A Monte-Carlo simulation of our ability to detect binary stars has therefore been performed following the guidelines described by Duquennoy & Mayor (1991). First, N binary systems (where N is the number of stars in the observed sample being tested) are generated by drawing T_j and ω_j ($1 \leq j \leq N$) from uniform random distributions, i_j from a $\sin i$ probability distribution (implying random orientation of the orbital poles on the sky), and P_j , e_j and Q_j from their observed distributions extrapolated in several different ways (see Sect. 2.5.2).

The synthetic binary j is then attributed the line-width index Sb_j of the j th star in the real sample, and similarly a set of observation dates $t_{j,k}$ ($1 \leq k \leq n_j^{\text{obs}}$, n_j^{obs} being the number of observations of the real star j) and a set of internal velocity errors $\epsilon_{j,k}^{\text{int}}$. The intrinsic radial-velocity jitter observed for S stars (and, to a much lesser extent, for barium stars; see Fig. 2.1 and Sect. 2.3) has to be included in the simulation. To that purpose, a parabolic fit to the trend observed in Fig. 2.1 has been used to associate a radial-velocity jitter ϵ_j^{jit} to the selected line width Sb_j . Synthetic velocities $V_{j,k}$ are then computed for the observation dates $t_{j,k}$ from the orbital elements, with an added error drawn from a gaussian distribution of standard deviation $\epsilon_j = [(\overline{\epsilon_j^{\text{int}}})^2 + (\epsilon_j^{\text{jit}})^2]^{1/2}$, $\overline{\epsilon_j^{\text{int}}}$ being the average internal error on one measurement of star j . The few stars measured by other authors² have been attributed sets of observation dates, internal velocity errors, line-width indices and jitter from stars of our sample having comparable orbital elements.

Finally, the binary star j is flagged as detected if $P_\nu(\chi_j^2) < 0.01$, where $P_\nu(\chi^2)$ is the χ^2 probability function with $\nu = n_j^{\text{obs}} - 1$ degrees of freedom, and $\chi_j^2 = (n_j^{\text{obs}} - 1)(\sigma_j/\epsilon_j)^2$, σ_j being the unbiased dispersion of the n_j^{obs} synthetic velocities of star j . The detection rate is then N_{bin}/N , where N_{bin} is the number of stars with $P_\nu(\chi_j^2) < 0.01$.

This procedure is repeated until 100 sets of N stars have been generated, which is sufficient for the *average* detection rate to reach an asymptotic value. The above method has been applied separately for the sample of 37 barium

²HD 165141 has not been included in the incompleteness study described in this section, because it was added to Table 2.5 later on

stars with strong anomalies, of 40 mild barium stars and of 28 S stars with $Sb < 5 \text{ km s}^{-1}$ (referred to as non-Mira S stars in the following). This particular choice for the Sb threshold is motivated by the fact that on Fig. 2.1, Tc-poor S stars (that are expected to belong to binary systems) are restricted to $Sb < 5 \text{ km s}^{-1}$. The method has not been applied to Mira S stars because of the uncertain (and probably large) radial-velocity jitter affecting these stars (Sects. 2.3, 2.5.3 and Fig. 2.1).

2.5.2 Detection rates for specific P , e and Q distributions

The main difficulty of the Monte-Carlo method outlined in Sect. 2.5.1 is that the *real* distributions of period, eccentricity and Q are not completely known, since the very detection biases we want to evaluate render the *observed* distributions incomplete. Different choices have therefore been made on how to complete the observed distributions, and the sensitivity of the estimated binary detection rates on these choices is evaluated *a posteriori*.

The distribution of ratios Q is likely to have little impact on the detection biases. Therefore, the observed distribution as derived in Sect. 2.9 has been adopted. Three different cases are considered for the period and eccentricity distributions, as follows:

(i) Uniform distribution in the $(e, \log P)$ diagram

Figure 2.2 shows the curves of iso-probability detection for strong barium, mild barium and non-Mira S stars in the $(e, \log P)$ plane. To derive these probabilities, the $(e, \log P)$ plane has been uniformly covered by a mesh of 480 points, which is equivalent to adopting uniform $\log P$ and e distributions. For each of these mesh points, $100N$ (i.e. about 3000) synthetic binaries have been generated as indicated above, in order that the detection probability be mainly set by P and e rather than i, T and ω . As seen on Fig. 2.2, the detection probability drops tremendously for $P \gtrsim 8000 \text{ d}$, because of the finite timespan of the observations, which started in 1985 for most strong barium stars, and in 1986 for most mild barium and S stars. For S stars, the intrinsic jitter affecting their radial velocities also contributes to lower the detection rate.

(ii) Observed P and e distributions

In this case, the observed P and e distributions are assumed to represent the *real* distributions, as if there were no systems with periods longer or eccentricities larger than those currently detected in the real samples. This is a conservative choice that allows one to estimate the *maximum* detection rate. With this crude hypothesis, an unfavorable spatial or temporal orientation of the binary system is the only possible cause of non-detection. Eccentricities and periods of the synthetic binaries were drawn in accordance with their observed distribution in the $(e, \log P)$ diagram, using the rejection method described by Press et al. (1992).

The binary detection rates obtained for the three samples under these hypotheses are listed in Table 2.1 under item Monte-Carlo (ii).

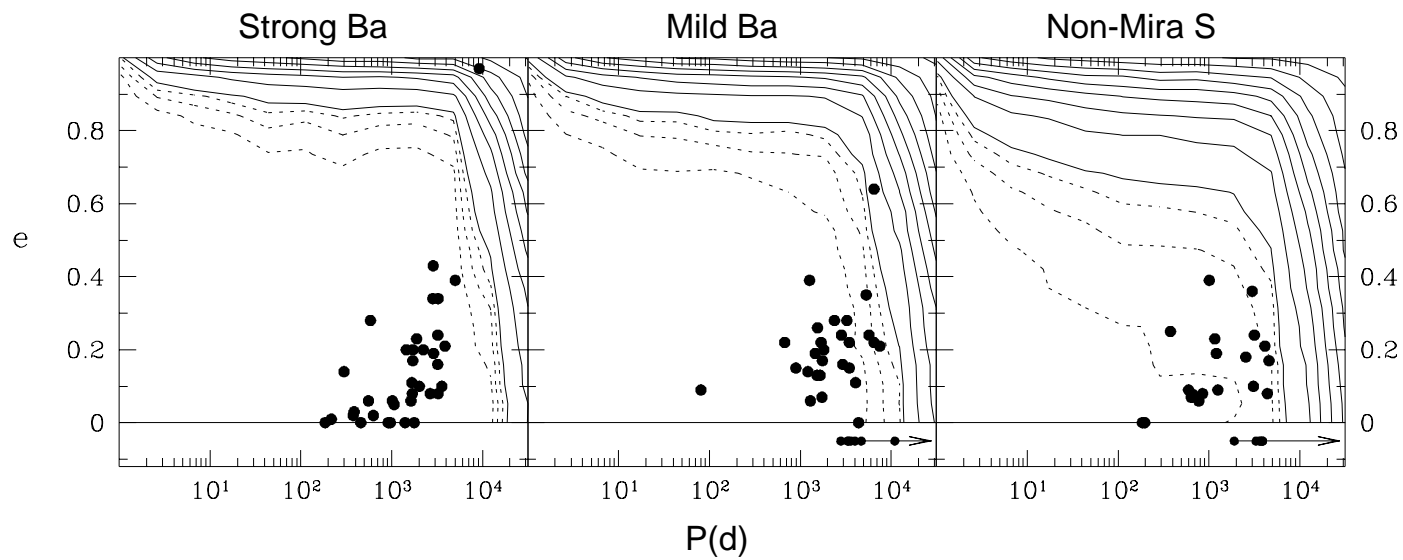


Figure 2.2: The iso-probability curves in the $(e, \log P)$ plane for detecting binary systems among strong barium, mild barium and non-Mira S stars. The dotted curves correspond to detection probabilities of 97.5%, 95% and 92.5% (decreasing towards the upper right corner), and the solid curves to probabilities of 90%, 80%, 70%,... In the lower part of each diagram are represented binary stars for which only a lower limit is available on the period

Table 2.1: Comparison of the simulated and observed binary detection rates for strong barium stars, mild barium stars and non-Mira S stars ($Sb < 5 \text{ km s}^{-1}$). The quoted uncertainty corresponds to the standard deviation of the detection rates for the 100 stochastically independent sets generated

	strong Ba	mild Ba	S ($Sb < 5 \text{ km s}^{-1}$)
Observed	94.6% = 35/37	85.0% = 34/40 to 92.5% = 37/40	85.7% = 24/28
Monte- Carlo (ii)	97.9 ± 3.0% =(36.2 ± 1.1)/37	93.0 ± 5.0% =(37.2 ± 2.0)/40	96.8 ± 4.0% =(27.1 ± 1.1)/28
Monte- Carlo (iii)	95.7 ± 4.0% =(35.4 ± 1.5)/37	89.4 ± 6.0% =(35.8 ± 2.4)/40	89.5 ± 6.0% =(25.0 ± 1.5)/28

(iii) *Extrapolated P and e distributions*

In this last case, the real period distribution is assumed to be identical to the observed distribution at short periods. Its long-period tail includes the $N_{\text{no-P}}$ stars having no orbital period currently available (i.e. stars with only a lower limit available on P , or even stars with constant radial velocities) but assumed to be very long-period binaries. More precisely, the $N_{\text{no-P}}$ stars are uniformly redistributed over the period bins ranging from P_{inf} to 20000 d, where P_{inf} is the first period bin containing a star from the $N_{\text{no-P}}$ subsample. Eccentricities are supposed to be uniformly distributed under the curve $e = (\log P - 1)^2/7$.

The corresponding binary detection rates are listed in Table 2.1 under item Monte-Carlo (iii).

What are the main causes of non-detection? In the case of mild barium stars for example, the non-detected binaries in simulation (iii) are distributed as follows, in decreasing order of importance: $e > 0.8$ for 47.3%, $P > 10^4\text{d}$ for 32.7%, $-\pi/10 < \omega(\text{mod}\pi) < \pi/10$ for 20.7% (because the radial-velocity curve remains very flat over a large fraction of the orbital cycle around apoastron), $\sin i < 0.1$ for 4.5%, and a combination of various less severe conditions for 9.8%. Note that, since a star may belong to more than one of these categories, the sum of the above percentages exceeds 100%. In more practical terms, these numbers translate into 6.6% of the undetected binaries having a radial-velocity semi-amplitude $K < 0.4 \text{ km s}^{-1}$ too small in comparison with the instrumental accuracy, while 37.8% remained undetected because of an incomplete phase coverage ($\Delta t < P/4$) and 26.6% because the number of measurements is too small (< 8).

2.5.3 Discussion

The detection rates obtained for the various cases considered in Sect. 2.5.2 are summarized in Table 2.1, where they are compared with the observed rates.

If binarity were not the rule among barium stars, the observed rates of binaries would be significantly lower than the predicted ones. Here on the contrary, there is a good agreement between the Monte-Carlo predictions and the observed binary rates among mild and strong Ba stars. One may therefore conclude that *binarity is a necessary condition to produce chemically-peculiar red giants like mild and strong Ba stars*. The agreement is slightly better for the Monte-Carlo simulation (iii) extrapolating the period distribution up to 20000 d. The few barium stars with undetected radial-velocity variations are thus likely binaries with very long periods or with unfavourably-oriented orbits.

The situation is more tricky for S stars. The application of the Monte-Carlo method to the *whole* sample of S stars is hampered by our ignorance of the exact amount of jitter in the radial velocities of Mira stars with large Sb indices (see Fig. 2.1). Therefore the Monte-Carlo simulation cannot be used to evaluate the rate of binaries among the whole sample of S stars (as we did for barium stars). The problem is less severe for S stars with $Sb < 5 \text{ km s}^{-1}$, where the jitter is smaller ($< 1 \text{ km s}^{-1}$) and may be estimated with more confidence. Moreover, the fact that Tc-poor S stars (i.e. extrinsic S stars suspected of belonging to binary systems) appear to be restricted to $Sb < 5 \text{ km s}^{-1}$ provides an independent justification for applying the Monte-Carlo simulation to that subsample. The observed binary rate for S stars with $Sb < 5 \text{ km s}^{-1}$ is close to the one predicted with the extrapolated P and e distributions (case iii in Table 2.1). This result is thus consistent with the hypothesis that all S stars with $Sb < 5 \text{ km s}^{-1}$ are members of binary systems [Note that, for S stars, the case (iii) predictions have to be preferred over the case (ii) ones, since the period distribution of S stars is most probably incomplete at large periods, due to a more limited time coverage than in the case of barium stars]. However, this agreement should not be overinterpreted, as the $Sb < 5 \text{ km s}^{-1}$ limit between extrinsic and intrinsic S stars may be somewhat fuzzy.

Are there binaries in our sample of intrinsic S stars? For these stars, the intrinsic jitter may possibly induce variations of the same order of magnitude as those caused by binarity, and thus renders the detection of possible binaries very delicate. However, several arguments indicate that binary stars are probably not very frequent among the intrinsic S stars of our sample. The upper panel of Fig. 2.3 shows the distribution of the radial-velocities standard deviation $\sigma(V_r)$ *predicted* by the Monte-Carlo simulation for a sample of binary stars having orbital parameters matching those of the binary S stars, and with an intrinsic jitter of 1 km s^{-1} . As expected, the *observed* $\sigma(V_r)$ distribution for binary S stars (middle panel of Fig. 2.3) matches the simulated distribution (allowing for large statistical fluctuations due to the small number of stars observed). On the contrary, the observed $\sigma(V_r)$ distribution for Mira S stars (lower panel of Fig. 2.3) differs markedly from that of binary S stars, since the former distribution peaks at $\sigma(V_r) \sim 1.5 \text{ km s}^{-1}$ and is rapidly falling off at larger $\sigma(V_r)$. The paucity of Mira S stars with $2 \leq \sigma(V_r) \leq 6 \text{ km s}^{-1}$ must therefore reflect the low percentage of binaries among this group. The minimum value of the jitter (1 km s^{-1}) adopted in the simulation is a conservative choice; a larger jitter

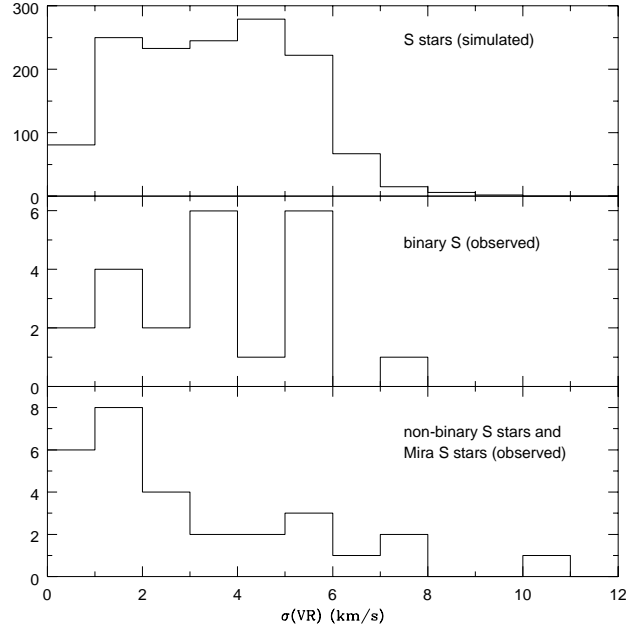


Figure 2.3: The *simulated* $\sigma(V_r)$ distribution for binary S stars (upper panel), and the *observed* distribution for real S stars (lower two panels). HD 191589 and HD 332077, the two binary S stars with very discrepant mass functions, lie outside the boundaries of the middle panel, with $\sigma(V_r)=14.4$ and 18.5 km s^{-1} respectively

would shift the simulated $\sigma(V_r)$ distribution (upper panel) towards larger $\sigma(V_r)$ values, thus strengthening the above conclusion.

Although binarity is not required to produce intrinsic S stars and is indeed not frequent in the sample considered in this work, binary stars may nevertheless exist among them as in any class of stars. A few intrinsic S stars with main sequence companions are known, from the composite nature of their spectrum at minimum light. They include T Sgr, W Aql, WY Cas (Herbig 1965; Culver & Ianna 1975), and possibly S Lyr (Merrill 1956a), as well as the close visual binary π^1 Gru (Feast 1953). A Te-rich S star with a WD companion is also known (σ^1 Ori; Ake & Johnson 1988).

2.6 The $(e, \log P)$ diagram

The $(e, \log P)$ diagram is a very useful tool to study binary evolution, as the various processes modifying the orbital parameters in the course of the evolution

(like tidal interaction, RLOF or wind accretion) imprint distinctive signatures on the ($e, \log P$) diagram [see the various papers in Duquennoy & Mayor (1992)]. The ($e, \log P$) diagram for various classes of red giants of interest here is displayed in Fig. 2.4.

The sample of G and K giants from open clusters presented in Fig. 2.4 (from Mermilliod 1996) will be used as a reference sample to which the binaries involving PRG stars may be compared. A striking feature of this ($e, \log P$) diagram is the relative paucity of systems with $e < 0.1$ and orbital periods longer than 350 d. A similar lack of circular systems is observed among binary systems involving solar-type main-sequence primaries (Duquennoy & Mayor 1991; Duquennoy et al. 1992), the threshold period (10 d) being much shorter in this case. On the contrary, many systems with periods shorter than this threshold have circular orbits.

Both features are the result of physical processes that operated in the former history of these systems. Tidal effects on the more evolved component nearly filling its Roche lobe are responsible for the circularization of the closest binaries in a given (coeval) sample. The threshold period is then set by the largest radius reached by the more evolved component in its former evolution (Duquennoy et al. 1992; Mermilliod & Mayor 1996). The lack of circular systems above the tidal circularization threshold has been interpreted as an indication that binary systems form in eccentric orbits. A theoretical support to this hypothesis is provided by Lubow & Artymowicz (1992). These authors show that the interaction between the young binary system and a circumbinary disk containing proto-stellar residual material may increase a moderate initial eccentricity, thus giving rise to the observed lack of circular orbits among unevolved systems.

The ($e, \log P$) diagram of barium stars is markedly different from that of cluster giants, for (i) barium stars nearly fill the low-eccentricity gap observed among unevolved binaries³, (ii) the minimum and maximum periods for a circular orbit are $P_1 \sim 200$ d and $P_2 \sim 4400$ d, respectively, among barium stars, as compared to 50 and 350 d for cluster giants, and (iii) at a given orbital period, the maximum eccentricity found among barium systems is much smaller than for cluster giants. Still, it is important to note that quite large eccentricities ($e \sim 0.97$, HD 123949) are found among barium stars, yet at large periods ($P \sim 9200$ d). The ($e, \log P$) diagrams of S and CH stars, and their threshold periods P_1 and P_2 in particular, are very similar to those of barium stars.

The differences between the ($e, \log P$) diagrams of PRG and cluster binaries reflect the fact that the orbits of PRG systems have been shaped by the mass-transfer process responsible for their chemical peculiarities, whereas most of the cluster binaries are probably pre-mass transfer binaries. The ($e, \log P$) diagram of PRG stars may also have been altered to some extent by tidal effects occurring in more recent phases (e.g., when low-mass barium stars currently in the clump

³The newly derived orbits for barium systems were never forced to be circular, even though the criterion of Lucy & Sweeney (1971) may indicate that the data is compatible with the hypothesis $e = 0$ at the 5% level. Given the general appearance of the ($e, \log P$) diagram (Fig. 2.4), there is no physical reason not to accept small albeit non-zero eccentricities

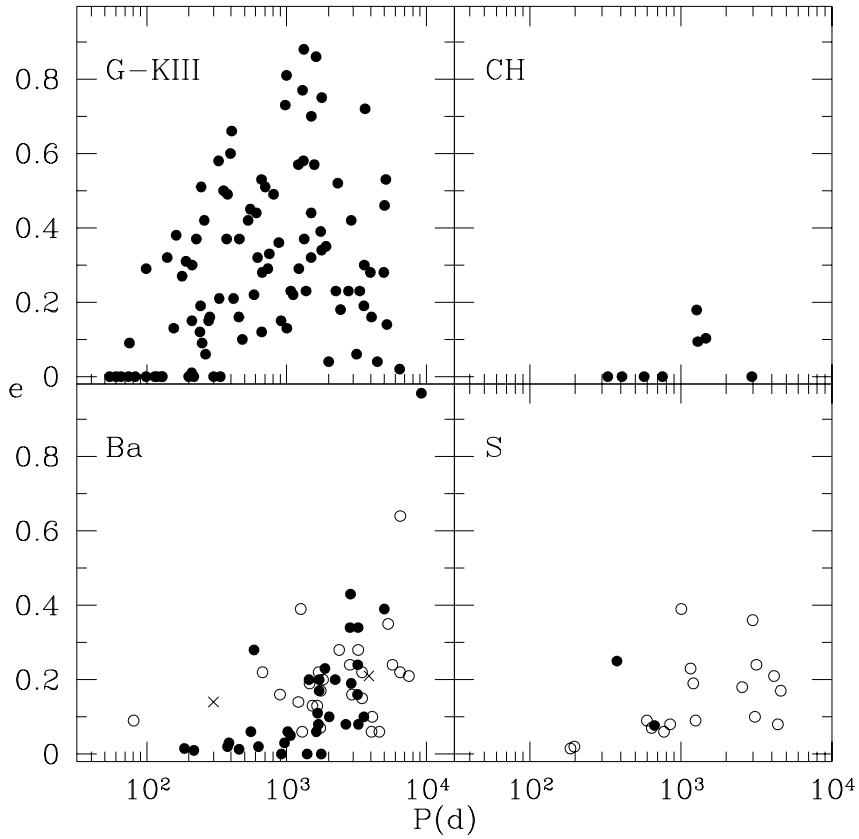


Figure 2.4: The $(e, \log P)$ diagram for various samples of red giant stars:
 Lower left panel: Barium stars. Mild (Ba<1 – Ba2, from Table 2.5) and strong (Ba3 – Ba5, from Table 2.9) barium stars are represented by open and filled circles, respectively. The crosses identify the two pairs of the triple hierarchical system BD+38°118;
 Upper left panel: Binaries involving G and K giants in open clusters (Mermilliod 1996);
 Upper right panel: CH stars (McClure & Woodsworth 1990);
 Lower right panel: S stars from Table 2.11 (Note that HD 121447, the border case between barium and S stars, has been included in both samples). The filled circles correspond to HD 191589 and HD 332077, two S stars with unusually large mass functions (see Sect. 2.9)

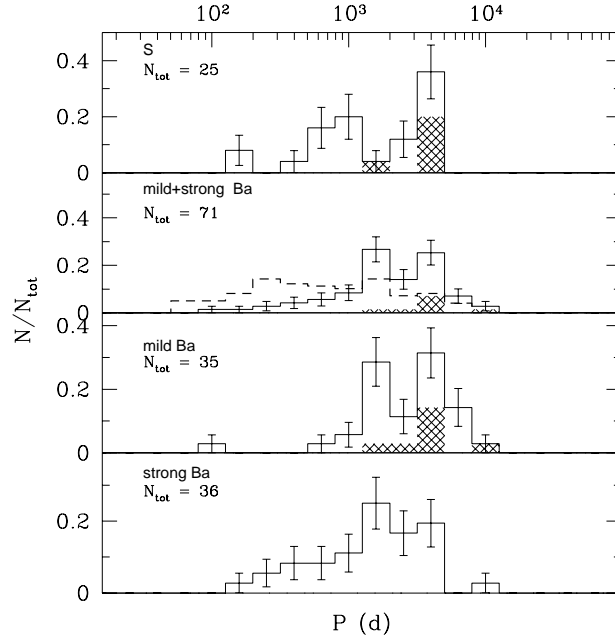


Figure 2.5: Period distributions for various families of PRG stars. Shaded regions in the histograms denote systems with only a lower limit available on the orbital period. For comparison, the thick dashed line in the mild+strong Ba panel provides the period distribution for the sample of normal giants in open clusters (Mermilliod 1996; see Fig. 2.4). The error bars on the histograms correspond to the statistical error expected for a Poisson distribution

evolved up the RGB), thus complicating its interpretation in terms of mass-transfer only (see Sect. 2.7). Detailed models of binary evolution are therefore required to fully interpret the ($e, \log P$) diagram of PRG stars.

Two barium stars deserve some comments. As already noted in Sect. 2.4.1, BD+38°118 is a triple system. The large eccentricity ($e = 0.14$) of the inner pair ($P = 300$ d) may therefore not be representative of barium systems and should probably not be regarded as a constraint on the mass-transfer process that shaped the barium-star orbits. Mazeh & Shaham (1979) and Mazeh (1990) have shown that, in a triple system, the dynamical interaction of the inner binary with the third body prevents the total circularization of the inner orbit. However, the oscillation of the eccentricity of the inner binary obtained in the cases considered by these authors has an amplitude (of the order of 0.05) much smaller than the current eccentricity of BD+38°118. It is not clear therefore whether such a dynamical interaction in a triple system may be responsible for the large eccentricity of the inner pair in BD+38°118. Another possibility is that

Table 2.2: Summary of the distinctive features of the period distributions of mild and strong barium stars

	Strong Ba	Mild Ba
• short-period mode ($P \lesssim 1500$ d)	$e < 0.08$	no short-period mode ^a
• long-period mode ($P \gtrsim 1500$ d)	mild and strong barium stars in this mode are indistinguishable $e > 0.08$	
• upper-period cutoff	5000 d ^b	> 11000 d

^aexcept for the peculiar system HD 77247

^bexcept for the special case HD 123949: $P \sim 9200$ d, $e = 0.97$

the mass transfer responsible for the barium syndrome actually originated from the distant third companion, whereas the inner pair consisting of the barium giant and a low-mass main sequence companion has orbital elements typical of unevolved systems like those involving giants in clusters. The mass functions of the two pairs are similar (see Sect. 2.9) and do not contradict the above statement, although they cannot be used to confirm it either.

Another remarkable system is HD 77247, with $P = 80.5$ d and $e = 0.09 \pm 0.01$. There is no indication whatsoever from the $O - C$ residuals of the orbit of McClure & Woodsworth (1990) that this star may belong to a triple system. Yet its orbit should have been circularized by the tidal processes at work in giants, unless that star is much younger than the cluster giants displayed in Fig. 2.4 (see Duquennoy et al. 1992). An interesting property in that respect is the fact that the star has anomalously broad spectral lines ($Sb = 5.8 \text{ km s}^{-1}$; Table 2.5), an indication that it is either a luminous G (super)giant or that it is rapidly rotating.

2.7 Period distributions

The orbital-period distributions of mild barium stars, strong barium stars and S stars are compared in Fig. 2.5, and their distinctive features are outlined in Table 2.2. The significance of the two modes identified in the period and eccentricity distributions of strong barium stars may be grasped by considering the Roche radii corresponding to the mode boundaries. Adopting $2.1 M_{\odot}$ as the typical mass of strong-barium systems ($1.5 + 0.6 M_{\odot}$; see Table 2.4), the ~ 1500 d threshold between the low- and long-period modes translates into $A \sim 700 R_{\odot}$ and $R_{\text{Roche}} \sim 200 R_{\odot}$ for the Roche radius around the former AGB companion in its final stage (when its mass amounts to $\sim 0.6 M_{\odot}$). Since

this Roche radius is of the order of AGB radii, the threshold between the short- and long-period modes is probably related to the different mass transfer modes arising in detached and semi-detached binary systems (see Sect. 2.11). The lower boundary of the short-period mode (~ 200 d) corresponds to $A \sim 180 R_{\odot}$, or $R_{\text{Roche}} \sim 85 R_{\odot}$ around the barium star. Since this Roche radius is of the order of radii reached on the RGB, the lower end of the short-period mode is likely altered by tidal circularization or even RLOF occurring as the current barium star evolves on the RGB (see Sect. 2.12).

The upper period cutoff for strong barium stars (which is meaningful, since the sample is complete) is significantly smaller than that of mild barium stars, as expected in the framework of mass transfer through wind accretion (Boffin & Jorissen 1988; Jorissen & Boffin 1992; Sect. 2.10). The level of chemical peculiarities of a barium star depends, among other parameters, on the amount of matter transferred onto it. Since that amount may in turn be expected to be smaller in wider (i.e. longer-period)⁴ systems, it is not surprising that the long-period cutoff is larger for mild barium stars. The period cutoffs observed for strong and mild barium stars (5000 and > 11000 d respectively) therefore put constraints on the efficiency of wind accretion, to be used in future simulations.

More generally, milder chemical peculiarities are expected in longer-period systems. However, the broad overlap between the period distributions of mild and strong barium stars (Fig. 2.5) suggests that the scatter in a (period, chemical anomaly) diagram will be large. It is therefore likely that other parameters play an important role in controlling the level of chemical peculiarities. That question will be addressed in Sects. 2.8 and 2.10.

2.8 Is there a correlation between barium intensity and orbital period?

The existence of a correlation between the orbital separation (or more precisely, periastron distance) and the level of chemical peculiarities would clearly be of key importance for understanding the mass transfer process at work in the progenitor systems of barium stars. Unfortunately, these quantities are not easily available for our complete sample, as not all stars have been the target of detailed abundance analyses on one hand, and on the other hand, the orbital separations cannot be derived for spectroscopic binaries with one observed spectrum without further assumptions.

Jorissen et al. (1998) have shown that although there is a general tendency for longer-period systems to exhibit less severe peculiarities (their Figs. 6 and 7), there is a considerable scatter that can not be attributed to uncertainties

⁴It is in fact the periastron distance rather than the orbital period which is the key parameter in this respect. The long period (~ 9200 d) observed for the strong barium star HD 123949 is therefore not relevant, since its very large eccentricity yields a periastron distance much smaller than in systems with $P \sim 5000$ d and smaller eccentricities

Table 2.3: Normal giants in barium-like binary systems, from Jorissen et al. (1998)

160538		K0III + WD	904	Berdyugina (1994)	DR Dra
33856	1698	K0.5III	1031	McWilliam (1990)	
13611	649	G8III + WD?	1642	McWilliam (1990)	ξ^1 Cet
169156	6884	K0III	2374	McWilliam (1990)	
66216	3149	K2III	2438	McWilliam (1990)	

in the determination of the level of chemical peculiarity by different authors⁵.

Moreover, the very existence of several giants with *normal* heavy-element abundances, albeit in binary systems with barium-like orbital elements, is another clear indication that the orbital separation is not the only parameter controlling the level of chemical peculiarities in barium stars. These barium-like binary systems involving a normal giant are listed in Table 2.3 and have been collected by Jorissen et al. (1998) from the catalogue of Boffin et al. (1993), listing all spectroscopic binary systems with a giant component. That catalogue has been searched for systems involving a red giant with normal heavy-element abundances according to McWilliam (1990), and falling in the region $e < 0.1$, $P > 350$ d of the $(e, \log P)$ diagram (Fig. 2.4). That region of the $(e, \log P)$ diagram is normally not populated by pre-mass-transfer systems, as discussed in Sect. 2.6, so that the unseen component in these systems may be supposed to be a WD. No direct confirmation for the presence of a WD is however available for HD 33856 and HD 66216. For HD 13611 ($=\xi^1$ Ceti), Böhm-Vitense & Johnson (1985) reported some UV excess that they attribute to a WD companion, though that statement has subsequently been questioned (Jorissen & Boffin 1992; Fekel et al. 1993). The clearest case of a post-mass-transfer system consisting of a WD and a *normal* red giant is undoubtedly HD 160538 ($=$ DR Dra). Orbital elements ($P = 904$ d, $e = 0.07$) have been obtained by Fekel et al. (1993), along with definite evidence for the presence of a hot WD. An abundance analysis of that star has recently been carried out by Berdyugina (1994), who concludes that HD 160538 is a solar-metallicity giant ($[\text{Fe}/\text{H}] = -0.05$) with normal Zr, Ba and La abundances.

These counter-examples (especially DR Dra) strongly suggest that *binarity is not a sufficient condition to produce a barium star!* Another condition – like a low metallicity? – seems thus required to form a barium star, and such a hidden parameter may, at least in part, be responsible for the blurred correlation between the orbital period and the intensity of the chemical anomalies. Unfortunately, it is difficult to evaluate the exact influence of metallicity on that correlation, because a homogeneous set of metallicity determinations is lacking for the stars in our sample. Large systematic differences may indeed be present between the metallicity determinations by different authors, as discussed e.g. by Busso et al. (1995). As an illustration, metallicities ranging from -0.45 to

⁵The scatter is even more severe if one considers periastron distance instead of orbital period

+0.13 have been published for HD 46407! Nevertheless CH stars are found to have high heavy-element overabundances with respect to barium stars (Fig. 7 of Jorissen et al. 1998: these low-metallicity stars have the largest $[s/Fe]$ values at any given orbital period). This lends strong support to the idea that metallicity is the hidden parameter controlling the level of chemical peculiarities at a given orbital period. Kovács (1985) also noticed that there is a correlation between $[Ba/Fe]$ and metallicity $[Fe/H]$: strong barium stars generally have a metallicity lower than mild barium stars (see also the recent compilation of Busso et al. (1995), and North et al. (1994) for a similar finding among barium *dwarfs*). Clayton (1988) provided a theoretical foundation for that empirical finding: if $^{13}C(\alpha, n)^{16}O$ is the neutron source responsible for the operation of the s-process, its efficiency in terms of neutron exposure is expected to be larger in a low-metallicity environment. Therefore, barium stars would be easier to produce in a low-metallicity population. That question will be discussed in more details in Sect. 2.10, since there are obviously other parameters involved (like the dilution factor and the amount of matter transferred from the former AGB companion) whose impact should be evaluated as well.

2.9 The mass-function distributions

2.9.1 Barium and CH stars

The cumulative frequency distribution of mass functions $f(M)$ conveys information on the masses of the two components in the binary system, since

$$f(M) = \frac{M_2^3}{(M_1 + M_2)^2} \sin^3 i \equiv Q \sin^3 i, \quad (2.2)$$

M_1 and M_2 being the masses of the red giant and of its companion, respectively. As shown by Webbink (1986) and McClure & Woodsworth (1990), the $f(M)$ distribution of peculiar red giants like barium and CH stars is very different from that of normal red giants. The PRG distributions are in fact compatible with a narrow range of Q values, convolved with random orbital inclinations. McClure & Woodsworth (1990) obtained $Q = 0.041 \pm 0.010 M_\odot$ for their sample of 16 barium stars, and $Q = 0.095 \pm 0.015 M_\odot$ for CH stars. Such narrow Q distributions are indeed expected if the companions of PRG stars are WD stars with masses spanning a narrow range, as is the case for field WDs (Reid 1996). On the contrary, since the companions of normal giants in binary systems ought not be WDs, their masses may span a much wider range (the only constraint being then $M_2 \leq M_1$), thus contrasting with the PRG $f(M)$ distributions.

The larger samples considered in the present work make it possible to derive the distributions of Q separately for mild and strong barium stars. These distributions have been extracted from the observed distribution of $f(M)$ by two different methods. In the first method, the observed $f(M)$ distribution is simply compared to simulated distributions assuming random orbital inclinations and gaussian distributions (of mean \overline{M}_i and standard deviation σ_i , $i = 1, 2$) for the

Table 2.4: Average masses \overline{M}_1 of the giant star in various PRG families as derived from the cumulative frequency distribution of the mass functions, for two different values of the companion average mass \overline{M}_2 . N is the number of available orbits

Family	N	\overline{Q} (M_\odot)	\overline{M}_1		Ref
			$\overline{M}_2 = 0.60$ (M_\odot)	$\overline{M}_2 = 0.67$ (M_\odot)	
CH	8	0.095	0.9	1.1	2
Barium (strong)	36	0.049	1.5	1.9	1
Barium (mild)	27	0.035	1.9	2.3	1
Barium (total)	63	0.043	1.65	2.0	1
S (extrinsic)	17 ^a	0.041	1.6	2.0	1

Remark: a: the two peculiar S stars HD 191589 and HDE 332077 were not included (see Sect. 2.9.2)

References: 1. This work; 2: McClure & Woodsworth (1990)

masses M_i of the two components. Since $f(M)$ depends upon the masses only through the ratio $Q = M_2^3/(M_1 + M_2)^2$, almost equally good fits (expressed in terms of the greatest distance D between the synthetic and observed $f(M)$ distributions) are obtained for different combinations of \overline{M}_1 and \overline{M}_2 , all corresponding to the same value of \overline{Q} . The value of \overline{Q} minimizing D for the different PRG families is listed in Table 2.4. The synthetic and observed $f(M)$ distributions are compared in Fig. 2.6. The best fits are obtained with $\sigma_1 = 0.2 M_\odot$ and $\sigma_2 = 0.04 M_\odot$.

A similar analysis performed by North et al. (1999) on a sample of *dwarf* barium stars provided the first independent estimate of the average companion mass. Unlike the barium giants, the barium dwarfs offer the possibility to directly derive their masses by fitting evolutionary tracks to their observed surface gravities and effective temperatures. The known distribution of primary masses and the average ratio Q derived from the $f(M)$ distribution then yield an average mass \overline{M}_2 of $0.67 \pm 0.09 M_\odot$ for the companion. Assuming that dwarf barium stars, giant barium stars and extrinsic S stars represent successive stages along the same evolutionary path (Sects. 2.12 and Chap. 1), the \overline{M}_2 value derived by North et al. (1999) for the companions of dwarf barium stars may be adopted to derive the average mass \overline{M}_1 of the giant for the different PRG families listed in Table 2.4. For comparison, the average mass \overline{M}_1 corresponding to $\overline{M}_2 = 0.60 M_\odot$ has also been listed.

The second method, described by Cerf & Boffin (1994) and based on the Richardson-Lucy iterative inversion algorithm, fully confirms the above results.

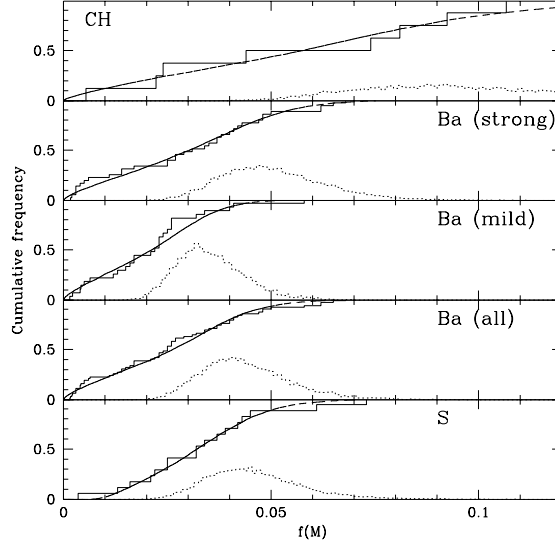


Figure 2.6: Comparison of the synthetic (dashed line) and observed (solid line) mass-function distributions for CH stars (top panel, with data from McClure & Woodsworth (1990)), strong barium stars (second panel from top, from Table 2.9), mild barium stars (third panel from top, from Table 2.5), all barium stars (fourth panel from top), and S stars (bottom panel, from Table 2.11). For S stars, the synthetic distribution has been constructed by adopting a detection threshold $i > 36^\circ$ to simulate the deficit of systems with small mass functions (see text). The dotted line corresponds to the distribution of Q

Figure 2.7 shows the extracted distributions of mass ratios $q = M_2/M_1$ and masses M_1 when M_2 is fixed at $0.6 M_\odot$.

The $f(M)$ distributions of CH stars, mild barium stars and strong barium stars are clearly distinct, and this difference is reflected in the corresponding average masses \overline{M}_1 listed in Table 2.4. A Kolmogorov-Smirnov test confirms the significance of this difference, since the null hypothesis that the distributions of mild and strong barium stars are extracted from the same parent population may be rejected with a first kind risk of only 0.6%.

Although the difference in the Q distributions of mild barium stars, strong barium stars and CH stars may equally well result from a difference in the giant or companion masses, the different kinematical properties reported for these families suggest a difference in the respective masses of the *giant* star. The kinematics of CH stars is typical of a halo population (McClure 1984ab and references therein), whereas barium stars belong to a disk population. Moreover, there are several pieces of evidence that mild barium stars belong to a somewhat

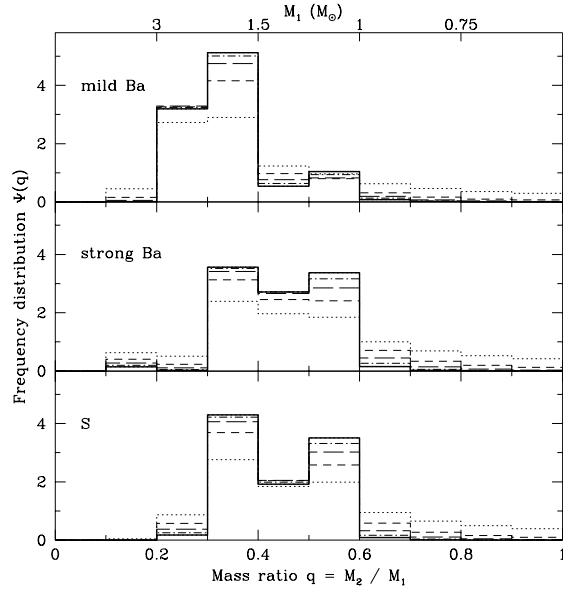


Figure 2.7: Distributions of mass ratios $q = M_2/M_1$ extracted from the observed $f(M)$ distributions using the Richardson-Lucy iterative algorithm, for mild barium stars (upper panel), strong barium stars (middle panel) and S stars (lower panel). During the inversion process, M_2 has been fixed at $0.6 M_\odot$. The corresponding mass M_1 of the giant star can be read from the upper scale. The various lines refer to the distributions obtained after 2 (dotted line), 4 (short-dashed line), 6 (long-dashed line), 8 (dash-dotted line) and 10 (thick line) iterations

younger population than strong barium stars. Catchpole et al. (1977; see also Lü 1991) showed that the velocity dispersion of mild barium stars is smaller than that of strong barium stars. From a statistical analysis of the positions of barium stars in the Hertzsprung-Russell diagram based on Hipparcos parallaxes, Mennessier et al. (1997) conclude that mild barium stars are mostly clump giants with a mass in the range $2.5 - 4.5 M_\odot$, whereas strong barium stars populate the giant branch and have masses in the range $1 - 3 M_\odot$. These mass estimates are consistent with those derived from the mass-function distributions (Fig. 2.7).

It may thus be concluded that mild barium stars, strong barium stars and CH stars represent a sequence of increasingly older galactic populations.

2.9.2 S stars

Figure 2.8 compares the cumulative distributions of mass functions for barium and S stars. Apart from a deficit of systems with small mass functions, the $f(M)$

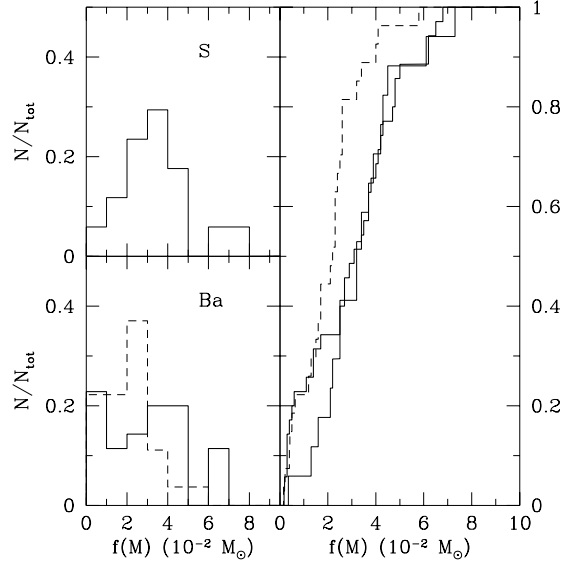


Figure 2.8: Comparison of the mass-function distributions of barium stars (thick solid line: strong barium stars; thin dashed line: mild barium stars) and S stars (thin solid line). The mass functions of HD 191589 and HDE 332077 were not included in the comparison

distribution of S stars is very similar to that of strong barium stars. The deficit of S systems with small mass functions $f(M)$ can probably be attributed to the difficulty of detecting small-amplitude binaries for these stars with a substantial radial-velocity jitter (Sects. 2.3 and 2.5.2, and Figs. 2.1 and 2.2).

Note that the two S stars HD 191589 and HDE 332077 were not included in the comparison, since they have very discrepant mass functions of 0.395 and 1.25 M_{\odot} , respectively (Table 2.11). A-type companions were detected for these stars with the *International Ultraviolet Explorer* (Ake & Johnson 1992; Ake et al. 1992), consistent with their mass functions. From the current radial-velocity data, there is no indication that these systems might be triple. The evolutionary status of these Tc-poor S stars is currently unknown.

2.10 Mild vs. strong barium stars: entangled effects of orbital dynamics and galactic population

In the previous sections, mild and strong barium stars have been seen to differ in many respects: (i) short-period ($P \lesssim 1500$ d), nearly-circular systems are lack-

ing among mild barium stars, (ii) there is a tendency for systems with longer periods to have milder chemical anomalies, although the large scatter in that relation suggests that some other parameter (like metallicity?) partially controls the level of chemical anomalies, (iii) strong barium stars generally have lower metallicities than mild barium stars, (iv) mild barium stars have smaller mass functions on average, and (v) mild barium stars are kinematically younger than strong barium stars.

The previous facts consistently suggest that mild barium stars belong to a younger, more metal-rich and more massive population than strong barium stars. In this section, we investigate the consequences of this difference in galactic population on the mass-transfer process. For that purpose, the chemical anomalies of mild and strong barium stars are computed using a simple dynamical model, assuming that the former AGB progenitor of the present WD has dumped heavy-element-rich matter onto its companion.

The parameters controlling the intensity of chemical anomalies in barium stars may be easily identified with the aid of the following formula, relating the overabundance factor s of heavy elements in the envelope of the barium star (i.e. the ratio between the abundances after completion of the accretion and dilution processes, and the initial envelope abundances) to their overabundance f in the material accreted from the former AGB star:

$$s = \frac{f\Delta M_{\text{Ba}} + M_{\text{Ba},0} - M_{\text{Ba,core}}}{\Delta M_{\text{Ba}} + M_{\text{Ba},0} - M_{\text{Ba,core}}} \equiv fF + (1 - F), \quad (2.3)$$

where F is the dilution factor of the accreted matter ΔM_{Ba} in the envelope of mass $(M_{\text{Ba},0} - M_{\text{Ba,core}} + \Delta M_{\text{Ba}})$. Here, $M_{\text{Ba},0}$ and $M_{\text{Ba,core}}$ denote the initial total mass and core mass, respectively, of the accreting barium star. The accreted mass ΔM_{Ba} is computed from the relation

$$\Delta M_{\text{Ba}} = \beta(M_{\text{AGB},0} - M_{\text{WD}}), \quad (2.4)$$

where β corresponds to the fraction of the mass lost by the former AGB star of mass $M_{\text{AGB},0}$ (at the start of the thermally-pulsing phase) that is actually accreted by the barium star. For the sake of simplicity, it is assumed that all cases considered below undergo wind accretion (so that predictions will be restricted to systems with $P \gtrsim 1500$ d, in accordance with the discussion of Sect. 2.7). The Bondi & Hoyle (1944) prescription will therefore be adopted for computing the accretion efficiency β (see Theuns et al. 1996 for more details):

$$\beta = \frac{\alpha}{A^2} \left(\frac{GM_{\text{Ba}}}{v_w^2} \right)^2 \frac{1}{[1 + (v_{\text{orb}}/v_w)^2]^{3/2}}, \quad (2.5)$$

or using Kepler's third law:

$$\beta = \alpha\mu^2 \frac{k^4}{[1 + k^2]^{1.5}}, \quad (2.6)$$

where $k \equiv v_{\text{orb}}/v_w$, v_{orb} and v_w being the relative orbital velocity ($2\pi A/P$) and the wind velocity, respectively, G is the gravitational constant, A is the orbital

separation, $\mu \equiv M_{\text{Ba}}/(M_{\text{AGB}} + M_{\text{Ba}})$, and α is a scaling parameter. In the above relation, it has been assumed that the wind is highly supersonic. Detailed hydrodynamic simulations (Theuns et al. 1996) have shown that $\alpha \sim 0.05$ in the situation of interest here.

The above relations thus indicate that the following parameters will have some impact on the level of chemical anomalies:

- (i) a large orbital separation will result in a small accretion cross section (Eq. 2.5, valid for a wind-accretion scenario). Note, however, that the functional dependence of β with A is more complicated than the simple explicit A^{-2} factor appearing in Eq. (2.5), since there is an implicit dependency through the orbital velocity v_{orb} ;
- (ii) a lower mass for the barium star results in a smaller dilution (i.e. larger F). However, the effect is opposite on the accretion cross section (Eq. 2.5), notwithstanding the implicit dependence through v_{orb} ;
- (iii) a smaller metallicity probably results in larger heavy-element overabundances f in the AGB progenitor (see the discussion at the end of Sect. 2.8). As low-metallicity giants are expected to have low masses, this effect is strongly coupled with (ii);
- (iv) a larger mass for the AGB progenitor results in more mass being lost and thus accreted by the companion; a more massive WD is also produced.

The above qualitative discussion shows that the various relevant parameters are strongly coupled with each other, thus calling for detailed calculations. Because in the framework of the simple wind-accretion model adopted here, the accretion rate depends upon the orbital separation (see Eq. 2.5), the resulting overabundance s must be computed by taking into account the variation of the orbital separation in the course of the mass transfer process. Neglecting the anisotropy in the mass loss process induced by the accretion, as well as a possible transfer of linear momentum from the wind to the accreting star (Theuns et al. 1996), the variation of the orbital separation obeys the equation:

$$\frac{\dot{A}}{A} = -\frac{\dot{M}_1 + \dot{M}_2}{M_1 + M_2}. \quad (2.7)$$

The amount of accreted matter has been computed by integrating Eqs.(2.3)–(2.7) using a Runge-Kutta scheme, starting with $M_{\text{AGB},0}$ equal to M_{Ba} (the present mass of the barium star), and integrating till $M_{\text{AGB}} = M_{\text{WD}} = 0.67 M_{\odot}$ (see Tab. 2.4). This initial condition ensures that the AGB star was initially slightly more massive than the barium star, and evolved faster. The amount of mass accreted thus represents a lower limit, as the AGB star might have been more massive initially.

Different combinations of parameters have been considered, so as to evaluate the relative importance of items (i), (ii) and (iii) listed above. To evaluate the impact of the population difference between strong and mild barium stars (see Table 2.4), cases with $M_{\text{Ba}} = 1.8$ (mimicking strong barium stars, and labelled L in the following) and $2.4 M_{\odot}$ (mimicking mild barium stars, and labelled H in the following) have been considered. To evaluate the impact of metallicity (item iii), surface s-process overabundances f of 130 and 40 in low- and high-metallicity

AGB stars, respectively, were considered (labelled l and h , respectively, in the following). The overabundance s of heavy elements for cases Hh, Lh and Ll is shown on Fig. 2.9 as a function of the *final* orbital period P (for $P \gtrsim 1500$ d, as shorter final periods most probably involve RLOF, not adequately described by the present scheme). The overabundance f of heavy elements in the accreted matter is clearly of utmost importance in controlling the pollution level s . In particular, it is clear that different giant masses (Table 2.4) cannot explain the different pollution levels of mild and strong barium stars (compare cases Lh and Hh on Fig. 2.9). The respective overabundances s obtained in cases Hh and Lh are even opposite to what is expected from the observations, since the more massive mild barium stars (Hh) would be *more polluted* than the strong barium stars (Lh) for a given f ! This contradiction results from the fact that more mass was allowed to be exchanged in the ‘mild barium’ systems because the AGB progenitor was supposed to be more massive in the more massive mild barium systems than in the strong barium systems (see above).

The mass of the AGB progenitor sensitively controls both the amount of mass that can be exchanged (thus fixing the pollution level) and the mass of the WD (thus fixing Q). It offers therefore a way to link the differences in pollution levels and mass functions that are observed in mild and strong barium stars. However, because that explanation cannot account for the kinematic differences observed between mild and strong barium stars (Sect. 2.9.1), we favour an explanation in terms of a difference in the f values characterizing the matter accreted by the barium stars belonging to the H and L populations having different metallicities. We find that, with the choice $f = 40$ and 130, the difference between mild and strong barium stars is largely one of population, strong barium stars belonging almost exclusively to a low-mass low-metallicity population characterized by a large value of f (represented by case Ll). Some merging between the H and L populations inevitably occurs for mild barium stars, however, since they contain all stars with $0.2 \lesssim \log s \lesssim 0.5$ (see Fig. 2.9). This prediction receives some support from the mass distribution of mild barium stars presented in Fig. 2.7. Although mild barium stars are dominated by high-mass objects ($M_1 \sim 1.5 - 3 M_\odot$, corresponding to the H population in the above simulations), there is a small tail of less massive objects which suggests that mild barium stars are indeed a mixture of populations H and L.

The above values of f appear plausible in view of the s-process overabundances reported by Utsumi (1985) and Kipper et al. (1996) in N-type carbon stars, supposed to be representative of the former AGB mass-losing star in the barium systems. However, the parameter f is admittedly not very tightly constrained by our simple model. It is therefore encouraging that the value of f chosen to reproduce the upper period cutoff of strong barium stars (in case Ll) predicts that mild barium stars can be produced in systems with periods up to a few 10^4 d which is consistent with the longest periods observed among mild barium stars (Sect. 2.5.3).

Another argument related to CH stars lends strong support to the idea that f increases in low-metallicity populations, and is the principal factor controlling the pollution levels of PRG stars. Although the periods of CH stars span the

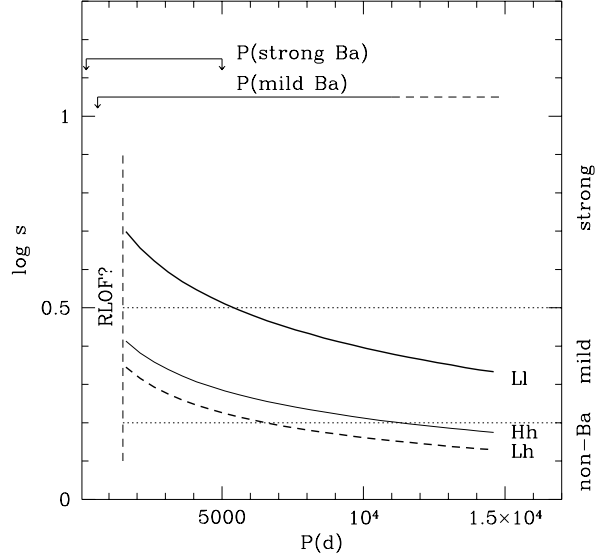


Figure 2.9: Schematic predictions of the wind-accretion scenario [Eqs. (2.3) – (2.7)] for the cases L1, Lh and Hh defined in the text. The dotted lines mark the (somewhat arbitrary) separation between strong, mild and non-barium stars. The range in periods spanned by mild and strong barium stars is represented by the horizontal lines in the upper part of the figure

same range as those of barium stars (Fig. 2.4), their heavy-element overabundances at a given period are generally larger than those of barium stars [Fig. 7 and Table 8 of Jorissen et al. (1998)]. Applying the method described above to CH stars, it is found that values of f of the order of 300 at least are required to account for the observed overabundance levels s . The operation of the s -process must therefore have been very efficient in the low-metallicity AGB star responsible for the pollution of the CH star envelope (see also the discussion in Sect. 2.8). There is a very distinct property of the heavy-element abundance distribution observed in CH stars that confirms this fact. Heavy s -process elements ('hs') like Ba are comparatively more overabundant than light s -process elements ('ls') like Y, with $[hs/ls] \geq 0.4$ (Vanture 1992c). This situation is only encountered when the neutron exposure τ which characterizes the efficiency of the s -process reaches values as large as 1 mb^{-1} (Vanture 1992c). Such values lead to overabundances of heavy s -elements that are comparatively larger than for smaller τ (e.g. Fig. 5 of Busso et al. 1995), in agreement with the above requirement for large f values in CH systems.

2.11 Short-period Ba systems and the question of RLOF

The mass-transfer model [Eqs. (2.3) – (2.7)] used in Sect. 2.10 to evaluate the respective importance of the various parameters entering the problem is extremely schematic. In particular, it assumes that mass transfer occurs through wind accretion. On one hand, the fact that barium stars have non-circular orbits indeed points against RLOF in a semi-detached system, as tidal effects will efficiently circularize the orbit when the giant is about to fill its Roche lobe. But on the other hand, RLOF seems unavoidable for the barium stars with the shortest periods, since their orbital separation is too small to have accommodated a large AGB star in a detached binary system in the past (see in particular the case of HD 121447, having the second shortest orbital period among barium stars; Jorissen et al. 1995). Adopting for instance $M_{\text{AGB}} = 0.6 M_{\odot}$, $M_{\text{Ba}} = 1.5 M_{\odot}$ and $P = 1500$ d yields a Roche radius of about $200 R_{\odot}$, much smaller than typical radii of $\sim 500 R_{\odot}$ observed for cool ($T_{\text{eff}} \sim 2200$ K) Mira stars (e.g. Van Belle et al. 1996). In such circumstances, it seems unavoidable that at least the shortest-period systems among barium stars result from RLOF.

The main difficulty with RLOF is that, when this process involves a giant star with a convective envelope (as is the case for AGB stars), and when this star is the more massive star in the system, the mass transfer then occurs on a dynamical time scale ('unstable case C' mass transfer) and is expected to lead to a dramatic orbital shrinkage. A common envelope generally forms at that stage, causing a strong drag on the embedded stars and resulting in the formation of cataclysmic variable stars with orbital periods of a few hours (e.g. Meyer & Meyer-Hofmeister 1979; De Kool 1992; Iben & Tutukov 1993; Ritter 1996).

Barium stars must somehow have avoided this evolutionary channel. There must be a way to do so, as indicated by the mere existence of short-period (as short as 116 days) binary post-AGB stars: an AGB star can not fit in most of the binary systems holding a post-AGB star (Van Winckel 1999)!

In the remainder of this section, several ways out of the cataclysmic channel are briefly suggested.

First, the eccentricity of most barium, S and post-AGB binary systems is non-zero. Mass loss may have started (and occurred?) at periastron only, thus increasing the eccentricity still, as noted by Van Winckel et al. (1995), allowing an AGB star to survive. Alternatively, as noted in Sect. 2.6, the orbital eccentricity may have developed *after* the AGB phase, through a tidal interaction with a massive circumbinary disk.

Second, unstable mass transfer models do not yet take into account cyclic diameter variations occurring in Mira stars: periodic changes with pulsation phase in the angular diameter of Mira variables have been recently observed with amplitude up to 35% and 45% of the smallest value for the Mira R Leo and the technetium-rich (thus TPAGB) S star χ Cygni, respectively (Burns et al. 1998; Young et al. 1999).

Third, it is possible that the common envelope phase developing during un-

stable case C mass transfer does not lead to a dramatic orbital shrinkage if mechanisms internal to the AGB star reduce the effective binding energy of its envelope (like the recombination energy in the hydrogen and helium ionization zones, excitation of non-radial pulsation modes, shock-heating, dust-driven winds...; Iben & Livio 1993). In those cases, not so much energy ought to be extracted from the orbit to expell the common envelope, thus reducing (and even perhaps suppressing) the orbital decay. Due consideration of the thermal energy of the AGB envelope reduces its effective binding energy and the orbital shrinkage associated with a common-envelope phase is therefore limited. Han et al. (1995) have shown that barium systems like HD 77247 with periods as short as 80 d may form under such circumstances.

Fourth, the dynamical instability associated with case C mass transfer is suppressed when the mass-losing star is *less massive* than its companion (Pastetter & Ritter 1989), with $q < q_{\text{crit}} < 1$, where $q = M_{\text{AGB}}/M_{\text{Ba}}$ and q_{crit} is given by Hjellming & Webbink (1987; see also Hjellming 1989). This situation is encountered if a strong mass loss by wind steadily reducing the mass of the AGB star reversed the mass ratio prior to the onset of RLOF. Tout & Eggleton (1988) have shown that the mass ratio is easily reversed if the mass loss rate of the AGB star is tidally enhanced by the companion ('Companion-Reinforced Attrition Process', CRAP) so to exceed the Reimers rate by one or two orders of magnitude. By including this effect, Han et al. (1995) were able to stabilize the RLOF of many systems, which ended up as barium systems with periods in the range 250 – 2500 d.

Finally, the very concept of the Roche lobe may be irrelevant for systems involving a mass-losing star where the wind-driving force may substantially reduce the effective gravity of the mass-losing star (see the discussion in Theuns & Jorissen 1993). The existence of an extra-force driving the mass loss will clearly modify the shape of the equipotential surfaces, as shown by Schuerman (1972). The geometry of X-ray binaries involving mass-losing supergiants (Bolton 1975; Kondo et al. 1976), and possibly also of the yellow symbiotic-barium star BD–21°3873 (Smith et al. 1997), are indeed observed to deviate from the predictions made with the usual Jacobi integral describing the restricted three-body equipotential surfaces. In particular, if the effective gravity is reduced below some threshold depending upon the mass ratio, the critical Roche equipotential will degenerate into a surface including *both* the Lagrangian points L_1 and L_2 (if the mass-losing star is the more massive component) or L_1 and L_3 (in the opposite case). Matter will thus not necessarily be confined to the lobe surrounding the accreting component, but may escape from the system through L_2 or L_3 , after forming a circumbinary disk. Furthermore, in the case of a strong wind, the particles have initially non-zero kinetic energy taken from the internal energy of the mass-losing star, that makes the equipotentials escapable barriers. Therefore, only a limited fraction of the mass lost by the AGB star is accreted by the companion, and such a reduced accretion rate will be less prone to trigger the expansion of the accreting star envelope, at the origin of the common envelope formation. The mass flows in these situations are complex, as shown by recent *Smooth Particle Hydrodynamics* simulations

(Theuns & Jorissen 1993; Theuns et al. 1996).

2.12 Do S stars evolve from barium stars?

The orbital properties of S stars appear to be identical to those of barium stars, as apparent from Fig. 2.4 [$(e, \log P)$ diagram] and Figs. 2.6 and 2.8 (mass-function distribution). This similarity is a strong indication that binary S stars are simply the descendants of barium stars as they cool while ascending either the RGB or the E-AGB⁶. Because the evolution is slower on the RGB than on the E-AGB, it may actually be expected that binary S stars be dominated by stars on the upper RGB rather than on the E-AGB. In this case, *they ought to be low-mass stars* (because only low-mass stars develop a red giant branch), in agreement with the value $1.6 M_{\odot}$ derived from their average Q (Table 2.4).

It is expected that at some point in their evolution on the RGB the S stars with the shortest periods ($P \lesssim 600$ d) will overflow their Roche lobe. In that respect, it should be noted that the hottest (i.e. least evolved) S star in our sample, HD 121447, has the shortest period among S stars. The detailed analysis of this system performed by Jorissen et al. (1995) concludes that the giant will overflow its Roche lobe before reaching the RGB-tip, with a dramatic fate for the binary system as described in Sect. 2.11 in relation with unstable case C mass transfer.

Another puzzling S star is Hen 108, the second shortest-period S star, with an orbital period of only 197 days. Such a short orbital period sets strong constraints on the radius of the giant star that has to fit inside its Roche lobe. Indeed, supposing the mass of the companion white dwarf to be $0.6 M_{\odot}$, the radius of the Roche lobe around the primary S star is $\sim 50 R_{\odot}$, showing only little sensitivity to the primary mass (taken inside the reasonable limits $1-4 M_{\odot}$). Given an effective temperature of ~ 3700 K as derived from the $V - K$ colour index and the calibration by Ridgway et al. (1980), and an absolute bolometric magnitude in the range $-2 \leq M_{bol} \leq -3.5$ (Chap. 3), the resulting radius is between $54 R_{\odot}$ and $109 R_{\odot}$. Hence this star must be extremely close to overflow its Roche lobe⁷.

The various processes that prevented the orbital decay of the binary system in a former stage of its evolution, when the AGB progenitor of the present WD filled its Roche lobe, are no longer applicable to this second RLOF event. First, the mass ratio can no longer be inverted easily, as the companion is already a low-mass WD, so that case C mass transfer is necessarily dynamically unstable. Second, the envelope of a RGB star is more tightly bound than that of an evolved AGB star (since it is less extended and its ‘gravity-reducing’ wind is much weaker), so that more energy has to be extracted from the orbit to expell the common envelope, resulting in a stronger orbital decay.

⁶Strictly speaking, the S and barium phases may even be intermingled in the sequence Ba (lower RGB) - S (upper RGB) - Ba (He clump) - S (E-AGB and TP-AGB)

⁷This star could be expected to exhibit a symbiotic activity; however a high-resolution spectrum at H_{α} (Chap. 6) revealed no emission line whatsoever

2.13 Conclusions

Radial-velocity monitoring of a complete sample of barium stars with strong anomalies reveals that 35 out of 37 stars show clear evidence of binary motion. For mild barium stars, that frequency amounts to 34/40 (or 37/40 if one includes the suspected binaries). A Monte-Carlo simulation shows that these frequencies are compatible with the hypothesis that *all* the observed stars are binary systems, some of them remaining undetected because of unfavourable orbital orientation or time sampling. We conclude therefore that there is no need to invoke a barium-star formation mechanism other than one (like mass transfer) directly related to the binary nature of these stars. In other words, *binarity appears to be a necessary condition to form a barium star*. It seems, however, that it is not a sufficient condition, since binary systems with barium-like orbital elements but no heavy-element overabundances seem to exist (e.g. DR Dra). It has been argued that a metallicity lower than solar may be the other parameter required to form a barium star. The increasing levels of heavy-element overabundances observed in the sequence mild Ba – strong Ba – CH stars support that hypothesis, since this sequence is also one of increasing age (and thus, to first order, of decreasing metallicity), as revealed by their kinematical properties.

The $(e, \log P)$ diagram of PRG stars clearly shows the signature of mass transfer, since the maximum eccentricity observed at a given orbital period is much smaller than in a comparison sample of normal giants in clusters. Mass transfer rather must thus be held responsible for the chemical peculiarities exhibited by PRG stars. A distinctive feature of the $(e, \log P)$ diagram of barium stars is the presence of two distinct modes: a short-period mode ($P \lesssim 1500$ d) comprising nearly-circular orbits ($e < 0.08$), populated by strong barium stars only, and a long-period mode made exclusively of non-circular orbits. At this point, it is not clear whether the nearly circular orbits of the short-period mode bear the signature of RLOF, or whether they arise from tidal circularization on the RGB long after the mass-transfer process. Detailed models of binary evolution are required to answer that question.

The comparison of the mass-function distributions of mild and strong barium stars confirms that the difference between them is mainly one of galactic population rather than of orbital separation, since mild barium stars host more massive giants than strong barium stars. The loose correlation that is observed between the orbital period and the level of heavy-element overabundances is another indication that a parameter not directly related to the orbital dynamics has a strong impact on the pollution level of the barium star. All these facts fit together nicely if the s-process operation is more efficient in a low-metallicity population. Provided that the reaction $^{13}\text{C}(\alpha, n)^{16}\text{O}$ is the neutron source responsible for the operation of the s-process, such a correlation between metallicity and s-process efficiency is indeed predicted on very general theoretical grounds. In this framework, the giant star in Pop.II CH systems has accreted material much enriched in heavy elements by its former AGB companion. Therefore, stars of old, low-metallicity populations like CH stars (and to a lesser extent, strong barium stars) exhibit, *for a given orbital period*, much larger

heavy-element overabundances than stars belonging to a younger population.

A radial-velocity monitoring of S stars confirms that Tc-poor S stars are all binaries and are the cool descendants of the barium stars on the RGB or E-AGB, since they have similar orbital periods and mass functions. There is a suggestion, however, that the short-period tail of S stars may be truncated at about 200 d due to RLOF occurring on the RGB. Similarly, for Pop.II stars, yellow barium-symbiotic systems like AG Dra and BD-21°3873 are the cool descendants of the hotter CH stars. Two Tc-poor S stars, HDE 332077 and HD 191589, have unusually large mass functions, and an A-type companion has been detected in both cases with IUE, as well as in 57 Peg (see also Chap. 3). The evolutionary status of these stars is currently unclear.

Table 2.5: Orbital elements for mild (Ba<1, Ba1 and Ba2) barium stars. Column 2 provides the spectral subclass (> 0 if K type, < 0 if G type) and column 3 the Ba index, from Lü et al. (1983). The columns labeled $\bar{\epsilon}_1$ and N give the average error on one measurement and the number of measurements, respectively. A dash in column S_b indicates that the spectral line width is smaller than the instrumental profile. For orbits obtained from instruments other than CORAVEL, the S_b parameter is not available ('na'). When an orbital solution is available, γ is the systemic radial velocity; otherwise, it is the average radial-velocity with its standard deviation. $\Delta(38 - 41)$ is a photometric index characterizing the strength of the Ba anomaly (see text). The numbers in column 'Ref.' refer to Table 5, which gives the reference where the complete set of orbital parameters for the considered system may be found

HD/DM	Sp.	Ba	P (d)	e	$f(M)$ (M_\odot)	$O - C$ (km/s)	$\bar{\epsilon}_1$ (km/s)	N	S_b (km/s)	γ (km/s)	$\Delta(38 - 41)$	Ref.
22589	-5	< 1	5721.2±454	0.24±0.17 ^a	0.0042±0.0025	0.22	0.37	19	1.1	-28.0±0.6	-0.03	1
26886	-8	1	1263.2±3.7	0.39±0.02	0.025 ±0.002	0.40	0.32	23	2.0	+3.8±0.1	+0.02	2
27271	-8	1	1693.8±9.1	0.22±0.02	0.024 ±0.001	0.31	0.30	23	1.2	-18.1±0.1	-0.01	2
40430	0	1	> 3700				0.34	15	1.7	-23.9±1.0	-0.03	1
49841	-8	1	897.1 ±1.8	0.16±0.01	0.032 ±0.002	0.33	0.32	21	1.0	+10.9±0.1	-0.09	2
51959 ^g	2	1	> 3700				0.34	21	-	+38.9±0.8	+0.07	1
53199	-8	2	7500	0.21±0.22 ^a	0.026 ±0.001	0.17	0.36	11	1.1	+23.3±0.1	-0.07	2
58121	0	1	1214.3±5.7	0.14±0.02	0.015 ±0.001	0.24	0.30	23	1.3	+10.2±0.1	-0.04	2
58368	0	2	672.7 ±1.3	0.22±0.02	0.021 ±0.001	0.39	na	31	na	+37.8±0.1	-0.11	13
59852	-9	1	3463.9±53.8	0.15±0.06	0.0022±0.0004	0.27	0.34	19	-	+0.1±0.1	-0.10	1
77247 ^{c,d}	-5	1	80.53 ±0.01	0.09±0.01	0.0050±0.0001	0.50	na	66	5.8	-19.7±0.1	na	0,13
91208	0	1	1754.0±13.3	0.17±0.02	0.022 ±0.002	0.39	0.32	24	0.7	+0.2±0.1	-0.05	1
95193	0	1	1653.7±9.0	0.13±0.02	0.026 ±0.001	0.26	0.32	18	0.8	-7.3±0.1	-0.06	1
98839 ^b	-7	< 1	> 11000					56	na	-1:	na	5
101079	1	1	> 1500				0.34	7	1.2	-2.2±0.2	-0.17	2
104979	0	1	> 4700				0.29	25	0.7	-30.8±0.4	+0.07	2
131670 ^{c,e}	1	1	2929.7±12.2	0.16±0.01	0.040 ±0.002	0.36	0.30	55	0.6	-25.1±0.1	-0.13	1,13
134698	1	1	> 3600				0.33	22	0.5	-29.5±1.6	-0.20	1
139195	1	1	5324 ±19	0.35±0.02	0.026 ±0.002	0.7	na	107	-	+6.3±0.1	-0.02	12

Table 2.5: (continued)

HD/DM	Sp.	Ba	P (d)	e	$f(M)$ (M_{\odot})	$O - C$ (km/s)	$\bar{\epsilon}_1$ (km/s)	N	S_b (km/s)	γ (km/s)	$\Delta(38 - 41)$	Ref.
143899	-8	1	1461.6±6.9	0.19±0.02	0.017 ±0.001	0.27	0.35	26	0.3	-29.8±0.1	-0.05	1
165141	0	1	> 2100					10	na	+10.2±1.8	-0.14	4,23
180622	1	1	4049.2±37.7	0.06±0.10 ^a	0.070 ±0.020	0.25	0.30	10	-	+39.2±1.1	-0.10	2
196673 ^{c,d}	2	2	6500	0.64±0.03	0.013 ±0.002	0.47	0.5	51	3.0	-24.6±0.1	0.00	1,13
199394 ^{c,d}	-8	1	4606.5±351 ^f	0.06±0.06 ^a	0.023 ±0.003	0.40	na	52	1.1	-5.6±0.2	-0.15	0,13
200063	3	1	1735.4±8.1	0.07±0.04 ^a	0.058 ±0.004	0.23	0.29	10	2.3	-58.3±0.2	-0.10	2
202109 ^g	-8	1	6489.0±31.0	0.22±0.03	0.023 ±0.003	0.8	na	112	0.0	+16.7±0.1	-0.06	11
204075 ^{c,d}	-5	2	2378.2±55	0.28±0.07	0.004 ±0.001	0.52	na	32	4.9	+2.1±0.1	-0.15	0,13
205011 ^{c,d}	1	1	2836.8±10	0.24±0.02	0.034 ±0.003	0.45	na	41	1.4	+11.5±0.1	-0.13	0,13
210946	1	1	1529.5±4.1	0.13±0.01	0.041 ±0.001	0.26	0.31	30	1.3	-4.3±0.1	-0.11	2
216219	-1	1	4098.0±111.5	0.10±0.04	0.013 ±0.001	0.37	0.33	29	2.0	-7.2±0.1	-0.07	2
223617 ^{c,d,g}	2	2	1293.7±3.9	0.06±0.02	0.0064±0.0004	0.34	na	39	0.4	+28.5±0.1	-0.10	2,13
288174	0	1	1824.3±7.1	0.19±0.01	0.017 ±0.001	0.15	0.33	14	0.9	+34.7±0.1	-0.12	1
-01° 3022	1	1	3252.5±31.4	0.28±0.02	0.016 ±0.001	0.25	0.36	26	1.0	-35.4±0.1	-0.15	1
-10° 4311	-0	1	> 3400				0.45	33	1.5	+52.7±2.9	-0.14	1
-14° 2678	0	< 1	3470.5±107	0.22±0.04	0.023 ±0.002	0.39	0.38	15	2.9	+4.9±0.1	+0.06	1

Remarks:

- a: data compatible with circular orbit at 5% confidence level (Lucy-Sweeney test);
- b: not listed in Lü et al. (1983), but present in Lü (1991);
- c: Combined CORAVEL/DAO orbit;
- d: A DAO-CORAVEL offset of -0.46 km s^{-1} has been applied to the DAO measurements;
- e: A DAO-CORAVEL offset of -0.73 km s^{-1} has been applied to the DAO measurements;
- f: A somewhat more accurate period ($4382 \pm 91 \text{ d}$) is obtained by forcing $e = 0$;
- g: Acceleration solution listed in the Hipparcos Double and Multiple Systems Annex (ESA 1997)

Table 2.6: Suspected binary mild barium stars. The numbers in column ‘Ref.’ refer to the papers listed in Tab. 2.17

HD	Sp.	Ba	N	Δt (d)	V_r (km/s)	$\sigma(V_r)$ (km/s)	$\bar{\epsilon}_1$ (km/s)	S_b (km/s)	$\Delta(38 - 41)$	Ref.	Rem.
18182	0	0	22	3451	25.76	0.45	0.32	—	−0.03	0	
183915	0	2	9	4073	−50.08	0.50	0.29	0.3	−0.18	0,13	
218356	2	2	13	6201	−27.86	1.17	0.29	3.6	−0.13	0,19	56 Peg (K0IIp + WD)

Table 2.7: Mild barium stars with no evidence of binary motion. The numbers in column ‘Ref.’ refer to the papers listed in Tab. 2.17

HD	Sp.	Ba	N	Δt (d)	V_r (km/s)	$\sigma(V_r)$ (km/s)	$\bar{\epsilon}_1$ (km/s)	S_b (km/s)	$\Delta(38 - 41)$	Ref.	Rem.
50843	1	1	20	4437	12.21	0.33	0.33	–	–0.03	0	
95345	2	1	26	3036	5.48	0.21	0.28	0.7	+0.07	0	
119185	0	1	17	2869	–74.51	0.24	0.36	0.8	–0.05	0	
130255	0	1	26	2956	40.19	0.33	0.32	–	+0.01	0,9	subgiant CH

Table 2.8: Supergiants misclassified as mild barium stars. The numbers in column ‘Ref.’ refer to the papers listed in Tab. 2.17

HD	Sp.	Ba	N	Δt (d)	V_r (km/s)	$\sigma(V_r)$ (km/s)	$\bar{\epsilon}_1$ (km/s)	S_b (km/s)	$\Delta(38 - 41)$	Ref.	Rem.
65699	0	0	21	5163	11.17	0.27	0.31	6.0	-0.01	0,16	
206778	2	1	94	6204	2.82	0.56	0.27	5.8	+0.06	0,16	ϵ Peg (K2II/Ib var)

Table 2.9: Same as Table 2.5 for strong (Ba3, Ba4 and Ba5) barium stars. The numbers in column ‘Ref.’ refer to the papers listed in Tab. 2.17

HD/DM/ others	Sp.	Ba	P (d)	e	$f(M)$ (M_{\odot})	$O - C$ (km/s)	$\bar{\tau}_1$ (km/s)	N	S_b (km/s)	γ (km/s)	Δ (38 - 41)	Ref.
5424	1	4	1881.5±18.6	0.23 ±0.04	0.005 ±0.0004	0.18	0.30	13	–	–0.3±0.1	–0.11	1
16458 ^g	1	5	2018 ±12	0.10 ±0.02	0.041 ±0.003	0.38	na	36	na	+20.3±0.1	–0.13	13
20394	0	4	2226 ±22	0.20 ±0.03	0.0020±0.0002	0.34	-	87	–	+24.2±0.1	–0.09	6
24035	4	4	377.8 ±0.3	0.02 ±0.01 ^a	0.047 ±0.003	0.19	0.29	15	–	–12.5±0.1	–0.26	1
31487	1	5	1066.4±2.6	0.05 ±0.01	0.038 ±0.002	0.33	na	35	na	–4.2±0.7	na	13
36598	2	4	2652.8±22.7	0.08 ±0.02	0.037 ±0.002	0.21	0.27	11	–	+44.1±0.1	–0.18	1
42537	4	5	3216.2±54.7	0.16 ±0.05	0.027 ±0.005	0.43	0.30	12	1.9	–2.5±0.2	–0.31	1
43389	2	5	1689.0±8.7	0.08 ±0.02	0.043 ±0.002	0.35	0.32	24	0.6	+53.1±0.1	–0.16	2
44896	3	5	628.9 ±0.9	0.02 ±0.01 ^a	0.048 ±0.001	0.21	0.26	19	1.9	+52.2±0.1	–0.17	2
46407 ^{b,e}	0	3	457.4 ±0.1	0.013±0.008 ^a	0.035 ±0.001	0.40	0.29	68	1.8	–3.4±0.1	–0.21	2,13
49641	1	3	1768 ±23	0.0	0.0031±0.0004	0.42	na	35	na	+4.4±0.1	–0.14	13
50082	0	4	2896.0±21.3	0.19 ±0.02	0.027 ±0.002	0.35	0.31	29	1.1	–17.4±0.1	–0.12	2
60197	3	5	3243.8±66.3	0.34 ±0.05	0.0028±0.0006	0.31	0.27	14	3.0	+54.3±0.1	–0.05	1
84678	2	4	1629.9±10.4	0.06 ±0.02 ^a	0.062 ±0.003	0.30	0.29	12	0.8	+27.9±0.1	–0.31	1
88562	2	4	1445.0±8.5	0.20 ±0.02	0.048 ±0.003	0.44	0.32	23	0.7	+11.8±0.1	–0.04	1
92626	0	5	918.2 ±1.2	0.00 ±0.01 ^a	0.042 ±0.002	0.32	0.27	35	0.5	+16.3±0.1	–0.29	2
100503	3	5	554.4 ±1.9	0.06 ±0.05 ^a	0.011 ±0.001	0.55	0.28	16	1.7	–8.9±0.1	–0.22	1
101013 ^e	0	5	1711 ±4	0.20 ±0.01	0.037 ±0.001	0.58	na	118	1.4	–14.5±0.1	–0.17	13,20

Table 2.9: (continued)

HD/DM/ others	Sp. Ba	P (d)	e	$f(M)$ (M_{\odot})	$O - C$ (km/s)	\bar{e}_1 (km/s)	N	S_b (km/s)	γ (km/s)	Δ (38 - 41)	Ref.
107541	0 4	3569.9±46.1	0.10 ±0.03	0.029 ±0.002	0.28	0.31	16	0.1	+88.1±0.1	-0.26	2
120620	0 4	217.2 ±0.1	0.01 ±0.01 ^a	0.062 ±0.001	0.42	0.36	28	-	+33.2±0.1	-0.18	1
121447	7 5	185.7 ±0.1	0.015±0.013 ^a	0.025 ±0.001	0.47	0.32	26	2.8	-11.9±0.1	-0.26	7
123949	6 4	9200	0.97 ±0.06	0.105 ±0.64	0.30	0.33	25	0.6	-10.8±0.3	-0.19	1
154430	2 4	1668.1±17.4	0.11 ±0.03 ^a	0.034 ±0.003	0.48	0.29	15	1.3	-38.1±0.1	-0.04	1
178717	4 5	2866 ±21	0.43 ±0.03	0.006 ±0.001	0.47	na	46	2.0	-16.4±0.1	-0.20	13
196445	2 4	3221.3±43.0	0.24 ±0.02	0.031 ±0.002	0.23	0.29	12	0.6	-25.5±0.1	-0.22	1
199939	0 4	584.9 ±0.7	0.28 ±0.01	0.025 ±0.001	0.47	na	52	1.6	-41.7±0.1	-0.25	13
201657	1 4	1710.4±15.0	0.17 ±0.07	0.004 ±0.001	0.29	0.31	15	-	-27.7±0.2	-0.24	2
201824	0 4	2837 ±13	0.34 ±0.02	0.040 ±0.003	0.45	-	86	0.8	-31.1±0.1	-0.18	6
211594	0 4	1018.9±2.7	0.06 ±0.01	0.0140±0.0005	0.33	0.30	49	1.0	-9.9±0.1	-0.39	2
211954	2 5	5000	0.39 ±0.08	0.017 ±0.005	0.35	0.32	14	-	-6.1±0.1	-0.22	1
+38°118(a+b) ^c	2 5	299.4 ±0.2	0.14 ±0.01	0.0141±0.0004	0.30	0.31	30	1.4	-18.7±0.1	-0.19	1
+38°118(ab+c) ^c	2 5	3876.7±112.2	0.21 ±0.06	0.0017±0.0004	0.29	0.31	30	1.4	-18.3±0.1	-0.19	1
-42°2048	2 4	3260.0±28.3	0.08 ±0.02	0.065 ±0.004	0.24	0.29	12	1.4	+40.5±0.1	-0.16	1
-64°4333 ^d	0 4	386.0 ±0.5	0.03 ±0.01 ^a	0.068 ±0.003	0.31	0.33	16	-	+8.3±0.2	-0.29	1
Lü 163	-5 5	965.1 ±16.0	0.03 ±0.07 ^a	0.0029±0.0006	0.57	0.39	14	-	+2.8±0.2	-0.39	1
NGC 2420 X	- 5	1402 ±10	0.0	0.050 ±0.005	0.50	na	16	-	+78.2±0.2	na	13,21

Remarks:

- a: data compatible with circular orbit at 5% confidence level (Lucy-Sweeney test);
- b: Combined CORAVEL/DAO orbit; A DAO-CORAVEL offset of -0.19 km s^{-1} has been applied to the DAO measurements;
- c: triple system;
- d: CpD;
- e: Orbital solution listed in the Hipparcos Double and Multiple Systems Annex (ESA 1997);
- g: Acceleration solution listed in the Hipparcos Double and Multiple Systems Annex (ESA 1997)

Table 2.10: Strong barium stars with no evidence for binary motion. The numbers in column ‘Ref.’ refer to the papers listed in Tab. 2.17

HD	Sp.	Ba	N	Δt (d)	V_r (km/s)	$\sigma(V_r)$ (km/s)	$\bar{\tau}_1$ (km/s)	S_b (km/s)	$\Delta(38 - 41)$	Ref.	Rem.
19014	4	5	18	3272	13.3	0.47	0.28	2.2	-0.01	0	jitter only?
65854	1	3	30	3369	0.5	0.42	na	na	na	13	

Table 2.11: Orbital elements of S stars. Column 2, labeled GCGSS, lists the star number in the *General Catalogue of Galactic S Stars* (Stephenson 1984). The numbers in column ‘Ref.’ and ‘Ref. Tc’ refer to the papers listed in Tab. 2.17

HD/DMGCGSS	Sp.	P (d)	e	$f(M)$ (M_{\odot})	$O - C$ (km/s)	$\bar{\epsilon}_1$ (km/s)	N	S_b (km/s)	γ (km/s)	Ref. orb.	Tc	Ref. Tc	Rem.
7351	26 S3/2	4593 ±110	0.17 ±0.03	0.073 ±0.007	0.68	0.31	50	3.3	+1.5±0.1	3,4	n	15	HR 363
22649 ^f	79 S4/2	596.2 ±0.2	0.09 ±0.02	0.037 ±0.003	0.8	na	53	na	-22.3±0.1	18	n	15	HR 1105
30959 ^d	114 S3/1	> 1900				0.29	12	4.3	-8.8±0.7	1,14	y	15	σ^1 Ori
35155	133 S4,1	640.5 ±2.8	0.07 ±0.03	0.032 ±0.003	0.81 ^c	0.33	19	3.5	+79.7±0.2	0,10	n	15	
246818	156 S	2548.5±73.2	0.18 ±0.11 ^e	0.0035±0.0015	0.59	0.37	17	2.8	-45.5±0.2	1	n	8	+05° 1000
288833	233 S3/2	> 3900				0.38	18	3.5	+81.1±1.0	1	n	8	+02° 1307
49368	260 S3/2	2995.9±67.1	0.36 ±0.05	0.022 ±0.003	0.58	0.34	23	4.3	+49.8±0.1	1	n	15	V613 Mon
63733	411 S4/3	1160.7±8.9	0.23 ±0.03	0.025 ±0.003	0.38	0.32	14	3.5	+1.9±0.1	1	y?	15	
95875	720 S3,3	197.2 ±0.4	0.02 ±0.04 ^e	0.059 ±0.009	0.70	0.28	10	4.0	+40.6±1.1	1	n	0	Hen 108
121447	- S0	185.7 ±0.1	0.015±0.013 ^e	0.025 ±0.001	0.47	0.32	26	2.8	-11.9±0.1	7	n	17	
170970	1053 S3/1	4392 ±202	0.08 ±0.04 ^e	0.021 ±0.002	0.33	0.30	39	3.9	-35.8±0.1	1	y?	15	
184185	1140 S3*4	> 3400				0.43	22	4.3	+1.5±1.6	1	-	-	-21° 5435
191226	1192 M1S	1210.4±4.3	0.19 ±0.02	0.013 ±0.001	0.38	0.30	36	4.2	-25.0±0.1	3	n	15	
191589	1194 S	377.3 ±0.1	0.25 ±0.003	0.394 ±0.005	0.29	0.30	41	3.1	-9.7±0.1	1	n	15	
218634 ^e	1322 M4S	> 3700				0.36	28	5.6	+20.1±2.3	0,22	n	8	57 Peg

Table 2.11: (continued)

HD/DM	GCGSS Sp.	P (d)	e	$f(M)$ (M_{\odot})	$O - C$ (km/s)	$\bar{\epsilon}_1$ (km/s)	N	S_b (km/s)	γ (km/s)	Ref. orb.	Tc	Ref.	Rem.
332077	1201 S3,1	669.1 \pm 1.0	0.077 \pm 0.007	1.25 \pm 0.02	0.66	0.46	39	10.2	-5.2 \pm 0.1	0,10	n	8	
343486	1092 S6,3	3165.7 \pm 37.6	0.24 \pm 0.03	0.039 \pm 0.005	0.82	0.43	37	3.8	+4.9 \pm 0.1	1	-	-	
+21 $^{\circ}$ 255 ^b	45 S3/1	4137 \pm 317	0.21 \pm 0.04	0.032 \pm 0.004	0.51	0.33	36	3.2	-38.5 \pm 0.3	1	n	8	
+24 $^{\circ}$ 620	87 S4,2	773.4 \pm 5.5	0.06 \pm 0.03 ^a	0.042 \pm 0.005	0.82	0.41	19	4.0	-21.0 \pm 0.2	0,10	n	8	
+22 $^{\circ}$ 700	96 S6,1	849.5 \pm 8.8	0.08 \pm 0.06 ^a	0.043 \pm 0.008	1.14	0.48	20	4.9	+40.5 \pm 0.3	0,10	n	8	
+79 $^{\circ}$ 156	106 S4,2	> 3900				0.39	19	4.3	-33.0 \pm 2.1	1	n	8	
+23 $^{\circ}$ 3093	981 S5,4	1008.1 \pm 4.8	0.39 \pm 0.03	0.045 \pm 0.005	0.81	0.41	30	3.8	-44.1 \pm 0.2	0,10	n	8	
+23 $^{\circ}$ 3992	1209 S3,3	3095.6 \pm 41.7	0.10 \pm 0.03 ^a	0.034 \pm 0.004	0.71	0.37	43	4.3	-26.7 \pm 0.1	1	n	8	
+31 $^{\circ}$ 4391	1267 S2/4	> 3600				0.37	28	3.3	+25.2 \pm 1.6	1	-	-	
+28 $^{\circ}$ 4592	1334 S2/3:	1252.9 \pm 3.5	0.09 \pm 0.02	0.016 \pm 0.001	0.32	0.34	34	3.2	-37.5 \pm 0.1	1	n	8	

Remarks:

- a: Data compatible with circular orbit at 5% confidence level (Lucy-Sweeney test);
- b: Visual binary; the S star is BD+21 $^{\circ}$ 255 = PPM 91178 = SAO 75009 = HIC 8876, whereas its visual K-type companion (BD+21 $^{\circ}$ 255p = PPM 91177 = SAO 75008) is also a spectroscopic binary whose orbit is given in Jorissen & Mayor (1992);
- c: Two outlying measurements (at phase 0.38 and 0.93 deviating by 1.40 and -1.98 km s $^{-1}$, respectively) were kept in the present orbital solution. No obvious instrumental origin could be found to account for these outlying measurements, which may have a real - but as yet unidentified - physical cause in this strongly interacting system (Ake et al. 1991);
- d: The WD companion of σ^1 Ori has been detected by IUE (Ake & Johnson 1988);
- e: 57 Peg has a composite spectrum S+A6V (Van Eck et al. 1998);
- f: Orbital solution listed in the Hipparcos Double and Multiple Systems Annex (ESA 1997)

Table 2.12: Non-binary (misclassified?) S stars

HD/DM	GCGSS	Sp.	N	Δt (d)	V_r (km/s)	$\sigma(V_r)$ (km/s)	$\bar{\epsilon}_1$ (km/s)	S_b (km/s)	Tc	Ref. Tc	Rem.
262427	247	S?	10	3622	+34.61	0.37	0.31	2.3	-	-	S class from Perraud (1959)
+22° 4385	1271	S2	26	3607	-2.63	0.36	0.36	2.6	-	-	S class from Vyssotsky & Balz (1958)

Table 2.13: S stars with radial-velocity jitter. The numbers in column ‘Ref. Tc’ refer to the papers listed in Tab. 2.17

HD/DM	GCGSS	Sp.	N	Δt (d)	V_r (km/s)	$\sigma(V_r)$ (km/s)	$\bar{\epsilon}_1$ (km/s)	S_b (km/s)	Tc	Ref. Tc	Rem.
BD−10°1334	176	Sr	16	3613	+22.72	1.39	0.48	7.1	-	-	
BD+15°1200	219	S4/2	19	3933	+46.77	1.47	0.45	5.2	-	-	
61913	382	M3S	12	1860	−15.68	0.65	0.30	4.9	dbfl	17	NZ Gem = HR 2967
BD−04°2121	416	S5/2	18	3585	+31.83	1.04	0.38	5.6	yes	8	
BD−21°2601	554	S3*3	14	3308	+44.72	1.07	0.36	3.5	no	0	
BD+20°4267	1158	Swk	19	3009	+26.69	1.59	0.41	6.9	-	-	
189581	1178	S4*2	19	3399	−17.04	0.78	0.34	4.5	no	15	
BD+04°4354	1193	S4*3	13	3006	−8.79	0.63	0.39	5.3	yes	8	
192446	1198	S6/1	17	3245	−22.48	0.79	0.42	6.0	yes	8	
216672	1315	S4/1	30	3251	+12.47	0.76	0.31	4.9	yes	15	HR Peg = HR 8714

Table 2.14: Mira S stars. The numbers in column ‘Ref. Tc’ refer to the papers listed in Tab. 2.17

HD	GCGSS	Var	Sp.	N	Δt (d)	V_r (km/s)	$\sigma(V_r)$ (km/s)	$\bar{\epsilon}_1$ (km/s)	S_b (km/s)	Tc	Ref. Tc	Rem.
1967	14	R And	S5-7/4-5e	9	1924	-4.85	4.92	0.54	9.6	yes	17	
4350	12	U Cas	S5/3e	5	729	-51.62	7.97	0.78	8.5	yes	17	
14028	49	W And	S7/1e	3	1856	-38.34	0.70	0.42	4.2	yes	17	
29147	103	T Cam	S6/5e	3	641	-11.09	5.28	0.55	11.5	yes	17	
53791	307	R Gem	S5/5	7	2126	-45.55	4.05	0.58	11.7	yes	17	
70276	494	V Cnc	S3/6e	4	2126	-4.71	10.17	0.48	10.3	dbfl	17	
110813	803	S UMa	S3/6e	13	2667	+1.46	5.15	0.45	10.1	yes	17	binary?
117287	-	R Hya	M6e-M9eS	16	2924	-9.69	2.06	0.70	9.6	prob	17	
185456	1150	R Cyg	S6/6e	4	767	-29.45	2.42	0.58	13.2	yes	17	
187796	1165	χ Cyg	S7/1.5e	12	2976	+3.24	3.19	0.61	8.3	yes	17	
190629	1188	AA Cyg	S6/3	31	2931	+11.41	1.33	0.42	8.7	yes	17	
195763	1226	Z Del	S4/2e	3	348	+37.43	3.52	0.93	9.7	yes	17	
211610	1292	X Aqr	S6,3e	7	1746	+11.67	7.20	0.75	8.3	prob	17	

Table 2.15: SC Stars. The numbers in column ‘Ref.’ refer to the papers listed in Tab. 2.17

HD/DM	GCGSS	Var	Sp.	N	Δt (d)	V_r (km/s)	$\sigma(V_r)$ (km/s)	$\bar{\epsilon}_1$ (km/s)	S_b (km/s)	Tc	Ref. Tc	Rem.
286340	117	GP Ori	SC7/8	15	3614	+82.78	2.09	0.45	7.0	-	-	
44544	212	FU Mon	S7/7	17	3720	-25.86	1.71	0.48	7.2	-	-	
BD-04°1617	244	V372 Mon	SC7/7	13	3341	+16.66	2.93	0.46	7.3	-	-	
BD-08°1900	344		S4/6	17	3619	+72.47	1.54	0.40	5.4	-	-	binary?
54300		R CMi	CS	16	3740	+45.76	6.06	0.52	12.2	yes	17	pseudo-orbit
198164		CY Cyg	CS	27	3613	+4.52	1.02	0.34	6.9	yes	17	
209890		RZ Peg	C9	21	2932	-32.32	6.51	0.56	14.9	yes	17	pseudo-orbit

Table 2.16: Tc-poor carbon stars. The column labelled GCCCS refers to the entry number in the *General Catalogue of Cool Carbon Stars* (Stephenson 1973)

HD	GCCCS	Var	Sp.	N	Δt (d)	V_r (km/s)	$\sigma(V_r)$ (km/s)	$\bar{\tau}_1$ (km/s)	S_b (km/s)	Rem.
46687	537	UU Aur	C5,3	6	857	13.5	1.27	0.28	5.8	
76221	1338	X Cnc	C5,4	15	2117	-6.0	1.13	0.35	4.8	binary?
108105	1999	SS Vir	C6,3	16	1976	2.4	3.30	0.62	6.6	pseudo-orbit

Table 2.17: References to Tables 2.5–2.16

0	This work
1	Udry et al. (1998a)
2	Udry et al. (1998b)
3	Carquillat et al. (1998)
4	Jorissen et al. (1996)
5	Griffin (1996)
6	Griffin et al. (1996)
7	Jorissen et al. (1995)
8	Jorissen et al. (1993)
9	Lambert et al. (1993)
10	Jorissen & Mayor (1992)
11	Griffin & Keenan (1992)
12	Griffin (1991)
13	McClure & Woodsworth (1990)
14	Ake & Johnson (1988)
15	Smith & Lambert (1988)
16	Smith & Lambert (1987)
17	Little et al. (1987)
18	Griffin (1984)
19	Schindler et al. (1982)
20	Griffin & Griffin (1980)
21	McClure et al. (1974)
22	Hackos & Peery (1968)
23	Fekel et al. (1993)

Chapter 3

The HIPPARCOS Hertzsprung-Russell diagram of S stars

3.1 Introduction

A direct prediction of the binary scenario for S stars is the brighter luminosity of intrinsic S stars with respect to extrinsic S stars. The check of this prediction has been hampered till now by the difficulty in evaluating the absolute magnitude of S stars. Methods used so far include individual parallaxes (χ Cyg: Stein 1991), membership in a binary system with a detected main sequence companion (π^1 Gru: Feast 1953; 57 Peg: Hackos & Peery 1968; T Sgr: Culver & Ianna 1975), membership in a moving group (π^1 Gru, R Hya: Eggen 1972b; R And, HR 363, o^1 Ori: Eggen 1972a), membership in a cluster or association (WY Cas: Mavridis 1960; TT9, TT12: Feast et al. 1976), Ca II K-line emission width (HD 191630, 57 Peg: Warner 1965; o^1 Ori: Boesgaard 1969). Most of these individual estimates were used by Scalo (1976) to locate S stars in the Hertzsprung-Russell (HR) diagram, with the conclusion that they fall above the luminosity threshold for TP-AGB stars, as derived from the early AGB model calculations available to Scalo. Although Scalo's conclusion appears to support the customary M-S-C sequence, statistical estimates based on the kinematics or space distribution of S stars pointed out a systematic difference between the average luminosity of non- or weakly-variable S stars and of Mira S stars, the latter being about 3 visual magnitudes brighter than the former (Takayanagi 1960; Yorke & Wing 1979). Such a segregation apparent in these early studies might already hint at the current dichotomy between extrinsic and intrinsic S stars. The rather heterogeneous set of former luminosity determinations for S stars, along with our revised understanding of their evolutionary status, prompted the present study, based on the trigonometrical parallaxes provided by the HIPPARCOS

satellite. Its aim is to locate Tc-rich and Tc-poor S stars in the Hertzsprung-Russell (HR) diagram, and to compare their respective locations with stellar evolutionary tracks.

Our HIPPARCOS sample of S stars is described in Sect. 3.2. The method used for deriving their bolometric magnitudes is detailed in Sect. 3.3. The HR diagram of S stars is discussed in Sect. 3.4, with special emphasis on the comparison with theoretical evolutionary tracks and with S and C stars in the Magellanic Clouds. Finally, the correlation between the infrared colours of S stars and their location on the giant branches is discussed in Sect. 3.5.

The HIPPARCOS parallaxes used in this study did not take into account the orbital elements. Yet, if the orbital period is of the order of one year, it is very difficult to distinguish the motion of the star due to binarity (orbital contribution) from the motion of the earth around the Sun (parallactic contribution), and thus to get a meaningful parallax. However, a subsequent reduction of the HIPPARCOS material, taking into account the binary orbit, does not lead to any significant changes in any of the S stars parallaxes (Pourbaix 1999, priv. comm.).

3.2 S stars in the HIPPARCOS catalogue

A full discussion of the HIPPARCOS mission can be found in the HIPPARCOS catalogue (ESA 1997). Cross-identifications between the HIPPARCOS catalogue and the *General Catalogue of Galactic S Stars* (Stephenson 1984; GCGSS) yield 63 stars in common between the two catalogues. Of these, 22 are part of the HIPPARCOS general survey (a systematic monitoring of all stars down to magnitudes 7.3 – 9, depending on galactic latitude and spectral type), and 41 belong to samples included in the HIPPARCOS Input Catalogue (Turon & al. 1992, 1992b, 1993) for a particular purpose. The sample of S stars studied here can thus in no way be considered as a complete sample, since it rather reflects the particular interests prevailing at the time of construction of the HIPPARCOS Input Catalogue. A comparison with the GCGSS indicates that the HIPPARCOS sample of S stars is nevertheless complete down to $V = 7.5$.

Table 3.1 lists various identifications of the S stars considered in this work. The different columns contain the following data:

1. HIPPARCOS Input Catalogue (HIC) number;
- 2-3. GCGSS and HD numbers;
4. variable name in the the *General Catalogue of Variable Stars* (Kholopov et al. 1985; GCVS);
5. variability type from the GCVS;
6. spectral type from the GCGSS;
7. presence (y) or absence (n) of technetium lines [from Little et al. (1987), Smith & Lambert (1988), from the compilation of Jorissen et al. (1993), or from Chap. 5 in the case of HIC 28297];
- 8-9. annual parallax π and its standard error σ_π (both expressed in milliarcseconds).

Table 3.2 lists the basic photometric properties of the S stars in the HIPPARCOS sample. The various columns contain the following data:

1. HIC number;
- 2-3. median H_p magnitude and its standard error σ_{H_p} ;
4. colour excess E_{B-V} ;
5. Johnson V_J magnitude from the HIPPARCOS catalogue;
6. dereddened $(V - K)_0$ colour index;
7. dereddened K_0 magnitude;
8. bolometric correction BC_K to the K magnitude;
9. bolometric magnitude M_{bol} (see Sect. 3.3 for details about the derivation of the quantities listed in columns 4–9);
10. method used for deriving the bolometric correction: (1) by integrating under the energy curve, or (2) from the $(BC_K, V - K)$ relation of Bessell & Wood (1984);
11. source for the HIPPARCOS $(V - I)_C$ colour [A-G: from VRI_C photometry; H-K: from UBV_J photometry; L-P: from HIPPARCOS and Star Mapper photometry; Q: specific treatment applied to long-period variables; R: from spectral type; see the HIPPARCOS and Tycho Catalogues (ESA 1997, Vol. 1, *Introduction and Guide to the Data*) for details];
12. duplicity flag (field H59 of the HIPPARCOS catalogue; see Sect. 3.4.1);
13. other identifications [‘Hen’ refers to the survey of S stars by Henize (1960)].

One star (HIC 42650 = GCGSS 544) appears outlying in many respects. With the largest parallax in the sample and the second faintest H_p magnitude, it is intrinsically much fainter than all the other stars in the sample. It is also somewhat bluer, with $(B - V)_J = 1.39$ and $(V - I)_C = 1.65$, compared to average colour indices of $\langle (B - V)_J \rangle = 1.79$ and $\langle (V - I)_C \rangle = 2.72$ for the whole sample.

A low-resolution spectrum ($\Delta\lambda \sim 0.3$ nm) of this star, covering the spectral range 440 – 820 nm, has been obtained at the *European Southern Observatory* (ESO, La Silla, Chile) on the 1.52-m telescope equipped with the Boller & Chivens spectrograph (grating #23 + filter GG 420; 114 \AA mm^{-1}) and a Loral/Lesser thinned, UV-flooded 2048x2048 CCD (CCD#39; 15 \mu m pixels). The flux response curve of the system has been calibrated using the spectrophotometric standard star LTT 4816.

The spectrum of GCGSS 544 appears to be that of a M0-M1 dwarf, as can be seen on Fig. 3.1 from the strong MgH ($\lambda 478.0$ and $\lambda 521.1$) and CaH ($\lambda 638.2$ and $\lambda 638.9$) bands, as well as from the strong Na D line superimposed on moderately strong TiO bands (Jaschek & Jaschek 1987). This classification is consistent with its absolute visual magnitude $M_v = 8.6$ derived from its HIPPARCOS parallax and V_J magnitude. That star is thus misclassified as S star, since there is no trace whatsoever of ZrO bands in its spectrum.

The case of T Cet (= HIC 1728) is also conflicting, since it was classified as M5-6Se in the original paper by Keenan (1954) defining the S class, and reclassified as M5-6Ib-II in the Michigan Spectral Survey (Houk & Cowley 1975). The spectra of supergiants and weak S-type stars look very similar at the low

Table 3.1: S stars in the HIPPARCOS catalogue: Identifications and parallaxes

HIC	GCGSS	HD	Var	Var type	Sp.	T _c	π	σ_{π}
621	3	310			S3,1	n	2.50	0.69
1728	8	1760	T Cet	SRc	M5-6Se; M5-6Ib-II	y	4.21	0.84
1901	9	1967	R And	M	S5-7/4-5e	y	-0.06	6.49
5091	22	6409			M2wkS	n	2.43	0.89
5772	26	7351			S3/2	n	3.21	0.82
8876	45				S3/1	n	-1.92	1.50
10687	49	14028	W And	M	S7/1e	y	-1.17	3.17
17296	79	22649	BD Cam	Lb	S4/2	n	6.27	0.63
21688	104	29704			S:	n	1.84	1.00
22667	114	30959	<i>o</i> ¹ Ori	SRb	S3/1	y	6.02	0.94
25092	133	35155			S4,1	n	1.32	0.99
26718	149	37536	NO Aur	Lc	M2S	y	2.38	0.97
28297	178	40706			S2,1	n	1.17	0.88
30301	212	44544	FU Mon	SR	S7/7 (SC)		0.30	1.58
32627	260	49368	V613 Mon	SRb:	S3/2	n	1.65	1.11
32671	265	49683			M4S		-0.18	1.07
33824	283	51610	R Lyn	M	S5/5e		-3.39	1.79
34356	307	53791	R Gem	M	S4*1	y	-6.22	6.50
35045	312	54587	AA Cam	Lb	M5S	y	1.24	1.02
36288	347	58521	Y Lyn	SRc	M6S	y	4.03	1.33
37521	382	61913	NZ Gem	SR	M3S	n?	3.19	0.79
38217	411	63733			S4/3	y?	0.00	0.99
38502	422	64332	NQ Pup	Lb	S5/2	y	3.01	1.11
38772	436		SU Pup	M	S4,2		-1.75	1.81
40977	494	70276	V Cnc	M	S3/6e		26.58	42.74
45058	589	78712	RS Cnc	SRc:	M6S	y	8.21	0.98
54396	722	96360			M3	n	2.10	0.90
59844	788		BH Cru	M	S5,8e (SC)		1.64	0.99
62126	803	110813	S UMa	M	S3/6e	y	0.63	0.94
64613	815				S3,3		-1.90	2.99
64778	816	115236	UY Cen	SR	S6/8 (CS)		1.66	1.04
66783	826	118685			S6,2	n	3.42	0.65
67070	829				M1wkS	n	2.27	1.06
68837			U Cir	SR	C		-1.92	1.51
71348	804	110994	BQ Oct	Lb:	S5,1		2.08	0.57
72989	867	131217			S6,2	n	4.24	1.02

Table 3.1: (Continued)

HIC	GCGSS	HD	Var	Var type	Sp.	T _c	π	σ_{π}
77619	903	142143	ST Her	SRb	M6.5S	y	3.22	0.75
81970	937				M2S	n	3.32	1.14
82038	938	151011			Swk	n	4.30	1.07
87850		163990	OP Her	SRb	M6S	y	3.26	0.54
88620	1014	164392					2.09	1.06
88940	1023	165774			S4,6	n	0.23	1.50
89316	1025	165843			S2.1		1.47	1.05
90723	1053	170970			S3/1	y	1.83	0.67
94706	1117	180196	T Sgr	M	S5/6e	y	-31.67	9.28
97629	1165	187796	χ Cyg	M	S7/1.5e	y	9.43	1.36
98856	1188	190629	AA Cyg	SRb	S6/3	y	0.86	0.88
99124	1192	191226			M1S-M3SIIIa	n	0.39	0.71
99312	1194	191589			S:	n	2.25	0.77
99758	1195	191630			S4,4	y	1.18	0.81
100599	1211		V865 Aql	M	S7,2		-1.28	1.91
101270	1224	195665	AD Cyg	Lb	S5/5		-0.96	1.15
103476	1254	199799			MS		2.16	0.82
110146	1292	211610	X Aqr	M	S6,3e:		-4.01	5.73
110478	1294	212087	π^1 Gru	SRb	S5,7:	y	6.54	1.01
112227	1304	215336			Swk	n	0.74	0.92
112784	1309		SX Peg	M	S3/6e		2.12	2.99
113131	1315	216672	HR Peg	SRb	S4/1	y	3.37	0.94
114347	1322	218634	57 Peg	SRa	M4S	n	4.28	0.88
115965	1334				S2/3:	n	1.72	1.26
HIPPARCOS close visual binaries								
19853	89	26816			S	y	3.79	1.05
27066	157				S		1.13	3.50
Misclassified S star								
42650	544				MS ^a		32.13	1.50
Comparison barium star								
68023		121447			K7IIIBa5; S0	n ^b	428±71	pc ^c

Remarks:

a: HIC 42650 is an early M dwarf rather than a MS star

b: Little et al. 1987

c: Distance derived by Mennessier et al. 1997 from a maximum-likelihood estimator based on the HIPPARCOS parallax

Table 3.2: S stars in the HIPPARCOS catalogue: Photometry

HIC	H_p	σ_{H_p}	E_{B-V}	V_J	$(V-K)_0$	K_0	BC_K	M_{bol}	S_{V-I}	Dupl	Other ident.
621	7.570	0.003	0.000	7.50	4.38	3.12	2.74	-2.14	2	O	Hen 1
1728	5.439	0.033	0.000	5.61	6.5	-0.89	2.91	-4.85	1	O	
1901	10.705	0.011		10.71		-0.11				K	V
5091	7.462	0.004	0.042	7.44	5.04	2.27	2.84	-2.95	2	O	
5772	6.395	0.004	0.049	6.33	4.65	1.53	2.68	-3.25	1	F	HR 363
8876	9.072	0.002		8.97						L	+21°255
10687	8.075	0.226		8.60		0.7				O	
17296	5.095	0.003	0.041	5.06	4.78	0.15	2.77	-3.09	1	C	O
21688	8.225	0.009	0.000	8.23	5.64	2.59	2.91	-3.16	2	O	Hen 1105
22667	4.702	0.005	0.121	4.71	4.96	-0.62	2.85	-3.87	1	O	Hen 3
25092	6.882	0.011	0.128	6.82	4.46	1.97	2.76	-4.66	2	F	V
26718	6.243	0.011	0.245	6.23	4.67	0.8	2.74	-4.57	1	C	
28297	8.987	0.002	0.029	8.88						L	Hen 7
30301	8.520	0.032	0.327	9.76	7.35	1.4	3.03		1	O	
32627	7.749	0.004	0.051	7.73	4.93	2.64	2.83	-3.43	2	O	
32671	8.232	0.006		8.38		2.07				O	
33824	9.922	0.029		9.93		1.91				K	
34356	7.529	0.456		7.53		2.12				P	V
35045	7.578	0.007	0.039	7.69	6.01	1.56	2.95	-5.01	2	O	V
36288	6.897	0.005	0.058	7.27	7.63	-0.54	3.08	-4.43	1	O	V
37521	5.587	0.003	0.027	5.55	4.85	0.61	2.86	-4.01	1	G	HR 2967
38217	7.981	0.002		7.90						F	
38502	7.532	0.015	0.072	7.52	5.17	2.13	2.86	-2.61	2	F	V
38772	9.609	0.218		9.64		2.64				K	Hen 32
40977	9.262	0.152	0.004	9.25						K	X
45058	5.450	0.026	0.002	6.04	7.74	-1.71	3.07	-4.06	1	O	
54396	8.075	0.006	0.000	8.05						O	
59844	7.737	0.118	0.163	7.74						K	Hen 120
62126	8.909	0.148	0.000	8.94	5.95	2.99	2.87		1	K	
64613	11.404	0.021		11.33		2.85				K	Hen 134, -30°10427
64778	6.787	0.033	0.088	6.85	6.09	0.49	2.85	-5.55	1	L	V
66783	6.832	0.007	0.062	6.91	5.82	0.9	2.93	-3.49	2	O	Hen 135 Hen 138
67070	8.541	0.002	0.009	8.43						L	-2°3726
68837	9.609	0.013		9.54						J	V
71348	6.806	0.005	0.106	6.82	5.16	1.33	2.86	-4.21	2	O	C* 2142 Hen 127
72989	7.425	0.004	0.204	7.45						O	Hen 150

Table 3.2: (continued)

HIC	H_p	σ_{H_p}	E_{B-V}	V_J	$(V-K)_0$	K_0	BC_K	M_{bol}	S_{V-I}	Dupl	Other ident.
77619	6.920	0.026	0.000	7.69	8.55	-0.86	3.11	-5.20	2	O	
81970	7.803	0.004	0.173	7.99	5.63	1.83	2.91	-2.64	2	O	-13°4495
82038	6.689	0.002	0.190	6.60	4.59	1.43	2.78	-2.62	2	L	
87850	6.105	0.010	0.022	6.22	6.09	0.06	2.92	-4.45	1	O	
88620	8.448	0.004	0.072	8.39						O	Hen 183
88940	8.211	0.003	0.186	8.17						O	Hen 186
89316	8.412	0.005	0.082	8.37						O	Hen 187
90723	7.457	0.002	0.041	7.42	4.88	2.41	2.82	-3.45	2	O	
94706	10.826	0.223		10.78		1.05	3.14		1	K	V
97629	6.169	0.168	0.004	7.91	7.69	-1.73	3.27	-3.58	1	O	V
98856	8.159	0.037	0.491	8.16	6.26	0.39	2.94		1	K	
99124	7.374	0.002	0.491	7.28	3.4	2.37	2.52		2	L	
99312	7.368	0.001	0.081	7.26						H	
99758	6.757	0.004	0.029	6.74	5.05	1.6	2.71	-5.33	1	O	Hen 197
100599	9.642	0.134		10.34		1.49				Q	+0°4492
101270	8.607	0.011		8.61		1.18				K	
103476	7.248	0.016	0.071	7.36	5.99	1.15	2.95	-4.22	2	O	
110146	10.188	0.179		10.82		2.9				Q	V
110478	5.495	0.011	0.000	6.42	8.55	-2.13	3.12	-4.93	1	O	V
112227	7.929	0.001	0.089	7.82						L	Hen 202
112784	9.241	0.176	0.056	9.25						K	V
113131	6.346	0.016	0.050	6.39	5.47	0.77	2.86	-3.73	1	O	V
114347	5.033	0.011	0.024	5.05	5.47	-0.5	3	-4.34	1	F	HR 8714
115965	9.536	0.003	0.056	9.43						K	+28°4592
HIPPARCOS close visual binaries											
19853	7.607	0.010	0.120	7.90						O	C
27066	11.274	0.010	0.327	11.12						R	C
Misclassified S star											
42650	11.118	0.005	0.009	11.03						I	
Comparison barium star											
68023			0.056		3.78	4.090	2.69	-1.40	1		

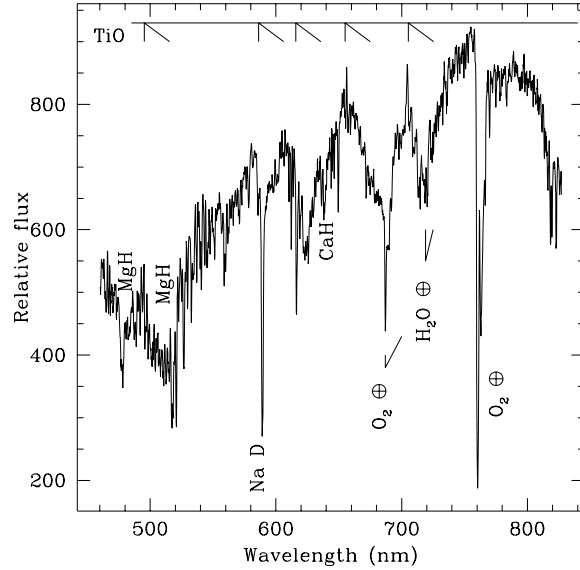


Figure 3.1: The spectrum of HIC 42650 = GCGSS 544, with the principal spectral features identified

plate dispersions used in classification work, and are therefore easily confused (e.g., Lloyd Evans & Catchpole 1989). T Cet has nevertheless been kept in our final list until higher resolution spectra resolve these equivocal classifications.

The star HIC 27066 (= GCGSS 157) has HIPPARCOS colours that do not match those of an S star [$(B - V)_J = 0.80$ and $(V - I)_C = 0.83$]. HIPPARCOS found it to be a close visual binary with a separation of 0.262 arcsec, the companion being 1.55 mag fainter in the H_p band. The colour indices measured by HIPPARCOS correspond to the composite light from the system.

The only other S star found by HIPPARCOS to be a close visual binary (with an angular separation of 0.18 arcsec) is HIC 19853. Although its colour indices are not atypical for a late-type star, the measured colours must clearly be composite since the companion is only 0.35 mag fainter in the H_p band.

These two stars have been excluded from our final sample. Among the 61 remaining S stars, 20 do exhibit technetium lines in their spectrum, 21 do not, and the Tc content is unknown for the remaining 20 stars.

The only trigonometrical parallax for an S star with a small relative error available in the literature prior to the HIPPARCOS mission is that obtained by Stein (1991) for the Mira S star χ Cyg. His value (8.8 ± 1.9 mas) is in good agreement with the HIPPARCOS parallax listed in Table 3.1.

3.3 Colours and bolometric magnitudes

3.3.1 Colours

Although the $(B - V)_J$ and $(V - I)_C$ (where the subscripts J and C stand for the Johnson and Cousins photometric systems, respectively) colour indices are directly provided by the HIPPARCOS catalogue, we felt that the $(V - K)_J$ colour index, derived on a case-by-case basis, is a more appropriate temperature indicator. For most of the stars in our sample, the $(V - I)_C$ index listed in the HIPPARCOS catalogue has been derived from a fiducial relation $(V - I)_C = f(B - V)_J$ calibrated on normal M giants (as indicated by the flags H-P in column S_{V-I} of Table 3.2). Several S stars in our sample, however, fall outside the validity range of such a calibration, so that $(V - I)_C$ as provided by the HIPPARCOS catalogue is not a reliable temperature indicator for our purpose.

As discussed by Ridgway et al. (1980), $B - V$ for late-type stars is not a good temperature indicator either, because the temperature has opposite effects on $B - V$: when the temperature decreases, the absorption in the V band due to TiO bands increases (thus decreasing $B - V$), whereas the black body continuum tends to increase the $B - V$ index. By contrast, these two effects act together to increase $V - K$.

The $V - K$ index has therefore been constructed from individual K magnitudes collected from the literature, mostly from the *Two-Micron Sky Survey* (Neugebauer & Leighton 1969; TMSS), but also from Wing & Yorke (1977), Catchpole et al. (1979), Chen et al. (1988), Noguchi et al. (1991) and Fouqué et al. (1992); it is available for 46 stars as listed in Table 3.2. The adopted V magnitude corresponds to the V_J magnitude listed in the HIPPARCOS catalogue. It has been obtained by the HIPPARCOS reduction consortia from a $(H_p - V_J, (V - I)_C)$ relation, with $(V - I)_C$ derived by different methods as listed in column S_{V-I} of Table 3.2. According to the HIPPARCOS reduction consortia (ESA 1997, Vol. 1, *Introduction and Guide to the Data*), that relation is quite well defined from classical photometry in the range $-0.4 < (V - I)_C < 3.0$ (which holds for 47 S stars), with uncertainties of less than 0.01 mag. The red extension down to $(V - I)_C = 5.4$ (15 S stars) was defined using observations of Mira variables devoted to that purpose, resulting in an uncertainty of 0.03–0.05 mag. For indices down to $(V - I)_C = 9.0$ [only χ Cyg is concerned, with $(V - I)_C = 6.1$], the HIPPARCOS reduction consortia adopted a linear extrapolation of the previous relation. To avoid the uncertainties inherent to such an extrapolation, a (flux) average of the numerous V_J measurements of χ Cyg available in the literature has been preferred over the linear extrapolation.

In summary, the uncertainty on V_J introduced by the colour transformation applied on H_p is largely offset by the fact that the H_p magnitude is a good time average over a uniform period of time (the duration of the HIPPARCOS mission), the same for all the stars. As discussed in Sect. 3.4.1, the intrinsic variability of S stars is indeed a major source of uncertainty on their location in the HR diagram.

3.3.2 Bolometric magnitudes

Since most of the flux from S stars is radiated in the near-infrared, the bolometric correction is best determined from near-infrared magnitudes. Moreover, the near-infrared and bolometric variability is much smaller than the visual amplitude of variations (Mira-type variables which vary typically by 6 to 8 mag in the visual region, vary by less than 1 mag in the K band; Feast et al. 1982). Therefore, the bolometric correction BC_K in the K band (defined as $M_{\text{bol}} = K + BC_K$) has been adopted in this work (and listed in Table 3.2).

In order to compute bolometric corrections, an extensive set of magnitudes ranging from the ultraviolet to the far IR has been collected from the literature. This set includes Johnson $UBVRIJHKLM$ magnitudes when available, as well as good quality fluxes at 4.2, 11.0, 19.8 and 27.4 μm from the Revised Air Force Four-Color Infrared Sky Survey (Price & Murdock 1983), and four-colour infrared photometry from Gillett et al. (1971). The IRAS 12, 25, 60 and 100 μm fluxes (with a quality flag 3) from the second edition of the *Point Source Catalogue* (IRAS Science Team 1988) were also used, or when available, the reprocessed IRAS fluxes provided by Jorissen & Knapp (1998). When several measurements in the same filter are available, a flux average has been computed.

All magnitudes bluer than 4.8 μm have been corrected for interstellar reddening and absorption, using the extinction law as provided by Cohen et al. (1981) for the $BVRIHKL$ filters and by Koornneef (1983) for the J and M filters. The visual extinction A_V was derived either from Neckel & Klare (1980) with the distance derived from the HIPPARCOS parallax, or from Burstein & Heiles (1982) for stars with galactic latitudes $|b| > 10^\circ$. In the latter case, the E_{B-V} value provided by Burstein & Heiles (1982) was reduced by the factor $[1 - \exp(-10d \sin |b|)]$, where d stands for the distance in kpc. In the remaining cases, the cosecant formula (Feast et al. 1990) was used:

$$E_{B-V} = 0.032 (\text{cosec}|b| - 1) [1 - \exp(-10 d \sin |b|)]$$

The adopted E_{B-V} values are listed in Table 3.2.

The dereddened $BVRIJKLM$ magnitudes have then been converted into fluxes using the zero-magnitude fluxes provided by Johnson (1966). This particular choice will be justified below. The zero-magnitude flux in the H band was taken from Jaschek (1978) and, for the remaining bands, from the original papers quoted above.

A limited sample of 17 stars have enough broad-band colours available ($BVRIJK$, as well as IRAS 12, 25 and 60 μm) to derive the bolometric magnitude by a direct integration of the available fluxes over wavelength. More precisely, the trapezoidal rule has been used on the curve λF_λ versus $\log \lambda$. The zero point of the bolometric magnitude has been defined from the requirement that $L = 3.86 \cdot 10^{33} \text{ erg s}^{-1}$ corresponds to $M_{\text{bol}} = 4.75$ for the Sun.

If the available photometric data was too scarce to derive the bolometric magnitude from a direct integration, it has been derived instead from the $(BC_K, V - K)$ relation of Bessell & Wood (1984) applicable to oxygen-rich stars.

For the 17 S stars where both methods are applicable, they yield consistent results (with a r.m.s. deviation of 0.1 mag), provided that the zero-magnitude fluxes of Johnson (1966) be adopted (as was done by Bessell & Wood 1984). If the zero-magnitude fluxes listed by Jaschek (1978) are used instead, somewhat lower bolometric corrections BC_K (i.e. brighter bolometric magnitudes, by about 0.06 mag) are obtained.

A bolometric magnitude $M_{\text{bol}} = -3.74$, based on the same HIPPARCOS parallax, has recently been derived by Van Leeuwen et al. (1997) for χ Cyg, and agrees well with our value -3.58 listed in Table 3.2.

3.4 The HR diagram of S stars

The $V - K$ colours and the bolometric magnitudes derived as discussed in Sect. 3.3, combined with the HIPPARCOS parallaxes, provide the HR diagram of S stars presented in Fig. 3.2. Only the 30 S stars with an available K magnitude and with $0 < \sigma_\pi / \pi < 0.85$ (see Fig. 3.3) have been plotted. Despite the sometimes large uncertainties affecting $V - K$ or M_{bol} (as discussed in Sect. 3.4.1 below), a segregation between extrinsic and intrinsic S stars is readily apparent, with *extrinsic S stars being intrinsically fainter and bluer than intrinsic S stars*.

3.4.1 Uncertainties on the HR diagram

The two major sources of uncertainty on the position of an S star in the HR diagram are the stellar intrinsic variability and the error on the parallax π .

The intrinsic variability of S stars has an impact on both $V - K$ and M_{bol} . The variability in the V band and, to a lesser extent, in the K band, leads to a variation of $V - K$, and thus of BC_K (Sect. 3.3.2). If BC_K was derived from simultaneous V and K measurements, it could be expected that the variations in K and in BC_K would cancel to a large extent, thus leaving only a moderate variation in M_{bol} . However, since the V and K data used in this study do not result from simultaneous observations, the expected cancellation will not occur. Its impact on M_{bol} is, however, difficult to evaluate. It seems nevertheless unlikely that this effect could lead to a systematic upwards shift of all intrinsic S stars that would be responsible for the observed segregation between intrinsic and extrinsic S stars. The impact of the intrinsic variability on $V - K$ is easier to estimate. Its effect is shown on Fig. 3.2 from the variation recorded in the H_p magnitude over the ~ 1230 d duration of the HIPPARCOS mission. The smaller variation due to K has not been taken into account. Clearly, the uncertainty on $V - K$ due to the intrinsic variability does not jeopardize the observed segregation between extrinsic and intrinsic S stars. An interesting by-product of Fig. 3.2 is the increase of the amplitude of variations towards cooler and more luminous stars [see also Eyer & Grenon (1997) and Jorissen et al. (1997)].

The impact on the bolometric magnitude of the uncertainty on the parallax is shown in Fig. 3.4, presenting (separately for intrinsic and extrinsic S stars) the

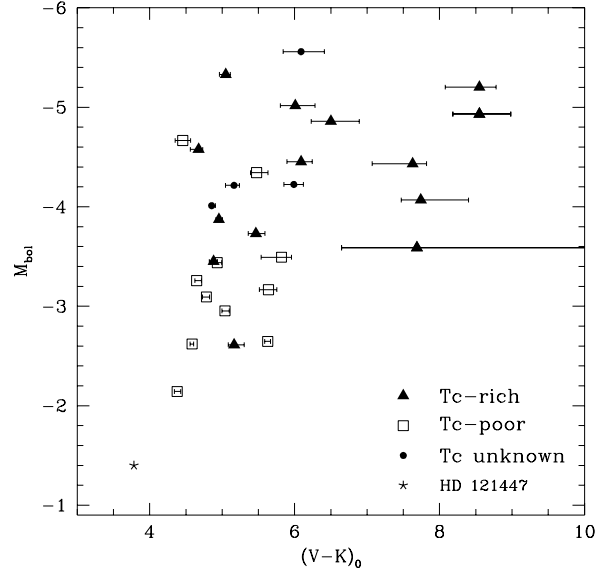


Figure 3.2: The HR diagram for S stars with $0 < \sigma_\pi/\pi < 0.85$. Filled triangles correspond to Te-rich S stars, open squares to Te-poor S stars and dots to S stars with unknown Te. HD 121447, the boundary case between Ba and S stars (see Sect. 3.4.3), is represented by \star . The error bar provides the uncertainty on $V - K$ caused by the intrinsic variability of the HIPPARCOS H_p magnitude; it covers the range in H_p between the 5th and 95th percentiles

range of M_{bol} corresponding to $\pi \pm \sigma_\pi$ [see Arenou et al. (1995) and Lindegren (1995) for a discussion of the external errors of HIPPARCOS parallaxes and of the accuracy of the zero-point]. As discussed by Van Leeuwen et al. (1997), there is a specific error source on the parallax for nearby Mira variables, as some of these stars were found to have asymmetrical spatial light distributions. Changes in these asymmetries might affect the derived parallax. The flag 'V' in field H59 of the HIPPARCOS catalogue possibly reflects such effects, as it refers to a 'variability-induced mover'. This flag is set for 14 stars in our sample, mostly nearby Miras (see column 'Dupl' in Table 3.2). Like Van Leeuwen et al. (1997), we assume that any such effect will add only additional random scatter to the mean results.

Part of the overlap in luminosity between extrinsic and intrinsic S stars in the HR diagram may actually be attributed to the large error bars of the interloping stars (NQ Pup and HD 170970¹ among intrinsic S stars, and HD 35155

¹The presence of Te in HD 170970 is somewhat uncertain, though, since the central wavelength of the blend containing the $\lambda 426.2$ Te line lies at the very boundary between Te-rich and Te-poor stars (Smith & Lambert 1988)

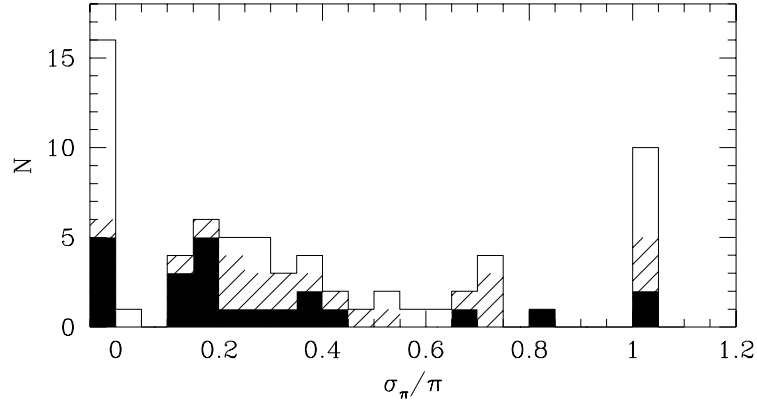


Figure 3.3: Distribution of the relative error σ_π/π on HIPPARCOS parallaxes π for S stars. The hatched and black parts of the histogram correspond to Tc-poor and Tc-rich S stars, respectively. Stars with negative parallaxes and stars with $\sigma_\pi/\pi > 0.85$ have been assigned to the leftmost and rightmost bins, respectively

among the extrinsic S stars). That explanation does not hold true, however, for the high-luminosity, Tc-poor S star 57 Peg ($M_{\text{bol}} = -4.3$), which has a small uncertainty on its parallax ($\sigma_\pi/\pi = 0.21$). That star is special in many respects, since it has an A6V companion instead of the WD companion expected for extrinsic S stars in the framework of the binary paradigm. It is further discussed in Van Eck et al. (1998).

The case of HD 35155 deserves further comments. This extrinsic S star has the second largest relative error on the parallax. It is a binary system with an orbital period of 641 ± 3 d in a nearly circular orbit, yielding an orbital separation of about 2 AU assuming typical masses of 1.6 and 0.6 M_\odot for the S star and its suspected white dwarf companion (see Chap. 2). The corresponding angular separation on the sky (a) will thus be about twice the annual parallax (since $a = A\pi$, where A is the orbital separation expressed in AU). There is no indication whatsoever that the orbital motion of HD 35155 has been detected by HIPPARCOS. However, since the orbital period is of the order of the duration of the HIPPARCOS mission and the parallax is small (1.32 ± 0.99 mas), this system represented a difficult challenge for the reduction consortia. The orbital motion has in fact been detected (flag 'O' in column 'Dupl' of Table 3.2) for another short-period S star (HIC 17296 = HD 22649; $P = 596$ d), but the situation is more favourable in this case, because of its larger parallax ($\pi = 6.27$ mas compared to $\pi = 1.32$ mas for HD 35155).

Finally, one should be aware that the observed distribution of absolute magnitudes of a sample of stars may be altered by various statistical biases, de-

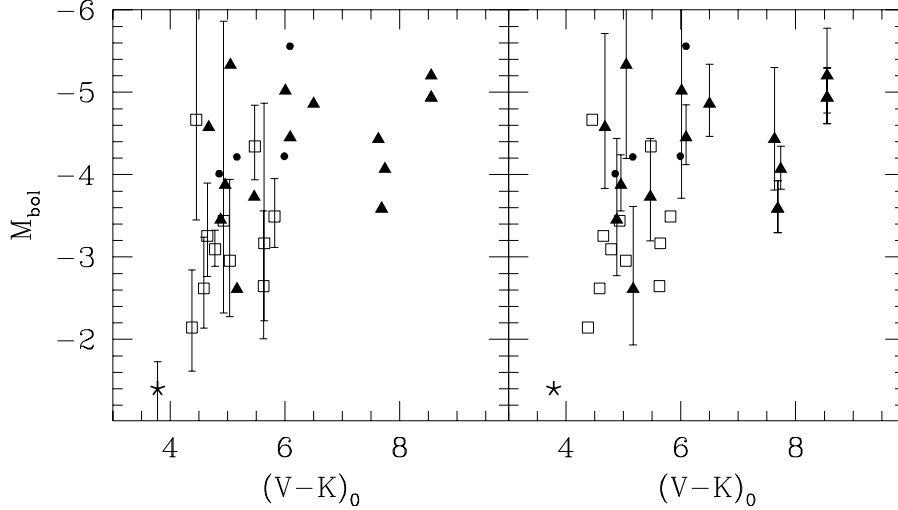


Figure 3.4: The uncertainty on M_{bol} due to the uncertainty σ_{π} on the parallax π . The error bar extends from $M_{\text{bol}}(\pi + \sigma_{\pi})$ to $M_{\text{bol}}(\pi - \sigma_{\pi})$. Left panel: parallactic errors for Tc-poor S stars; right panel: parallactic errors for Tc-rich S stars. Symbols are as in Fig. 3.2

pending on the selection criteria of the sample (e.g. Brown et al. 1997; Luri & Arenou 1997). The impact of such biases is examined in the next section.

3.4.2 An evaluation of the impact of statistical biases

The evaluation of the statistical biases altering the true absolute magnitude distribution of any given observed sample of stars requires the knowledge of the selection criteria defining that sample. Indeed, magnitude-limited samples are mostly affected by the Malmquist bias (Malmquist 1936), whereas the Lutz-Kelker bias plays an important role for parallax-limited samples (e.g. Lutz & Kelker 1973; Lutz 1979; Hanson 1979; Smith 1988). For the HIPPARCOS sample of S stars considered here, the selection criteria combine limits on the parallax with limits on the magnitude. Monte-Carlo simulations (see e.g. Pont et al. 1998) appear therefore more appropriate than an analytical approach to explore the biases resulting from the selection criteria and the observation errors when applied to a reasonable model of the parent population.

The main aim of the simulations presented in this section is to demonstrate that the segregation observed in the HR diagram between Tc-rich and Tc-poor S stars is not an artefact caused by statistical biases which might in principle operate differentially on the two families (because e.g. of different galactic

distributions), but that it must result instead from truly different luminosity distributions.

To this aim, a parent population of *Tc-rich* S stars is generated with the following properties:

- a large number ($> 300\,000$) of Tc-rich S stars are created, with a spatial distribution characterized by an exponential scale height of 180 pc (as derived for the Tc-rich stars of the Henize sample comprising 205 S stars; Chap. 7), and a uniform projected distribution on the galactic plane around the Sun;
- various bolometric-magnitude distributions are adopted (see below);
- the $(V - I)_J$ colour index is derived from the bolometric magnitude using a fiducial AGB fitted to our sample:

$$(V - I)_J = (0.5 - M_{\text{bol}}) / 1.5 + \sigma_{V-I} \text{ gauss}(0, 1) \quad (3.1)$$

where $\sigma_{V-I} = 0.6$ and $\text{gauss}(0, 1)$ is a random variable with a reduced normal distribution;

- the bolometric correction is computed from the $(BC_I, (V - I)_J)$ relation of Bessell & Wood (1984);
- the (unreddened) $V_{J,0}$ magnitude is deduced from the distance d , M_{bol} , BC_I and $(V - I)_J$;
- the $V_{J,0}$ magnitude is reddened according to the cosecant formula (Feast et al. 1990).

Stars are extracted from this parent population so as to reproduce the *observed* distribution of V_J magnitudes in the entire² HIPPARCOS sample of S stars. The “measured” parallax of each extracted star is then computed from its distance d by

$$\pi_{\text{measured}} = 1/d + \sigma_{\pi}(V_J) \text{ gauss}(0, 1) \quad (3.2)$$

where the (σ_{π}, V_J) relationship is derived from a least square fit to the HIPPARCOS data for S stars. The simulated star is then retained if it satisfies the condition $0 < \sigma_{\pi}/\pi < 0.85$ imposed on the star in order to be included in the HR diagram of Fig. 3.2.

In summary, the two selection criteria are:

- Condition I: the V_J distribution of the extracted sample of simulated stars has to reproduce the V_J distribution of the HIPPARCOS sample of S stars;

²The V_J distribution of the entire HIPPARCOS sample of S stars (60 stars when excluding the two close visual binaries and the misclassified S star; see Table 3.1) has been preferred over the V_J distribution of the 21 S stars known to be Tc-rich, because of its larger statistical significance and because the observed V_J distributions of Tc-rich and Tc-poor S stars are not significantly different.

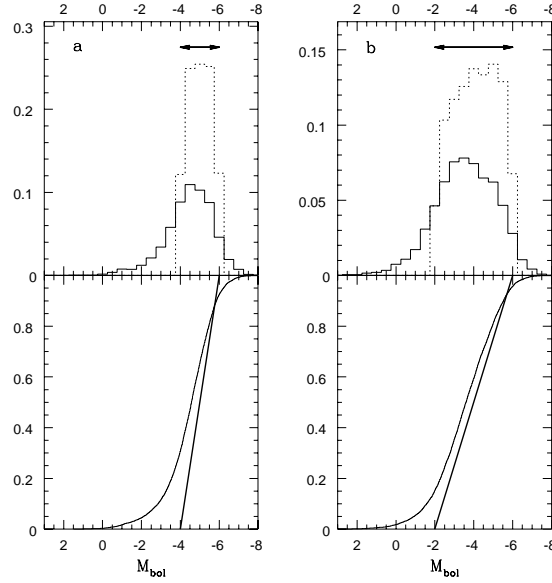


Figure 3.5: Bolometric magnitude distributions (upper panels) and their cumulative frequencies (lower panels) resulting from the Monte-Carlo simulations described in the text. The *parent* M_{bol} distributions are rectangular and span the range indicated by the arrows in the upper panels. In the lower panel, their cumulative frequency is represented by the thick solid line. The dotted line (resp. thin solid line) refers to the distribution of the Σ_{I} (resp. $\Sigma_{\text{I+II}}$) sample. Both histograms are drawn at the same scale, the dotted histogram being normalized to unity. Note that a Malmquist-type bias is responsible for the deviation of the dotted histogram from the original rectangular distribution, whereas a Lutz-Kelker-type bias causes the difference between the dotted- and the thin-solid histograms

- Condition II: $0 < \sigma_{\pi}/\pi < 0.85$.

The stars extracted from the parent population and satisfying condition I (resp. I+II) define what will be called in the following the sample Σ_{I} (resp. $\Sigma_{\text{I+II}}$). The sample Σ_{I} is supposed to represent the real HIPPARCOS sample.

Although the selection criteria that were used to include a given S star in the HIPPARCOS Input Catalogue are unknown to us, condition I ensures that they are implicitly met in our simulation. Besides, condition II is satisfied by 61% of the stars in Σ_{I} to be compared with 63% in the real HIPPARCOS sample of S stars. This good agreement constitutes a check of the internal consistency of our model as a whole.

The comparison between the M_{bol} distributions of the sample $\Sigma_{\text{I+II}}$ and of the parent sample then illustrates the impact of the statistical biases. This is

shown in Fig. 3.5 for rectangular parent distributions in the range $-4 \geq M_{\text{bol}} \geq -6$ (Fig. 3.5a) and in the range $-2 \geq M_{\text{bol}} \geq -6$ (Fig. 3.5b). The net effect of these biases is to transform the original rectangular distribution into a bell-shaped distribution, with a median shifted by 0.4 magnitude towards fainter objects, and with asymmetrical tails extending beyond the original limits. This spread is most pronounced on the fainter side of the distribution. The faintest *observed* S star in a sample of N objects must therefore be expected beyond the lower boundary of the *parent* distribution (at a bolometric magnitude corresponding to the cumulative frequency $1/N$). The amplitude of this offset does not depend on the median value of the parent distribution, but depends rather sensitively upon its width (compare Fig. 3.5a and Fig. 3.5b). For reasonable values of the width of this parent M_{bol} distribution, and adopting $N = 14$ as for the sample of Tc-rich S stars plotted in the HR diagram of Fig. 3.4, the offset value is found to lie between 0.7 and 1.5 mag. According to this statistics, the presence of the Tc-rich S star NQ Pup at $M_{\text{bol}} = -2.6$ (i.e. about 1 mag below the onset of the TPAGB) is nevertheless fully compatible with its location on the TPAGB (see Fig. 3.7). Furthermore, Fig. 3.5b demonstrates *ad absurdum* that the luminosity segregation between Tc-rich and Tc-poor S stars is not an artefact: if Tc-rich S stars with $-2 \geq M_{\text{bol}} \geq -4$ typical of Tc-poor S stars were to exist, they should have been detected indeed.

Two conclusions may thus be drawn from the above simulations:

- they demonstrate that the lack of low-luminosity Tc-rich S stars does not result from statistical biases, since these biases tend to *increase* the number of low-luminosity stars;
- when inferring the luminosity threshold for the appearance of Tc-rich S stars, it must be reminded that statistical biases tend to make the faintest Tc-rich S stars observed by HIPPARCOS appear *below* (between 0.7 and 1.5 mag) the true lower-luminosity boundary of the parent population.

3.4.3 Comparison with theoretical RGB and AGB evolutionary tracks

Figure 3.6 compares the position of S stars in the HR diagram with the RGB (i.e. up to the onset of core He-burning) for stars of different masses and of metallicity $Y = 0.3, Z = 0.02$ (Schaller et al. 1992). Figure 3.7 is the same as Fig. 3.6, but for the E-AGB, up to the first thermal pulse (Charbonnel et al. 1996).

The effective temperatures of all these models have been converted to $V - K$ colours using the calibration of Ridgway et al. (1980) for class III giants, which is strictly valid only in the range $2.2 < V - K < 6.8$.

The predicted location of the giant branch in the HR diagram is known to depend sensitively upon model parameters like the convective mixing length or the atmospheric opacities. For the Geneva evolutionary tracks used here, these model parameters have been calibrated so as to reproduce the observed location

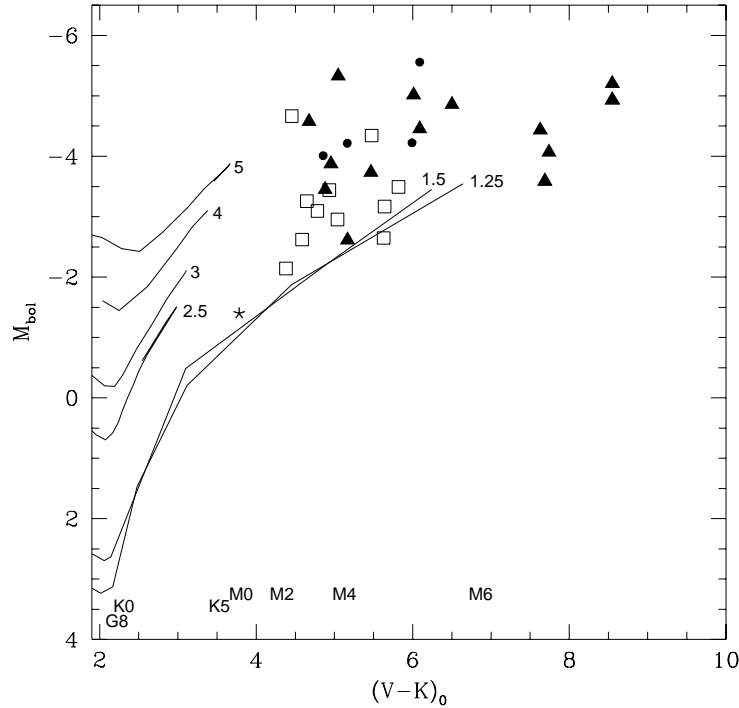


Figure 3.6: The location of the RGB (up to the onset of core He-burning) for stars of various masses (as labelled, in M_{\odot}) and metallicity $Y = 0.3$, $Z = 0.02$, according to Schaller et al. (1992). The $(V - K)$, (spectral types) calibration is from Ridgway et al. (1980). Other symbols are as in Fig. 3.2

of the red giant branches of more than 75 clusters (Schaller et al. 1992). The comparison of these tracks with the observed location of the S stars in the HR diagram is thus meaningful. The main result of the present study is apparent on Fig. 3.7: the onset of thermal pulses matches well the limit between intrinsic and extrinsic S stars, so that *Tc-rich intrinsic S stars may be associated with thermally-pulsing AGB stars* (the only possible exception being NQ Pup, but see the discussion about errors below).

The previous result provides interesting constraints on the occurrence of both the s-process and the third dredge-up in thermally-pulsing AGB stars, by suggesting that those processes operate from the very first thermal pulses on, a conclusion already reached by several authors (e.g., Richer 1981; Scalo & Miller 1981; Miller & Scalo 1982) from the luminosity distribution of carbon stars in the Magellanic Clouds (see, however, the discussion of Sect. 3.4.4). Because there is little change in luminosity from one pulse to the next (see Fig. 3.7), and

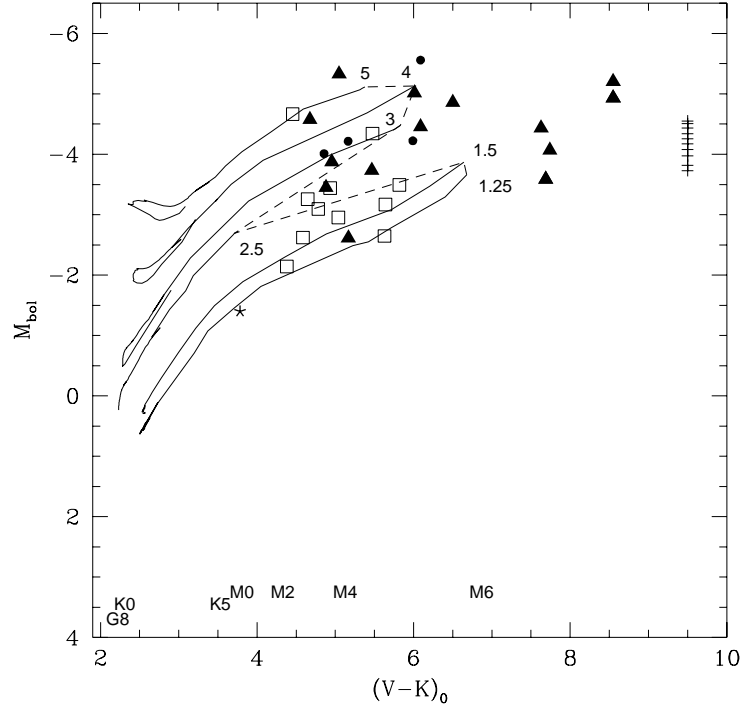


Figure 3.7: Same as Fig. 3.6, but for the early AGB up to the first thermal pulse (Charbonnel et al. 1996). To guide the eye, a dashed line connects the starting point of the TP-AGB on the various tracks. The crosses along the right-hand axis provide the luminosities of the first ten thermal pulses in a $1.5 M_{\odot}$, $Z = 0.008$ star (corresponding to the LMC metallicity) computed by Wagenhuber & Tuchman (1996). Other symbols are as in Fig. 3.2

because of the uncertainties affecting the location of individual S stars in the HR diagram, it is difficult, however, to set a limit on the exact number of pulses necessary to change a normal M giant into an (intrinsic) S star. Moreover, the statistical biases discussed in Sect. 3.4.2 shift the lower boundary of the observed luminosity distribution of Tc-rich S stars *below* the true threshold. The Monte-Carlo simulations presented in Sect. 3.4.2 predict that the faintest star in the sample of 14 Tc-rich S stars displayed in Fig. 3.7 will be observed 0.7 to 1.5 mag below the lower boundary of the true luminosity distribution (see Fig. 3.5). This is well in line with the observed location of the Tc-rich S star NQ Pup (see Sect. 3.4.1) below the TP-AGB threshold luminosity.

As far as extrinsic S stars are concerned, the present data alone do not permit to distinguish between them populating the RGB or the E-AGB of low-

mass stars. Neither does the mass-transfer scenario set any constraint on the *current* evolutionary stage of the extrinsic S star. However, when both the RGB and the E-AGB are possible, evolutionary time-scale considerations clearly favor the RGB over the AGB. Besides, the analysis of the orbital elements (Chap. 2) points towards them being low-mass stars, with an average mass of $1.6 \pm 0.2 M_{\odot}$. This value is in excellent agreement with their position in the HR diagram of Fig. 3.6 [two exceptions are HD 35155 and 57 Peg; see Sects. 3.4.1 and Van Eck et al. (1998)].

Note that the lower left boundary of the region occupied by extrinsic S stars is set by the condition that T_{eff} be low enough in order that ZrO bands may form. Such a threshold roughly corresponds to the transition between K and M giants (see the spectral types labelling Fig. 3.6), so that extrinsic S stars should merge into the KIII barium stars at lower luminosities and higher T_{eff} along the RGB (see also Chap. 2). As an example, the transition object HD 121447, classified either as K7IIIBa5 (Lü 1991) or S0 (Keenan 1950), has been located in Fig. 3.6 following the methods presented in Sect. 3.3, using the photometry obtained by Hakkila & McNamara (1987) and the HIPPARCOS distance provided by Mennessier et al. (1997).

3.4.4 Comparison with S and carbon stars in external systems

Several S stars have been found in the Magellanic Clouds and in a few other nearby galaxies, allowing a direct comparison of their luminosities with those of galactic S stars derived from the HIPPARCOS trigonometric parallaxes (Fig. 3.8):

- In a study of 90 long-period variables in the Magellanic Clouds, Wood et al. (1983) identified 14 MS stars (labelled as W83 on Fig. 3.8) in the range $-7 \leq M_{\text{bol}} \leq -5$;
- In a magnitude-limited survey of several fields in the outer regions of the northern LMC, Reid & Mould (1985) identified 10 S stars (labelled as R85 on Fig. 3.8) in the range $-5.0 \leq M_{\text{bol}} \leq -3.9$;
- In a sample extracted from the faint tail of the Westerlund et al. (1981) LMC survey of late-type giants, Lundgren (1988) finds 6 S stars (labelled as L88 on Fig. 3.8) in the range $-5.7 \leq M_{\text{bol}} \leq -4.8$;
- Bessell et al. (1983) and Lloyd Evans (1983b, 1984) find 16 S stars (labelled as B83, L83 and L84 on Fig. 3.8, with bolometric magnitudes provided in Tables A1 and A2 of Westerlund et al. 1991) in LMC clusters with $-4.8 \leq M_{\text{bol}} \leq -4.4$ (excluding NGC 1651/3304, quite far from the cluster center, possibly a field star, and the close pair LE1+2 in NGC 1987);
- S stars have also been found in other galaxies: for example, Aaronson et al. (1985) find one S star with $M_{\text{bol}} = -5.15$ in NGC 6822, Brewer et al. (1996) discover one S star with $M_{\text{bol}} = -5.3$ in M31, and Lundgren

(1990) finds seven S stars in the range $-4.9 \leq M_{\text{bol}} \leq -3.1$ in the Fornax dwarf elliptical galaxy (labelled as L90 on Fig. 3.8).

The bolometric-magnitude range for all these S stars in external systems has been plotted in Fig. 3.8. Their luminosities are generally comparable to those of the galactic Tc-rich S stars, with the exception of the brighter W83 S stars. These W83 S stars extend up to the theoretical AGB tip corresponding to the Chandrasekhar limit for the degenerate core. Smith et al. (1995) have shown that, in the Magellanic Clouds, these S stars with $-7 \leq M_{\text{bol}} \leq -6$ are all Li-rich stars with $M \gtrsim 4 M_{\odot}$. In the solar neighbourhood, these Li-rich S stars are rare (Catchpole & Feast 1976; Lloyd Evans & Catchpole 1989). The only such star in the present HIPPARCOS sample is T Sgr, but its HIPPARCOS parallax is useless (Table 3.1).

Conversely, in all the external systems, there appears to be a lack of low-luminosity S stars with respect to the solar neighbourhood. In the Magellanic Cloud fields surveyed, this lack of low-luminosity S stars may clearly be attributed to the limited sensitivity of the surveys (see R85 and L88 in Fig. 3.8). The situation is different in the Magellanic Cloud clusters, where the available surveys are sensitive down to $M_{\text{bol}} = -4.0$ and find many M stars but no S stars in the range -4.0 to -4.4 . Does this mean that Tc-poor, extrinsic S stars are really absent from the Magellanic Cloud globular clusters? Possibly, although extrinsic S stars are mostly found at luminosities fainter than $M_{\text{bol}} = -3.5$ (i.e. below the RGB-tip), and were thus not properly surveyed in the Magellanic Cloud clusters. The absence of extrinsic S stars in the Magellanic Clouds clusters would not be surprising, though, given the situation encountered in galactic globular clusters. Barium and (low-luminosity) S stars are rare in galactic globular clusters (Vanture et al. 1994, and references therein). They are only present in the massive, low-concentration cluster ω Cen (Lloyd Evans 1983b), and their origin in that cluster is still unclear. Côté et al. (1997) have argued that the binary evolution leading to the formation of extrinsic heavy-element-rich stars is only possible in low-concentration clusters like ω Cen. In more concentrated clusters, hard binaries rapidly shrink to orbital separations not large enough to accommodate an AGB star. It would be of interest to check whether Magellanic Cloud globular clusters are indeed too concentrated to allow the formation of extrinsic S stars. However, the recent result that the barium and the low-luminosity S stars in ω Cen appear to have constant radial velocities (Mayor et al. 1996) challenges the above picture. It may indicate that the barium and low-luminosity S stars in ω Cen represent the extreme tail of the wide range in metal abundances observed in that particular globular cluster, as suggested by Lloyd Evans (1983b). Alternatively, these stars might have been enriched in the past by mass transfer in soft binary systems which were later dynamically disrupted.

The lack of low-luminosity S stars in the Fornax dwarf elliptical galaxy (L90 in Fig. 3.8) is probably related to the low-metallicity of that system ($[\text{Fe}/\text{H}] \sim -1.5$; Lundgren 1990). At such low metallicities, the red giant branch is shifted towards the blue, so that stars with luminosities typical of the galactic

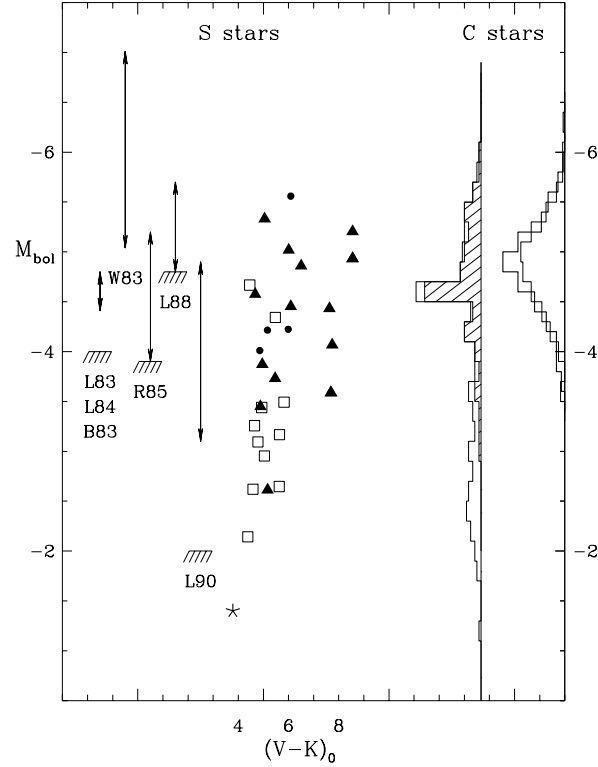


Figure 3.8: Comparison of the M_{bol} range of S stars in the solar neighbourhood (this work, symbols are as in Fig. 3.2) and in external systems:

- **S stars:** LMC clusters: L83 (Lloyd Evans 1983a), L84 (Lloyd Evans 1984), B83 (Bessell et al. 1983); Magellanic Cloud fields: W83 (Wood et al. 1983), R85 (Reid & Mould 1985), L88 (Lundgren 1988); Fornax dwarf elliptical galaxy: L90 (Lundgren 1990). Detection thresholds are also indicated.
- **C stars:** the rightmost histogram gives the luminosity function of the 186 LMC (thick line) and 134 SMC (thin line) C stars identified by Blanco et al. 1980), adopting 18.6 for the LMC distance modulus and 0.5 mag as the difference in distance moduli between the Clouds. The leftmost histogram provides the luminosity functions of C stars from the Westerlund et al. (1991) SMC survey (hatched) as well as from the deeper Westerlund et al. (1995) SMC survey (open)

Tc-poor S stars are actually of spectral type G or K in Fornax (see Smith et al. 1996, 1997 for a discussion on a similar situation in the galactic halo). No specific effort to find heavy-element-rich stars among the warm ('continuum') giants was attempted by Lundgren (1990). Contrarily to the situation prevailing in the Magellanic Cloud clusters discussed above, an S star is found in Fornax at the luminosity threshold ($M_{\text{bol}} = -3.2$) between 'continuum' (G or K) giants and M giants, suggesting that the lower luminosity cutoff observed for S stars in Fornax is just a spectral selection effect.

Deeper surveys are available for carbon stars, because of their more conspicuous spectral features. The luminosity distribution of the 134 SMC and 186 LMC carbon stars identified by the pioneering survey of Blanco et al. (1980) is shown in Fig. 3.8. It should be noted that the luminosity functions are almost identical for the LMC and SMC despite their different metallicities, so that the comparison with a more metal-rich galactic sample is not unreasonable. A GRISM survey of carbon stars in the SMC by Rebeiro et al. (1993; RAW) led to the discovery of 1707 such stars. For 100 of them, bolometric magnitudes were determined from *JHK* photometry (Westerlund et al. 1991), with a limiting magnitude of $M_{\text{bol}} \sim -3$. Their distribution is represented by the hatched histogram on Fig. 3.8. A subsequent photometric and spectroscopic survey has been devoted to the $\sim 5\%$ among RAW objects having $M_{\text{bol}} > -3$ (Westerlund et al. 1995; Fig. 3.8). *The range of absolute bolometric magnitudes for carbon stars from the deeper SMC survey now totally covers that of galactic S stars, including its low-luminosity tail.*

The nature of the SMC low-luminosity carbon stars is still debated. They might either be contaminating *dwarf* carbon (dC) stars from our own Galaxy, or low-luminosity carbon stars equivalent to the galactic R carbon stars, or may be extrinsic carbon stars formed by mass transfer across a binary system like galactic extrinsic S stars [as already suggested by Barnbaum & Morris (1993)]. Westerlund et al. (1995) reject the first hypothesis, mainly because none (except two) of their carbon stars have colours similar to the known galactic dC stars, and moreover, none exhibits a strong C_2 band head at 619.1 nm, a feature exhibited by galactic dC stars. The last two hypotheses offer interesting alternatives that remain to be investigated. It should also be noted that the possibility that some of the low-luminosity SMC carbon stars be extrinsic carbon stars makes it difficult to use the SMC carbon-star luminosity distribution to derive the luminosity threshold for the occurrence of the s-process and third dredge-up along the AGB (see the discussion in Sect. 3.4.3). Further observations are clearly required in order to distinguish intrinsic carbon stars from possible extrinsic carbon stars.

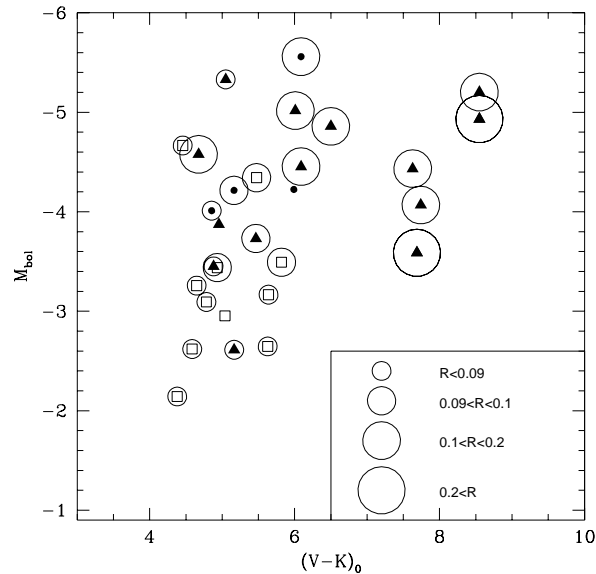


Figure 3.9: Infrared excess along the giant branches, as measured by the ratio $R = F(12\mu\text{m})/F(2.2\mu\text{m})$. The dichotomy between extrinsic and intrinsic S stars is clearly apparent. Symbols are as in Fig. 3.2

3.5 Infrared excess and position along the giant branches

Infrared excesses revealing the presence of cool circumstellar material are a common feature of late-type giants (e.g., van der Veen & Habing 1988; Habing 1996). These excesses are often associated with intrinsic stellar variability. Hacking et al. (1985) have shown that the brightest IRAS $12\mu\text{m}$ sources outside the galactic plane are long-period variables (LPV). Similarly, in globular clusters, all stars with a $10\mu\text{m}$ excess are LPVs (Frogel & Elias 1988), and moreover, they are found only above the RGB tip. These IR excesses are associated with a strong mass loss, which thus appears to be the rule among LPVs. It is expected to be much smaller in non-pulsating AGB and RGB stars (e.g., Habing 1987). Consequently, S stars with large photometric variability and infrared excesses are expected to be found among the most luminous stars. Indeed, it was already shown in Fig. 3.2 that variability in the HIPPARCOS H_p band tends to increase with luminosity. The present data offer the possibility to investigate as well the evolution of the IR excesses probing mass loss along the giant branches in the HR diagram.

The ratio $R = F(12\mu\text{m})/F(2.2\mu\text{m})$, probing the presence of cool circumstellar material emitting at $12\mu\text{m}$, has been derived from the IRAS PSC and from

the K magnitude, whenever available (using the calibration of Beckwith et al. (1976) to convert K magnitudes into fluxes at $2.2 \mu\text{m}$). As already shown by Jorissen et al. (1993), there is a clear segregation of S stars according to their value of R . All Tc-deficient S stars have $0.075 \lesssim R \lesssim 0.093$, consistent with photospheric blackbody colours ($R = 0.073$ for $T_{\text{eff}} = 4000$ K and $R = 0.093$ for $T_{\text{eff}} = 3150$ K, which corresponds to the T_{eff} range spanned by extrinsic S stars). On the contrary, intrinsic S stars generally have $R > 0.1$, indicative of circumstellar dust. This segregation is a further indication of the inhomogeneous nature of the family of S stars.

As expected, Fig. 3.9 clearly shows that $R < 0.1$ indices are restricted to the RGB (or E-AGB), whereas S stars on the AGB have larger and larger R indices as they evolve towards cooler T_{eff} .

3.6 Conclusions

The HR diagram of S stars constructed from HIPPARCOS parallaxes fully confirms the dichotomy of S stars, by showing that:

- extrinsic S stars are hotter and intrinsically fainter than intrinsic S stars;
- extrinsic S stars are low-mass stars populating either the RGB or the E-AGB, and in any case are found *below* the luminosity threshold marking the onset of thermal pulses on the AGB. Therefore, their chemical peculiarities cannot originate from internal nucleosynthesis and dredge-up processes occurring along the TP-AGB. Their binary nature suggests instead that their chemical peculiarities originate from mass transfer;
- on the contrary, Tc-rich S stars are found just above the TP-AGB luminosity threshold. Their location in the HR diagram indicates that s-process nucleosynthesis and third dredge-up must be operative quite early on the TP-AGB.

Chapter 4

The Henize sample of S stars: general context

Half of a century ago, no catalogue of S stars existed. There was Keenan's (1954) list, but many others had since then been reported, and there were rumours about Henize's unpublished list.

Karl G. Henize was a graduate student at the University of Michigan when he was sent, in 1949-51, to the Lamont-Russey Observatory, near Bloemfontein, South Africa, in order to take plates for the Michigan-Mount Wilson survey of the southern sky for H_α emission objects. This survey was a joint venture utilizing the 10.5 inch red-corrected Mount Wilson camera equipped with a 15° objective prism, and the University of Michigan Lamont-Russey Observatory facilities (Henize 1954; Wray 1966).

He obtained three sets of plates (all plates were in the red region, because the purpose was to study stars with H_α emission): the short (8 min) and medium (120 min) exposure plates covered the entire sky south of -25° , and the long (240 min) exposure plates covered a band 20° wide centered on the galactic equator from $l = 240^\circ$ to 10° (mostly confined to declinations below -25°). The short series was designed to reach to 8^{th} magnitude, the medium exposure series from 8^{th} to 11^{th} magnitude and the long exposure series was designed to record from 10^{th} to 13^{th} magnitude (Wray 1966).

Henize got his Ph.D. in 1954, then worked at the Smithsonian before getting a faculty position at Northwestern University near Chicago. He published several papers on H_α emission stars; at some point he realized he could distinguish S stars from M stars, and that he was finding many S stars that were new. There was a rumour that Henize had submitted a paper containing his list for publication, but that the referee had raised a number of objections (probably about the discussion of space density and population type), and Henize never revised the paper. That was probably about the time that Henize joined NASA's astronaut program, so perhaps he was no longer very motivated to work on problems of S stars. Anyway, he still attended AAS meetings and other meetings, and in

1960 he gave a talk at an AAS meeting, the abstract of which can be found in Henize (1960):

A catalogue of 145 S stars found on the objective-prism spectrum plates of the Michigan-Mount Wilson Southern H_α Survey has been compiled. This survey covers the sky south of declination -25° uniformly to the red magnitude 10.5. The spectra cover the red-yellow region with a dispersion of $450\text{\AA}/\text{mm}$ at H_α and permit classification of most of the stars by the Keenan system through comparison of ZrO bands at $\lambda 6345$ and $\lambda 6474$ with TiO bands at $\lambda 5861$ and $\lambda 6159$ (Keenan 1954). [...] In addition to the 145 clearly identifiable S stars, 18 stars with weak and somewhat uncertain ZrO and 4 stars with uncertain ZrO together with extremely strong sodium D absorption were found. The latter stars, which appear similar to WZ Cas, are VY Aps, UY Cen, CD -60:3017 and Anon $08^h 45^m .9, -70^\circ 35'$ (1875).

There were also 29 stars labelled “uncertain ZrO” in that unpublished list, which thus contains 196 S stars.

By the end of 1963 Henize produced a longer list, in which some stars of 1960 had disappeared, and with new stars added. It is rather likely that Henize had time to further inspect his plates and to cross check originally questionable objects. Most probably the same plates were used: indeed Henize took no further objective prism plates (Stephenson priv. comm.); and he did not perform any sort of systematic search on the the long-exposure plates before Wray’s work, initiated in 1965 (Wray, priv. comm.¹).

Also present in this new list is a distinct set of additional stars located north of -25° . It is not clear from where these 31 S stars came from – probably from other plates that were available at Michigan – but he kept them separate, giving them higher numbers. So we do not know the limiting magnitude of the plates where extra 31 stars were found, but they were probably mostly similar to the southern survey plates – at least, the stars found seem to have similar magnitudes. They apparently comprise two separate sets of plates, obtained at epochs contemporaneous with the end of his survey: S stars in Sagittarius and Vulpecula and S stars in Cygnus.

This longer list was renumbered and lead to the final 1965 list, superseding the one described in 1960, so that the earlier one is no longer relevant. In

¹On this problem, Dr. J. Wray further notes: “Knowing Karl, and his keen interest in the problems of selection effects, sample contamination and completeness, I would opt for the assumption that any additions that were not specifically noted as being extraneous to a prior population sample definition would be legitimate members of the population sample, i.e., they would be confirmed on plates of similar exposure, wavelength coverage, etc. Although the long-exposure plates were certainly available to him, he would have been the first to point out that using the long-exposure plates to confirm questionable objects found on short or medium exposure plates would clearly bias part of the group towards fainter magnitudes. I am confident that he would have made some mention of that in the 1965 publication if he had done so.”

the 1965 list, the S stars south of -25° have numbers 1-205 (in order of right ascension), and those north of -25° have numbers 206-236. This list was never published, but was widely circulated. It is actually published in that its stars are listed in the first and second editions of Stephenson's catalogues of galactic S stars. They are indicated as "Henun" (Henize, unpublished) [except for Hen 116 ($\alpha_{1900} = 11^h 43'.0$; $\delta_{1900} = -64^\circ 46'$) that was omitted]. In the following we refer to the first 205 stars of this list as "the Henize sample of S stars"².

In this list, 14 stars are "uncertain" (:), most likely because they were the ones near the plate limit, or contaminated by a nearby star; 42 stars have no spectral classification, 68 are classified as mild (abundance class 1-3), 52 as moderate (4-6), and 29 as strong(7-9)³.

It is not clear whether the 1965 list is supposed to include all S stars south of -25° , or only the newly discovered ones. The difference is not great, because rather few S stars were known in the deep south before the Henize survey. Some long-known S stars such as π^1 Gruis do have Henize numbers. That star is quite bright ($V = 6.6$), certainly brighter than 8^{th} mag, so one wonders if Henize noticed it as an S star on his short-exposure plates or if he included it because it was known. This emphasizes the point that the "plate limit" of a survey is not a definite number but depends on many things. An S star with only a weak 6474\AA band will not be noticed if the 6474\AA region is overexposed, but the 6474\AA band is quite strong in π^1 Gru and Henize was probably able to see it despite the overexposure. In Stephenson's catalogue, there are six stars brighter than $V = 8$ and south of -25° that are not in the Henize survey; however, at least two of them (CSS 500 and 796) are misclassified as S (see Tab. 1.1), while three additional objects (CSS 853, 729 and 1170) are classified as normal M giants in the Michigan spectral survey. Hence Henize may have missed a few mild S stars brighter than 8, due to overexposure, but the numbers would be small (of course, he must have missed some variable stars due to their being at the wrong phase when the plates were taken). Therefore it can probably be considered that the survey attempts to be complete in a sphere, rather than a shell.

Meanwhile, Henize turned over his 42 deep plates to a Northwestern University student named James Wray, whose dissertation is dated 1966. Wray, like Henize, was originally interested in H_α emission objects (and found many of them in the LMC, for example), but he also found about 50 new S stars. These are listed in Yorke and Wing's catalogue by their Wray numbers – which go above 300, since evidently the same list included other things besides S stars.

²The Henize S stars are referred to as "Hen nnn" in this work; this notation corresponds to the "Henun nnn" of Stephenson (1984), though they are referred to as "Hen 4-*nnn*" in the Simbad database

³Also included are 28 "related" objects such as SC stars, and MS stars which did not meet Keenan's definition for abundance class 1. They are labelled "stars with very doubtful ZrO", and were left unnumbered. They are not included in either Stephenson's catalogues nor Wing and Yorke's catalogue

The Wray S stars are mostly fainter than the Henize S stars, although there may be a few exceptions. Besides S stars, the search of medium exposure plates by Henize also resulted in the discovery of over 1000 Be stars, 150 probable planetary nebulae and about 300 carbon stars (Wray 1966).

To conclude with, the Henize sample of S stars constitutes the only homogeneous magnitude-limited search for S stars covering all galactic latitudes, from the galactic equator up to the galactic pole. The next chapters focus on this stellar sample and aim at deriving the respective properties of its extrinsic and intrinsic S stars. Chap 5 is devoted to high resolution spectra obtained for 72 stars in order to derive their technetium content. Data concerning low-resolution spectroscopy, photometry and radial-velocity are presented in Chap 6. A global analysis (multivariate classification) of the whole material collected on the Henize sample is performed in Chap. 7 and permit to characterize the distinctive features of extrinsic and intrinsic S stars.

Chapter 5

The technetium dichotomy

5.1 Introduction

Element 43 was predicted on the basis of the periodic table by Mendeleev, who suggested that it would be very similar to manganese and gave it the name *ekamanganese*. In 1925, three German chemists announced its detection by means of lines in the X-ray spectrum, and gave it the name *masurium*; but their discovery was not confirmed and is now considered erroneous, although their parallel discovery of rhenium, element 75, was valid. Actually element 43 was first produced in 1937 in the cyclotron at Berkeley, by bombarding a sample of molybdenum with deuterons. It was identified by E. Segré and C. Perrier, who named it technetium (after the greek *τεχνητικο*, artificial) because it was the first element to be produced artificially. A few years later it was found among the products of uranium fission (Merrill 1956b). Technetium has three long-lived isotopes, ^{97}Tc (half life 2.6×10^6 years), ^{98}Tc (1.5×10^6 years), ^{99}Tc (2.1×10^5 years), as well as 20 short-lived isotopes and isomers. All Tc isotopes are radioactive and therefore highly toxic¹.

Technetium was first identified in the spectra of some M and S stars by Merrill (1952). As discussed in Sect. 1.1.3, models predict technetium to be a good tracer of TPAGB stars. From the observational point of view, almost all Miras variables (irrespective of their spectral types) with period longer than 300 days (being thus high-luminosity AGB stars, according to the period-luminosity relation) show technetium in their spectra (Little-Marenin & Little 1987; Smith & Lambert 1986; Smith & Lambert 1988). Moreover, virtually all the S stars identified as TPAGB stars in Chap. 3 thanks to the HIPPARCOS parallaxes

¹At 298 K technetium is a silvery-grey solid metal that tarnishes slowly in moist air. In everyday's life, technetium is a byproduct of the nuclear industry. It is used as a corrosion inhibitor for steel (limited to closed systems since technetium is radioactive), and medical imaging agent. $^{99\text{m}}\text{Tc}$ is used as a radioactive tracer (informations provided by the WebElements database of Mark Winter [<http://www.shef.ac.uk/chemistry/web-elements/>])

turn out to be Tc-rich. Therefore, it seems probable that all s-process enriched TPAGB stars indeed exhibit technetium lines.

The very fact that not all S stars exhibit Tc lines is most probably the evidence that they are not all on the TPAGB. As mentioned in Chap. 1, extrinsic S stars, that are members of binary systems, owe their chemical peculiarities to the accretion of s-process-rich matter from an evolved companion rather than to self-nucleosynthesis. They are technetium-poor, because enough time has elapsed for the technetium to decay since the mass transfer event. The ^{99}Tc half-life is indeed much shorter than any stellar evolutionary timescale (but the TPAGB).

Besides technetium detection, several spectroscopic criteria (of various efficiencies) aiming at distinguishing extrinsic from intrinsic S stars have been mentioned in the literature [e.g. oxygen isotopic ratio (Smith & Lambert 1990), presence of the He I $\lambda 10830$ line (Brown et al. 1990), zirconium isotopic ratio (Busso et al. 1992)], but technetium detection appears to be, by far, the most secure and tractable way to unmask extrinsic S stars.

It is crucial to distinguish extrinsic from intrinsic S stars in the present study of the Henize sample of S stars, in order to disentangle the two sub-families and to study their respective characteristics. Furthermore, a survey of technetium in such a large sample of S stars may be expected to provide further constraints on the s-process environment in AGB stars (e.g. interpulse s-process versus thermal-pulse s-process, thermal-pulse duration and temperature versus ^{99}Tc half-life).

The present chapter deals with high-resolution technetium spectra obtained for 72 Henize stars. Some additional K, M and symbiotic stars data are also presented.

5.2 Observations and reduction

5.2.1 Instrumental set-up

The high-resolution spectra used in the present study were obtained during several runs (1991-1998) at the European Southern Observatory, with the Coudé Echelle Spectrometer (CES) fed by the 1.4m Coudé Auxiliary Telescope (CAT). The 1991-1993 runs were performed with the short camera (f/1.8) and CCD #9 (RCA SID 503 thinned, backside illuminated, 1024×640 pixels of $15 \mu\text{m}$), whereas the long camera (f/4.7) and CCD #38 (Loral/Lesser thinned, backside illuminated, UV flooded, 2688×512 pixels of $15 \mu\text{m}$) were used during the 1997-1998 runs. Details on these configurations can be found in Lindgren & Gilliotte (1989) and Kaper & Pasquini (1996). The resolution ranges from 0.14\AA ($R=30\,000$) to 0.07\AA ($R=60\,000$) for a central wavelength of 4250\AA . The spectra approximately cover the wavelength range $\lambda\lambda 4230\text{-}4270\text{\AA}$.

5.2.2 Stellar samples

The observed stars are a subset of the sample of 205 S stars collected by Henize (Chap. 4). Given the limitations on the CAT pointing and on the detectors sensitivity, only stars with $\delta > -75^\circ$, $V < 11$ and $B - V < 2$ (translating into 70 objects) could be observed in a reasonable amount of time, i.e. less than 1h30 per star. A few bright redder stars could also be observed (but see the discussion on SC stars in Sect. 5.3.2). A sample of bright M stars with an excess at $60\mu\text{m}$ (indicative of a possibly detached dust shell; see Zijlstra et al. 1992), as well as the two symbiotic stars RW Hya and SY Mus, and some radial-velocity standards have also been observed. Three non-Henize S stars from our radial-velocity monitoring (Chap. 2) have been included as well. The log of the observations, including the instrumental setting, is given in Table 5.1 and, for Henize stars, in Table 5.2.

These tables are organized as follows:

- in Table 5.1, the first column identifies the star by its HD, HR or BD number, while in Table 5.2 the Henize and GCGSS numbers (Stephenson 1984) are listed in the first two columns;
- the spectral type is quoted next; in Table 5.2, spectral types are from Stephenson (1984);
- the next two columns list the civil date of the observation (day month year) and the Julian date (JD - 2 448 000.5);
- the column CCD provides the instrumental setting (9-sh: CCD #9 + short camera; 38-l: CCD #38 + long camera);
- the next column indicates the spectral resolution;
- the next six columns give, for the two considered technetium blends (at 4262\AA and 4238\AA , respectively), the (Doppler-shift corrected) central wavelength of the technetium blend ($\lambda - 4200\text{\AA}$), the standard deviation on the Doppler shift (σ , in \AA) and the signal-to-noise ratio (see text);
- the technetium-rich (y) or technetium-poor (n) status is given next;
- the last column contains additional remarks.

5.2.3 Data reduction and S/N ratio

The CCD frames were corrected for the electronic offset (bias) and for the relative pixel-to-pixel response variations (flat-field). Wavelength calibration was performed from thorium lamp spectra taken several times per night. An optimal extraction of the spectra was performed according to the method of Horne (1986). The whole reduction sequence was performed within the ‘long’ context of the MIDAS software package.

The signal-to-noise (S/N) ratio was estimated for each spectrum in the following way: three S/N values were computed for the three best exposed CCD lines (along the dispersion axis), in the neighborhood of the spectral region of interest (either 4262\AA or 4238\AA). These three S/N values were then combined according to Eq. 17 of Newberry (1991). When the exposure time on a given star has been split in two (in order to reduce cosmics detrimental effect), the final

Table 5.1: Observations log and results for non-Henize stars.

HD/BD	type	cdate	Jdate	CCD	R	4262Å blend			4238Å blend			Tc	Remarks
						λ	σ	S/N	λ	σ	S/N		
• M stars													
HR 4938	M3.5III	160393	1063.3	9-sh	45000	62.104	0.012	41	38.366	0.028	29	n	V789 Cen
HR 5064	K5-M0III	150393	1062.3	9-sh	45000	62.097	0.010	76	38.353	0.030	61	n	
HR 5134	M5III	150393	1062.3	9-sh	45000	62.069	0.015	70	38.356	0.037	53	n	V744 Cen
• M stars with 60μm excess													
73341	M3/M4III	300593	1138.0	9-sh	45000	62.103	0.011	33	38.370	0.030	25	n	SAO 236108
91094	M1III	300593	1138.0	9-sh	45000	62.099	0.014	39	38.357	0.025	34	n	SAO 250981
179199	M2III	290593	1137.4	9-sh	45000	62.097	0.017	18	38.354	0.032	15	n	SAO 162305
181620	M2III	290593	1137.4	9-sh	45000	62.109	0.016	29	38.368	0.025	23	n	V4415 Sgr;SAO 211215
• Symbiotic stars													
100336	M4.5	160393	1063.2	9-sh	45000	62.094	0.020	11	38.347	0.029	8	n	SY Mus
117970	M2	150393	1062.2	9-sh	45000	62.115	0.011	31	38.363	0.042	24	n	RW Hya
• Non-Henize S stars													
1760	M5-6Se	300792	834.4	9-sh	30000	62.230	0.020	65	38.142	0.030	55	y	T Ceti (also M5-6Ib-II)
-21°2601	S3*3	310197	2480.2	38-1	60000	62.097	0.007	22	38.365	0.024	16	n	
-08°1900	S4/6	240298	2869.0	38-1	60000	62.239	0.029	15	38.256	0.035	11	y	
+04°4356	S4*3	290593	1137.3	9-sh	45000	62.210	0.015	19	38.079	0.033	11	y	see note
• Radial velocity standards													
80170	K5III	240298	2869.1	38-1	60000	62.099	0.011	84	38.356	0.018	66	n	
108903	M3.5III	240298	2869.3	38-1	60000	62.104	0.012	233	38.372	0.016	182	n	γ Cru A

Note: The S star BD+04°4356 = GCGSS 1193 = SAO 125493 = IRAS 20062+0451 has been erroneously associated by MacConnell (MacConnell 1982) with the nearby (non-S) star BD+04°4354. The coordinates in the original paper are nevertheless correct. Since then, this error has propagated in the literature (Stephenson 1984, Jorissen et al. 1993, Chen et al. 1995, Jorissen et al. 1998, Udry et al. 1998a), although in all these papers the measured star was indeed the S star BD+04°4356.

Table 5.2: Same as Table 5.1 but for Henize S stars.

Hen	GC-GSS	HD/DM	type	cdate	Jdate	CCD	R	4262Å blend			4238Å blend			Tc	Remarks
								λ	σ	S/N	λ	σ	S/N		
1	3	310	S3,1	210991	521.2	9-sh	30000	62.107	0.008	36	38.375	0.013	34	n	
2	39	9810	S2,1	210991	521.3	9-sh	30000	62.094	0.015	21	38.372	0.014	18	n	
3	104	29704	S:	210991	521.3	9-sh	30000	62.088	0.019	26	38.396	0.016	23	n	
5	139		S3,3	010297	2481.0	38-1	60000	62.089	0.007	18	38.394	0.010	12	n	
6	141		S5,2	300197	2479.1	38-1	60000	62.091	0.008	22	38.379	0.015	11	n	
7	178	40706	S2,1	150393	1062.0	9-sh	45000	62.126	0.022	22	38.367	0.025	20	n	
8	202	-39°2449	S5,6	010297	2481.1	38-1	60000	62.227	0.020	18	38.194	0.042	14	y	
9	204	-60°1381	S3,3	160393	1063.0	9-sh	45000	62.099	0.008	16	38.349	0.024	13	n	
14	242	-34°3019	S2,5	160393	1063.1	9-sh	45000	62.104	0.004	13	38.363	0.023	10	n	
16	248		S:	310197	2480.2	38-1	60000	62.258	0.019	13	38.172	0.014	7	y	
18	294	-28°3719	S6,8e	150393	1062.0	9-sh	45000	62.072	0.032	13	38.378	0.033	10	n	
19	328			310197	2480.1	38-1	60000	62.229	0.015	16	38.233	0.021	12	y	
20	342	-45°3132		310197	2480.0	38-1	60000	62.230	0.016	27	38.120	0.017	16	y	
28	390	62340	S4,4	010297	2481.1	38-1	60000	62.079	0.016	36	38.381	0.011	26	n	
31	434	65152	S1,1	150393	1062.1	9-sh	45000	62.093	0.009	31	38.369	0.026	27	n	
34	446		S7,2	010297	2481.1	38-1	60000	62.254	0.022	39	38.193	0.013	30	y	X Vol
35	447	-71°435	S1,1	300197	2479.1	38-1	60000	62.078	0.010	19	38.375	0.026	11	n	
36	448	-31°5393	S3,1	150393	1062.1	9-sh	45000	62.222	0.011	22	38.141	0.028	17	y	
37	456	-41°3702	S4,2	010297	2481.2	38-1	60000	62.260	0.004	19	38.090	0.017	12	y	
39	461	-65°601	S6,2	010297	2481.2	38-1	60000	62.238	0.004	31	38.118	0.014	21	y	
41	474	-27°5131	S4,2	010297	2481.2	38-1	60000	62.219	0.027	31	38.210	0.019	23	y	
43	487	-26°5801	S4,4	240298	2869.1	38-1	60000	62.099	0.012	15	38.348	0.026	10	n	
45	490	-32°5117		010297	2481.3	38-1	60000	62.212	0.015	25	38.147	0.019	18	y	
57	559		S4,2	310197	2480.2	38-1	60000	62.221	0.021	21	38.145	0.019	14	y	
63	588	-33°5772	S4,1	300197	2479.2	38-1	60000	62.103	0.013	15	38.364	0.017	10	n	
64	591	-28°6970	S7/5e	010297	2481.3	38-1	60000	62.252	0.010	17	38.181	0.031	7	y	
66	593	-33°5803	S5,2	310197	2480.3	38-1	60000	62.226	0.029	18	38.138	0.013	12	y	
79	653		S5,2	240298	2869.2	38-1	60000	62.097	0.011	19	38.388	0.023	14	n	
80	656		S5,6	150393	1062.2	9-sh	45000	62.254	0.017	15	38.138	0.022	12	y	KN Car

Table 5.2: (continued)

Hen	GC-GSS	HD/DM	type	cdate	Jdate	CCD	R	4262Å blend			4238Å blend			Tc	Remarks
								λ	σ	S/N	λ	σ	S/N		
88	667	-30° 8296	S5,2	300197	2479.3	38-1	60000	62.220	0.012	15	38.122	0.008	10	y	
89	668		S3,1	300197	2479.3	38-1	60000	62.223	0.018	18	38.091	0.012	9	y	
90	672	-54° 3378	S5,6	240298	2869.2	38-1	60000	62.083	0.008	22	38.372	0.021	16	n	
95	693		S4,2	300593	1138.0	9-sh	45000	62.229	0.016	12	38.138	0.020	8	y	
97	696		S5,2	290593	1137.1	9-sh	45000	62.224	0.006	21	38.148	0.033	16	y	HP Vel
101	704		S5,4	240298	2869.3	38-1	60000	62.247	0.037	21	38.165	0.032	15	y	Z Ant
104	714	95013	S5,4	300593	1138.1	9-sh	45000	62.208	0.015	10	38.176	0.008	6	y	
108	720	95875	S3,3	300197	2479.3	38-1	60000	62.087	0.014	34	38.368	0.017	21	n	
119	778	104361	S3,3	010297	2481.4	38-1	60000	62.084	0.010	27	38.377	0.015	16	n	
121	792	-27° 8661	S4,6e	300593	1138.1	9-sh	30000	62.098	0.016	10	38.374	0.035	8	n	
123	795	-47° 7642	S4,2	160393	1063.3	9-sh	45000	62.096	0.013	20	38.358	0.027	14	n	CSV101280
126	802		S4,2	240298	2869.4	38-1	60000	62.100	0.018	17	38.368	0.022	12	n	
129	808	-46° 8238	S4,4	290593	1137.1	9-sh	45000	62.073	0.018	14	38.384	0.034	11	n	
132	813	-72° 869	S4,6	300593	1138.2	9-sh	30000	62.081	0.011	12	38.355	0.038	9	n	
133	814	114586	S5,4	240298	2869.3	38-1	60000	62.073	0.008	20	38.367	0.021	16	n	
137	824	-50° 7894		160393	1063.3	9-sh	45000	62.088	0.013	22	38.366	0.028	14	n	
138	826	118685	S6,2	150393	1062.3	9-sh	45000	62.092	0.008	32	38.367	0.027	25	n	-71 963
140	832	120179	S3,1	310197	2480.3	38-1	60000	-	-	36	-	-	27	y	see text
140	832	120179	S3,1	300593	1138.2	9-sh	30000	-	-	26	-	-	20	y	see text
141	834	120460	S8,5	230597	2592.2	38-1	60000	62.250	0.044	19	38.181	0.018	12	y	VX Cen
143	839	122434	S3,1	010297	2481.4	38-1	60000	62.092	0.013	27	38.372	0.019	19	n	-41 8409
147	858	-25° 10393	S3,3	290593	1137.2	9-sh	45000	62.084	0.024	9	38.356	0.015	7	n	
149	864	130859	S4,2	150393	1062.4	9-sh	45000	62.102	0.007	13	38.370	0.023	10	n	
150	867	131217	S6,2	010892	836.0	9-sh	30000	62.093	0.012	6	38.376	0.037	5	n	
162	927		S5,2	300593	1138.3	9-sh	30000	62.239	0.016	18	38.181	0.039	14	y	
173	962		S4,2	300593	1138.3	9-sh	30000	62.096	0.015	9	38.336	0.044	7	n	
175	974	156957	S6/3+	310792	835.1	9-sh	30000	62.243	0.032	21	38.142	0.027	16	y	V635 Sco
177	977	-32° 12687	S:	230597	2592.4	38-1	60000	62.232	0.032	24	38.107	0.027	12	y	
178	978	157335	S5,4	300593	1138.4	9-sh	30000	62.272	0.020	10	38.118	0.049	6	y	V521 Oph

Table 5.2: (continued)

Hen	GC- GSS	HD/DM	type	cdate	Jdate	CCD	R	4262Å blend			4238Å blend			Tc	Remarks
								λ	σ	S/N	λ	σ	S/N		
179	994	160379	S5,2	150393	1062.4	9-sh	45000	62.090	0.012	17	38.369	0.025	13	n	
182	1010	163896	S4,2	310792	835.2	9-sh	30000	62.082	0.008	25	38.376	0.027	22	n	V745 Sgr
183	1014	164392		310792	835.1	9-sh	30000	62.089	0.013	26	38.369	0.029	22	n	
186	1023	165774	S4,6	210991	521.0	9-sh	30000	62.090	0.011	30	38.375	0.012	26	n	
187	1025	165843	S2,1	300593	1138.4	9-sh	30000	62.084	0.014	20	38.388	0.038	14	n	
191	1056	171100	S5,4	310792	835.2	9-sh	30000	62.244	0.021	19	38.166	0.035	15	y	V3574 Sgr
193	1074	-23°14695	S4,2	300792	834.2	9-sh	30000	62.106	0.006	9	38.344	0.018	8	n	
197	1195	191630	S4,4	210991	521.0	9-sh	30000	62.216	0.014	50	38.147	0.011	42	y	
199	1212			310792	835.3	9-sh	30000	62.094	0.013	14	38.363	0.021	12	n	
201	1275	-26°15676	S3,3	300792	834.3	9-sh	30000	62.098	0.013	15	38.366	0.045	13	n	
202	1294		S5,7:	210991	521.1	9-sh	30000	62.270	0.034	27	38.191	0.011	17	y	π ¹ Gru
203	1295		S4,4	300792	834.3	9-sh	30000	62.067	0.017	12	38.358	0.033	12	n	
204	1303		S6,6	310792	835.3	9-sh	30000	62.116	0.016	19	38.368	0.023	17	n	CSV103101

S/N ratio was computed using Eq. 18 of Newberry (1991). The degradation of the S/N ratio due to flat-field correction has not been taken into account, since flat-fields have little degrading effect for the low S/N values under consideration. The S/N ratio values are listed in Tables 5.1 and 5.2 for each target star. Because of the CCD spectral response, the S/N ratio near 4238Å is systematically lower than the one near 4262Å. All the spectra are plotted in Appendix A.

5.3 Analysis

5.3.1 Fit of the technetium blends

The three strong resonance lines of Tc I are located at 4238Å, 4262Å and 4297Å, with intensity ratios of 3:4:5. All three lines are severely blended (Little-Marenin & Little 1979, their Table III). With the adopted instrumental configurations, a single exposure spans 35 to 50Å; it is thus possible to observe simultaneously the 4238Å and 4262Å lines. In this analysis we follow the guidelines provided in the landmark paper of Smith & Lambert (1988) and therefore concentrate on the most useful 4262Å line, while the 4238Å line is used as an independent confirmation.

Fig. 5.1 shows examples of spectra in the 4262Å region for an M3-4 giant (HD 73341) and for seven S stars (four being technetium-poor: Hen 3, 187, 31, 7 and three technetium-rich: Hen 140, 39 and 202 = π^1 Gru). It can be seen that the Tc $\lambda 4262.270\text{\AA}$ line is blended with two features; the bluest includes primarily Nb I (4262.050Å) and Gd II (4262.087Å), and the reddest Cr I (4262.373Å) (see Fig. 5.1). A weaker contribution of Nd II at 4262.228Å, almost on the top of the Tc I line, may also be present. These composite features are much weaker than the Tc I resonance line at its maximum strength; moreover, the Nb I-Gd II blend and the Tc I line are 0.18Å apart. Therefore the shape and location of the Nb I-Gd II (-Tc I) blend (hereafter called X_{4262} feature) clearly depends on whether it contains the technetium line or not. Quantitatively, the minimum of a gaussian fitted to a Tc-containing X_{4262} feature is shifted redward by $\sim 0.14\text{\AA}$ with respect to the minimum of a gaussian fitted to a no-Tc X_{4262} feature; such a shift is easily detectable on our spectra (compare Hen 3 or Hen 7 with Hen 39 on Fig. 5.1).

In practice, each spectrum has been rebinned to zero-redshift in the following way: 10 nearby ($\leq 5\text{\AA}$ on either side) apparently unblended stellar features with unambiguous identification, are adopted as wavelength standards. Gaussian profiles are fitted to these lines and provide a mean redshift. The wavelength of the X_{4262} feature is then computed as the minimum of a gaussian centered on the X_{4262} feature of the redshift-corrected spectrum. Typical uncertainties on the X_{4262} wavelength amount to 0.013Å for technetium-poor stars and 0.020Å for technetium-rich stars (as derived from the standard deviation on the mean redshift).

The same method is applied to the 4238Å technetium line, where the CH-La II blend has been taken as the X_{4238} feature (Fig. 5.2). Typical uncertainties

on the X_{4238} wavelength are slightly larger (0.023\AA for Tc-rich S stars and 0.025\AA for Tc-poor S stars) because of the lower S/N ratio and the stronger blending at 4238\AA . Results are listed in Tables 5.1 and 5.2; the X_{4238} and X_{4262} features always yield consistent results regarding the absence or presence of technetium, except for Hen 140 (=HD 120179).

This star is indeed unique in having very weak technetium features (see Figs. 5.1 and 5.2). A second spectrum, taken 3.5 years later, is almost identical to the one displayed in Fig. 5.1 and 5.2. The blind application of gaussian fitting to the X_{4238} feature of Hen 140 yields a central wavelength that would qualify it as Tc-poor; however, the extreme weakness of the pseudo-emission separating the La II-CH blend from the Sm II line as seen in Hen 140 (Fig. 5.2) is unusual for Tc-poor stars, and suggests the presence of a weak technetium line, as confirmed from the appearance of the X_{4262} feature. We therefore believe that Hen 140 is the unique example in our sample of an S star with very weak Tc lines.

In all the other cases, technetium (non-) detection relies on the location of the minimum of a gaussian fitted to the X_{4262} (or X_{4238}) blend.

Are there, with this method, risks (i) to misclassify as Tc-rich a truly Tc-poor star, and (ii) to misclassify as Tc-poor a truly Tc-rich star? We show in the remaining of this section that both risks are most probably non-existent in the present study.

Error (i) could, in principle, affect very luminous Tc-poor stars, because their large macroturbulence would broaden their X_{4262} feature, which could then possibly mimic a Tc-rich feature.

In order to test this hypothesis, gaussian filters of different widths have been applied to Tc-poor spectra, so as to make their line widths comparable to those of the stars classified as Tc-rich. The resulting plots are displayed in Fig. 5.3 and 5.4. This simulation shows that even the largest macroturbulence value observed in our sample (T Ceti) is not large enough to make truly Tc-poor stars appear as Tc-rich from the broadening of their X_{4262} feature. That conclusion is however somewhat less obvious when considering the X_{4238} feature. Hence this risk cannot be excluded for very luminous stars (class I or II) if observed at low resolution ($R < 30\,000$).

Error (ii) could, in principle, occur for stars displaying a ‘weak technetium line’ (weaker than the Tc lines of Hen 140 discussed above) with an intensity not large enough to shift the X_{4262} blend redward from the Tc-poor wavelength. In fact, some stars in our sample exhibit an ‘ambiguous’ X_{4262} blend, in the sense that the pseudo-emission located between the Nb I-Gd II lines and the Cr I line becomes very weak or even disappears, mimicking a ‘weak technetium line’ (a typical example is Hen 7 on Fig. 5.1). Such a star is classified by our method as technetium-poor, for the minimum of the X_{4262} blend remains unchanged with respect to the no-Tc cases.

In fact, all intermediates exist between the ‘unambiguous’ X_{4262} Tc-poor blends (with a clear central pseudo-emission, see HD 73341 and Hen 3 on Fig. 5.1) and the ‘ambiguous’ X_{4262} blends (where this pseudo-emission is absent, as in Hen 7); two typical transition cases are plotted on Fig. 5.1 (Hen 187

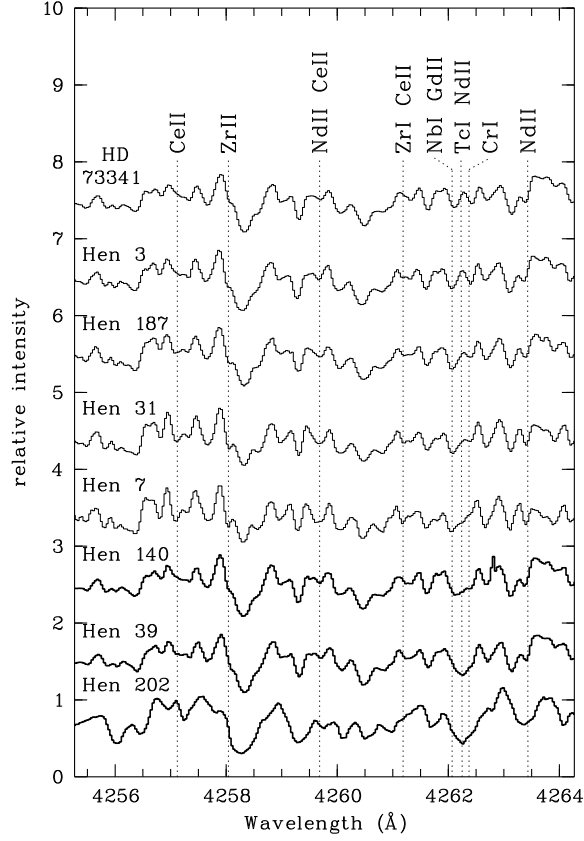


Figure 5.1: Spectra in the 4262Å region. The top spectrum is HD 73341, a normal giant (M3/M4III); the other spectra correspond to Henize S stars. Technetium-poor spectra are plotted with a thin line; technetium-rich spectra with a thick line. Hen 3, 187, 31, 7 are typical Tc-poor stars; Hen 39 and 202 are typical Tc-rich stars. The Tc-rich spectrum of Hen 140 is unique in our sample and remarkable because of its very weak Tc lines (see Sect. 5.3.1). All spectra are plotted on the same relative intensity scale. The local pseudo-continuum point has been taken as an average of the fluxes at 4239.1, 4244.1, 4247.1 and 4265.4Å; for the sake of clarity, each spectrum (except the lowest one) is vertically shifted by 1 unit with respect to the spectrum below it. Some spectral features of s-process elements are identified (see text)

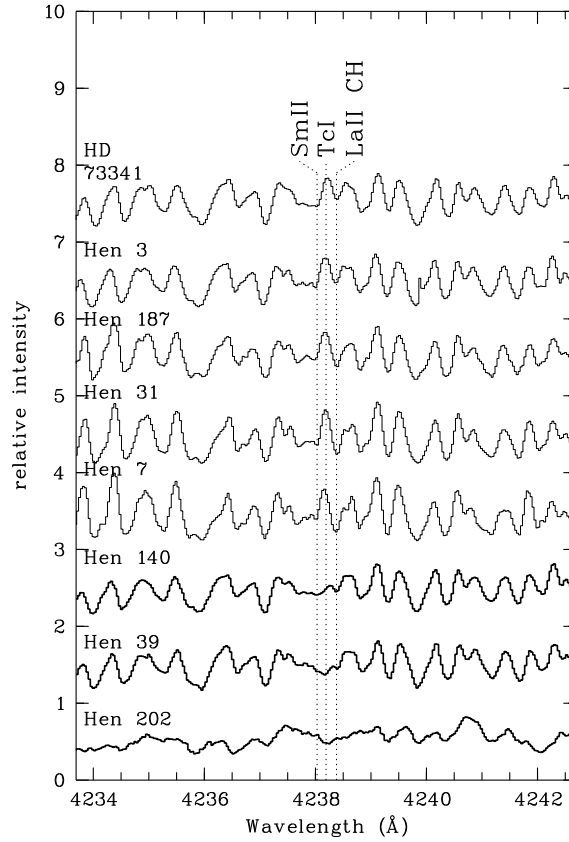


Figure 5.2: Same as Fig. 5.1 for the 4238Å region

and Hen 31). These ‘ambiguous’ spectra were taken during different observing runs; the shape of the X_{4262} blend is independent of the resolution and of the S/N ratio of the spectra.

Do these ‘ambiguous’ spectra correspond to stars with a weak technetium line, intermediate between the clear Tc-poor and Tc-rich cases? In fact these ‘ambiguous’ spectra are clearly different from the spectrum of the weakly Tc-rich star Hen 140, for *their* X_{4238} feature is identical to the X_{4238} feature of the *unambiguous* Tc-poor stars (Fig. 5.2), which clearly indicates that technetium is absent in these stars.

It may therefore be concluded that our method of gaussian fit to the X_{4238} and X_{4262} features is able to properly separate technetium-rich from technetium-poor S stars.

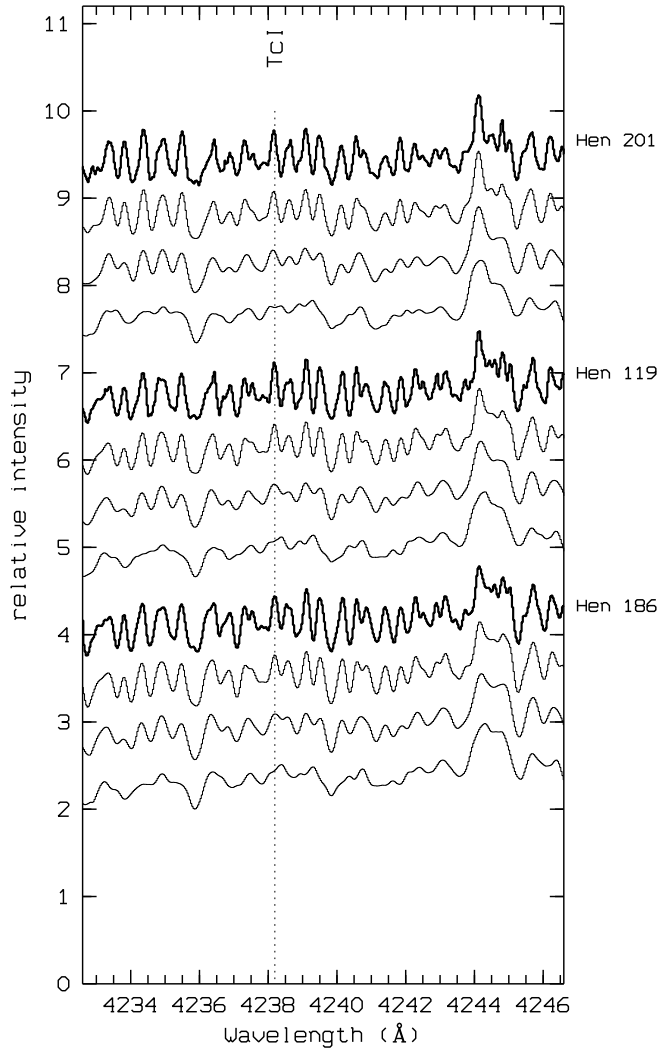


Figure 5.3: Artificial broadening of three Tc-poor spectra at 4238.191 Å. Raw spectra are plotted with a thick line

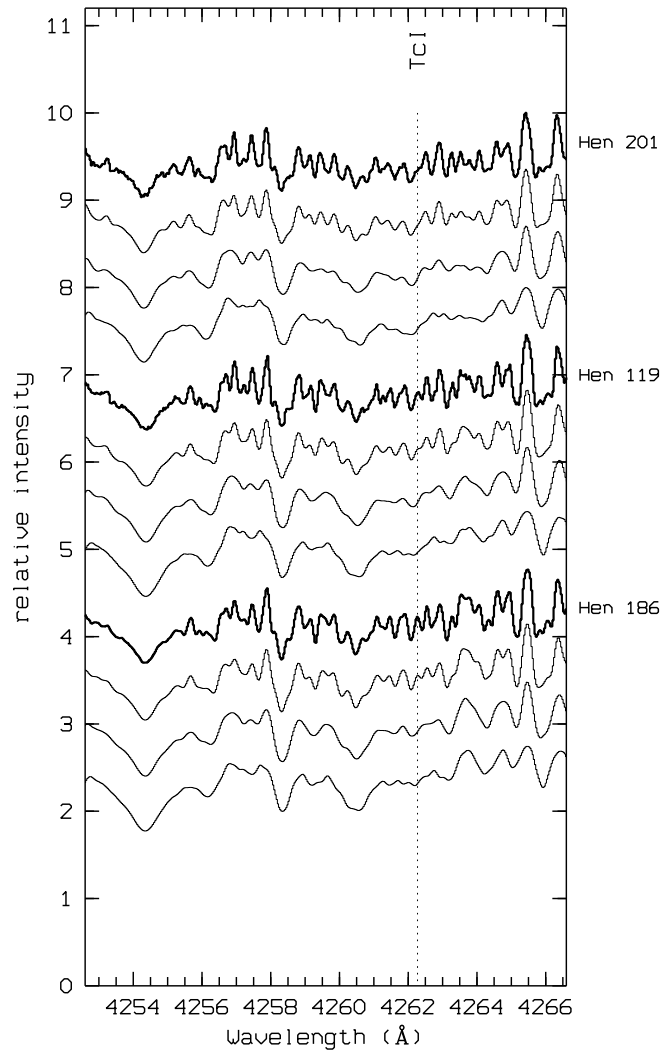


Figure 5.4: Artificial broadening of three Tc-poor spectra at 4262.270 Å . Raw spectra are plotted with a thick line

What then causes the variety of X_{4262} features observed in Fig. 5.1 for technetium-poor S stars? The spectral sequence going from Hen 3 to Hen 7 on Fig. 5.1 is not a temperature sequence. The temperature of the stars of our sample have been derived from the $V - K$ colour index using the Ridgway et al. (1980) calibration, the K magnitudes from Catchpole et al. (1979) and our Geneva photometry. Although the bulk of technetium-rich S stars are clearly cooler than technetium-poor S stars (see also Chap. 3), there is no sign whatsoever of a possible correlation between the shape of the X_{4262} blend of technetium-poor stars and their temperature. MOOG (Snedden 1974) synthetic spectra (for stars with $T_{\text{eff}} \sim 3400 - 3800$ K as derived from their $V - K$ index) indicate that neither gravity nor metallicity can significantly modify the X_{4262} blend.

A closer inspection of the spectral sequence of Fig. 5.1 (from HD 73341 to Hen 7) reveals that several lines become stronger as the central pseudo-emission of the X_{4262} blend weakens. The major contributors to these features, identified with the help of synthetic spectra, are indicated on the top of Fig. 5.1. It is noteworthy that *all these elements are s-process elements*. The sequence of spectra (drawn with a thin line) in Fig. 5.1 is thus, from top to bottom, a sequence of increasing s-process line strengths (s-process lines being weak, as expected, in the M star HD 73341). The line which progressively blends the X_{4262} feature of technetium-poor stars is thus probably an s-process line as well. Since it cannot be technetium (see above), a good candidate is the 4262.228\AA line of Nd II, or perhaps the wing of the Gd II line at 4262.087\AA .

It is not surprising to find a wide range of s-process enhancements among technetium-poor S stars, since these stars have accreted their s-process-enriched matter from a companion star. Hence the level of chemical peculiarities is not linked to the evolutionary status of the star, but rather depends upon the amount of s-process accreted matter (see discussion in Chap. 2).

These s-process lines are more difficult to see in the technetium-rich S stars, probably because in these cooler and more luminous stars, lines are broader (because of a larger macroturbulence) and the molecular blanketing is more severe.

5.3.2 Misclassified and SC stars

The method outlined in Sect. 5.3.1 cannot be applied to four stars of our sample which exhibit peculiar spectra (Hen 22, 135, 154 and 198).

In order to check the assignment of the Henize stars to spectral type S, low-resolution spectra have been obtained for all stars from Hen 3 to Hen 165. In fact, Hen 22 and 154 emerged as the only two misclassified stars (Sect. 6.6.3). They show no sign of ZrO bands whatsoever in their spectra; Hen 22 is rather a late G (\sim G8) giant and Hen 154 a mid-K (\sim K3-5) giant.

As far as Hen 135 and Hen 198 are concerned, Fig. 5.5 shows that the spectra of these stars are very different from those of other S stars of the Henize sample. Many spectral features adopted as wavelength standards, as well as

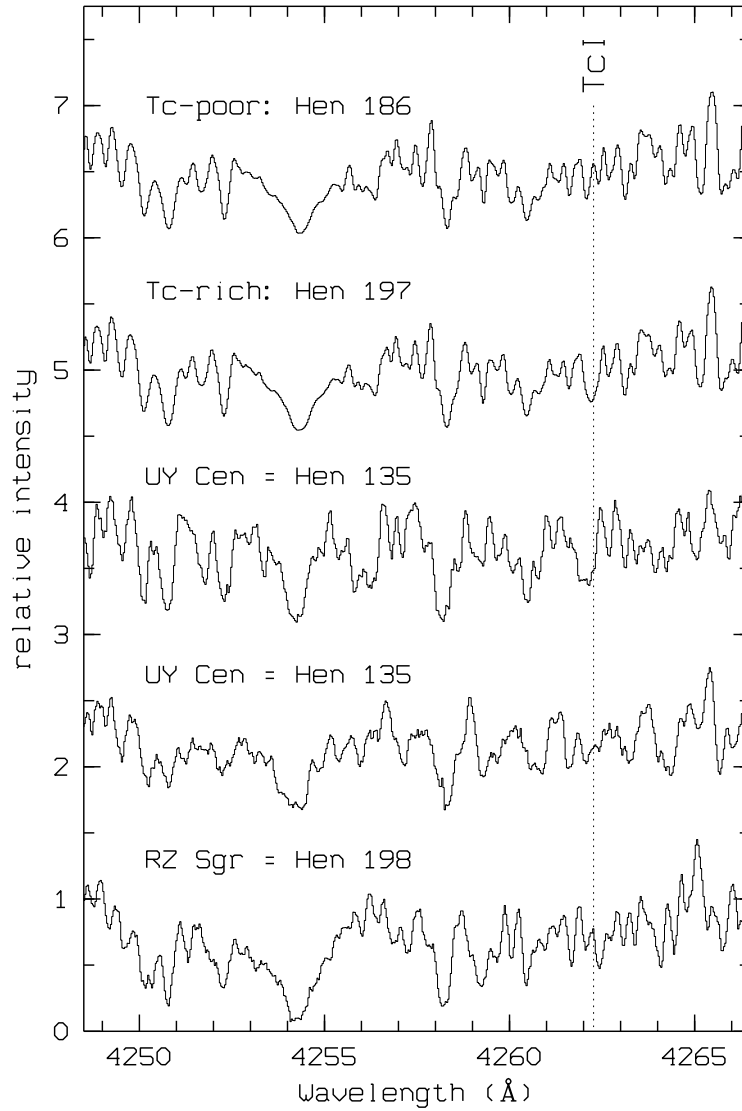


Figure 5.5: Same as Fig. 5.1, but for two prototype S stars (Hen 186, Tc-poor and Hen 197, Tc-rich), and for the two outstanding stars UY Cen (SC) and RZ Sgr. Note the striking differences between the lower and upper spectra of UY Cen, taken on March 16, 1993 and on January 31, 1997, respectively. The local pseudo-continuum point is defined as in Fig. 5.1; for the sake of clarity, each spectrum (except the lowest one) is vertically shifted by 1.5 unit with respect to the spectrum below it

the technetium blend, are difficult or even impossible to identify in the spectra of Hen 135 and Hen 198. In fact, we show below that these two stars are the only two SC stars in the subsample of Henize S stars observed with the CAT². Hen 135 ($V \sim 7$) and Hen 198 ($V \sim 7 - 10$) were indeed the only very red stars ($B - V > 2$) which were bright enough to allow spectra to be taken in the violet.

SC stars are known to have very peculiar spectra. Their spectrum is filled with strong atomic lines and almost no molecular bands in the optical, a consequence of their C/O ratio being very close to unity (Scalo 1973). Catchpole & Feast (1971) define SC stars from the following three criteria: (i) extremely strong Na D lines, (ii) drop in the continuum intensity shortward of 4500Å, and (iii) bands of ZrO and CN simultaneously present (though quite weak), as well as general resemblance of the spectrum (i.e. regarding ‘the absolute and relative strength of metal lines’) with that of UY Cen.

Hen 135 (=UY Cen) is thus the prototype SC star. Our two spectra of that star (taken in March 1993 and January 1997, see Fig. 5.5) are quite different; in particular the shape of the X_{4262} feature has changed noticeably. Therefore it is hazardous to infer the technetium content of UY Cen from these data alone without the help of appropriate model atmospheres and synthetic spectra, which is beyond the scope of this work.

Hen 198 (=RZ Sgr) has an Se-type spectrum; Stephenson (1984) quotes the HD catalogue noting that ‘the spectrum is similar to class N, but does not belong to that class’. It is probably associated with a reflection nebula (Whitelock 1994). RZ Sgr is a large-amplitude (~ 2.5 mag) SRb-type variable ($P = 203.6$ d). Its $H\alpha$ emission, as well as the TiO and ZrO band strengths, are variable. Catchpole & Feast (1976) also note that the Zr:Ti ratio of RZ Sgr is unusually high for an S star, and rather close to the one of N-type carbon stars.

Although RZ Sgr has not been classified as an SC star, it shares many common features with that family. Indeed, it reasonably meets the three criteria mentioned above for SC stars:

(i) Reid & Mould (1985) measured the strength of the Na D lines for several S, SC and C stars, including RZ Sgr. A spectrophotometric index of 1.07 is found for RZ Sgr, much larger than typical values for S stars (0.22 for BD+28°4592 and 0.28 for NQ Pup), but comparable to values obtained for SC stars (0.55 for LMC 441, 1.73 for R CMi, 2.57 for VX Aql). Thus RZ Sgr has abnormally strong Na D lines with respect to other S stars.

(ii) The ultraviolet flux deficiency of SC stars is clearly apparent from photometric data in the Geneva system. Indeed, the mean wavelengths of the B and V filters are $\lambda_0(B) = 4227\text{Å}$ and $\lambda_0(V) = 5488\text{Å}$ (Rufener & Nicolet 1988); therefore the $B - V$ index is highly sensitive to the ultraviolet flux deficiency of SC stars occurring for $\lambda < 4500\text{Å}$. SC stars have $B - V > 2$, whereas the bulk of S stars have $B - V < 2$. In that respect again, RZ Sgr ($2.0 < B - V < 3.0$) is typical of SC stars.

(iii) ZrO is present (although weak) in RZ Sgr; we found no information about

²Although the Henize sample contains several SC stars, they are usually too red, hence too faint at 4250Å, to be observed with the CAT.

the possible presence of CN bands. Infrared CO bands are stronger in RZ Sgr than in many other S and SC stars (Whitelock & Catchpole 1985), probably locking a great quantity of carbon.

The IRAS colours of RZ Sgr also share many similarities with SC stars: it is located in a region of the $(K - [12],[25] - [60])$ colour-colour diagram [‘region E’ as defined by Jorissen & Knapp (1998)] containing mainly SC stars with large $60\mu\text{m}$ excess and often resolved shells (see also Young et al. 1993).

All these arguments therefore indicate that RZ Sgr is closely related to the SC family. As pointed out for UY Cen, the 4262\AA and 4238\AA lines of Tc I are very difficult to analyse in SC stars. An assignment of these two stars to either the Tc-rich or Tc-poor group has therefore not been attempted here. Abia & Wallerstein (1998) nevertheless suggest that SC stars are Tc-rich, based on a quantitative analysis.

5.4 Discussion

5.4.1 The technetium dichotomy

The lower part of Fig. 5.6 shows the frequency histogram of the wavelength of the X_{4262} spectral feature for stars of Tables 5.1 and 5.2. The stars of our sample clearly segregate in two groups. The average wavelength of the bluer group is 4262.093\AA ; this group thus corresponds to Tc-poor S stars. The average wavelength of the redder group is 4262.235\AA , thus revealing the contribution of the Tc I 4262.270\AA line to the Gd II-Nb I blend. The standard deviation on the X_{4262} wavelengths is 0.012\AA for Tc-poor stars and 0.017\AA for Tc-rich stars. These values are in good agreement with the estimated errors on the X_{4262} wavelength (0.013\AA for Tc-poor and 0.020\AA for Tc-rich stars, Sect. 5.3.1).

The two groups are clearly separated by a 0.08\AA gap, *with no intermediate cases*. Therefore, in order to distinguish Tc-poor from Tc-rich stars (on our spectra of resolution in the range 30000-60000), a delimiting wavelength of 4262.16\AA may be safely adopted.

A similar conclusion holds for the X_{4238} feature (Fig. 5.7), where a boundary wavelength of 4238.29\AA unambiguously separates the two kinds of S stars. Fig. 5.7 further shows that the diagnostics provided by the X_{4238} and X_{4262} features are consistent with each other.

For comparison purpose the frequency histogram of the wavelength of the X_{4262} spectral feature as obtained by Smith & Lambert (1988) is plotted in the upper part of Fig. 5.6, for their sample of MS and S stars (their Table 2). The segregation into Tc-poor and Tc-rich S stars (with 4 stars falling on their boundary wavelength at 4262.14\AA) is not as clean as with our higher resolution spectra.

The small number of ‘transition stars’ in our sample (i.e. stars with weak Tc lines, the only case being Hen 140) is noteworthy. This result may provide constraints on the evolution with time of the technetium abundance along the TPAGB (Smith & Lambert 1988; Busso et al. 1992) and clearly deserves further

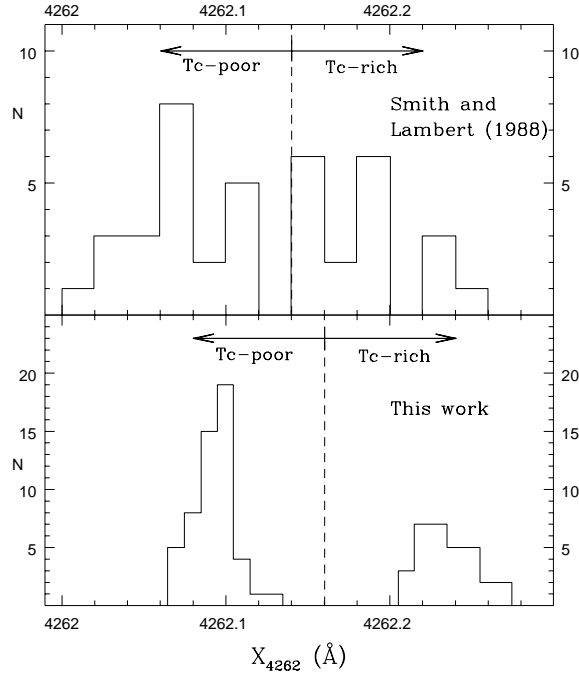


Figure 5.6: Frequency histograms of the wavelength of the X_{4262} spectral feature. Top: results of Smith & Lambert (1988) for their sample of MS and S stars; the dotted line delimits the boundary wavelength (4262.14Å) between Tc-poor and Tc-rich S stars, as adopted by Smith & Lambert (1988). Bottom: same for all stars of Tables 5.1 and 5.2, where the boundary wavelength has been taken at 4262.16Å

studies. For example, it would be of interest to investigate whether the small number of S stars with weak technetium lines found in our sample implies that the very first objects to dredge-up heavy elements on the TPAGB are not S stars but rather M stars. Indeed, the Tc detection threshold might not coincide with the ZrO detection threshold, as discussed in Sect. 1.1.3 (see Fig. 1.3). It is moreover necessary to disentangle abundance effects from atmospheric effects on the technetium line strength.

Although a more detailed study is deferred to a forthcoming study, it may already be mentioned at this point that the Tc/no-Tc dichotomy reported in this work is not due to technetium being entirely ionized in the warmer S stars. Indeed, the Tc I/(Tc I + Tc II) ratio is still $\sim 40\%$ in the warmest S stars ($T_{\text{eff}}=3800$ K) while it amounts to $\sim 70\%$ at $T_{\text{eff}}=3500$ K and to $\sim 95\%$ at $T_{\text{eff}}=3000$ K, according to the Saha ionization equilibrium formula (with representative electron densities taken from model atmospheres, see Tab. 5.3).

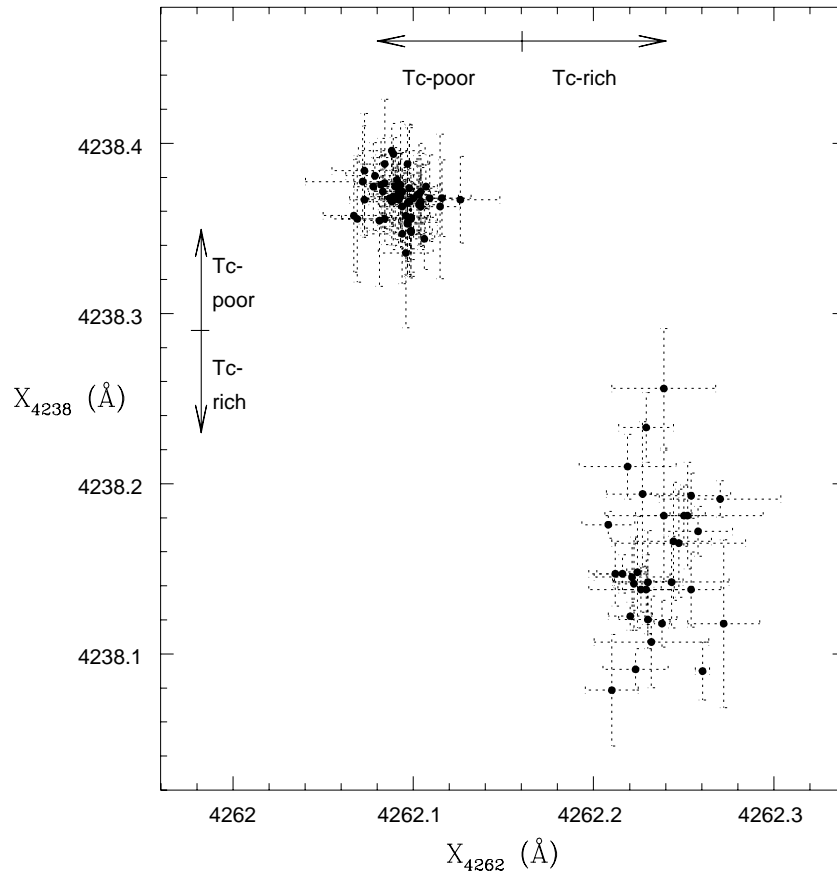


Figure 5.7: The wavelength of the X_{4262} Tc feature versus the wavelength of the X_{4238} Tc feature. Errorbars represent the standard deviation of the mean redshift (computed from the ~ 10 spectral features adopted as wavelength standards). The technetium class (Tc-rich or Tc-poor) derived from the X_{4238} blend always confirms the technetium class derived from the X_{4262} blend; the Tc-poor and Tc-rich regions are clearly distinct. The boundary wavelengths adopted in this study between Tc-rich and Tc-poor stars are 4262.16\AA for the X_{4262} feature (horizontal axis) and 4238.29\AA for the X_{4238} feature (vertical axis); they are indicated by arrows

Table 5.3: Percentages of neutral and ionized technetium for typical temperatures of red giants

Teff	gravity	% Tc I	% Tc II
• grid of MARCS models (Plez 1992; Plez et al. 1992; Bessell et al. 1998)			
2500.	-0.5	99.73	.27
2600.	-0.5	99.40	.60
2700.	-0.5	98.82	1.18
2800.	-0.4	97.82	2.18
2900.	-0.2	96.89	3.11
3000.	0.0	94.85	5.15
3100.	0.1	91.64	8.36
3200.	0.3	87.82	12.18
3250.	0.3	84.43	15.57
3400.	0.7	80.29	19.71
3500.	0.9	73.33	26.67
3650.	1.2	60.85	39.15
• Models from Bessell et al. (1998)			
3600.	-0.50	29.46	70.54
3600.	0.00	40.98	59.02
3600.	0.50	52.62	47.38
3600.	1.00	63.27	36.73
3800.	-0.50	12.84	87.16
3800.	0.00	17.72	82.28
3800.	0.50	26.60	73.40
3800.	1.00	37.09	62.91
3800.	1.50	48.23	51.77
4000.	0.00	6.43	93.57
4000.	0.50	12.74	87.26
4000.	1.00	20.21	79.79
4000.	1.50	29.90	70.10
4000.	2.00	41.12	58.88
4250.	0.50	3.72	96.28
4250.	1.00	6.49	93.51
4250.	1.50	10.91	89.09
4250.	2.00	17.43	82.57
4250.	2.50	26.19	73.81
4500.	1.00	2.10	97.90
4500.	1.50	3.70	96.30
4500.	2.00	6.36	93.64
4500.	2.50	10.56	89.44

5.4.2 M stars with $60\mu\text{m}$ excess and symbiotic stars

None of the four M stars with $60\mu\text{m}$ excess taken from the sample of Zijlstra et al. (1992) show technetium. This observation clearly indicates that these stars, which are surrounded by cool dust dating back to a former episode of strong mass loss, do not currently experience heavy elements synthesis followed by third dredge-ups. The same conclusion holds true for the two observed symbiotic stars (SY Mus and RW Hya).

5.5 Conclusion

High-resolution spectra have been obtained and analysed to infer the technetium content of 76 S, 8 M and 2 symbiotic stars. All the spectra are plotted in Appendix A. The presence or absence of technetium was deduced from the shape of two blends involving technetium at 4238\AA and 4262\AA (more precisely: from the wavelength of their minimum). However this method does not apply to SC stars. The technetium (non-)detection at 4238\AA is consistent with the result at 4262\AA . Only one ‘transition’ case (Hen 140 = HD 120179, a star where only weak lines of technetium are detectable) is found in our sample.

A resolution in excess of 30 000 is definitely required to provide unambiguous conclusions regarding presence or absence of technetium. For example, at 4262\AA , an s-process line (possibly Nd II) is suspected to sometimes mimic a weak technetium line (although the 4238\AA feature clearly shows that technetium is absent). The shape of the $\lambda 4262\text{\AA}$ feature varies from one Tc-poor star to another, depending on the s-process overabundance level, which is in turn a function of the amount of accreted matter by these binary S stars.

Among the 70 analysed Henize S stars, 41 turn out to be technetium-poor and 29 technetium-rich. That fraction may not be used, however, to infer the relative frequencies of intrinsic and extrinsic S stars, since the subsample of Henize S stars observed with the CAT is biased towards the brightest and bluest stars. The frequency of extrinsic/intrinsic S stars will be derived from the whole data set in Chap. 7.

Chapter 6

Additional observational characteristics of Henize S stars

6.1 Introduction

The present chapter continues with the discussion of the observational material collected on the S stars of the Henize sample. After a discussion of the radial-velocity data of the Henize S stars (Sect. 6.2), their Geneva photometry is examined (Sect. 6.3), as well as their *JHKL* (Sect. 6.4) and their IRAS (Sect. 6.5) photometry. Spectral indices computed from the low-resolution spectra are discussed in Sect. 6.6. All the data described in this chapter are listed in Tables B.1 to B.4 of Appendix B.

6.2 Radial velocities of S stars

6.2.1 CORAVEL monitoring of the Henize sample

Radial-velocity monitoring of the Henize sample of S stars has been performed between 1992 and 1997 on the Danish 1.54-m telescope at the European Southern Observatory (La Silla, Chile). A full description of the CORAVEL spectro-velocimeter can be found in Baranne et al. (1979). Basically, CORAVEL measures the velocity of a star by cross-correlating its spectrum with a mask reproducing about 1500 lines of neutral and ionized iron-group species from the spectrum of Arcturus (K1 III). The minimum of a gaussian fitted to the cross-correlation dip (cc-dip) thus obtained leads to the radial velocity of the star. Further information on the CORAVEL observation and reduction techniques can be found in Duquennoy et al. (1991). The heliocentric radial velocity data are listed in Table B.1.

6.2.2 Binariness in the Henize sample

Radial velocity curves and orbital parameters

Despite the fact that all extrinsic S stars ought to be binaries, the number of radial velocity measurements in the present survey was generally not sufficient to derive a reliable orbit, except in the cases listed in Table 6.1 and displayed in Fig. 6.1. Table 6.1 also provides a few very preliminary orbits derived from 6 or 7 measurements only.

These orbital parameters are typical of the few orbits already known for extrinsic S stars (see Chapter 2). The Henize sample contains in fact the S star with the second shortest orbital period known (Hen 108, $P = 197$ d). Such a short orbital period sets strong constraints on the radius of the S star that has to fit inside its Roche lobe. Indeed, supposing the mass of the companion white dwarf to be $0.6 M_{\odot}$, the radius of the Roche lobe around the S star is $\sim 50 R_{\odot}$, with little sensitivity to its adopted mass (taken within the reasonable limits $1-4 M_{\odot}$). Given an effective temperature of ~ 3700 K as derived from the $V - K$ colour index and the calibration of Ridgway et al. (1980), and an absolute bolometric magnitude in the range $-2 \leq M_{bol} \leq -3.5$ (Chap 3), the resulting radius lies in the range $54 R_{\odot}$ to $109 R_{\odot}$. Hence this star must be extremely close to filling its Roche lobe, or even currently undergoes a stable Roche-lobe overflow. In fact, this star could be expected to exhibit symbiotic activity; however a high-resolution spectrum of this star around H_{α} (Sect. 6.3.5) reveals no emission line whatsoever.

In fact, the only S star known to have a shorter period than Hen 108 is HD 121447 ($P = 186$ d, Table 2.9), an early S star (S0, Keenan 1950), also known as the coolest barium star (K7III Ba5, Lü 1991). This system was found to be an ellipsoidal variable (Jorissen et al. 1995). Due to its similarity with HD 121447, Hen 108 may be suspected to be an ellipsoidal variable as well; unfortunately the available photometric data are too scarce to check this hypothesis.

As far as the Henize S stars with fewer radial-velocity measurements are concerned, their radial-velocity standard deviation is expected to be larger for Tc-poor S stars than for Tc-rich S stars, because the intrinsic/extrinsic paradigm requires Tc-poor S stars to belong to binary systems. This is indeed the case, since the mean value of the radial-velocity standard deviation is $\langle \sigma(V_r) \rangle = 3.2 \pm 2.4$ (rms) km s^{-1} for Tc-poor S stars, as compared to 1.3 ± 0.7 (rms) km s^{-1} for Tc-rich S stars. This point will be further examined in Sect. 7.2.

6.2.3 The CORAVEL parameter Sb

In fact, some additional pieces of information may be derived from the CORAVEL cc-dip: in particular, the parameter Sb , defined as the reduced width of the cc-dip: it is computed from the observed width σ of the stellar cc-dip, corrected for the instrumental profile $\sigma_0 = 6.29 \text{ km s}^{-1}$ (i.e., the cc-dip of minor planets reflecting the sun light, corrected for the solar rotational velocity and photospheric turbulence): $Sb = (\sigma^2 - \sigma_0^2)^{1/2}$.

Table 6.1: Orbital elements for Henize S stars

Hen	P [days]	T [HJD -2 400 000]	e	γ [km s ⁻¹]	ω [deg]	K [km s ⁻¹]	$a \sin i$ [Gm]	f (m) M _⊙	N	$O - C$ [km s ⁻¹]	ΔT [days]
2	1146.97 2.05	38128.45 16.28	0.21 0.01	21.06 0.07	33.40 5.96	5.57 0.07	86.00 1.11	0.019 0.001	8	0.10	4931
108	197.24 0.30	48632.01 1.48	0.00 -	40.51 0.30	0.00 -	14.41 0.52	39.09 1.40	0.061 0.007	10	0.60	1826
121	763.63 5.89	49280.49 5.04	0.00 -	-5.495 0.30	0.00 -	10.54 0.51	110.69 5.40	0.092 0.013	11	0.96	1778
137	636.39 12.38	49699.02 24.16	0.44 0.17	-21.12 0.47	120.22 23.57	6.57 1.88	51.68 8.29	0.014 0.007	9	0.63	1780
147	335.76 1.09	49559.54 23.78	0.22 0.14	-8.13 0.60	195.56 31.33	11.01 2.39	49.58 10.86	0.043 0.028	8	0.52	1579
• preliminary orbits											
119	1300	48612	0.14	-23	254	7	118	0.039	6	0.20	1781
124	1983	51068	0.17	6	226	6	155	0.038	7	0.69	1414
183	889	49059	0.10:	-11	173	9	114	0.076	7	0.63	1827

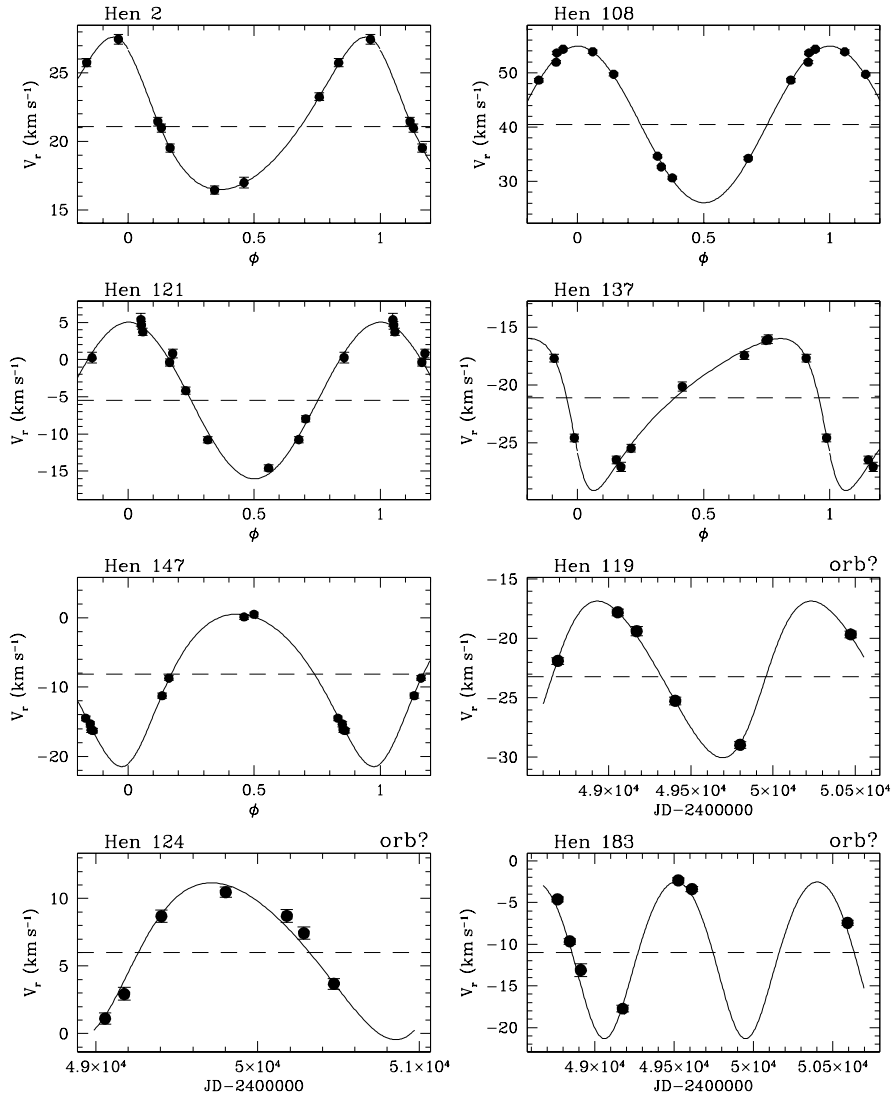


Figure 6.1: Orbits for 5 Henize S stars. The last three panels labelled “orb?” provide preliminary orbits

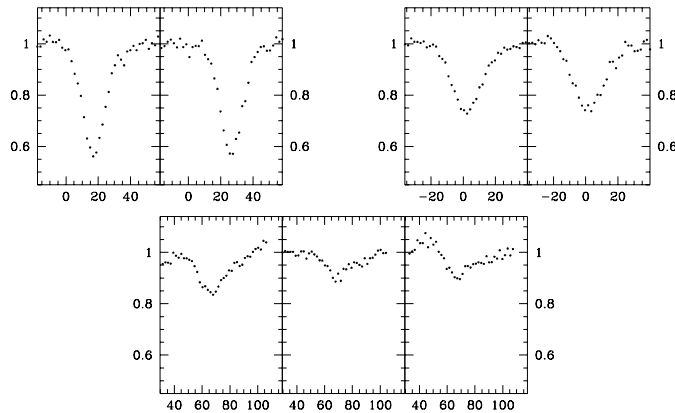


Figure 6.2: CORAVEL cross-correlation dips for the extrinsic, Tc-poor S star Hen 2 (upper part, left), for the intrinsic, technetium-rich S star Hen 97 (upper part, right) and for the Mira S star Hen 32 = SU Pup (lower part). The values of the Sb parameter are 4.2 km s^{-1} , 7.7 km s^{-1} and 8.5 km s^{-1} for Hen 2, Hen 97 and Hen 32, respectively

In relatively unevolved giants (like G, K, barium stars or Tc-poor S stars), the cc-dip is narrow, strongly contrasted and has a non-variable shape. On the contrary, the cc-dip of Mira stars is wide, shallow and strongly variable with time (see Figs. 2.1 and 6.2).

There are probably several reasons for the distorted cc-dips of Mira stars (Barbier et al. 1988). First, the atmosphere of a Mira star is characterized by a complex velocity field; the cc-dip of a Mira star is thus a combination of several (variable) cc-dips, each dip corresponding to a layer moving with a given velocity (Udry et al. 1998a; Wallerstein 1985). Hence the width of the resulting cc-dip is larger and more variable than if the star had a standing atmosphere. This link between Sb and the pulsational characteristics of the atmosphere is further confirmed by the strong trend of increasing Sb with increasing radial-velocity jitter (see Fig 2.1).

Second, the CORAVEL mask is optimized for Arcturus-type (K1) giants. In cooler stars like S stars, the relative line intensities are different, and additional molecular lines are encountered: such inadequacies of the mask with respect to the stellar spectrum are in part responsible for the shallower cc-dips of S stars (Alvarez, priv. comm.). The broadening of spectral lines due to macro-turbulence – previously believed to be the main cause of the cc-dip widening – probably plays only a minor role in shaping the cc-dip.

Since intrinsic S stars are by definition on the TPAGB, they are expected to be on average more evolved than extrinsic, mass-transfer S stars; their Sb parameter is consequently expected to be larger. This is indeed the case, as

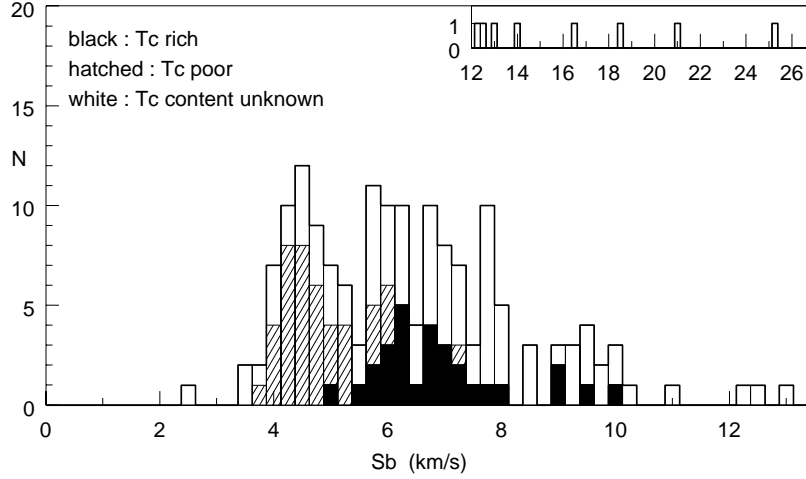


Figure 6.3: Histogram of the cc-dip widths (expressed in terms of Sb , see text) for the Henize S stars. The inset represents the large Sb tail of the histogram, concerning S Mira or SC stars

shown in Fig. 6.3: the distribution of the Sb parameter is clearly bimodal, the first peak ($Sb < 5.5 \text{ km s}^{-1}$) comprising mostly Tc-poor stars, and the second one ($Sb \geq 5.5 \text{ km s}^{-1}$) mainly Tc-rich stars. The lack of systems around $Sb \sim 5.5 \text{ km s}^{-1}$ is not dependent on the adopted binning of the data, but reveals the real of bimodal nature of the distribution. Hence, as suspected in Sect. 2.3, the Sb parameter appears to be a useful tool to distinguish, with a good statistical efficiency, intrinsic from extrinsic S stars, when no information on technetium is available.

6.3 Geneva photometry

The Henize sample of S stars has been monitored in the Geneva photometric system on the Swiss telescope at La Silla (Chile). Detailed information on this photometric system and on the data reduction can be found in Golay (1980), Rufener (1988) and Rufener & Nicolet (1988). Among the 205 S stars of the Henize sample, 179 could be reached with the 70 cm Swiss telescope, with an average of 4 good-quality photometric measurements (in all filters) per star.

6.3.1 Rejected measurements

Some photometric measurements have been discarded. They concern mostly misclassified stars, or stars with abnormal colours:

- *Misclassified stars:* Hen 22 and 154 are two stars misclassified as S, as revealed by low-resolution spectra (Sect. 6.6).
- *Single measurement revealing abnormally blue colours:* Only a single very blue measurement ($U - B = 2.26$; $B - V = 0.48$) is available for Hen 82; a nearby field main-sequence star could well have been measured instead of the faint and variable S star Hen 82. In fact, the S star Hen 82 is most probably a Mira (strong H_α and H_β emission on low-resolution spectrum, spectral type S5,8). Although Mira stars are known to sometimes exhibit such blue colours, Hen 82 has been removed from the photometric data set, given the lack of additional photometry confirming the blue colours of this star. The same holds true for Hen 181 (=V407 Sco; $U - B = 2.18$; $B - V = -0.53$).
- *Close visual binaries:* Several stars (Hen 47, 94, 105, 155) were found to be close visual binaries, and their photometric data have therefore not been considered for the analysis presented in Chap. 7.

In all these cases, two spectra separated by less than $10''$ (angular separation on the sky projected on the direction perpendicular to the slit, corresponding to less than 15 pixels on the CCD frame) have been recorded by the Boller & Chivens spectrograph (Sect. 6.6). Rough estimates of the companion spectral type could be obtained in all cases, but Hen 94 which is too faint: Hen 47 ($> 5''$): S + K4V; Hen 105 ($> 4''$): S + late BV or early AV; Hen 155 ($> 14''$): S + G5 IV-III. The numbers in parentheses provide a lower limit of the angular separation.

Hen 47 is the only one among those cases where the physical association between the two stars is clearly unlikely. The difference in absolute visual magnitudes between the S star and a K4V star is at least 7 magnitudes, but the observed difference in apparent visual magnitudes is less extreme, since the available photometry clearly reveals composite colours.

All these pairs lie within 2° of the galactic plane (except Hen 155 with $b = 20^\circ$) where crowding may be severe. If some of these pairs would nevertheless turn out to be physical, the less evolved main sequence companion would allow to set a lower limit on the mass of the S star, namely $> 3 M_\odot$ for Hen 105. These masses are compatible with S stars being intermediate-mass stars.

- *Magnitudes fainter than 16.5:* All magnitudes fainter than 16.5 were rejected, as well as their associated standard deviations, because at such faint magnitudes the flux contribution from the sky is dominating. For our S stars, magnitudes fainter than 16.5 only occur in the U filter, except for Hen 122 ($B = 17.453$), which is flagged in Table B.2.

The stars having $U > 16.5$ fall in two categories: (i) either the star has *some* of its U measurements fainter than $U = 16.5$; in that case only the measurements brighter than $U = 16.5$ were considered;

(ii) or the star has *all* its U measurements fainter than $U = 16.5$; no U

standard deviation is computed in that case. Column m_U indicates in Table B.2 the number of measurements fainter than $U = 16.5$.

6.3.2 Average colours and standard deviation

The average magnitudes were computed from the weighted fluxes according to Eq. 2 of Rufener (1988), where the weights refer to the quality of the measurements.

The reduced standard deviation σ_r is computed by quadratically subtracting the instrumental error σ_0 from the standard deviation σ . The instrumental error is computed by interpolating Fig. 2 of Barblan et al. (1998), giving the mean precision as a function of the magnitude in the case of Geneva photometric measurements. If $\sigma \leq \sigma_0$, then $\sigma_r = 0$. The reduced standard deviation has not been computed for magnitudes fainter than 16.5, because of the large uncertainties affecting the mean precision σ_0 at such faint magnitudes.

6.3.3 Dereddening

Each star has been dereddened according to the following procedure:

1. If $10^\circ \leq |b| < 45^\circ$, the colour excess E_{B-V} is taken from Burstein & Heiles (1982) and is multiplied by the factor $[1 - \exp(-10 r \sin |b|)]$, where r is the distance in kpc and b is the galactic latitude (Feast et al. 1990); 72 stars are concerned. The visual extinction is then computed with $A_V = R \times E_{B-V}$, where $R = 3.1$.
2. If $|b| < 7.6^\circ$, $A_V(r)$ is taken from Neckel & Klare (1980); 70 stars are concerned.
3. If $|b| \geq 45^\circ$, or if the star is not on the Milky Way fields defined by Neckel & Klare (1980), or if it falls outside their $A_V(r)$ diagram (i.e., if the star is located too far away), then the visual extinction is taken from Arenou et al. (1992); 37 stars are concerned.

The dereddening procedure then requires to assign absolute visual magnitudes to S stars. From HIPPARCOS parallaxes, intrinsic S stars are known to be brighter than extrinsic S stars (Chap. 3), but several factors (intrinsic variability, as well as the Lutz-Kelker bias) prevent from giving accurate average luminosities for both classes of S stars. The only previous large-scale estimate of absolute visual magnitudes of S stars is by Yorke & Wing (1979), who derived that the average M_V at maximum light is of the order -1.5 to -2.0 for Mira S stars (i.e., intrinsic S stars) and -1 for non-Mira S stars (presumably mostly extrinsic S stars).

In principle intrinsic S stars and extrinsic S stars should thus be assigned different absolute magnitudes (say $M_V = -1$ for extrinsic S stars and $M_V = -2$ for intrinsic S stars), depending on whether they have technetium or not. This approach has not been retained here since (i) the only unambiguous way to

distinguish extrinsic from intrinsic S stars is technetium detection, and this information is available only for 70 S stars (out of 205); the other parameters capable of segregating the two kinds of S stars have only a statistical efficiency (see Table 6.3), and (ii) this would introduce an *a priori* distinction between extrinsic and intrinsic S stars, which would be difficult to disentangle from possible genuine photometric differences derived subsequently.

While the intrinsic S stars are brighter than the extrinsic ones, they are also much redder, hence their V magnitude is dimmed. Therefore the single plausible value of $M_V = -1$ has been assigned, for dereddening purposes only, to both extrinsic and intrinsic S stars.

The dereddening process is iterated until convergence of the apparent V magnitude is achieved (to a level of 10^{-4} mag). The dereddened U and B magnitudes are then computed, using $E_{U-B} = 0.652 \times E_{B-V}$, a relation derived by Cramer (1994) for B stars in the Geneva photometric system (no such relation is available for late-type stars).

6.3.4 Colour-colour diagram

In the $(U - B, B - V)_0$ colour-colour diagram (Fig. 6.4), Tc-poor stars tend to cluster close to the normal giant sequence. The lack of extrinsic S stars with very blue and variable colours, that would be the signature of a nebular continuum as in symbiotic stars, will be further commented in Sect 6.3.5. Note also that information on the technetium content is only available for the bluest stars, since the technetium lines used in this study are located in the violet around 4260\AA .

Intrinsic S stars are known to be generally redder than extrinsic S stars (Chap. 3). This property is not clearly visible on Fig. 6.4, merely because of a strong observational bias: the reddest S stars were generally too faint in the U filter and do not therefore appear on Fig. 6.4, except for some relatively bright stars. In that respect it must be noted that the stars with $(B - V)_0 > 2$ are generally pure S stars (i.e., exhibiting only ZrO bands and no TiO) or SC stars; this point will be further discussed in Sect. 6.6.5. The extremely red star at $(U - B)_0 = 5.04$, $(B - V)_0 = 2.70$ is the bright prototype SC star Hen 135 = UY Cen.

On the contrary, many blue Miras are found where symbiotic S stars were expected [e.g., Hen 50: $(U - B)_0 = 2.0$, $(B - V)_0 = 0.3$, $\sigma(U) = 0.5$ or Hen 56: $(U - B)_0 = 1.6$, $(B - V)_0 = 1.2$, $\sigma(U) = 0.3$]. The blue colors of some Miras were already noted by Nakagiri & Yamashita (1979). The location of Miras in their $(U - B, B - V)$ diagram (their Figs. 17, 18 and 19) is very similar to the location of Henize blue Miras in Fig. 6.4. Nakagiri & Yamashita found that Miras describe loops in this part of the colour-colour diagram over a complete cycle. A similar behaviour is observed for prototypical Miras present in the Geneva photometric catalogue (e.g. R Hor, R Cnc or *o* Cet).

Because of the blue excursions of many Miras from the Henize sample, no clear distinction is observed between intrinsic and extrinsic S stars on the basis of the UBV colour indices. However, the blue Miras exhibit a much larger

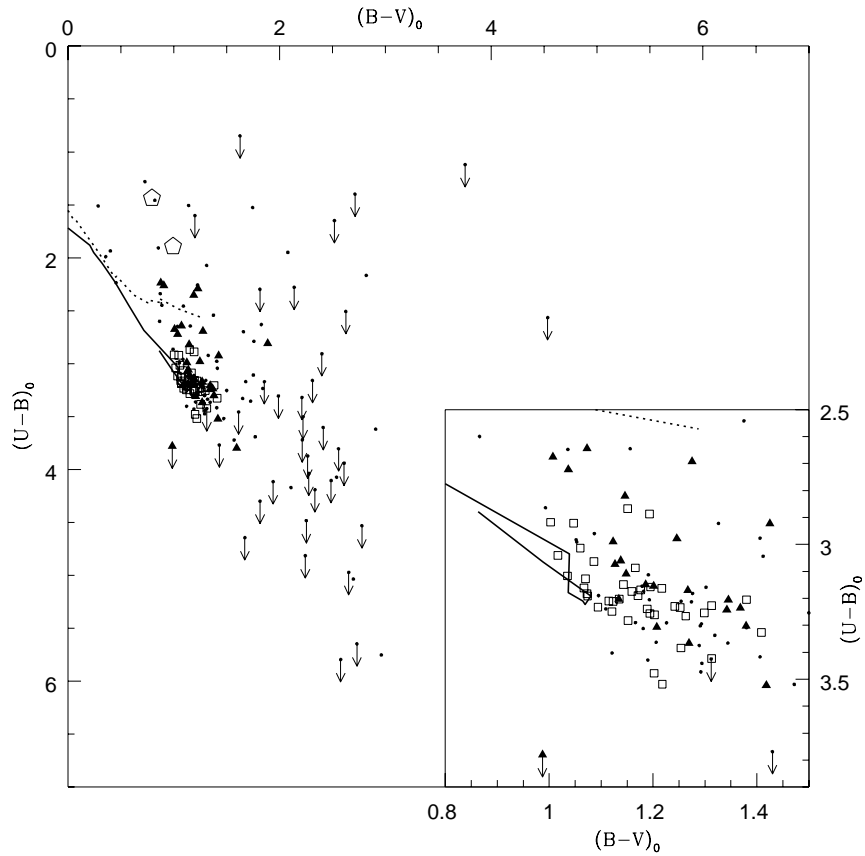


Figure 6.4: Dereddened colour-colour diagram, in the Geneva photometric system, of the Henize S stars. A zoom is presented in the lower-right inset. Tc-rich S stars are represented by black triangles, Tc-poor S stars by open squares, stars for which no Tc information is available by dots, and the two (Tc-poor) symbiotic S stars by open hexagons. The stars that have only upper limits on their U flux (Sect 6.3.1) are flagged with an arrow. The solid and dotted lines are the normal giant and dwarf sequences, respectively, from Grenon (1978)

variability than do extrinsic S stars (at least the non-symbiotic extrinsic): hence it is often possible to distinguish intrinsic from extrinsic S stars by combining colour indices and photometric variability information. This will be done in Sect. 7.1.

6.3.5 Symbiotic stars

Since all extrinsic S stars belong to binary systems, one could expect to see photometric signatures induced by the presence of their compact (white dwarf) companion, like in symbiotic systems. Indeed, symbiotic stars are interacting binaries in which the cool component is a late-type giant interacting with a compact companion (in most cases a white dwarf, sometimes a main-sequence or a neutron star). The mass loss of the giant star feeds a nebula which engulfs the components and gives rise to a veiling blue continuum and intense superposed nebular emission lines.

In fact, the U filter ($\sim 3050 - 3850\text{\AA}$), and, to a much lesser extent, the B filter ($\sim 3650 - 5150\text{\AA}$), are sensitive to the blue flux excess of symbiotic stars; as a consequence, symbiotic stars occupy extremely peculiar and variable locations in the $(U - B, B - V)_0$ colour-colour diagram. Excursions of symbiotic stars towards the blue in that colour-colour diagram were already noticed by Arkhipova & Noskova (1985), and are seen as well for prototypical symbiotic stars monitored in the Geneva photometric system (especially R Aqr and T CrB, and to a lesser extent, BL Tel, Z And and AG Peg).

Only two extrinsic S stars of the Henize sample exhibit abnormally blue colours in Fig. 6.4: Hen 18 and Hen 121. Their very peculiar and identical behaviour in the $(U - B, B - V)_0$ colour-colour diagram is illustrated by Fig. 6.5, where their individual photometric data are plotted.

Very few information on these two S stars is available in the literature. Though both stars were known as emission-line stars (Hen 18 is classified as S6,8e and Hen 121 as S4,6e by Henize (Stephenson 1984), this characteristic was not further investigated probably because H_α emission is a common feature among Mira S stars. They were both further observed in the near-infrared by Catchpole et al. (1979) and were detected by IRAS in the infrared (Chen et al. 1995).

The emission lines characteristic of symbiotic stars have been searched for in these two stars, as well as in 29 other ‘‘abnormally blue’’ stars of the Henize sample, with high-resolution spectroscopy performed in January 1998 at the European Southern Observatory, with the Coudé Echelle Spectrometer (CES) fed by the 1.4m Coudé Auxiliary Telescope (CAT), used in remote control. The long camera ($f/4.7$) and CCD #38 (Loral/Lesser thinned, backside illuminated, UV flooded, 2688×512 pixels of $15 \mu\text{m}$) were used. Details on these configurations can be found in Kaper & Pasquini (Kaper & Pasquini 1996). With a resolution of $R = 80000$ (ie: 0.082\AA at H_α), the spectra approximately cover the wavelength range $\lambda\lambda 6535 - 6610 \text{\AA}$ at H_α and $\lambda\lambda 6660 - 6735 \text{\AA}$ at He I. The data were reduced using the ‘long’ context of the MIDAS software package [bias subtraction, flat-field normalization, wavelength calibration through tho-

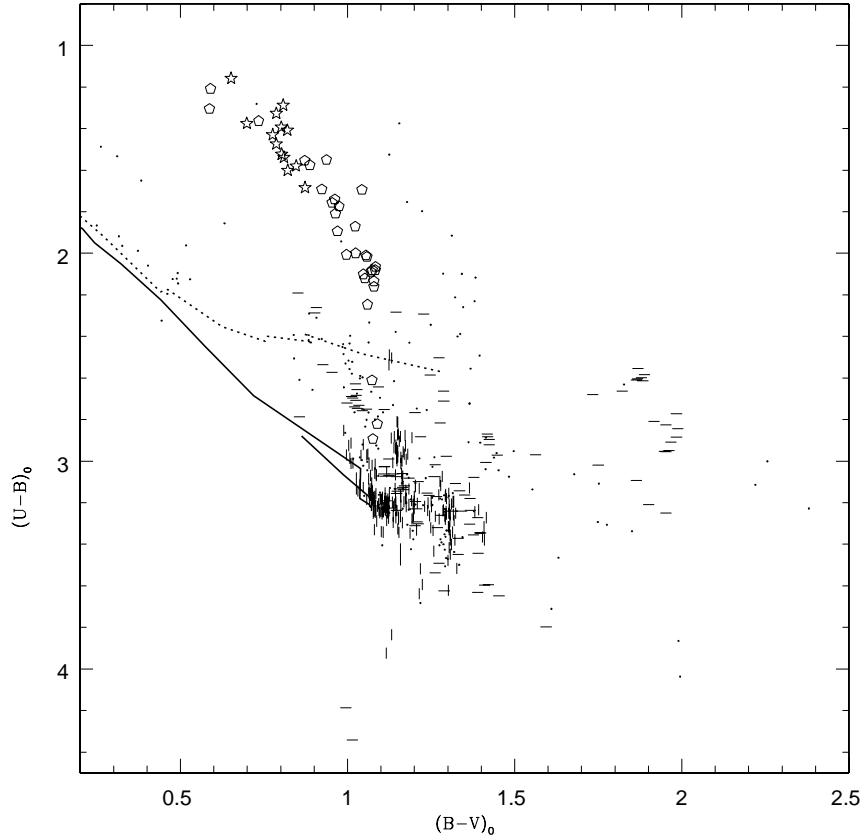


Figure 6.5: Dereddened colour-colour diagram, in the Geneva photometric system, of symbiotic and non-symbiotic S stars (individual measurements). Te-rich stars are represented by an horizontal dash, Te-poor stars by a vertical dash, stars for which no information on Te is available by dots. The measurements of Hen 18 and 121, the two symbiotic stars, are represented by stars symbols and empty hexagons, respectively (they are both Te-poor). The solid and dotted lines are the normal giant and dwarf sequences, respectively, from Grenon (1978)

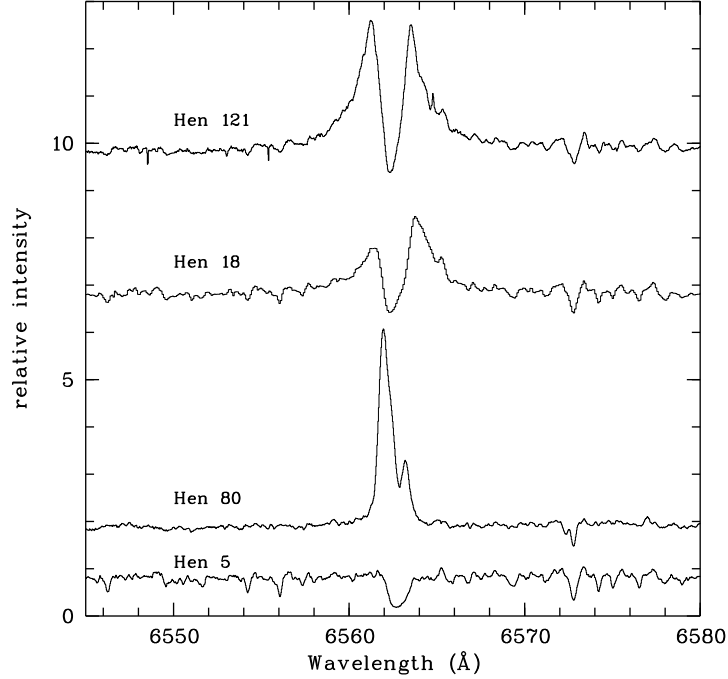


Figure 6.6: Spectra of S stars in the H_{α} region. From bottom to top: Hen 5: a non-symbiotic Tc-poor S star; Hen 80: a non-symbiotic Tc-rich Mira S star; Hen 18 and 121: the two (Tc-poor) new symbiotic S stars

rium lamp spectra taken roughly every hour, optimal extraction of the spectra according to Horne (1986)].

Both Hen 18 and 121 indeed show a definite, though weak, symbiotic activity, in that they exhibit the very broad ($\text{FWHM} \gtrsim 300 \text{ km s}^{-1}$) H_{α} emission with blue-shifted absorption typical of symbiotics (Fig. 6.6), but no other emission line. This H_{α} emission is clearly distinct from the Mira profile ($\text{FWHM} \lesssim 130 \text{ km s}^{-1}$) often shown by Mira (Tc-rich) S stars (see Hen 80 in Fig 6.6).

Though the symbiotic family comprises over 200 objects, only 3 symbiotic S stars were known to date (Jorissen 1997); Hen 18 and 121 constitute two new discoveries in this restricted family and, like the other symbiotic S stars, their symbiotic activity is moderate. These two stars are found to be binaries and their orbital periods ($P = 764 \text{ d}$ for Hen 121, $P > 1800 \text{ d}$ for Hen 18, see Table 6.1 and B.1) appear typical of those of normal extrinsic S stars.

The 29 additional “blue” S stars also examined for symbiotic activity did

not exhibit any symbiotic features at the epoch of observation. It is thus noteworthy that only the two stars Hen 18 and 121, out of the 29 blue Henize stars spectroscopically examined (and possibly out of the 172 stars having Geneva photometry) exhibit a clear symbiotic signature at the epoch of observation. This fact underlines that the key factor triggering symbiotic activity is not yet understood: it is not sufficient to have a red giant and a white dwarf in a binary system with periods typically in the range 200-10 000 days to develop symbiotic activity; some additional physical ingredients (involving metallicity, luminosity, masses of the components, mass loss, presence and properties of a disk fed by an enhanced mass loss?) are clearly required.

6.4 JHKL photometry

Observations in the J, H, K and L bands (1.2, 1.6, 2.2, and 3.4 μm) were obtained at the South African Astrophysical Observatory for 138 Henize stars.

These colours were dereddened using the colour excess E_{B-V} obtained in Sect. 6.3.3 combined with unpublished colour excess ratios for the SAAO system kindly made available by Dr. I. Glass (1999, priv. comm.).

6.5 IRAS photometry

Intrinsic and extrinsic S stars have been shown to segregate well in the ($K - [12], K - [25]$) diagram (Groenewegen 1993; Jorissen et al. 1993). Here the color index $K - [i]$ is defined as $K - [i] = K + 2.5 \times \log(F(i)/620)$, where $F(i)$ (in Jy) is the (non color-corrected) flux in the i band from IRAS PSC; conversion between the K magnitude and the 2.2 μm flux is performed according to the calibration of Beckwith (1976; 620 Jy corresponds to $K = 0$). Only IRAS good-quality fluxes (quality flag=3) have been retained; the corresponding $K - [12]$ and $K - [25]$ colour indices are listed in Table B.3. The IRAS fluxes of Hen 55 (= IRAS 08457-4548) have been disregarded, because this star is very near from IRAS 08459-4547 located about $2'$ to the east, possibly contaminating its IRAS fluxes. Despite a good quality flag (3 at 25 μm), Hen 2 (= IRAS 01309-7913) has not been included because its 25 μm flux is at the IRAS sensitivity limit (0.2 Jy) and leads to an unphysical $K - [25]$ colour falling to the blue of the Rayleigh-Jeans point.

Indeed, Fig. 6.7 nicely confirms the expected segregation among the S stars of the Henize sample. More precisely, a severe constraint may be set on Henize's extrinsic S stars: they always have $K - [25] < -4$ and $K - [12] < -2.5$. The ($[12] - [25], [25] - [60]$) colour-colour diagram is less useful, because good quality $[12] - [25]$ and $[25] - [60]$ colours are only available for 27 stars, among which only 7 are known to be Tc-rich and 1 is Tc-poor.

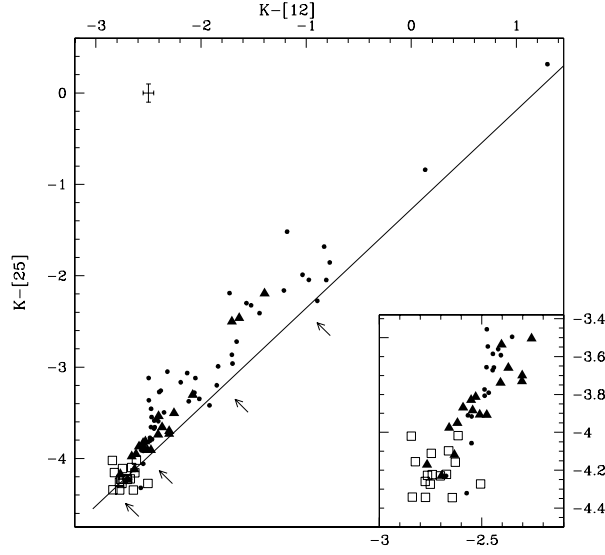


Figure 6.7: The $(K - [12], K - [25])$ colour-colour diagram of Henize S stars. Open squares stand for Tc-poor S stars, filled triangles for Tc-rich S stars and black dots for S stars with unknown technetium content. Only the good-quality (flag=3) IRAS measurements have been used. The error bars correspond to a typical uncertainty of 5 and 10% on the 12 and 25 μm fluxes, respectively. The solid line represents black body colours, with arrows corresponding to temperatures of 4000, 3000, 2000 and 1500 K (from lower left to upper right)

6.6 Low-resolution spectroscopy

6.6.1 Observations and reductions

Low-resolution spectra ($\Delta\lambda \sim 3\text{\AA}$), covering the spectral range 4400-8200 \AA , have been obtained at the European Southern Observatory (ESO, La Silla, Chile) on the 1.52m telescope equipped with the Boller & Chivens spectrograph (grating #23 + filter GG 420; 114 \AA mm^{-1}) and a Loral/Lesser thinned, UV flooded 2048×2048 CCD (CCD #39; $15\mu\text{m}$ pixels).

The CCD frames were corrected for the electronic offset (bias), for the relative pixel-to-pixel response variation (flat-field) and for the sky foreground lines. Wavelength calibration was performed from helium-argon lamp spectra taken at least every two spectra. An optimal extraction of the spectra was performed according to the method of Horne (1986). The extracted spectra were multiplied by the instrumental response function, obtained from the spectra of flux-calibrated standard stars (namely CD-32 $^{\circ}$ 9927, LTT 3218, LTT 4816).

The whole reduction sequence was performed within the “long” context of the MIDAS software package.

The signal-to-noise (S/N) ratio was estimated for each spectrum in the following way: three S/N values were computed for the three best exposed CCD lines (along the dispersion axis), in the neighbourhood of three spectral region of interest (~ 6000 , 7000 and 7500\AA). These S/N values were then combined according to Eq. 17 of Newberry (1991). When the exposure time on a given star has been split in two, the final S/N ratio was computed using Eq. 18 of Newberry (1991). The degradation of the S/N ratio due to flat-field correction has not been taken into account. The average of these three S/N ratio values are listed in Table B.4 for each target star.

Such low-resolution spectra have been obtained for 158 stars out of the 205 Henize S stars. Some spectral standards K stars, M stars and non-Henize S stars were also observed.

6.6.2 Construction of band-strength indices

These low-resolution spectra allow to distinguish subclasses inside the S family. To set this classification on a quantitative basis, band-strength indices have been constructed that indicate the strength of a specific band (or line) with respect to a nearby pseudo-continuum. More precisely, the index characterizing the band/line X_λ is defined as $I_{X,\lambda} = (C_{max} - B_{min})/C_{max}$, where C_{max} is the maximum “pseudo-continuum” flux inside the wavelength interval $[\lambda_{C,i}, \lambda_{C,f}]$, and B_{min} is the minimum “band” flux inside the wavelength interval $[\lambda_{B,i}, \lambda_{B,f}]$. The adopted values of $\lambda_{B,i}$, $\lambda_{B,f}$, $\lambda_{C,i}$ and $\lambda_{C,f}$ are listed in Table 6.2. An average index I_X for a given oxide is then computed as the mean strength of all the bands listed in Table 6.2 for that oxide.

The ZrO bands used in the computation of the mean ZrO index were taken from Table 1 of Ake (1979), but only the 7 bands not too strongly contaminated by TiO bands have finally been retained. In practice, Pearson’s correlation coefficients between each ZrO index and the average TiO index were computed for all non-pure S stars. If they were larger than 0.6, the corresponding ZrO band was rejected.

6.6.3 Misclassified stars

In fact such band-strength indices allow to efficiently unmask misclassified S stars, as shown on Fig. 6.8. Indeed, as far as non-S stars are concerned, K and M giants all have $I_{ZrO} < 0.1$ as expected, as well as the M dwarfs and supergiants. Furthermore, their temperature type nicely increases with the TiO index. On the contrary, virtually all Henize S stars have $I_{ZrO} > 0.1$, as well as the three additional well-known S stars for which spectra were also obtained (HD 35155, HD 49368, GG Pup). The only exceptions are Hen 4, 22, 58, 127 and 154, which have $I_{ZrO} < 0.1$.

Hen 4 and Hen 127 (both with $I_{ZrO} = 0.08$) have definite TiO bands but barely visible (possibly uncertain) ZrO bands. In fact, Hen 58 ($I_{ZrO} = 0.09$) and

Table 6.2: Wavelengths (in Å) used in the computation of the band indices defined in Sect. 6.6.2

name	$\lambda_{B,i}$	$\lambda_{B,f}$	$\lambda_{C,i}$	$\lambda_{C,f}$
Na D	5883	5903	5800	5847
ZrO	4640	4657	4600	4625
ZrO	5718	5735	5680	5720
ZrO	5748	5757	5680	5720
ZrO	6378	6382	6310	6345
ZrO	6412	6441	6310	6345
ZrO	6505	6530	6452	6475
ZrO	6541	6560	6452	6475
TiO	5448	5454	5410	5448
TiO	5591	5600	5500	5550
TiO	5615	5620	5500	5550
TiO	5759	5767	5680	5720
TiO	5810	5820	5800	5847
TiO	5847	5869	5800	5847
TiO	6159	6180	6067	6130
TiO	6187	6198	6067	6130
TiO	6651	6674	6452	6475
TiO	6681	6706	6452	6475
TiO	6714	6735	6452	6475
TiO	7054	7069	7014	7057
TiO	7125	7144	7014	7057
LaO	7380	7390	7362	7403
LaO	7403	7410	7362	7403

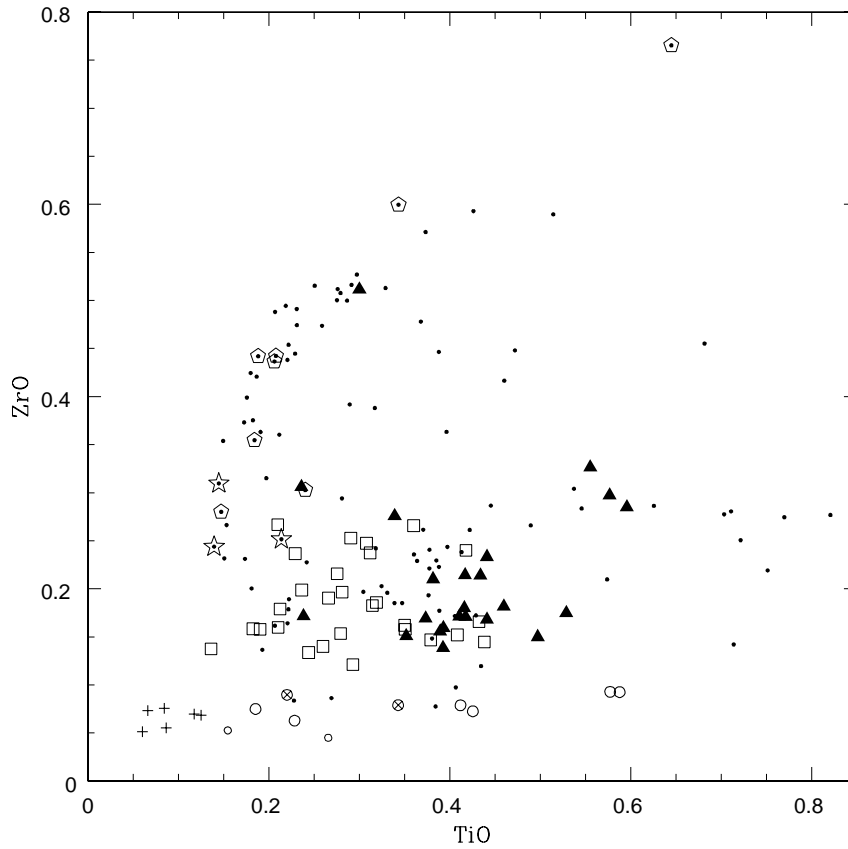


Figure 6.8: ZrO index versus TiO index, as derived from low-resolution spectra with $S/N \geq 60$. Symbols are as follows: pluses for late G or K stars, open circles for M giants, small open circles for M dwarfs, crossed circles for M supergiants, open squares for Tc-poor S stars, filled triangles for Tc-rich S stars, dots for stars with unknown Tc content, open hexagons for late S stars also belonging to the Westerlund-Olander sample, open star symbols for previously-known SC stars.

Hen 40 ($I_{ZrO} = 0.12$) somehow fall in the same category, while Hen 67, having $I_{ZrO} = 0.10$, is an S star (i.e. has well visible ZrO bands). Hence the boundary between M and S stars falls somewhere in the range $0.09 \leq I_{ZrO} \leq 0.12$, depending on temperature. The evidence for Hen 4, 40, 58 and 127 being misclassified as S stars is however too weak to justify their elimination from the final sample considered for analysis.

As far as Hen 22 and 154 are concerned, they are clearly misclassified as S stars. Besides, Hen 22 is classified as ‘S:’ by Henize. Both stars cannot be dwarfs because their NaD and MgH $\lambda 4780\text{\AA}$ features are too weak. Their prominent Ca I $\lambda 4455\text{\AA}$ line and their weak CN $\lambda 7895\text{\AA}$ band point towards them being giant stars rather than supergiants. Type Ia supergiants can certainly be ruled out because their absolute magnitudes ($M_v = -7.8$ and -7.5 for G8Ia and K3-5I respectively, Landolt & Börnstein 1982) would result in much too large heights above the galactic plane (7.5 kpc for Hen 154 and 13.2 kpc for Hen 22). Hen 154 is probably a late G giant (\sim G8), and Hen 22 a mid-K giant (\sim K3-5). These assignments are compatible with the Geneva photometry available for these two stars. In Fig. 6.8, they are the two stars with $I_{ZrO} \approx 0.05$ and $I_{TiO} < 0.1$.

Chen & Kwok (1993) mention that Hen 124 (= GCSS 447 = GCGSS 798) “is known to have been misclassified and is not an S star” without any other justification. However on the basis of our low-resolution spectra we confirm that Hen 124 is not misclassified and is indeed an S star.

To conclude with, the number of misclassified stars in the total sample is most probably very low, since out of the 158 Henize S stars with a low-resolution spectrum available, only two (Henize 22 and 154) turn out to be clearly non-S stars.

6.6.4 ZrO and TiO band strengths of S stars

The 158 spectra obtained not only allow to detect misclassified stars, but also to distinguish subclasses within the S family according to the strength of TiO, ZrO, LaO bands and sodium D lines.

The plane of ZrO and TiO indices displayed in Fig. 6.8 exhibits a complex structure. Although Tc-rich and Tc-poor S stars somehow segregate on the lower branch (i.e., in the region $I_{ZrO} \lesssim 0.3$), there is a second, curved branch extending upwards, which contains mainly SC stars and late, nearly pure or pure S stars with LaO bands.

The band strengths in S stars depend upon many parameters (temperature, C/O ratio, s-process abundances), and the interpretation of the trends observed on Fig. 6.8 in particular, and of the molecular band strengths of S stars in general, must therefore rely on detailed molecular-equilibrium calculations, as provided by e.g., Scalo & Ross (1976), Sauval (1978) and Piccirillo (1980).

In fact, Fig. 6.8 is a good illustration of the difficulty of classifying S stars solely on the basis of their ZrO and TiO band strengths. This was already recognised by Keenan & McNeil (1976) and Ake (1979), who replaced the old Keenan (1954) classification scheme (temperature and abundance classes defined by combining the ZrO and TiO band strengths) by a classification where the

TiO and ZrO indices are listed separately. Even then, additional information is needed (as provided by the Na D line index described in Sect. 6.6.5), because SC stars fall close to extrinsic S stars in Fig. 6.8. This difficulty mainly arises because as a star evolves along the AGB, its temperature is expected to decrease while its C/O ratio is expected to increase, but these two factors have opposite effects on the main band strengths.

Fig. 6.8 may actually be described in terms of a counter-clockwise loop of increasing C/O ratio. In fact, the classification scheme of Ake (1979), based on Piccirillo's results, uses the ZrO, TiO and YO band strengths to classify S stars in six classes of C/O ratios. Ake's classification implies that, when C/O evolves from 0.9 to unity, S stars describe a counter-clockwise loop in Fig. 6.8, from the right side of the lower branch ($I_{ZrO}=0.2$, $I_{TiO}=0.5$) up to the right side of the upper branch ($I_{ZrO}=0.5$, $I_{TiO}=0.3$) and down this branch to $I_{ZrO}=0.2$, $I_{TiO}=0.2$. The fact that C/O increases downward along the upper branch is confirmed by the following observations: (i) the higher regions of the upper branch are mostly populated by late and nearly pure S stars from the Westerlund-Olander survey (Westerlund & Olander 1978), a survey based on the LaO band strength. Strong LaO bands appear in cool stars with C/O ratios close to unity (Piccirillo 1980); (ii) SC stars (which are characterized by a C/O ratio almost unity) are located at the lower left end of the upper branch ($I_{TiO} \sim 0.15$, $I_{ZrO} \sim 0.25$).

Nevertheless, Piccirillo (1980) also stressed that the increase in C/O alone cannot account for the increasing strength of ZrO bands in the M-MS-S sequence for stars warmer than about 3000 K (see his Fig. 11), so that Zr enhancements no doubt have to be present as well. The molecular spectra of cool S stars reflect as well both s-process enhancements and C/O effects. In that respect, it must be noted that the five Tc-rich S stars with the greatest ZrO indices ($I_{ZrO} > 0.27$) are those having the most intense technetium lines (based on a visual inspection of the high resolution spectra of Chap. 5). The strength of the Tc line in these stars is related to a large Tc (and hence s-process) abundance rather than to a temperature effect, since the temperatures of these 5 stars with strong Tc lines span the whole range observed for Tc-rich S stars (as derived from the $V - K$ colour index and the calibration of Ridgway et al. 1980).

6.6.5 Na D index and SC stars

An index based on the strength of the sodium D line is an useful complement (Ake 1979) to the TiO and ZrO indices described in Sect. 6.6.4. In carbon stars, the Na D lines are widely used as a temperature indicator; however, in S stars, the Na D index is sensitive to both temperature and abundances (Keenan & Boeshaar 1980), because of the opacity of overlying bands of ZrO, TiO, and CN.

Fig. 6.9 illustrates the trend of the Na D index with $B - V$ color. For relatively low values (say, $I_{NaD} < 0.6$), the Na D index is known to be a good temperature indicator (Keenan & Boeshaar 1980; Ake 1979). It is therefore not surprising that Tc-rich S stars, which are cooler than Tc-poor S stars, have on average larger Na D indices.

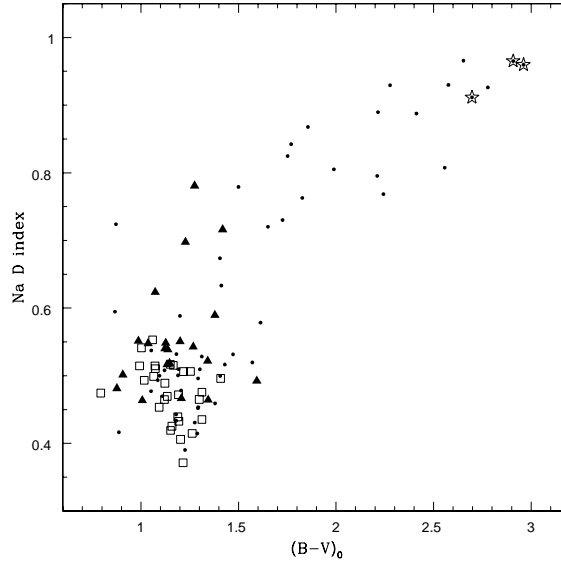


Figure 6.9: Na D line index (as derived from low-resolution spectra with $S/N \geq 60$) versus the dereddened $B - V$ colour index. Symbols are as follows: open squares for Tc-poor S stars, filled triangles for Tc-rich S stars, dots for stars with unknown Tc. The three previously known SC stars (Hen 120 = BH Cru, Hen 135 = UY Cen, Hen 157 = VY Aps) are denoted by star symbols. Note that no technetium information is available from the current work for pure S and SC stars because of the very weak flux emitted by these stars below 4500\AA , where the technetium resonance lines are located

For larger values of the Na D index (say, $I_{NaD} > 0.7$), the C/O ratio comes into play. At the top of the oblique sequence in Fig. 6.9 can be found the three SC stars of the Henize sample for which a low-resolution spectrum is available (Hen 120 = BH Cru = SC 4.5/8-e or SC 6/8-e or SC 7/8-e; Hen 135 = UY Cen = S 6/8- and Hen 157 = VY Aps; Catchpole & Feast 1971; Keenan & Boeshaar 1980); they are represented by an open star symbol in Fig. 6.9. The Henize stars populating the oblique sequence (from $I_{NaD} > 0.7$) are closely related to SC stars, since they fulfill the spectral criteria defined by Catchpole & Feast (1971): (i) extremely strong Na D lines, (ii) drop in the continuum intensity shortward of 4500\AA , and (iii) bands of ZrO and CN simultaneously present (though quite weak), as well as general resemblance of the spectrum (i.e. regarding ‘the absolute and relative strength of metal lines’) with that of UY Cen = Hen 135.

Indeed, criterion (i) is automatically satisfied, since stars in the oblique sequence have large Na D indices ($I_{NaD} > 0.7$), hence strong Na D lines. Cri-

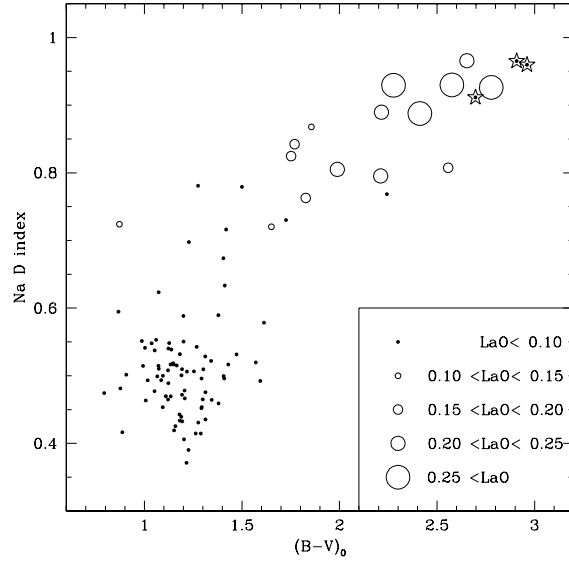


Figure 6.10: Same as Fig. 6.9, but with symbols coding the strength of the LaO bands, as defined in Sect. 6.6.2. The three previously known SC stars (Hen 120 = BH Cru, Hen 135 = UY Cen, Hen 157 = VY Aps) are denoted by star symbols

terion (ii) implies that SC stars have very red $B - V$ colour indices, since the effective wavelengths of the B and V filters are $\lambda_0(B) = 4227\text{\AA}$ and $\lambda_0(V) = 5488\text{\AA}$ (Rufener & Nicolet 1988). Therefore any flux deficiency occurring shortward of 4500\AA results in a large $B - V$ colour index, as observed. Criterion (iii) is also fulfilled since the stars in the oblique sequence in Fig. 6.9 are those populating the upper sequence in Fig. 6.8, i.e., have weak TiO bands and weak to moderate ZrO bands.

Nevertheless, the LaO bands provide an interesting additional piece of information indicating that the stars populating the oblique sequence in Fig. 6.9 cannot be considered as genuine SC stars – except for the three previously-known SC stars (marked with a star symbol) – despite the resemblances mentioned above, but that they rather are pure S stars.

The LaO bands are strong in stars with either a low effective temperature ($T_{\text{eff}} \lesssim 2500\text{ K}$) or a C/O ratio close to unity within a few percents (Piccirillo 1977; Piccirillo 1980). As seen on Fig. 6.10, the LaO band strength is very weak in the bulk of S stars with $(B - V)_0 < 1.5$, increases with $(B - V)_0$ above $(B - V)_0 = 1.5$, but is markedly weak again for the three genuine SC stars at the upper right end of the oblique sequence in Fig. 6.10. The absence of strong LaO bands in SC stars comes from the lack of free oxygen supply when C/O approaches unity. Therefore it is concluded that Hen 120, 135 and 157 are

the *only* genuine SC stars among the 158 Henize stars for which low-resolution spectra are available.

As far as stars populating the oblique sequence are concerned, all the Westerlund-Olander stars of the Henize sample have strong LaO indices (as expected since this survey used the LaO bands to detect S stars) and fall on the oblique sequence [they all have $(B - V)_0 > 2.2$ and $I_{NaD} > 0.8$]. All these stars have been classified as S/5 or S/6 and are mostly pure-S stars (Lloyd Evans & Catchpole 1989). Hence the intermediate stars located on the oblique sequence of Fig.6.10 are believed to be nearly-pure or pure S stars, and as such are intermediate between the bulk of S stars and SC stars.

6.7 Conclusion

At this point the various data collected on the S stars of the Henize sample (technetium spectra, radial-velocities, $UBVJHKL$ and IRAS photometry, low-resolution spectroscopy) have all been discussed. Several observational parameters derived from these data have been shown to be potentially able to distinguish, with various efficiencies, intrinsic S stars from their extrinsic masqueraders; the strengths and weaknesses of these various diagnostics are summarized in Table 6.3. The aim of the next chapter will be to perform a global analysis of this large data set, and to derive the respective properties of extrinsic and intrinsic S stars.

Table 6.3: Observational data, their discriminating power and their limitations

observational data	extrinsic stars	intrinsic stars	limitations	Ref.
• technetium	no	yes	only available for 70 stars (the bluest and/or brightest)	Sect. 5.4
• radial velocity	periodic variations	jitter	poor orbital coverage or unfavorably oriented orbits (pole-on) hinder the detection of extrinsic S star variability, while radial velocity jitter may mimic orbital motion for intrinsic S stars	Sect. 6.2.2
• shape of the CORAVEL <i>cc</i> -dip	deep and narrow	shallow and wide	fuzzy extrinsic/intrinsic boundary	Sect. 6.2.3
• <i>UBV</i> photometry	blue, non-variable	red, variable	blue Miras confuse the classification; lack of measurements for faint stars	Sect. 6.3.4
• IRAS	$K-[12] < -2.5$ $K-[25] < -4$	often $K-[12] > -2.5$ often $K-[25] > -4$	relatively few good-quality fluxes, especially for extrinsic stars	Sect. 6.5
• low-resolution spectroscopy	relatively weak TiO, ZrO and Na D	strong TiO or ZrO, strong Na D	fuzzy extrinsic/intrinsic boundaries; only available for 158 stars	Sect. 6.6

Chapter 7

Respective properties of extrinsic and intrinsic Henize S stars

*Being extrinsic is quite different
from being eccentric*
Habing (1996)

7.1 Multivariate classification

7.1.1 The problem

The problem in hand is to determine, among the 205 Henize S stars, which ones are the intrinsic (true TPAGB) stars, and which ones are the extrinsic (binary) stars, on the basis of the various observational parameters described in Chap. 5 and 6, and summarized in Table 6.3.

This problem is typically one of multivariate classification: N objects (the Henize sample of 205 stars) need to be classified according to m parameters (as listed in Table 6.3). The main available multivariate classification methods are thoroughly described in Murtagh & Heck (1987): principal component analysis (PCA), clustering analysis and discriminant analysis.

PCA finds new axes in the parameter space such that the spread of the projections of the individual points onto these axes is maximum (the largest spread corresponding to the first principal component, the second largest spread to the second principal component, etc). The main problem with PCA is that the first few principal components need not necessarily lie in the directions of natural group differences, and in fact group differences may often be hidden in the resultant plot. Therefore it is not an appropriate method for our purpose

of classifying stars in groups. An additional problem is that the components emerging from PCA are not always readily interpretable in physical terms. A more 'grouping-oriented' technique is discriminant analysis because it seeks a set of axes where the between-group/within-group variance is the largest. However the groups need to be defined in advance.

Cluster analysis is quite different from discriminant analysis since it actually builds up the various groups when no group assignment is available a priori (it is an *unsupervised* classification method)¹. Hence, among the plethora of multivariate data analysis techniques, cluster analysis seems the best suited to the present problem. Partitioning methods have been preferred over hierarchical methods: indeed, the former provide the best clustering for a given number of clusters, whereas the latter build up the clusters step after step, starting with every object in a different cluster, and then clustering together the most similar objects until one single cluster containing all the objects is obtained²; such hierarchical techniques can never repair what was done in the previous steps, and provide no guarantee that the best possible clustering for a given number of clusters has been obtained.

An additional complication comes from the incompleteness of our data set: not all the observational parameters are available for all the 205 stars. Such missing values prevent the blind application of any multivariate classification method. In fact, the widely recommended solution is to ignore completely objects that have *any* missing values. This option is not affordable here: it would reduce the sample size dramatically (e.g. only 70 stars out of 205 have the vital technetium data available), and would throw away an intolerably large amount of valuable information. Another alternative is to employ *imputation*, that is the insertion of an estimate for each missing value, thereby completing the data set. In the present case, such imputations could lead to seriously underestimating the variances, and blur or even erase the separation between intrinsic and extrinsic stars. A totally different method to handle stars with missing values has thus been designed, as described in Sect. 7.1.2.

7.1.2 The clustering algorithm

After a careful examination of the various available techniques, the clustering program CLARA described in Kaufman & Rousseeuw (1990) has been chosen and further adapted in order to classify *all* the stars, the *complete* stars (i.e., those stars having all the m parameters available on which clustering is performed) as well as the *uncomplete* ones (stars with some missing parameters).

The classification proceeds along the following steps:

1. The data are first normalized in order to avoid dependence on the measurement units: if x_{ij} is the j^{th} parameter of star i , \bar{x}_j the mean value

¹Cluster analysis has become known under a variety of names, such as numerical taxonomy, automatic classification, botryology, and typological analysis (Kaufman & Rousseeuw 1990)

²this is "agglomerative" clustering; for the opposite clustering direction, algorithms are named "divisive"

of the j^{th} parameter for all the stars, and σ_j its standard deviation, then the normalized value is computed as:

$$x'_{ij} = (x_{ij} - \bar{x}_j) / \sigma_j$$

2. In order to quantify the degree of dissimilarity between stars i_1 and i_2 , the Euclidian distance $d(i_1, i_2)$ is computed:

$$d(i_1, i_2) = \left[\sum_{j=1}^m (x'_{i_1j} - x'_{i_2j})^2 \right]^{1/2}$$

3. The number k of desired clusters is fixed in advance.
4. A seed sample of stars is drawn from the entire star set. In the original program CLARA, many random seed samples were successively chosen and the best resulting clustering was retained. In the present case, due to the many incomplete stars, a better strategy is to choose only one seed sample, once for all, as the sample of complete stars (Rousseeuw, priv. comm.). The CLARA program has thus been modified to this end.
5. The method then selects k stars, called *representative stars*, within the seed sample of complete stars. The k clusters are then constructed by assigning each complete star of the data set to the nearest representative star.

Of course, not every selection of k representative stars gives rise to a subsequent “good” clustering. The *optimal representative stars* will be those for which the average distance of the representative star to all the other (complete) objects of the same cluster is minimum. For a full description of the algorithm finding the optimal representative stars, we refer to Chapter 2 of Kaufman & Rousseeuw (1990).

6. The clusters are then completed by assigning each remaining uncomplete star to the nearest cluster: the distance between any uncomplete star and each cluster center of gravity (projected on the subspace where the uncomplete star is located, see Fig. 7.1) is computed; the uncomplete star is agglomerated to the cluster that minimizes this distance.

This algorithm is especially suitable here because it provides a representative star for each cluster, a very desirable feature for characterization purposes. The drawback of such an approach is that the representative stars of each cluster are chosen among complete stars only, hence they are not necessarily optimal representative of the uncomplete stars as well. The risk is thus to agglomerate some ‘exotic’ uncomplete star to some existing cluster (from which it is the closest on the basis of its available parameters), although this exotic star should in fact have been the seed of a new cluster. However, we feel this risk is rather unimportant given the purpose of the classification (distinguishing intrinsic from extrinsic S stars), because the available parameters of uncomplete

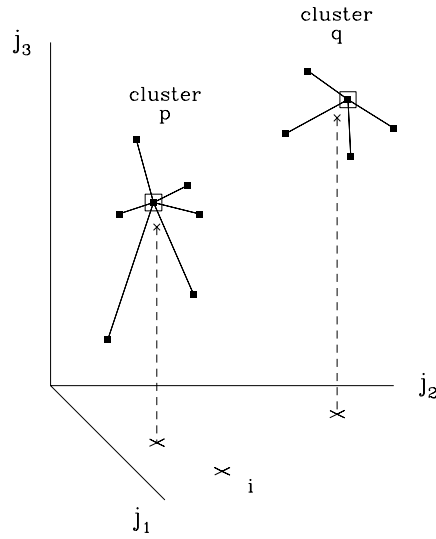


Figure 7.1: Schematic illustration of clustering (in a three-dimensional Euclidian parameter space j_1, j_2, j_3) for an uncomplete star i with parameter j_3 missing. The open squares indicate the best representative star of each cluster, the small crosses their center of gravity, and the large crosses the projection of their center of gravity on the subspace (j_1, j_2) of star i

stars often match correctly the corresponding parameters of complete stars. It might happen that some stars have outstanding photometric variations or very red colours, but these extreme stars will be automatically classified in the intrinsic groups, which is a correct assignment since such evolved stars are very unlikely to be extrinsic S stars.

Misclassifications can never be excluded by such clustering techniques. However, their major advantage over a 'handmade' classification lies in that they guarantee that the classification criteria will remain homogeneous for the 205 stars: all the available parameters will be taken into consideration in the same way from the first star to the very last.

7.1.3 Classification parameters

The number of parameters m used in the clustering is critical. It should not be too small, in order to limit the number of stars with none of the parameters available. Neither should it be too large, in order to maximize the number of complete stars and therefore to achieve a better definition of the clusters. Moreover, the classification parameters must have a real discriminating power,

otherwise they will blur the work done by the other more useful parameters.

After trials and errors, 10 parameters have been retained as giving the best possible clustering, i.e., the smallest number of obviously misclassified stars. These parameters, whose discriminating power was discussed in the previous chapters (see also Table 6.3), are: technetium, the width (Sb) and depth (PR) of the CORAVEL cc-dip, the radial velocity standard deviation $\sigma(V_r)$, the $(U - B)_0$, $(B - V)_0$, and K -[12] colour indices, and the photometric standard deviation $\sigma_{phot} = (\sigma(B)^2 + \sigma(V)^2)^{1/2}$. An “abundance index” $I = I_{ZrO} + I_{TiO} + I_{NaD}$ has also been included: as shown in Figs. 6.8 and 6.9, it remains small for Tc-poor stars, increases somewhat for Tc-rich stars because of slightly stronger TiO bands and/or ZrO bands, and reaches its highest values for pure S and SC stars, because of their strong Na D lines. The $(V - K)_0$ index has also been added in the parameter list because Tc-poor S stars often have bluer $(V - K)_0$ colours than Tc-rich S stars.

This choice results in 196 stars out of 205 having at least one parameter available, among which 33 stars have all of them available (“complete” stars). The 9 remaining stars are:

- Hen 22 and Hen 154, the two misclassified S stars (Sect. 6.6.3); they have been excluded from the cluster analysis;
- Hen 26, Hen 60, Hen 102 (=TT10) and Hen 116: no information whatsoever is available on these stars. Hen 116 [$\alpha_{1900} = 11^h 43^m .0$; $\delta_{1900} = -64^\circ 46'$ according to the unpublished list of Henize (1965)] is even missing in General Catalogue of Galactic S stars (Stephenson 1984). These stars may well be variable stars; however, without any piece of information to classify them, they have been excluded from the cluster analysis.
- Hen 33 and 176 are clearly located among intrinsic stars in the ([12]-[25],[25]-[60]) IRAS colour-colour diagram (Jorissen et al. 1993). Henize classified Hen 33 as an S5,8e star, which is more typical of intrinsic stars also. In the same vein, Hen 192 has a [12]-[25] index typical of intrinsic stars. These three stars are therefore included in the intrinsic group.

7.1.4 Clustering analysis: results

The number of clusters is also critical. Therefore clustering analyses with two and six clusters are presented and compared in the following paragraphs.

Two clusters

Since the S family is suspected to comprise two kinds of stars, clustering has first been attempted with two clusters. Their center of gravity is listed in Table 7.1, and individual assignments are provided in Table B.4. The correctness of the individual star assignments to one or the other cluster – and the possible ways to check it – will be discussed in more details in Sect. 7.1.5. At this point, it will just be mentioned that the clustering analysis with two clusters leads to only

one clearly misclassified star (Hen 152) and one puzzling case (Hen 189). Hen 152 has many characteristics of an intrinsic star, although it was classified in the extrinsic group. The reason for that misclassification lies in the two extremely discrepant radial velocity measurements [$\sigma(V_r) = 9 \text{ km s}^{-1}$], which brings the star near to the extrinsic group. In fact Hen 152 is most probably a pure S or SC star, because of its huge cc-dip width ($Sb=16 \text{ km s}^{-1}$), very red colours [$(B - V)_0 = 2.6$] and large photometric variability ($\sigma_{phot} = 0.6 \text{ mag}$).

Hen 189 is a puzzling case that has been classified in the intrinsic group by the algorithm. Indeed it is clearly different from “normal” extrinsic stars, because of its larger photometric variability. Its blue colors may tag it as either a symbiotic star or a blue Mira. However, no symbiotic-like H_α emission was observed at high resolution, but on the other hand, its deep and narrow cc-dip is not typical of Miras. Given this contradictory situation, it was kept in the intrinsic group.

Six clusters

Is it possible to further split the intrinsic and extrinsic classes into more subgroups? A classification in six clusters leads to relatively well-defined groups indeed. These groups and their center of gravity are listed in Table 7.1. However this subdivision does *not* mean that these six groups correspond to six types of physically-different stars. For example, the clustering algorithm produces two groups (#1 and #2) of extrinsic stars differing mainly in their radial-velocity standard deviations. Both groups are believed to contain binary stars, but group #2 contains more orbits closer to edge-on and/or with shorter periods and/or with a better sampling of the radial-velocity measurements, resulting in larger radial-velocity standard deviations.

The clusters are not as widely separated as in the two-clusters case. Hence more stars (4) are erroneously classified: Hen 49 and 152 are clearly misclassified as extrinsic stars, probably because of their large radial-velocity standard deviation or their unusual photometric behaviour. In fact they rather resemble pure S or SC stars. Hen 15 and 117 have been classified in the symbiotic group, though they are rather intrinsic stars; the reason here is probably the lack of data on these faint stars. These 4 stars have been re-assigned to the ‘second-best-choice’ cluster determined by the algorithm, which is in these four cases an intrinsic cluster.

All stars with less than 5 parameters available were examined individually; their classification seems to be correct.

The six-clusters classification may be compared to the two-clusters classification, by putting together groups #1, 2, and 3 in the same extrinsic (Tc-poor) category, and groups #4, 5 and 6 in the same intrinsic (Tc-rich) category. The same partitioning of the Henize sample is found than in the two-clusters case, except for 3 stars: Hen 46, 67 and 189 were previously classified in the intrinsic group and are now in the extrinsic group. These three stars are typical borderline cases (Hen 189 has been discussed above) and it is indeed very difficult to determine if they belong to the intrinsic group or to the extrinsic one

with the available data. It is however encouraging that the clustering algorithm yields identical results for the 193 remaining stars, separating in distinct groups intrinsic and extrinsic stars.

The group properties may be summarized as follows:

1. Extrinsic stars:
 - group 1: Tc-poor stars: narrow and deep cc-dip, UBV magnitudes almost constant and colors close to that of normal giants, photospheric IRAS colours, small abundance index I .
 - group 2: same as group 1, except for smaller radial-velocity standard deviations.
 - group 3: symbiotic stars, large-amplitude binaries and with extremely blue and variable photometric indices
2. Intrinsic stars:
 - group 4: “the less evolved” Tc-rich stars: the cc-dip is wider and shallower than in the (non-symbiotic) extrinsic groups, but not as distorted as in the other intrinsic groups (a typical example is Hen 97 in Fig. 6.2); the stars exhibit a moderate photometric variability and radial-velocity jitter, and redder colours than the extrinsic stars.
 - group 5: Tc-rich stars, intermediate between groups 4 and 6, with many blue Miras.
 - group 6: Tc-rich stars with strongly distorted cc-dips, strongly variable UBV photometry and large radial-velocity jitter. They present the highest values of the abundance index I and large infrared excesses.

7.1.5 Testing the validity of the cluster assignments

Technetium provides a way to check the quality of the classification presented in Sect. 7.1.4. Technetium is at the origin of the division of the S star family into extrinsic and intrinsic stars. Hence, if that division is sound, Tc-poor and Tc-rich stars should not be mixed in any given cluster. This is indeed the case. Even if technetium is one of the classification parameter, this result is not obvious, because the nine other parameters could easily blur the discriminating action of technetium, if there were no genuine underlying dichotomy in the S family.

This check appears especially valuable for the 37 incomplete stars (among 163) having nevertheless Tc data. This subsample of incomplete stars may be considered as a *test subsample*, because the clusters are defined independently of it (since they are defined from *complete* stars only, see Sect. 7.1.2). All these uncomplete stars are correctly classified, i.e., they are assigned to Tc-rich or Tc-poor clusters in agreement with their Tc content, despite the possible blurring action of the other parameters.

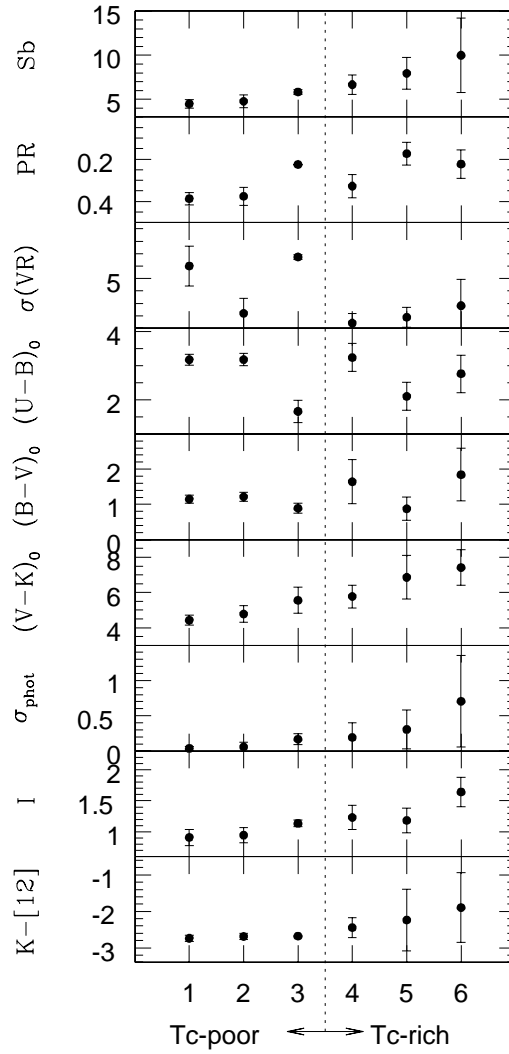


Figure 7.2: Average values and standard deviation (represented as error bars) of the 9 parameters used to derive the 6 clusters. The tenth parameter used in the clustering, technetium, is indicated at the bottom. The discrepant group #3 is the one made of the two symbiotic stars

Table 7.1: Clusters average properties. The cluster reference number is indicated in the first column, the number of stars in each cluster comes in the second column and the 10 classification parameters (see text) are listed next. The last column indicates the intrinsic or extrinsic nature of the considered cluster (based on its Tc content). In the 6-clusters classification, clusters have been ordered according to increasing Sb values. The cluster that consists of the two symbiotic S stars is also indicated

	N	Tc	Sb	PR	$\sigma(V_r)$	$(U - B)_0$	$(B - V)_0$	$(V - K)_0$	σ_{phot}	I	$K - [12]$	
• 2 clusters												
1	63	no	4.72	0.38	3.23	3.14	1.20	5.07	0.06	0.94	-2.70	ext
2	133	yes	7.96	0.27	1.98	2.89	1.65	7.07	0.42	1.42	-2.16	int
• 6 clusters												
1	15	no	4.48	0.39	6.00	3.18	1.15	4.43	0.04	0.91	-2.74	ext
2	49	no	4.77	0.38	2.20	3.18	1.22	4.78	0.06	0.95	-2.69	ext
3	2	no	5.83	0.23	6.74	1.66	0.89	5.56	0.17	1.14	-2.68	ext, symb
4	55	yes	6.66	0.33	1.41	3.24	1.64	5.78	0.19	1.23	-2.45	int
5	12	yes	7.95	0.17	1.88	2.10	0.88	6.86	0.31	1.18	-2.24	int
6	63	yes	10	0.22	2.82	2.77	1.84	7.42	0.71	1.64	-1.90	int

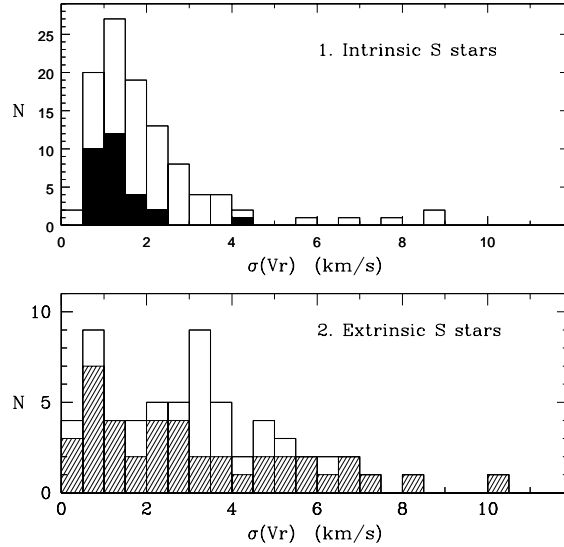


Figure 7.3: Histogram of the standard deviation $\sigma(V_r)$ of the radial velocity measurements for the S stars of the Henize sample. The intrinsic S stars (top) and extrinsic S stars (bottom) are separated according to the clustering algorithm presented in Sect. 7.1.4. Tc-rich and Tc-poor S stars are represented in black and hatched bins, respectively. The upper and lower histograms have different envelopes: the long tail of extrinsic S stars with large radial-velocity standard deviations (lower panel) reflects the binary nature of these stars

Therefore, as far as technetium is concerned, the present classification leads to no misclassification.

The classification finally retained is that with six clusters, where clusters 1, 2 and 3 are put together in the extrinsic class, and clusters 4, 5 and 6 constitute the intrinsic class. The three intrinsic stars Hen 33, 176 and 192 (with none of the classification parameters available) are incorporated in the intrinsic class (see Sect. 7.1.3). Hence the Henize sample of 205 stars comprises 66 extrinsic stars, 133 intrinsic stars, 4 unclassified stars and 2 non-S stars.

7.2 Radial-velocity variations in the Henize sample

The histograms of the radial-velocity standard deviation for intrinsic and extrinsic S stars are presented in Fig. 7.3. The intrinsic and extrinsic groups are separated according to the clustering algorithm described in Sect. 7.1.4.

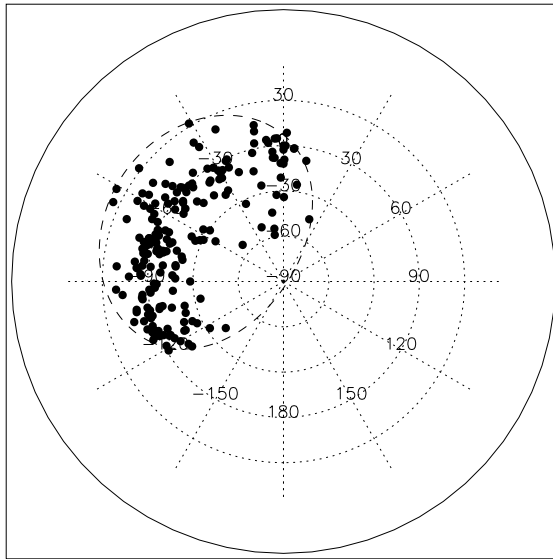


Figure 7.4: On this azimuthal projection of the Henize sample of S stars, the south galactic pole is located at the center. Concentric circles correspond to galactic latitudes -60° , -30° , 0° and 30° . The long-dashed line represents the limit $\delta = -25^\circ$, and shows that the south galactic pole has been fully surveyed

The distribution of the standard deviation of the radial-velocity measurements for intrinsic S stars is strongly peaked at $\sigma(V_r) \sim 1.5 \text{ km s}^{-1}$ and is rapidly falling off at larger $\sigma(V_r)$. It probably reflects the jitter associated with the turbulent atmosphere of pulsating AGB stars. The lack of intrinsic S stars with $\sigma(V_r) < 0.5 \text{ km s}^{-1}$ is also clearly visible.

On the contrary, the $\sigma(V_r)$ distribution for extrinsic S stars is much flatter, and this feature is, as expected, a clear signature of the large frequency of binaries among extrinsic S stars. The stars with $\sigma(V_r) < 0.5 \text{ km s}^{-1}$ are probably long-period and/or nearly pole-on binaries.

7.3 Galactic distribution

7.3.1 Extrapolation to the complete sphere

The Henize sample is limited on the sky by the simple criterion $\delta < -25^\circ$. Translating this condition into galactic coordinates reveals that the latitudes surveyed go from $b = +37^\circ$ down to the south galactic pole – a very desirable feature for estimating the galactic scale height of S stars (Fig. 7.4).

The unequal galactic longitude coverage $\Delta l(b)$ at different galactic latitudes

b in the Henize sample has been corrected by assigning a weight P_* to each star, defined as the inverse fraction of the circumference covered by the Henize sample at the star's latitude, for both hemispheres:

$$P_*(|b|) = 2 \times 360^\circ / [\Delta l(|b_*|) + \Delta l(-|b_*|)]$$

(the distribution of S stars is assumed to be symmetric with respect to the galactic equator and independent of l). In other words, $P_*(|b|)$ is the *effective number* of S stars at latitudes $|b|$ and $-|b|$, and the sum of the weights of all the stars of the Henize sample gives the total number of S stars that would have been detected if the whole galactic sphere had been surveyed (with a limiting magnitude $R = 10.5$), i.e., 632.

7.3.2 Estimates of bolometric magnitudes

Apparent bolometric magnitudes could be computed for 126 Henize S stars by integrating the spectral energy distribution derived from the Geneva U , B and V bands ($\lambda_{\text{eff}} = 3463, 4227$ and 5488 Å, respectively) and from the SAAO J , H , K and L bands ($\lambda_{\text{eff}} = 1.2, 1.6, 2.2$ and 3.4 μm , respectively). All the photometry was corrected from interstellar reddening as described in Sect. 6.3.3 and 6.4. The flux calibration for the SAAO photometry was kindly provided by Dr. I. Glass (1999, priv. comm.); for the Geneva photometry, it is taken from Rufener & Nicolet (1988). No correction has been applied for the contribution of the flux longward of 3.4 μm which is generally quite small ($< 5\%$ of the total energy distribution; Glass & Feast 1973). These apparent bolometric magnitudes are listed in the column m_{bol} in Table B.3.

Unfortunately these bolometric magnitudes are only available for the 126 stars that have measurements in all the $UBVJHKL$ bands. A second, less restrictive estimate of the bolometric magnitudes has thus been performed. For each of the six groups obtained through the clustering algorithm of Sect. 7.1.4, a bolometric correction in the V band (BC_V) has been calibrated from the stars that have a reliable apparent bolometric magnitude available from the integration of the $UBVJHKL$ fluxes (as explained above). This bolometric correction then allows to derive the bolometric magnitude of all the stars with a V magnitude available. Although that method allows to increase the sample to 170 stars (instead of 126 previously), the drawback is that the derived apparent bolometric magnitudes – and hence, the distances – are far less accurate, since the V filter catches only a small fraction of the total flux emitted by these red stars. These apparent bolometric magnitudes are listed in the column $m_{\text{bol},V}$ of Table B.3.

7.3.3 Distances

The sampling distance of the Henize sample must be estimated from its limiting magnitude $R = 10.5$, and requires the derivation of the bolometric correction to be applied to the R band (BC_R). The bolometric correction has been estimated

from data [m_{bol} and $(V - K)_0$] provided in Table 3.2 and from R magnitudes collected in the literature for the same stars: $BC_R = -0.40(V - K)_0 + 1.33$. Given the average $(V - K)_0$ colour indices of extrinsic and intrinsic S stars [$(V - K)_0 = 4.7$ and 6.5 , respectively] and the limiting magnitude of the Henize sample ($R = 10.5$), the limiting apparent bolometric magnitudes could be computed for both groups, i.e., $m_{bol,lim} = 9.9$ for extrinsic S stars and $m_{bol,lim} = 9.2$ for intrinsic S stars. Adopting reasonable absolute bolometric magnitudes of -3.1 and -4.4 for extrinsic and intrinsic S stars, respectively (Chap.3), we find that the maximum distances to which S stars have been observed in the Henize sample are 4.0 kpc for extrinsic S stars and 5.3 kpc for intrinsic S stars (in the absence of interstellar absorption).

7.3.4 Distribution on the galactic plane

The projection of Henize S stars onto the galactic plane is plotted in Fig. 7.5, along with the estimated sampling distance (Sect. 7.3.3). Although these sampling distances might appear somewhat overestimated when compared to the distance of the farthest detected star, it must be noted that Fig. 7.5 displays only those stars for which the apparent bolometric magnitude could be derived from direct integration of the $UBVJHKL$ fluxes (Sect. 7.3.3). Hence, 79 out of 205 stars have not been considered on Fig. 7.5, and those stars with missing UBV or $JHKL$ data are precisely the faintest, i.e., farthest, objects. Therefore, the maximum sampling distance displayed on Fig. 7.5 will nevertheless be considered as correct and will be used in the following.

As already mentioned in Chap. 1, there was a general consensus, before 1965, that the non-Mira S stars were spiral-arm objects or were found in OB associations, hence that they were younger than the majority of M giants (Keenan 1954; Nassau 1958; Takayanagi 1960). However, as noted by Yorka & Wing (1979), no systematic surveys for S stars at high galactic latitudes had yet been published, causing a strong bias in the available data.

The situation in that respect improved dramatically thanks to the Henize survey (Henize 1960), Wray's thesis (1966), the Westerlund survey (Westerlund 1964) and various red and near-infrared objective-prism surveys conducted at the Warner and Swasey Observatory (see Stephenson 1984). In their study of the galactic distribution of S stars using this material, Yorka & Wing (1979) found no concentration of S stars in the galactic plane as strong as that of extreme Population I objects, nor any association with the galactic arms or interstellar clouds.

The present work, based solely on the Henize sample, but distinguishing extrinsic S stars from intrinsic S stars, confirms their finding, since Fig. 7.5 shows no clear evidence for a concentration of either kind of S stars along the galactic arms.

Table 7.2: Exponential scale heights z_0 for extrinsic and intrinsic S stars derived by various methods (see text)

	m_{bol}	$N(\text{ext})$	$N(\text{int})$	$M_{bol}(\text{ext})$	$M_{bol}(\text{int})$	$z_0(\text{ext})$ (pc)	$z_0(\text{int})$ (pc)
a. \int UBVJHKL		51	75	-3.1 ± 1.0	-4.4 ± 1.0	580_{+320}^{-210}	220_{+120}^{-60} ($z \leq 1000$ pc)
b. \int UBVJHKL $V_0 < 10$		34	38	-3.1	-4.4	560	180
c. \int UBVJHKL $V_0 < 8.5$		11	10	-3.1	-4.4	810	260
d. $V_0 + BC_V$		65	105	-3.1	-4.4	520	170
Adopted						600 ± 100	200 ± 100

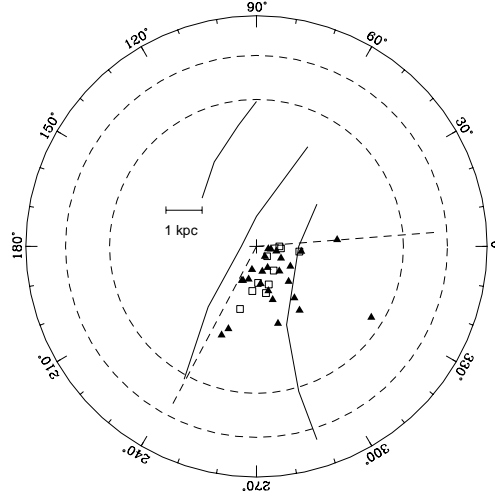


Figure 7.5: Projection of the Henize S stars on the galactic plane (the galactic center falls outside the frame towards the right; the central cross represents the position of the Sun). Only those stars with $|z| < 100$ pc have been retained. The three solid lines correspond to the galactic arms Perseus, Orion and Sagittarius from Vogt & Moffat (1975). The dashed straight lines correspond to the boundaries of the Henize sample in the galactic plane ($\delta < -25^\circ$) and the dashed circles to the sampling distances of 4.0 kpc (extrinsic S stars) and 5.3 kpc (intrinsic S stars)

7.3.5 Galactic scale heights

The density distribution of extrinsic and intrinsic S stars as a function of the height z above the galactic plane is displayed in Fig. 7.6. It has been computed from the observed star counts multiplied by the weights $P_*(|b|)$ (Sect. 7.3.1), divided by the volume $\pi \times (d_S^2 - z^2) \times dz$ sampled for a given bin $(z, z + dz)$, where d_S is the sampling distance estimated in Sect. 7.3.3.

The upper two panels of Fig. 7.6 present the density distribution for the stars whose distances could be derived from the bolometric apparent magnitudes computed from the $UBVJHKL$ fluxes (as explained in Sect. 7.3.3). The density distribution has been normalized to its value in the galactic plane so as to make it roughly independent from the estimated sampling distance (as long as $z \ll d_S$). However, the scale heights will nevertheless still depend upon the adopted absolute bolometric magnitude.

Adopting $M_{\text{bol}} = -4.4 \pm 1.0$ and $M_{\text{bol}} = -3.1 \pm 1.0$ for intrinsic and extrinsic

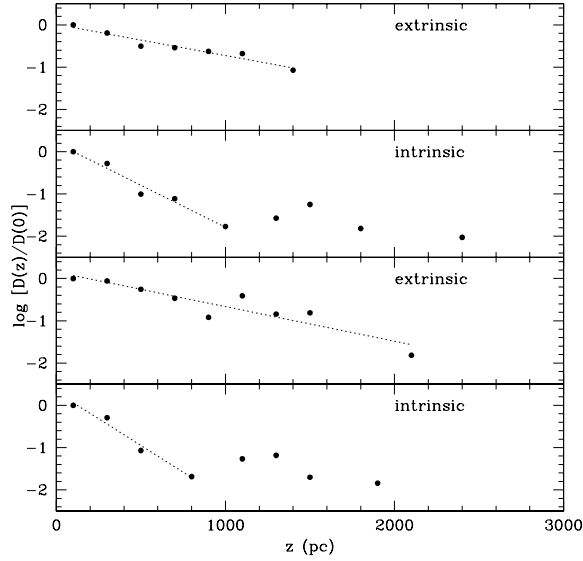


Figure 7.6: Logarithm of the density distribution perpendicular to the galactic plane for intrinsic and extrinsic S stars, normalized to the density in the plane. In the upper two panels, the distances were derived from the apparent bolometric magnitudes computed by integrating the $UBVJHKL$ fluxes. In the lower two panels, the apparent bolometric magnitudes were derived from V and a bolometric correction derived separately for each of the clusters of Table 7.1 (see text)

stars, respectively, exponential scale heights of 220_{+120}^{-60} pc and 580_{+320}^{-210} are obtained (case a of Table 7.2). Note that in the case of intrinsic S stars, points above ~ 1000 pc do not follow the exponential distribution defined from the star counts closer from the plane. They cannot be explained by invoking a contamination of the intrinsic sample by extrinsic stars, because the 6 stars responsible for these four outlying points above ~ 1000 pc are probably all intrinsic stars (2 are Tc-rich, none is Tc-poor). In fact, these outlying points probably result from the larger uncertainties altering the distances of these faint stars.

The above scale heights were derived from the subsample of 126 stars (out of 205 Henize S stars) for which the apparent bolometric magnitude could be reliably determined from the integration of the $UBVJHKL$ fluxes. In order to evaluate whether or not the scale heights derived from this particular subsample are somehow biased, scale heights derived from other subsamples are now computed.

First, the scale heights were determined for subsamples of different V_0 lim-

iting magnitudes extracted from the complete Henize sample. For example, in the Henize subsample limited to stars brighter than $V_0 = 10$ (72 stars), the bolometric magnitude is available for 85% of the stars; the derived scale heights are listed in case *b* of Table 7.2, and in case *c* if the limiting magnitude is $V_0 = 8.5$. The scale heights derived from these smaller albeit internally more complete samples still lead to a significant scale height difference between extrinsic and intrinsic S stars.

Second, the considered sample has been enlarged by deriving the apparent bolometric magnitudes from the V magnitude and the corresponding bolometric correction (as explained in Sect. 7.3.2). The corresponding density distributions are displayed in the lower two panels of Fig. 7.6, and the derived scale heights are listed in case *d* of Table 7.2. The difference between these scale heights and the previous ones is not surprising, given the much lower precision of the adopted bolometric magnitudes. However they confirm on a larger subsample that *the intrinsic S stars are much more concentrated towards the galactic plane than are the extrinsic S stars.*

Could this difference in scale height be spurious, and caused by our particular choice of the absolute bolometric magnitudes? We have stressed in Chap. 3 that the average bolometric magnitudes of intrinsic and extrinsic S stars, as derived from HIPPARCOS data, are subject to various biases which render these absolute magnitudes still somewhat uncertain. In order to force extrinsic and intrinsic S stars to have the same scale height, one has to impose a difference of nearly 4 magnitudes between their average absolute magnitudes (e.g., $M_{\text{bol,ext}} = -2$ and $M_{\text{bol,int}} = -6$, yielding an identical scale height of ~ 350 pc). Despite the remaining uncertainties on M_{bol} mentioned above, such a large difference in the bolometric magnitudes of extrinsic and intrinsic S stars is definitely incompatible with the available HIPPARCOS data (if anything, the existing biases would rather tend to decrease the observed gap between the average M_{bol} of extrinsic and intrinsic S stars; see Sect. 3.4.2 and Fig. 3.5).

Hence the difference in scale heights between extrinsic and intrinsic S stars is undoubtedly real, revealing that intrinsic and extrinsic S stars clearly belong to two different populations. Given the various estimates presented in Table 7.2 and their uncertainties, the adopted exponential scale heights are 600 ± 100 pc for extrinsic S stars and 200 ± 100 pc for intrinsic S stars. In fact, the scale height for intrinsic S stars happens to be comparable to that of planetary nebulae. Zijlstra & Pottasch (1991) derive an exponential scale height of 250 ± 50 pc. This good agreement is not unexpected since intrinsic S stars will shortly (i.e., within the duration of the TPAGB, which is short compared to the total stellar lifetime) eject their envelope and become planetary nebulae. It is also similar to the scale heights ($\sim 230 - 250$ pc) estimated for O-rich SRa, SRb and long-period ($P > 300$ d) Mira stars (Kerschbaum & Hron 1992; Jura & Kleinmann 1992a; Jura & Kleinmann 1992b). The exponential scale height of intrinsic S stars is in any case typical of disk stars, but the uncertainty on our determination precludes any detailed identification of the progenitors of intrinsic S stars with either massive or low-mass main sequence stars. The exponential scale height

of intrinsic S stars quoted in Table 7.2 (200 ± 100 pc) in fact encompasses values typical of both the young and old disks (see Fig. 5 of Gilmore & Reid 1983).

As far as extrinsic S stars are concerned, their exponential scale height of 600 ± 100 pc is smaller than the values usually quoted for the extended/thick disk (about 1400 pc; see the discussion of Reid & Majewski 1993). Nevertheless, it is similar to the scale height of short-period ($P < 300$ d) Miras (Jura 1994; Kerschbaum & Hron 1992), although that group may be a mixture of thin-disk and extended-disk stars having different metallicities and scale heights (Norris & Green 1989; Hron 1993). According to Norris & Green (1989, their Table 8), an exponential scale height of 600 ± 100 pc is typical of giants with metallicities in the range $[\text{Fe}/\text{H}] = -0.5$ to -0.4 .

7.4 The relative frequency of extrinsic/intrinsic S stars

7.4.1 Magnitude-limited sample

In the magnitude-limited Henize sample of 205 S stars, the separation of extrinsic and intrinsic S stars on the basis of the clustering algorithm described in Sect. 7.1 leads to 66 extrinsic S stars, 133 intrinsic S stars, 2 misclassified S stars, and 4 stars with no information at all (Hen 26, 60, 102, 116).

When correction is made for the unequal galactic longitude coverage at different galactic latitudes (see Sect. 7.3.1), the percentages of extrinsic and intrinsic S stars are $66 \pm 5\%$ and $34 \pm 5\%$, respectively, given the 4 unclassified stars and the estimated uncertainties on the clustering technique.

7.4.2 Volume-limited sample

Estimate 1: in the entire Henize sample

The relative frequency of extrinsic and intrinsic S stars in a volume-limited sample is subject to far more uncertainties, because it depends directly upon the estimated sampling distance. As noted above, the Henize sample comprises extrinsic S stars up to ~ 4.0 kpc and intrinsic S stars up to ~ 5.3 kpc. The respective surface densities of intrinsic/extrinsic S stars projected onto the plane then correspond to the total number of S stars of a given kind (extrapolated to all longitudes; Sect. 7.3.1) divided by the area sampled in the plane (since the scale height is much smaller than the sampling distance). The relative surface densities are then 47% for extrinsic S stars and 53% for intrinsic S stars. Large uncertainties affect these frequencies; in fact, by pushing all the uncertainties to their worst limits, the percentage of extrinsic stars can lie anywhere between 20 and 90% !

Estimate 2: in the solar neighbourhood

The relative star density in the solar neighbourhood, as derived from the normalization used in Fig. 7.6, is $D(0)_{int}/D(0)_{ext} = 1.9$, which leads to 35% of extrinsic stars and 65% of intrinsic stars. The higher fraction of intrinsic S stars with respect to extrinsic S stars is compatible with their greater concentration in the galactic plane, as derived in Sect. 7.3.5. Note that, unlike the scale heights derived in Sect. 7.3.5, the ratio $D(0)_{int}/D(0)_{ext}$ is directly affected by possible errors on the sampling distances.

Estimate 3: in a 1.5 kpc sphere

A frequency estimate independent of the sampling distance – subject to large uncertainties – may be obtained by considering the respective numbers of extrinsic and intrinsic S stars in a sphere of radius 1 kpc. Such a sphere is small enough to ensure completeness for both the extrinsic and intrinsic samples, and large enough with respect to the exponential scale heights to include most stars of both classes.

When using the apparent bolometric magnitudes derived from the V magnitude (as in case d of Table 7.2), the frequency of intrinsic S stars is estimated to be 69%.

7.4.3 The Henize survey as compared to other surveys

Fig. 7.7 compares the V magnitude and galactic-latitude distributions of several samples of S stars, as listed in Stephenson (1984). The Henize survey, as listed in Stephenson (1984), may in fact be the only homogeneous magnitude-limited survey that extends from the galactic plane up to high galactic latitudes. Nevertheless, other surveys subsequently detected additional S stars south of $\delta = -25^\circ$ and with V magnitudes in the same range as that of Henize. The most severe worry about the completeness of the Henize survey comes from the galactic plane survey of MacConnell (1979), with 189 stars south of $\delta = -25^\circ$ not belonging to the Henize sample. These stars missed by Henize can certainly not be all explained by a large photometric variability or by very small ($V - R$) colour indices that would push the R magnitudes of MacConnell's stars below Henize's detection threshold ($R = 10.5$). MacConnell notes that "better plate scale and slightly higher dispersion, larger aperture and excellent optics of the Curtis Schmidt telescope, improved emulsions and variability of some stars are all contributing factors. These will permit one to note stars having weaker ZrO enhancement that would otherwise be the case" (MacConnell 1979). The better plate scale is probably the leading factor that enabled MacConnell to recognise S spectra in crowded regions of the galactic plane.

Fig. 7.8 shows a comparison of the Henize and MacConnell samples in the region covered by both surveys ($\delta < -25^\circ$ and $|b| < 15^\circ$). The histograms display the eye estimates of the strength of ZrO and TiO bands (as found on K. Henize's unpublished notes, kindly communicated by V. Henize). This comparison is meaningful because Henize and MacConnell used similar plates and used

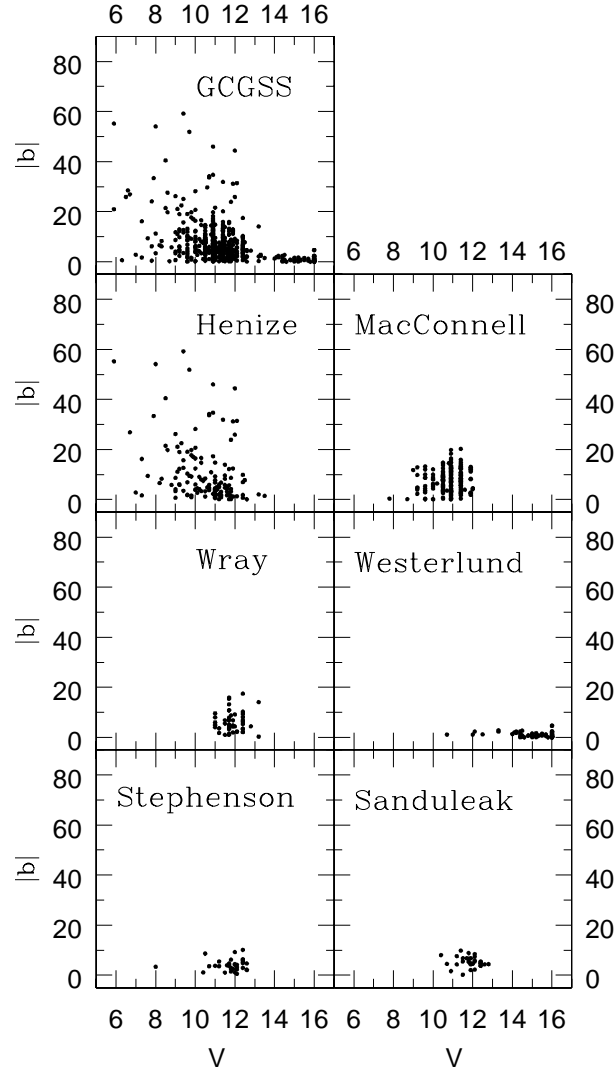


Figure 7.7: The galactic latitude distribution for S stars from various surveys, as a function of their V magnitude, as listed in Stephenson (1984). Only the stars south of $\delta = -25^\circ$ and with a V magnitude available in Stephenson (1984) have been plotted. For the MacConnell, Wray, Westerlund, Stephenson and Sanduleak surveys [see Stephenson (1984) for detailed references on these surveys], only stars not belonging to the Henize survey are plotted

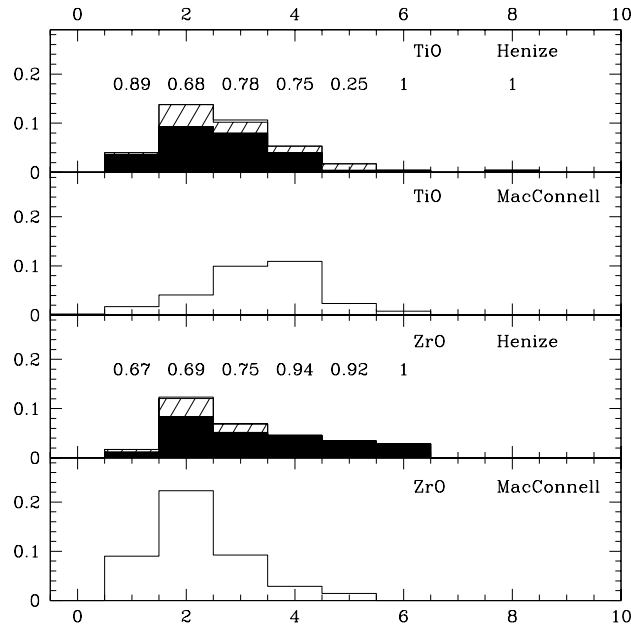


Figure 7.8: Comparison of the TiO and ZrO band-strength indices for S stars from the Henize and MacConnell (1979) surveys. Since Henize surveyed all declinations $\delta < -25^\circ$, and MacConnell virtually all galactic latitudes $|b| < 15^\circ$, only the stars matching both criteria have been plotted. Henize stars are assigned to the extrinsic (hatched) or intrinsic (black) groups according to the classification established in Sect. 7.1.4

quite the same ZrO and TiO bands, though there might be a small horizontal shift between the scale of MacConnell and that of Henize (there are no common stars with TiO and ZrO indices available in the two surveys, that would allow to fix a reference point). Most of the stars missed by Henize have high TiO indices and small ZrO indices. On the top of each bin in Fig. 7.8, the ratio intrinsic/total is indicated for the Henize stars. Assuming that the same fractions apply to the corresponding MacConnell bins, MacConnell's sample may be split into its extrinsic and intrinsic components. These numbers have then been added to the corresponding numbers of extrinsic and intrinsic Henize stars, in order to yield the extrinsic/intrinsic frequency in the total (Henize + MacConnell) sample. If the above method is applied on the TiO histograms, the extrinsic/intrinsic frequency remains unchanged. This can be understood from the fact that the bins contributing mostly in MacConnell's sample contain similar proportions of extrinsic/intrinsic stars. When considering the ZrO histograms, the extrinsic frequency is increased by a few percents in the (Henize + MacConnell) sample.

This results from the fact that MacConnell's sample contains mainly weak ZrO stars which tend to have a higher extrinsic frequency.

In any case these changes turn out to be much less important than the uncertainties from various other sources (see Sect. 7.4.2) affecting the frequencies derived for the sole Henize sample.

The Wray survey (Wray 1966), based on deeper plates, represents another important source of S stars not retained by Henize, although they were available to him (Wray, priv. comm.). However, including these objects found on such deeper plates covering only the galactic plane would clearly have biased the low galactic latitudes (where most intrinsic stars are found) towards fainter magnitudes.

7.5 Conclusions

Given the large number of observational parameters collected on the Henize sample of S stars, multivariate classification seemed the best suited to perform a homogeneous classification. The clustering algorithm used in this chapter indeed leads to well-defined stellar groups and is very efficient in separating extrinsic from intrinsic S stars, even for the "uncomplete" stars (i.e., that have missing parameters).

The binarity of extrinsic S stars is clearly apparent from their radial-velocity standard deviation distribution, whereas intrinsic S stars are mostly single evolved stars with pulsating envelopes.

Neither the extrinsic nor the intrinsic S stars of the Henize sample exhibit any clear concentration along the galactic arms, a conclusion already reached by Yorke & Wing (1979); however these authors did not distinguish extrinsic from intrinsic stars.

Despite uncertainties concerning the absolute magnitudes of S stars and the sampling distances, intrinsic S stars have been shown to be much more concentrated towards the galactic plane than extrinsic S stars. Trying to reconcile their galactic scale height leads to a clearly implausible luminosity difference. The retained exponential scale heights are 200 ± 100 pc and 600 ± 100 pc for intrinsic and extrinsic S stars, respectively. The frequency of extrinsic stars among S stars probably lies around 50%, but values as low as 30% and as high as 70% cannot be excluded giving the large remaining uncertainties.

Summary and conclusions

This brief chapter lists the major results, implications and afterthoughts based upon the present study of barium and S stars.

In the first part of this work, specific properties of red giant stars have been investigated thanks to original data sets: the binarity of barium and S stars, and the luminosities of S stars.

The set of orbital elements available for chemically-peculiar red giant stars has been considerably enlarged thanks to a decade-long CORAVEL radial-velocity monitoring of about 70 barium stars and 50 S stars. When account is made for the detection biases, the observed binary frequency among strong barium stars, mild barium stars and Tc-poor S stars is compatible with the hypothesis that they are all members of binary systems. The similarity between the orbital-period, eccentricity and mass-function distributions of Tc-poor S stars and barium stars confirms that Tc-poor S stars are the cooler analogs of barium stars.

A comparative analysis of the orbital elements of the various families of peculiar red giant stars, and of a sample of chemically-normal, binary giants in open clusters, revealed several interesting features. The eccentricity – period diagram of peculiar red giant stars clearly bears the signature of dissipative processes associated with mass transfer, since the maximum eccentricity observed at a given orbital period is much smaller than in the comparison sample of normal giants. The mass function distribution is compatible with the unseen companion being a white dwarf, which lends further support to the binary scenario. Assuming that the white dwarf companion has a mass in the range $0.60 \pm 0.04 M_{\odot}$, the masses of mild and strong barium stars amount to 1.9 ± 0.2 and $1.5 \pm 0.2 M_{\odot}$, respectively. Mild barium stars are not restricted to long-period systems, contrarily to what is expected if the smaller accretion efficiency in wider systems were the dominant factor controlling the pollution level of the extrinsic star. These results suggest that the difference between mild and strong barium stars is mainly one of galactic population rather than of orbital separation, in agreement with their respective kinematical properties.

There are indications that metallicity may be the parameter blurring the period–chemical anomaly relationship. Extrinsic stars thus seem to be produced more efficiently in low-metallicity populations. Conversely, normal giants in barium-like binary systems may exist in more metal-rich populations.

HIPPARCOS trigonometrical parallaxes made it possible to compare the location of Tc-rich and Tc-poor S stars in the Hertzsprung-Russell diagram: Tc-rich S stars were found to be cooler and intrinsically brighter than Tc-poor S stars. The impact of the statistical biases affecting HIPPARCOS parallaxes has been evaluated; these biases certainly do not endanger the luminosity segregation between intrinsic and extrinsic stars; however they prevent from giving accurate average magnitudes for both kinds of S stars.

The comparison with the Geneva evolutionary tracks reveals that the onset of thermal pulses on the asymptotic giant branch matches well the observed limit between Tc-poor and Tc-rich S stars. Tc-rich S stars are, as expected, identified with thermally-pulsing AGB stars of low and intermediate masses, whereas Tc-poor S stars comprise mostly low-mass stars located either on the red giant branch or on the early AGB. Their location in the HR diagram is consistent with the average mass of $1.6 \pm 0.2 M_{\odot}$ derived from their orbital mass-function distribution.

A comparison with the S stars identified in the Magellanic Clouds and in the Fornax dwarf elliptical galaxy reveals that they have luminosities similar to the galactic Tc-rich S stars. However, most of the surveys of S stars in the external systems did not reach the lower luminosities at which galactic Tc-poor S stars are found. The deep Westerlund survey of carbon stars in the SMC uncovered a family of faint carbon stars that may be the analogs of the low-luminosity, galactic Tc-poor S stars. Hence, dwarf carbon stars will certainly repay dedicated surveys. However, reliable luminosity diagnostics ought first to be determined.

Since extrinsic and intrinsic S stars supposedly form two distinct classes of stars, with completely different evolutionary histories, it may be expected that they differ in many of their physical properties. However, extrinsic and intrinsic S stars had never been separated in a large and well-defined sample. The second part of this work has aimed at filling this gap, by studying, thanks to a large-scale observing program, the Henize sample of 205 S stars covering all galactic latitudes.

First, this sample has been cleaned from a few misclassified non-S stars thanks to *UBV* Geneva photometry and low-resolution spectra. These low-resolution spectra were also successfully used to distinguish subclasses within the S family. In the future, appropriate model atmosphere calculations will allow to interpret these subclasses in terms of different temperatures, C/O ratios and s-process enhancements.

Dedicated Geneva photometry and high-resolution spectra allowed to uncover two new symbiotic S stars. Why only these two stars exhibit a symbiotic activity is still unclear, given the strong resemblance between extrinsic S stars and symbiotic stars in terms of (i) orbital elements of the binary systems and (ii) evolutionary status of their components.

The more stringent difference between extrinsic and intrinsic stars is their Tc content. The technetium-rich or -poor nature of 72 S stars was determined, and

indeed highlighted a clear dichotomy, with only one “intermediate” star (showing weak technetium lines). This dichotomy should be further investigated with abundance determinations thanks to model atmospheres, in order to achieve a better characterization of stars at the onset of the third dredge-up episodes on the thermally-pulsing AGB.

Apart from technetium, several other observational parameters were shown to be efficient in segregating intrinsic S stars from their extrinsic masqueraders (*UBV*, *JHKL* and IRAS photometry, radial-velocity standard deviation, shape of the CORAVEL cross-correlation dip, combination of band strength indices derived from low-resolution spectra). Multivariate classification has been performed on the Henize data sample in order to guarantee a classification as objective as possible and handling at the same time a large number of parameters.

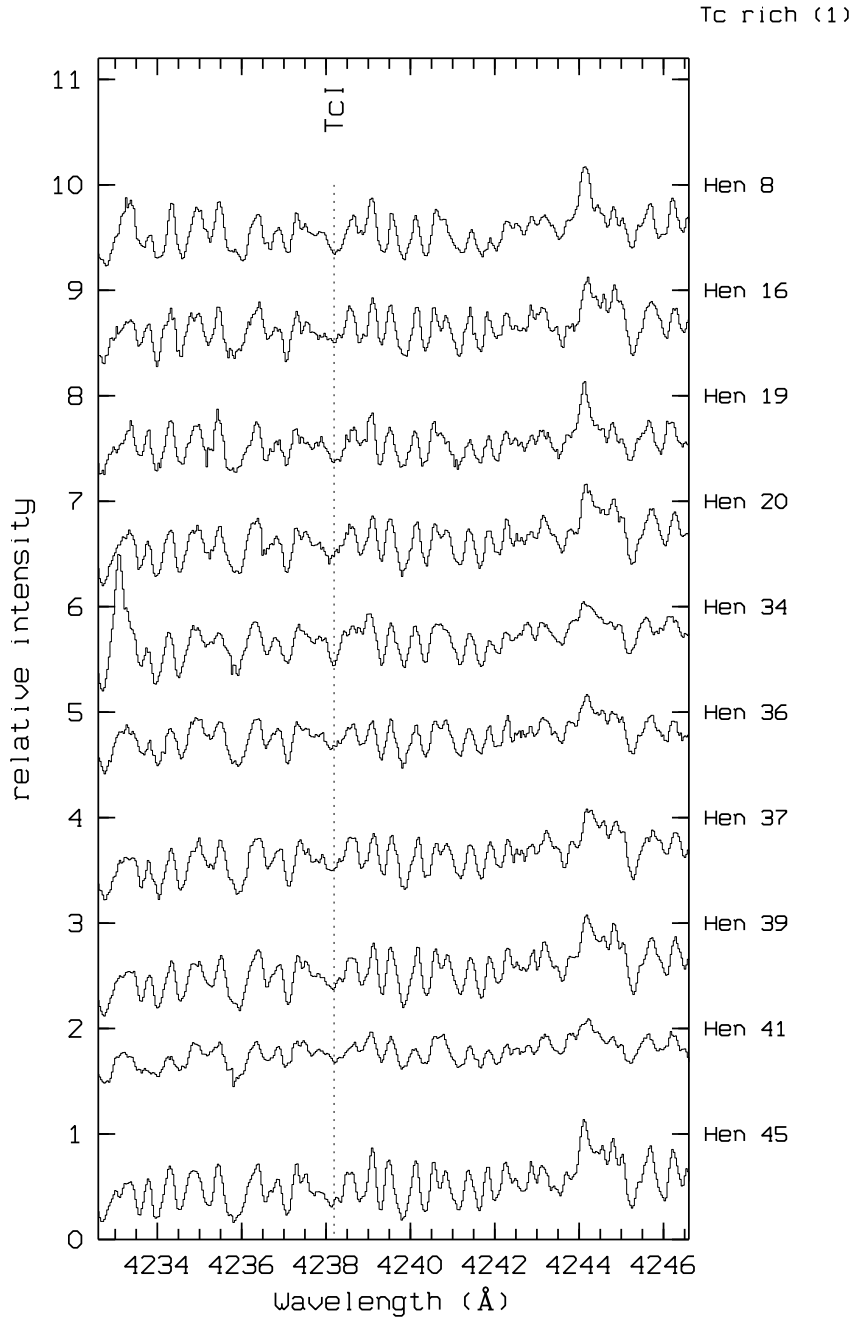
The resulting clustering separates efficiently extrinsic and intrinsic S stars, allowing to derive the respective properties of these two distinct stellar classes. The population difference between intrinsic and extrinsic S stars is for the first time demonstrated, since intrinsic S stars are clearly more concentrated towards the galactic plane than extrinsic S stars ($z_{int} = 200 \pm 100$ pc and $z_{ext} = 600 \pm 100$ pc), and are therefore believed to belong to a younger, more massive population. The respective proportions of extrinsic and intrinsic S stars are subject to large uncertainties mainly because of uncertain luminosities. There may be as many as 50% extrinsic stars among S stars in a volume-limited sample. Much more accurate estimates will soon be possible by looking at extrinsic S stars in external systems with ESO Very Large Telescopes.

Appendix A

Library of technetium spectra

The technetium spectra used in Chap. 5 are presented in this Appendix. Fig. A.1 to A.20 concern S stars from the Henize sample, as well as some additional S stars, M stars and the two symbiotic stars SY Mus and RW Hya. The stars plotted in Fig. A.1 to A.8 are technetium-poor, the ones in Fig. A.9 to A.20 are technetium-rich, while the SC stars of Fig. A.21 and A.22 have not been assigned to either group because of their very peculiar and variable spectra (see Sect. 5.3.2).

All spectra are plotted on the same relative intensity scale. The local pseudo-continuum point has been taken as an average of the fluxes at 4239.1, 4244.1, 4247.1 and 4265.4Å; for the sake of clarity, each spectrum (except the lowest one) is vertically shifted by 1 unit with respect to the spectrum below it. The left page displays the spectral region around the Tc I 4238.191Å line, and the right page the spectral region around the Tc I 4262.270Å line for the corresponding star.

Figure A.1: Tc-rich spectra at 4238.191 \AA

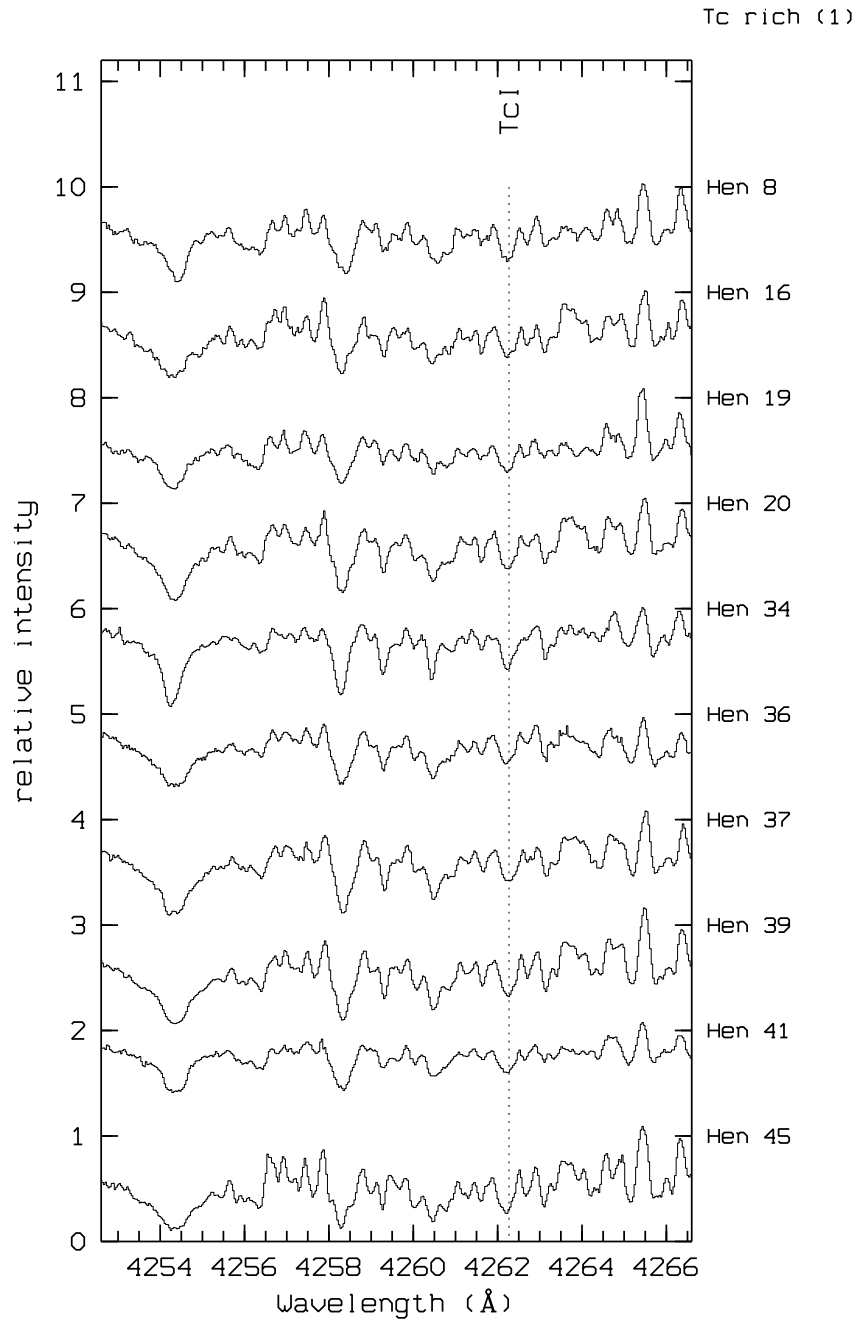
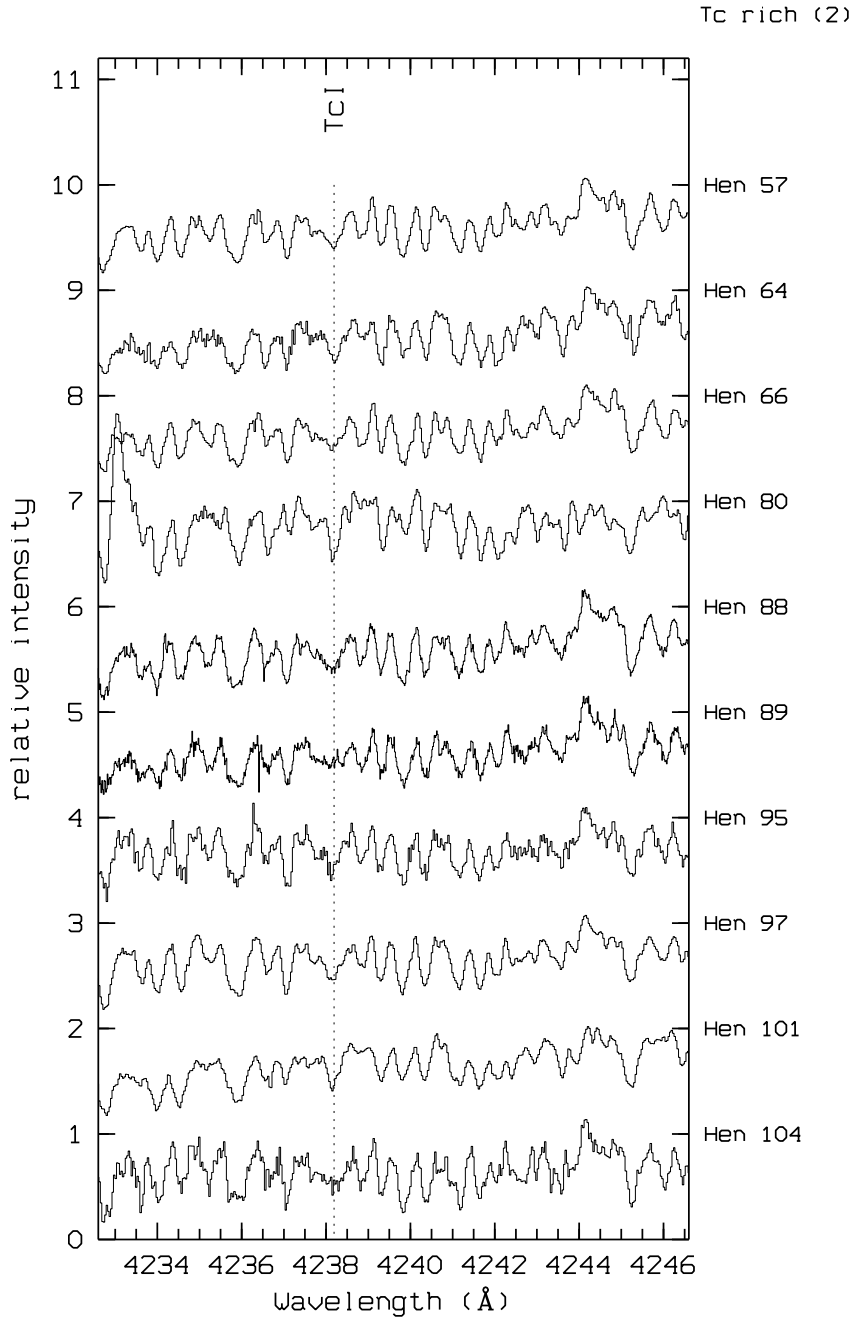


Figure A.2: Tc-rich spectra at 4262.270 Å

Figure A.3: Tc-rich spectra at 4238.191 \AA

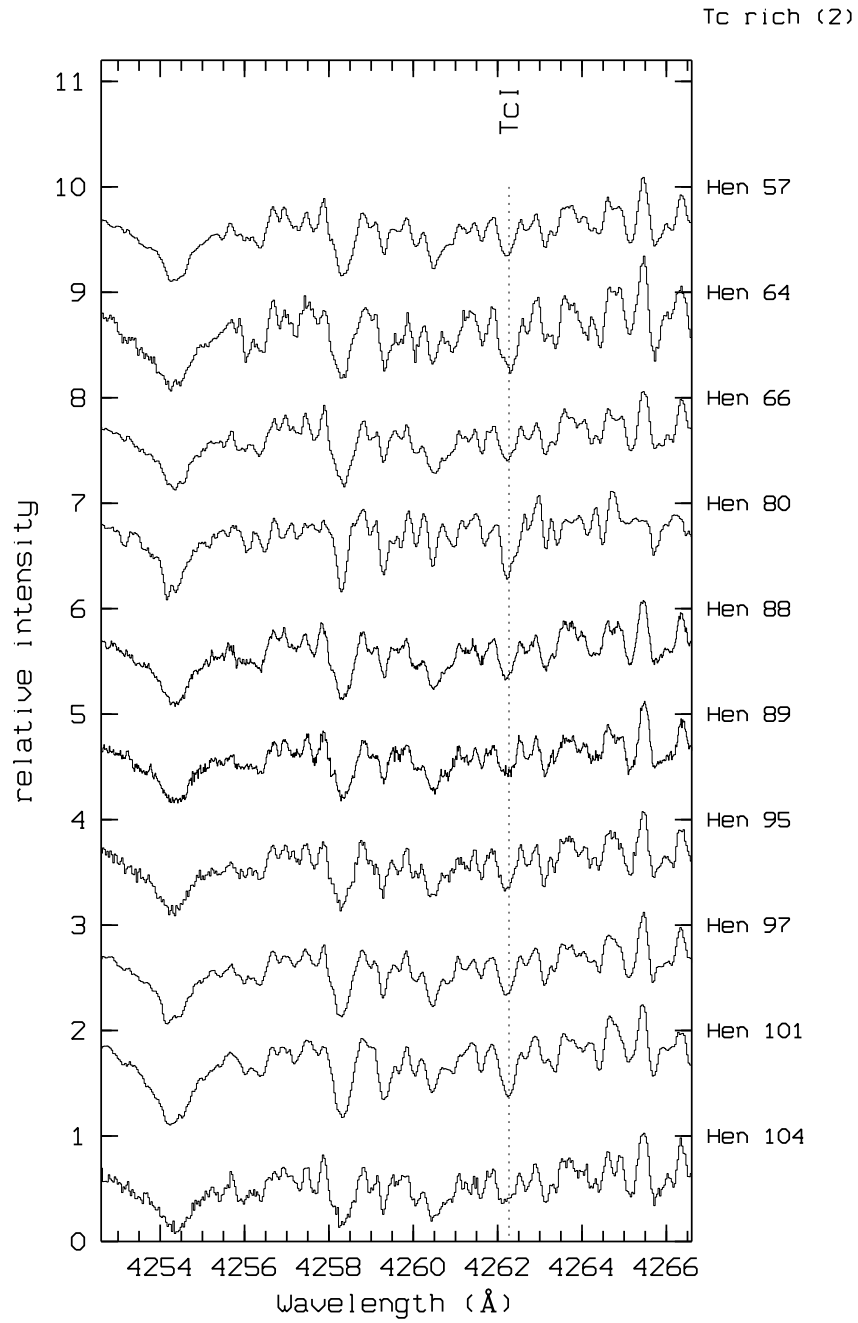


Figure A.4: Tc-rich spectra at 4262.270 Å

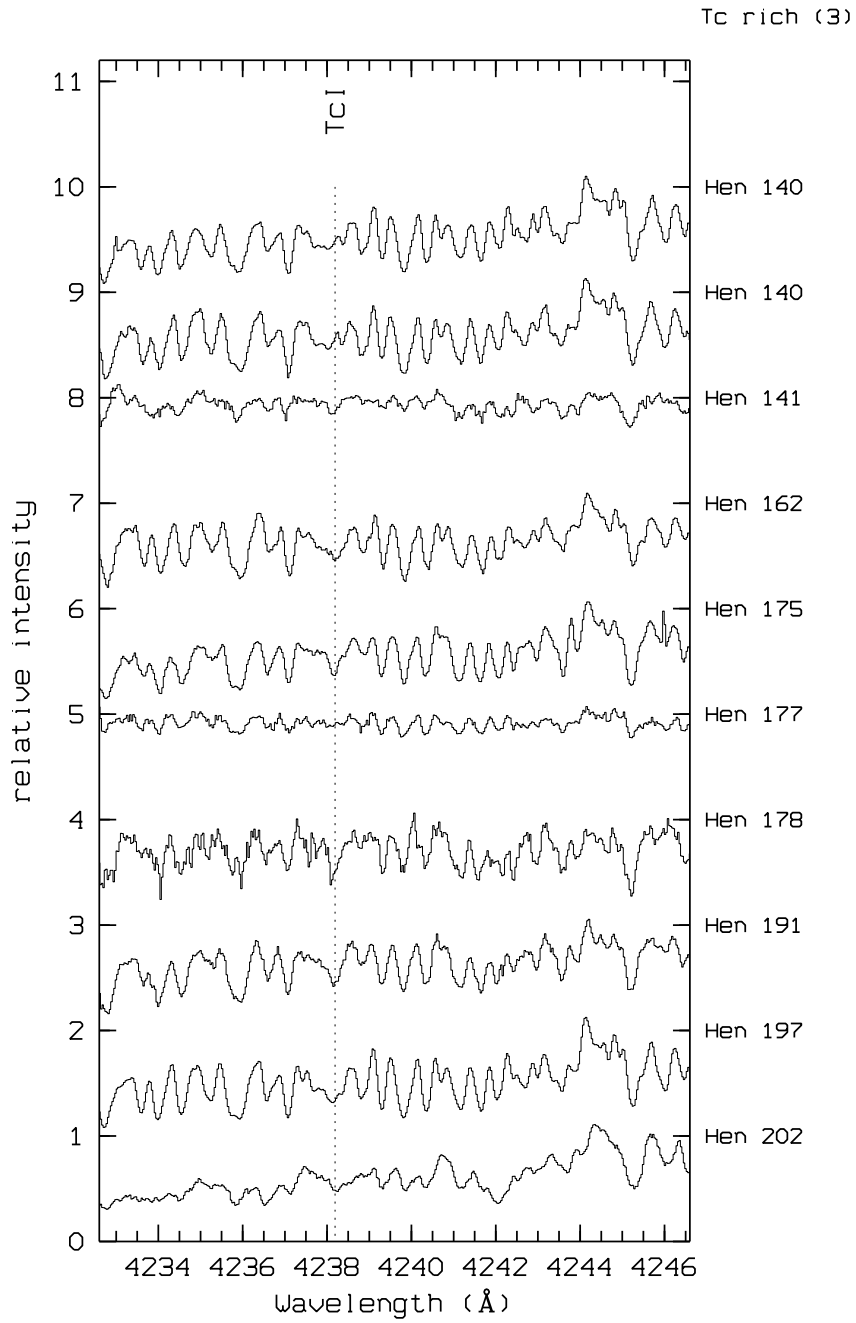


Figure A.5: Tc-rich spectra at 4238.191 Å

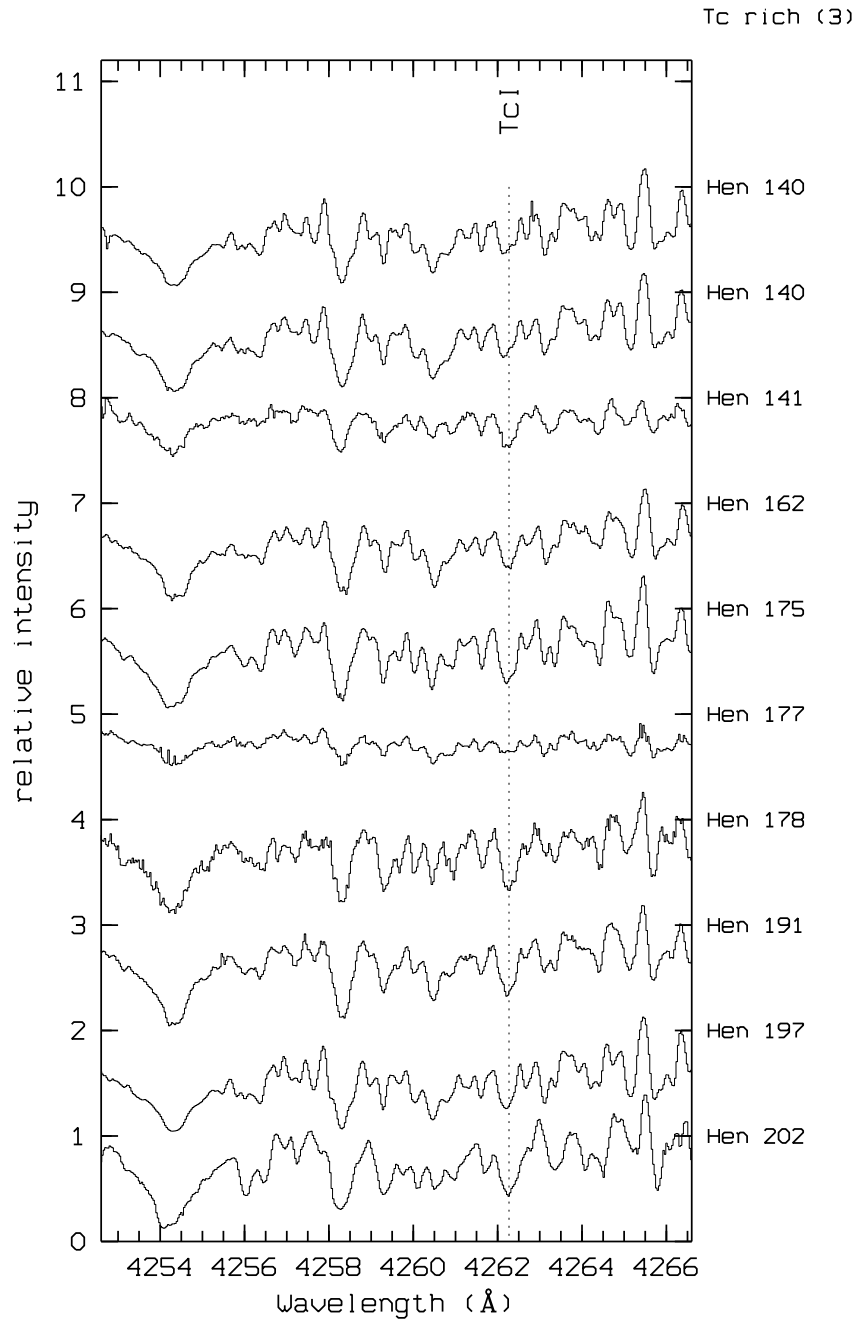
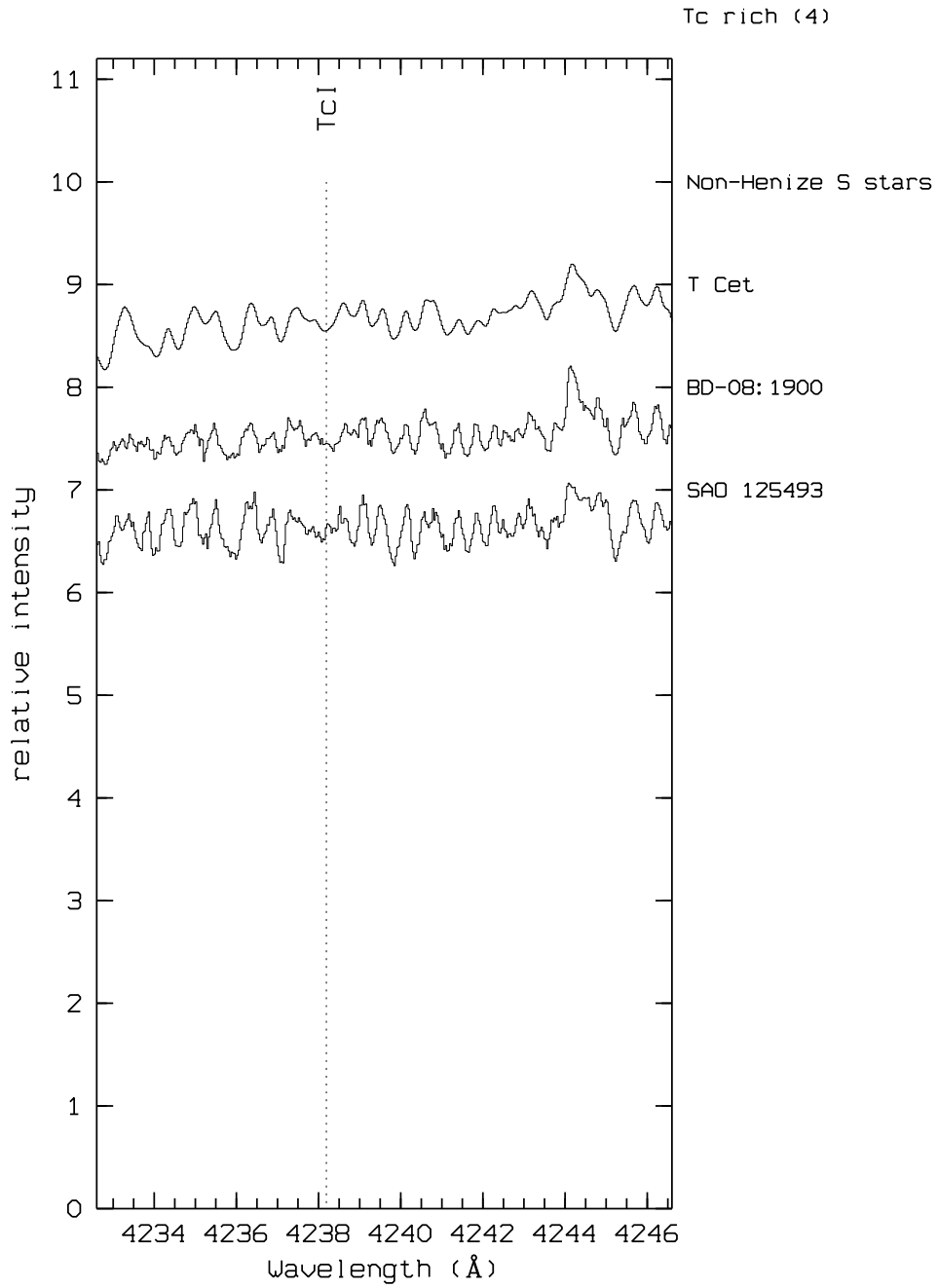
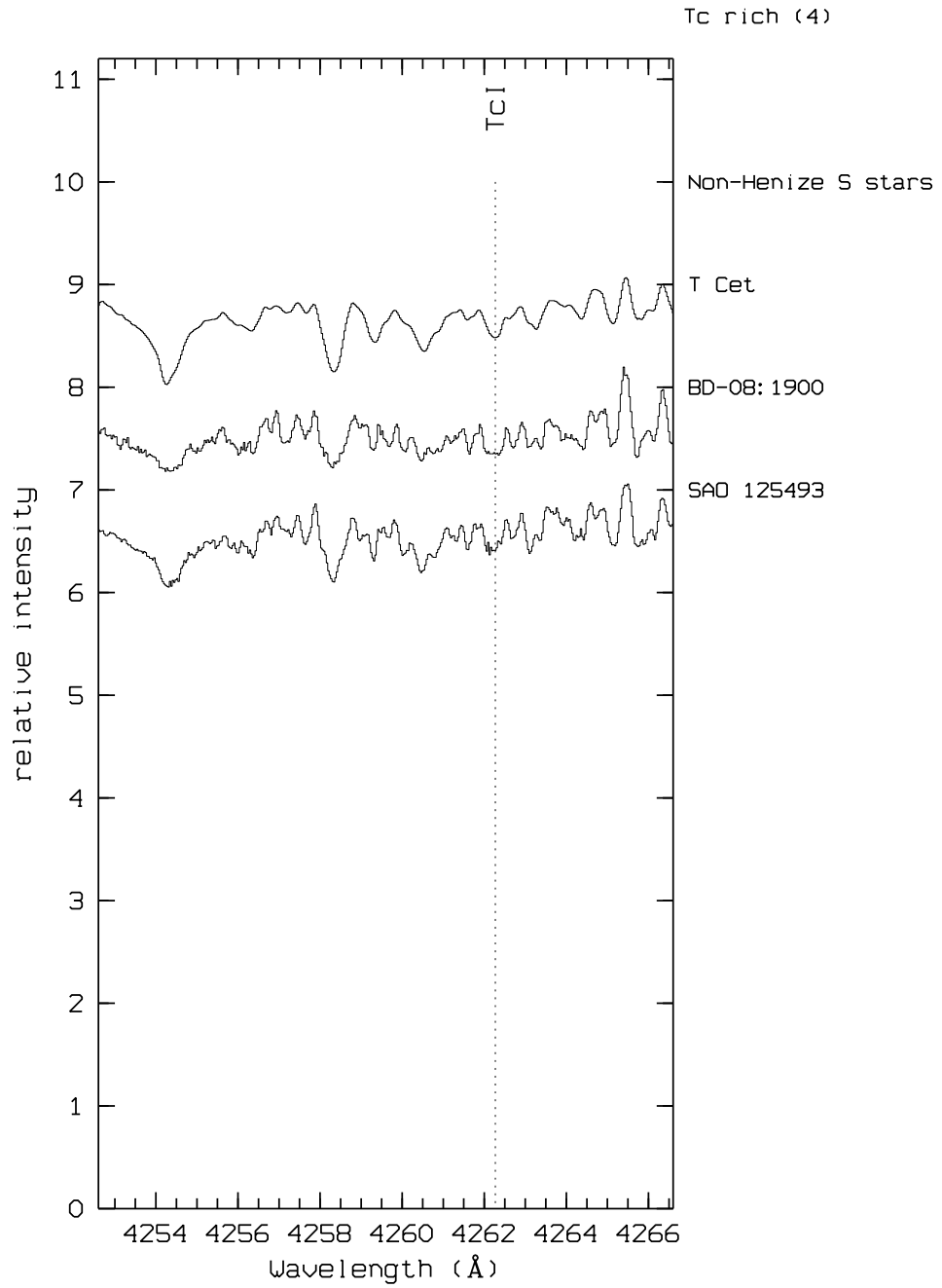


Figure A.6: Tc-rich spectra at 4262.270 Å

Figure A.7: Tc-rich spectra at 4238.191 \AA

Figure A.8: Tc-rich spectra at 4262.270 \AA

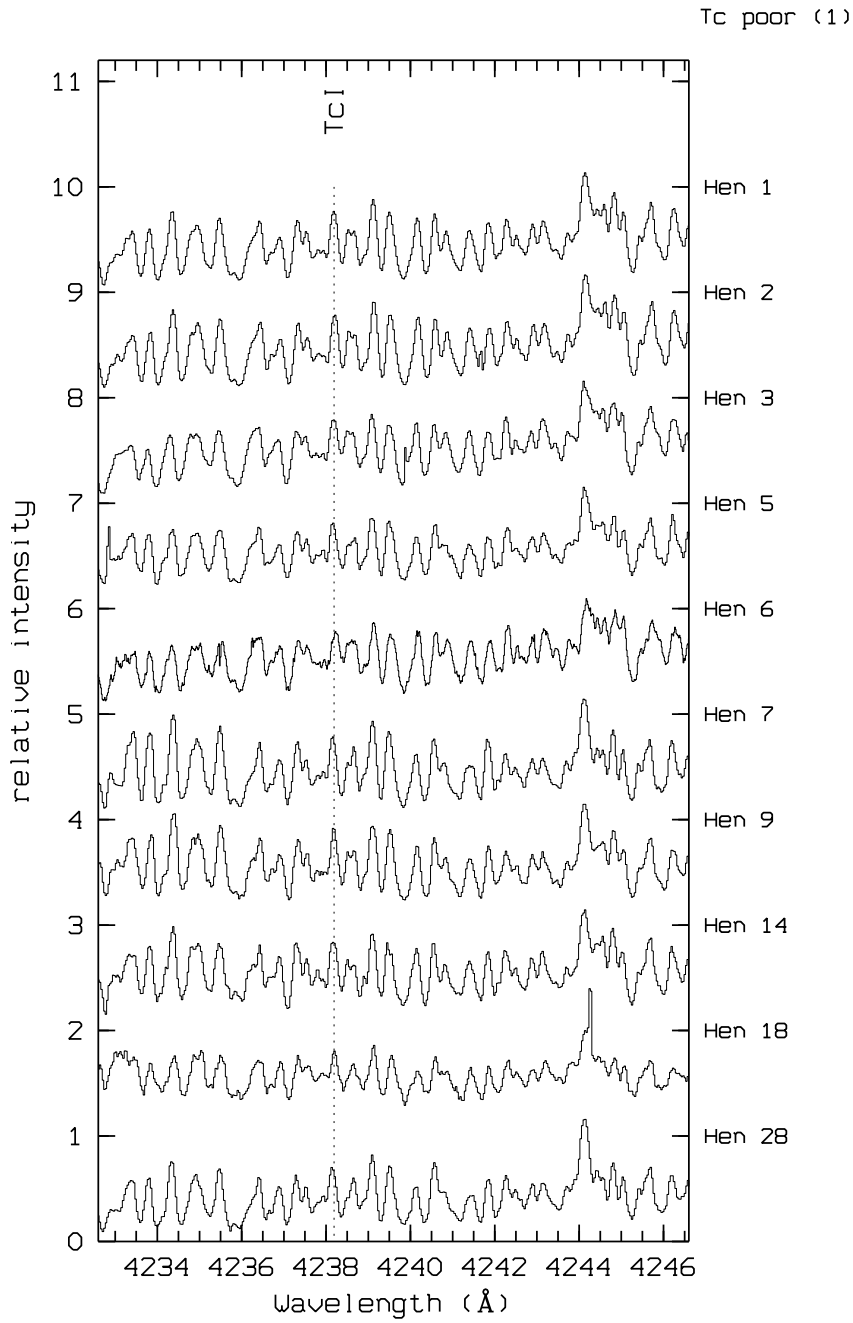


Figure A.9: Tc-poor spectra at 4238.191 Å

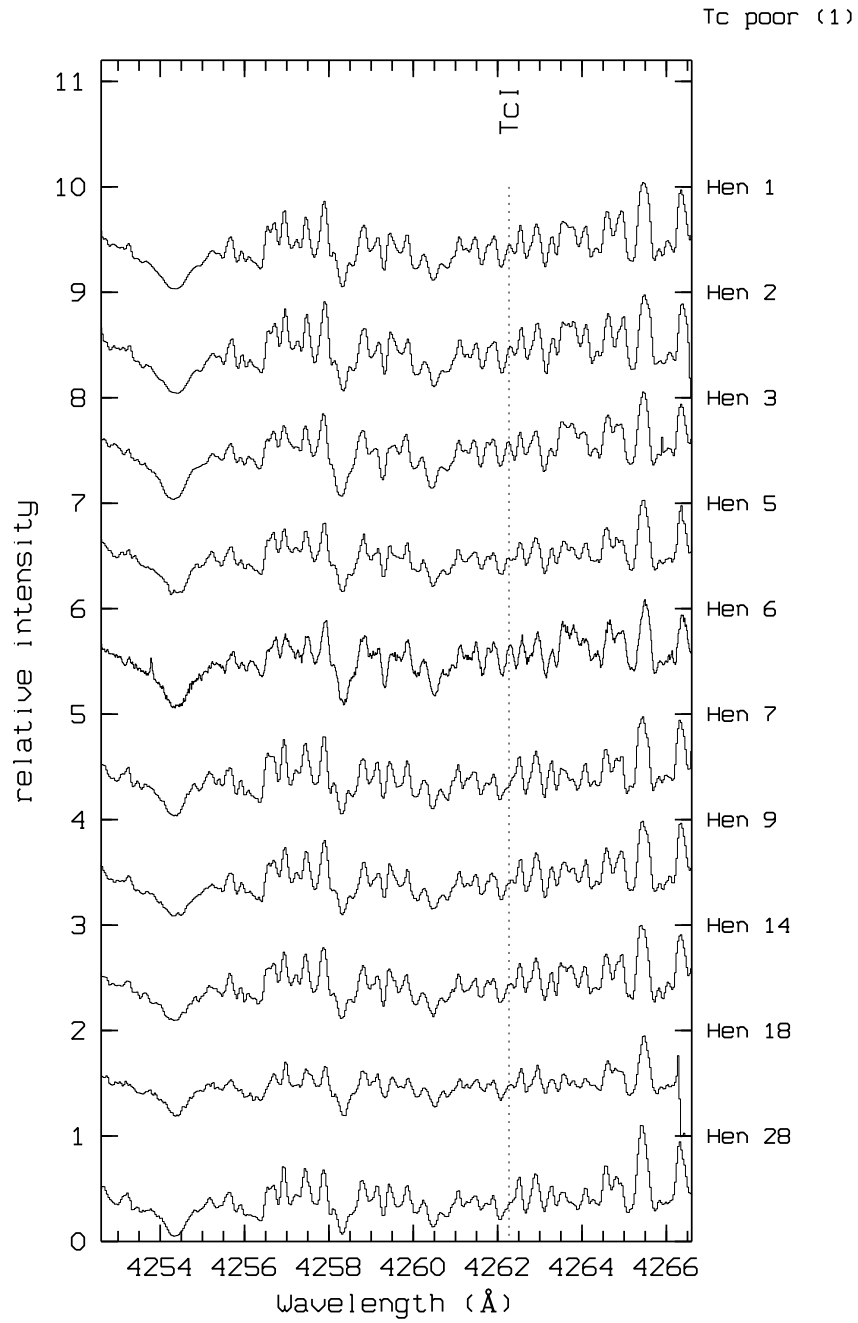


Figure A.10: Tc-poor spectra at 4262.270 Å

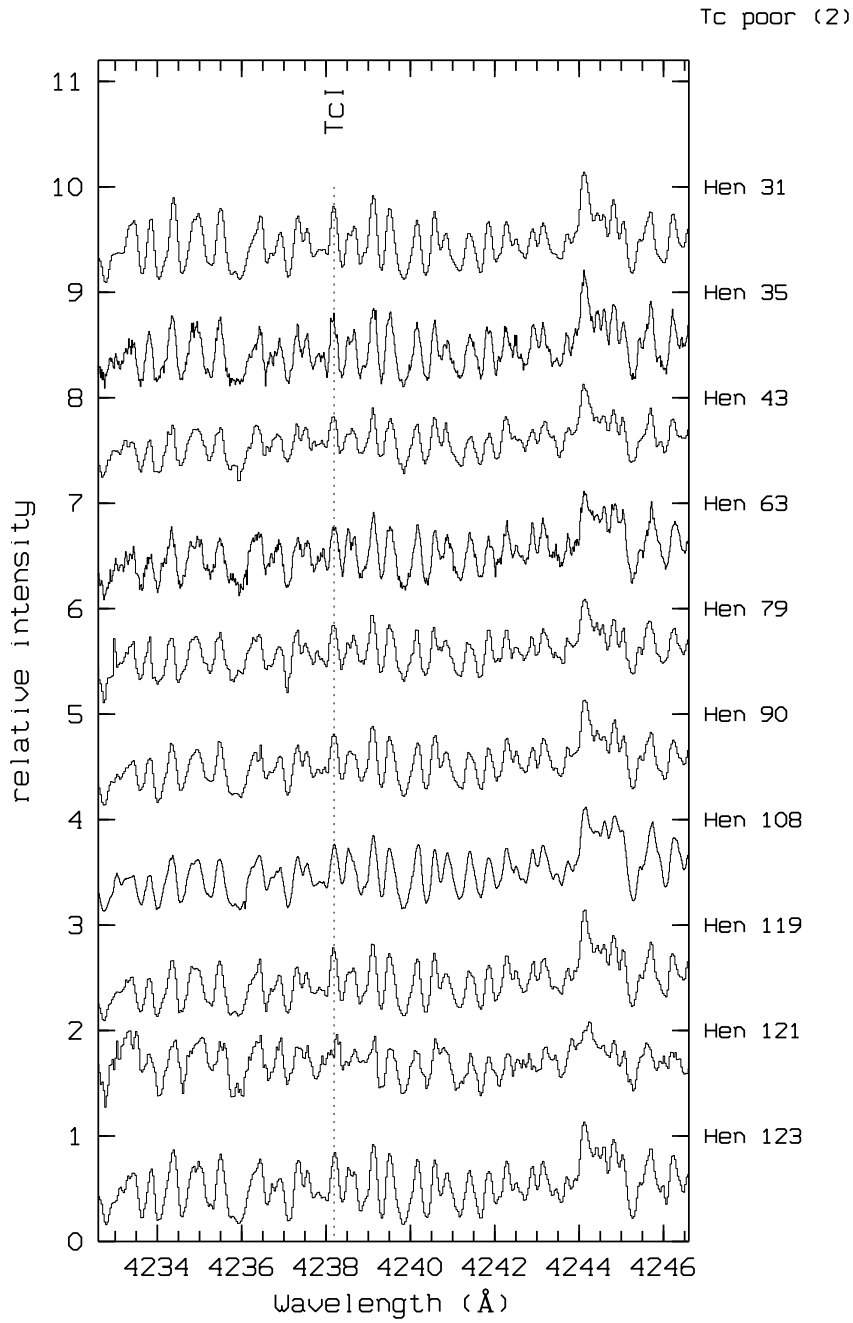


Figure A.11: Tc-poor spectra at 4238.191 Å

Tc poor (2)

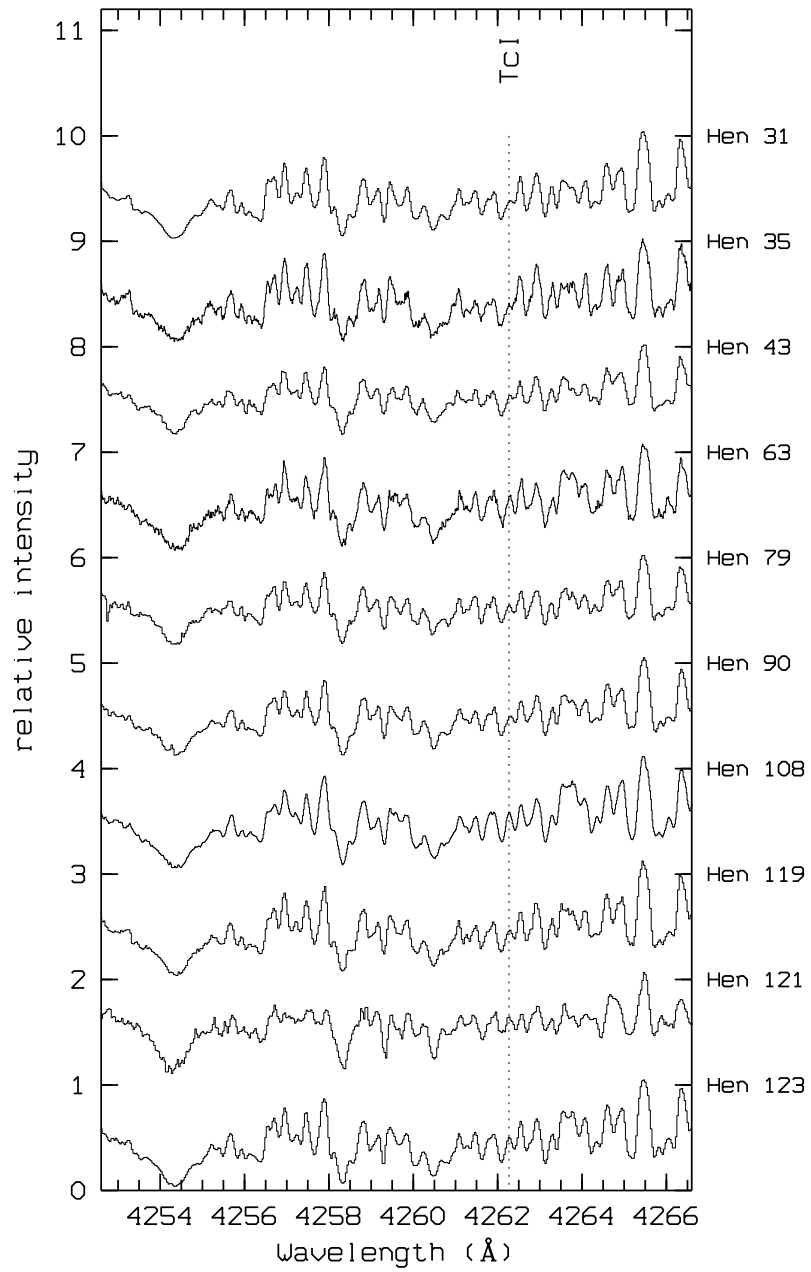


Figure A.12: Tc-poor spectra at 4262.270 Å

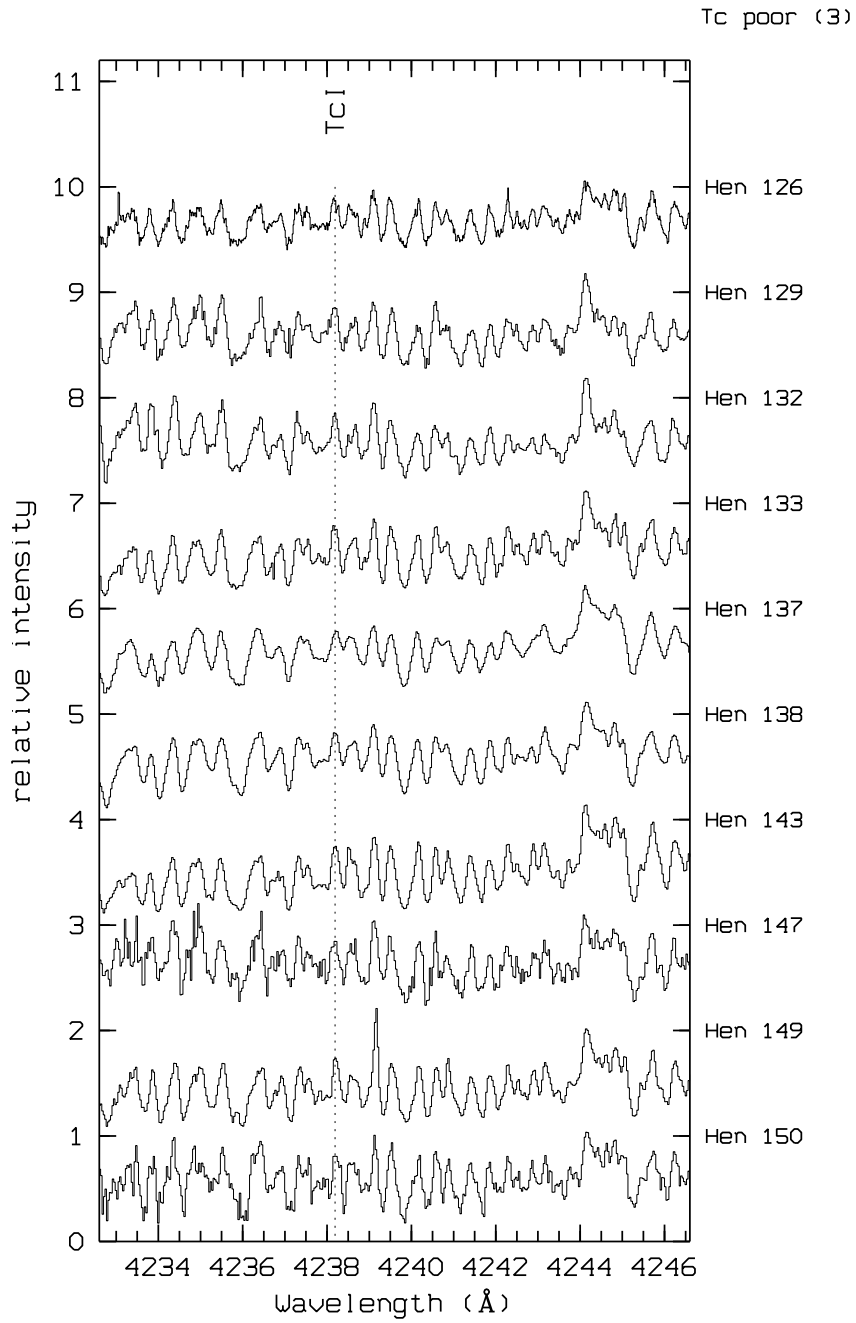


Figure A.13: Tc-poor spectra at 4238.191 Å

Tc poor (3)

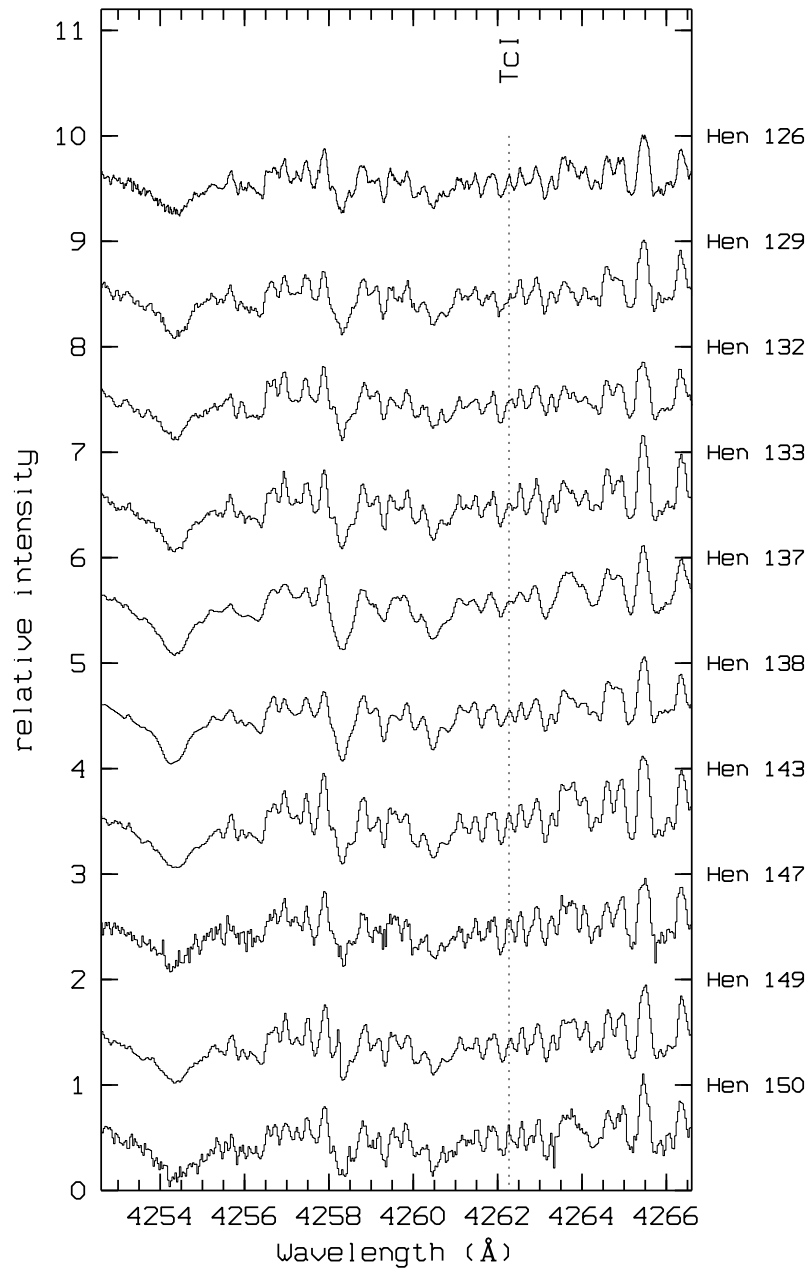


Figure A.14: Tc-poor spectra at 4262.270 Å

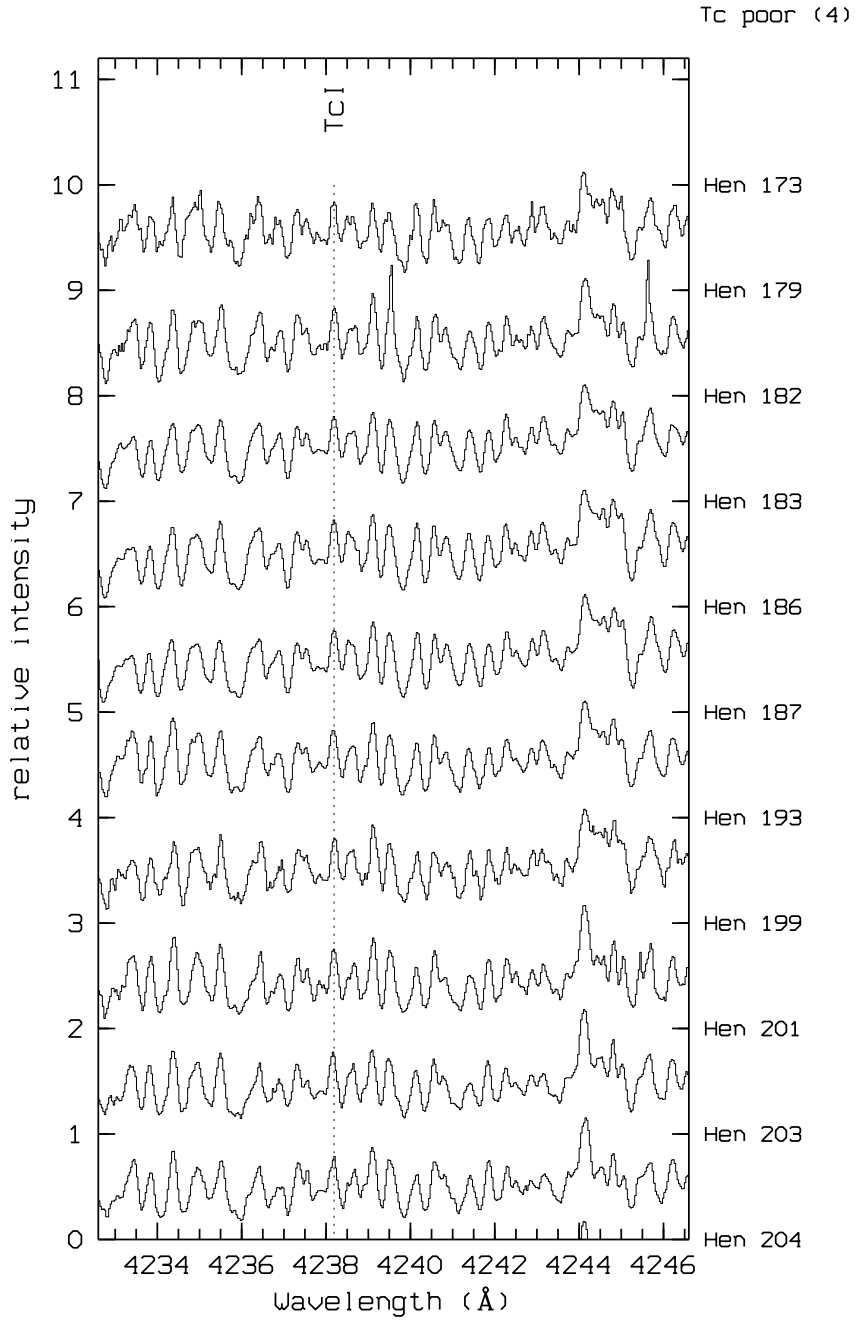


Figure A.15: Tc-poor spectra at 4238.191 Å

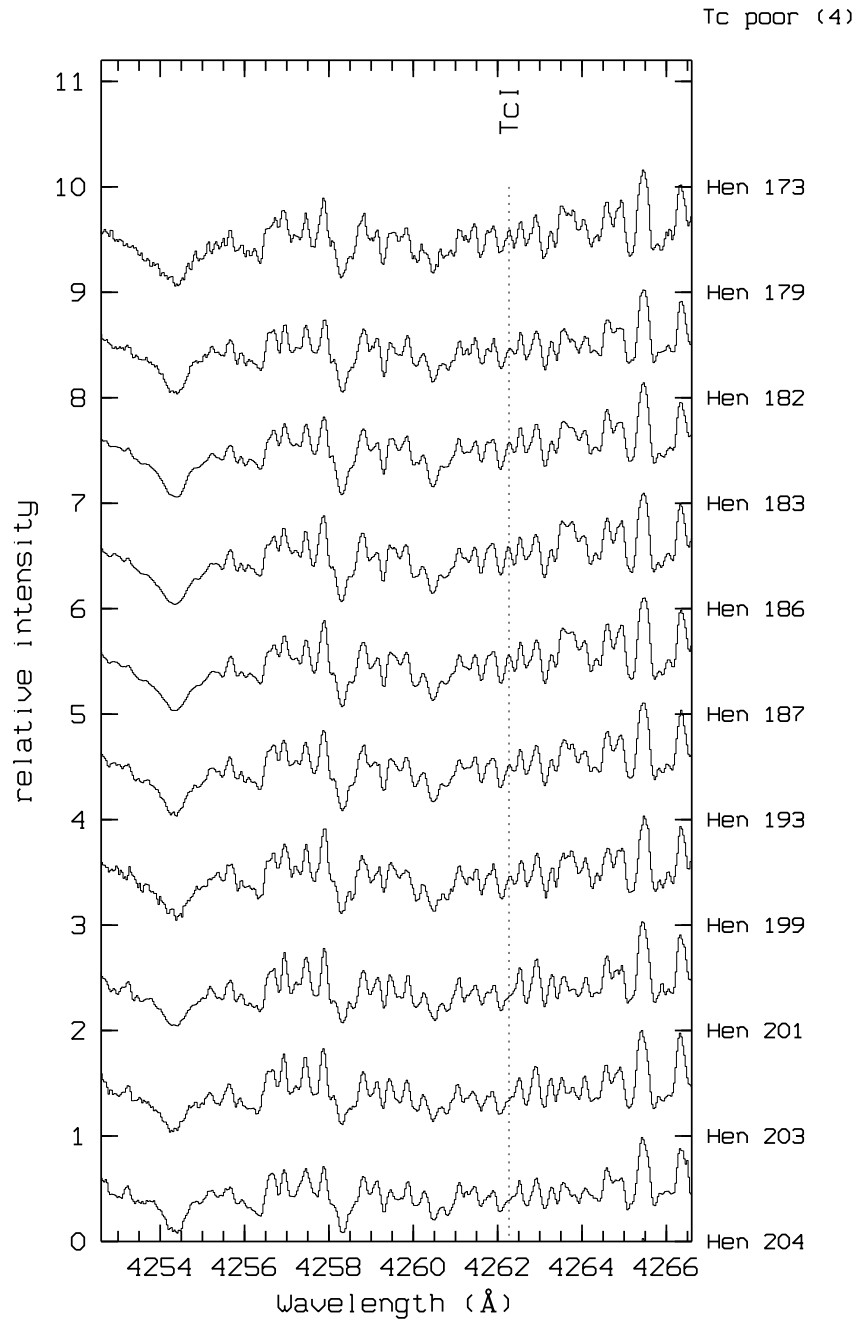
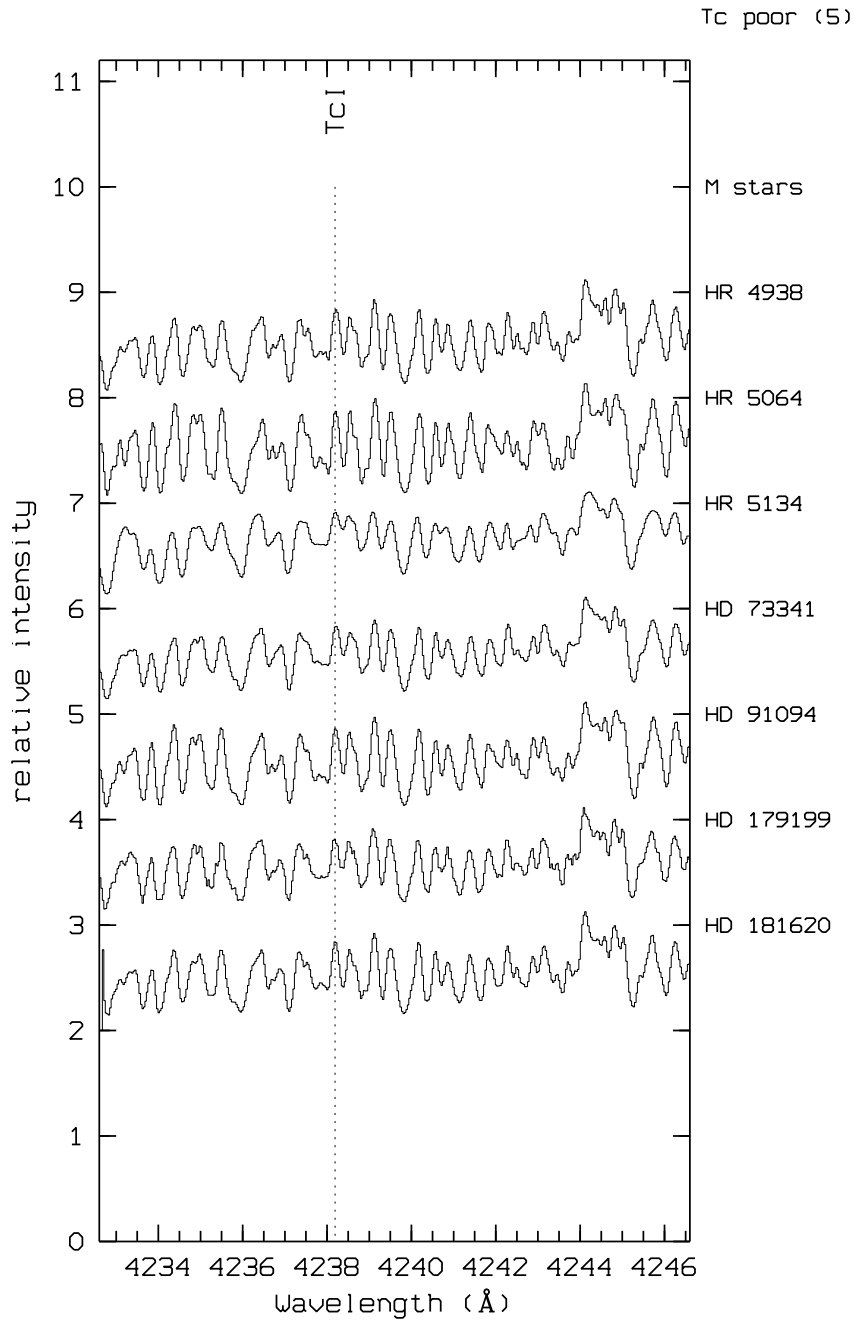


Figure A.16: Tc-poor spectra at 4262.270 Å

Figure A.17: Tc-poor spectra at 4238.191 \AA

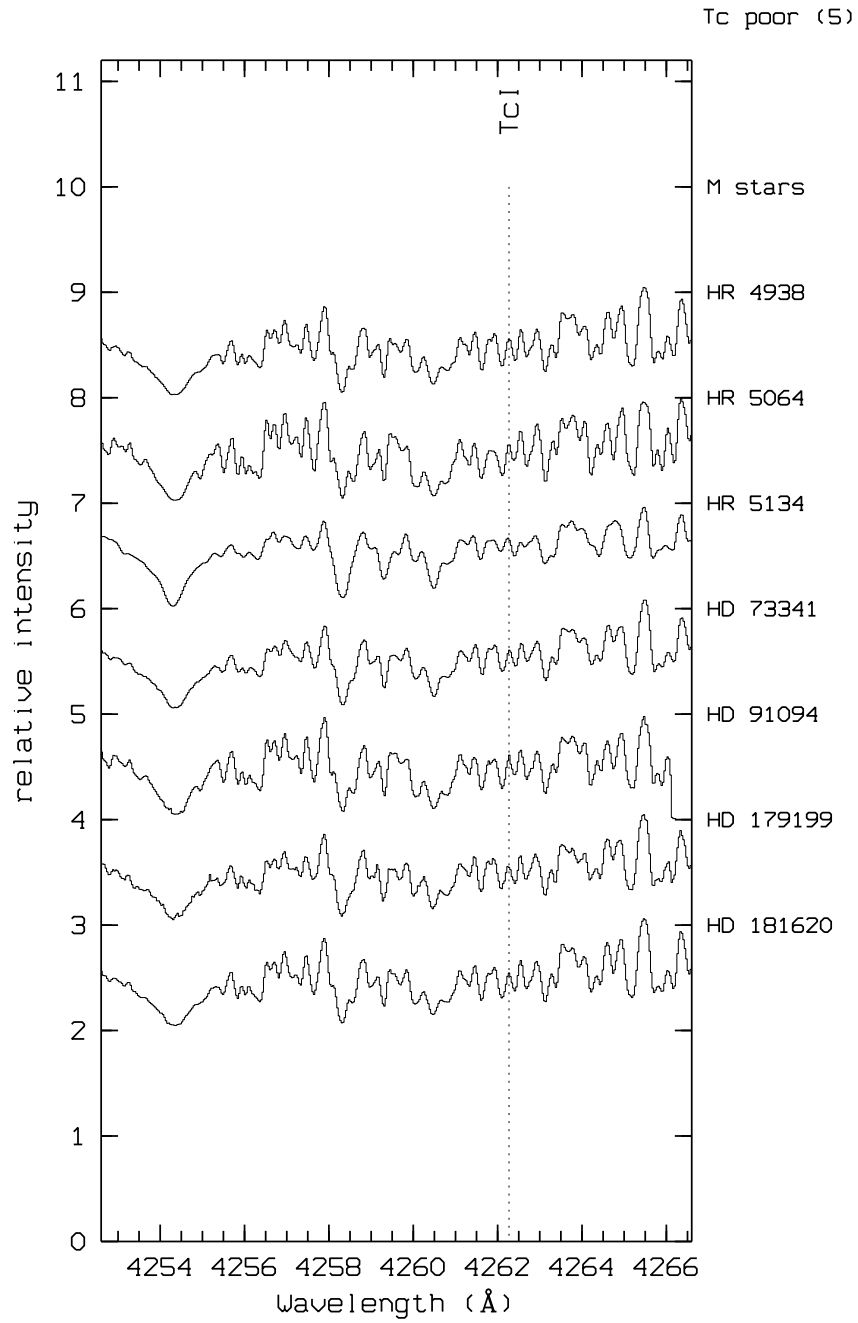
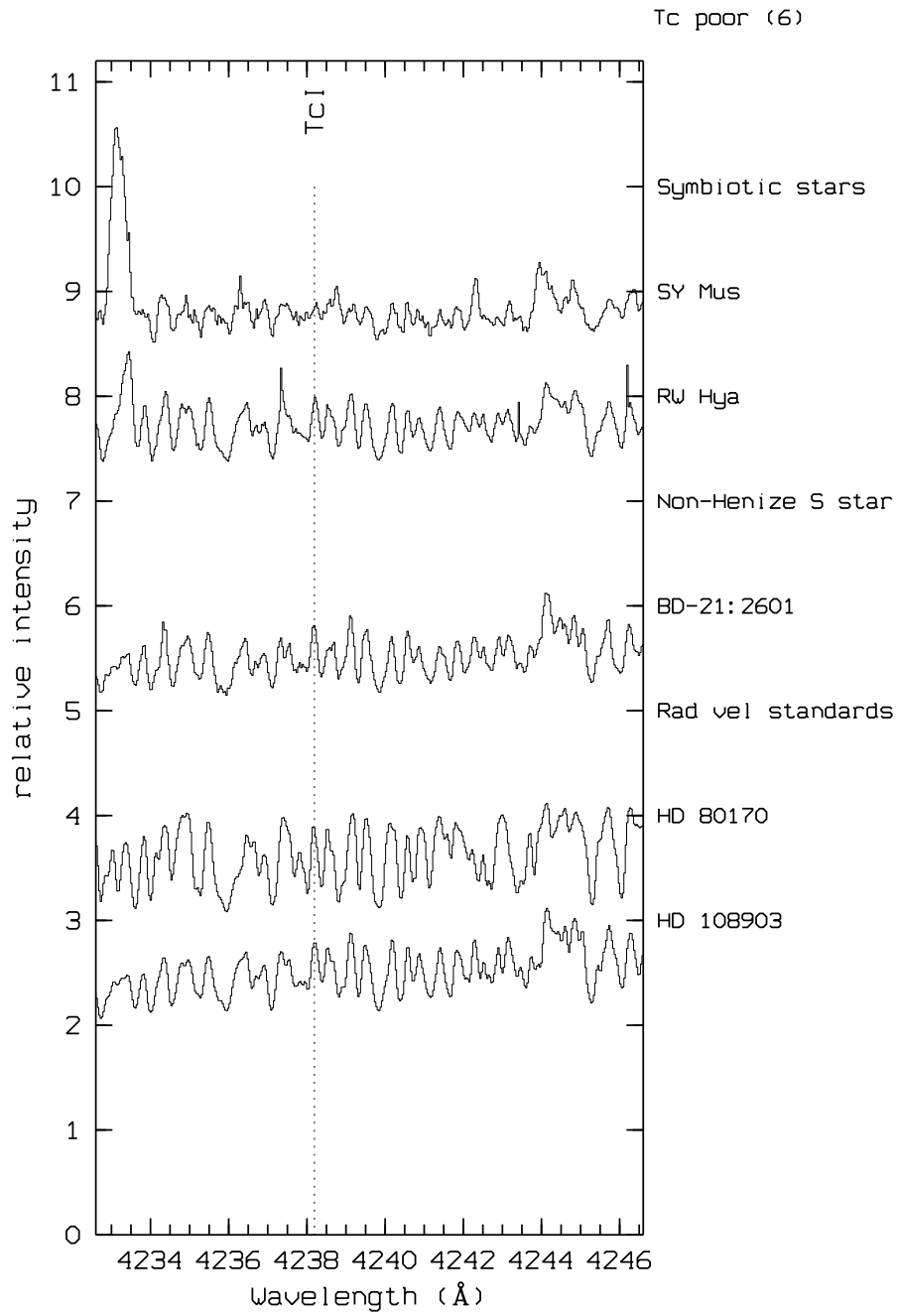


Figure A.18: Tc-poor spectra at 4262.270 Å

Figure A.19: Tc-poor spectra at 4238.191 \AA

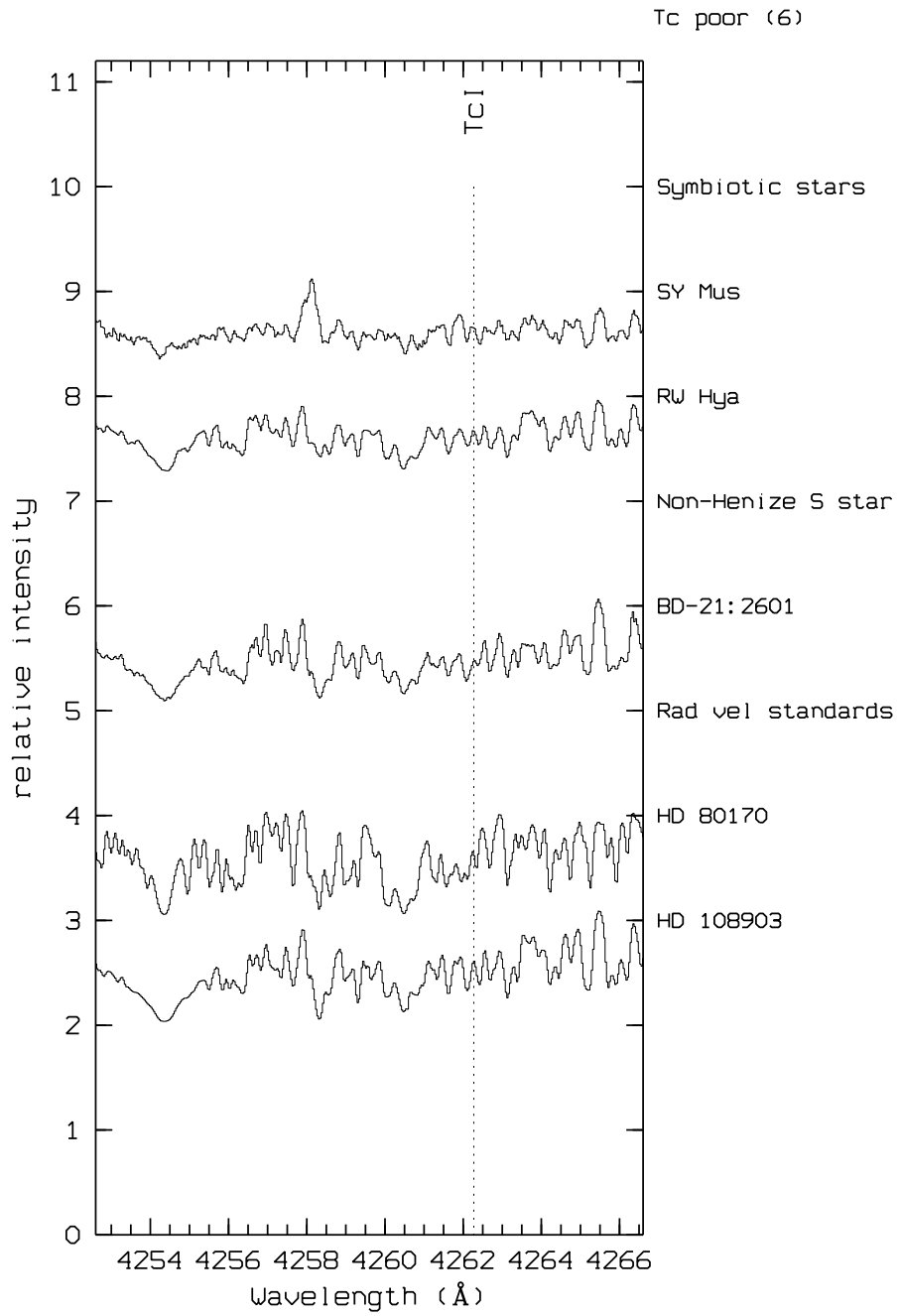


Figure A.20: Tc-poor spectra at 4262.270 Å

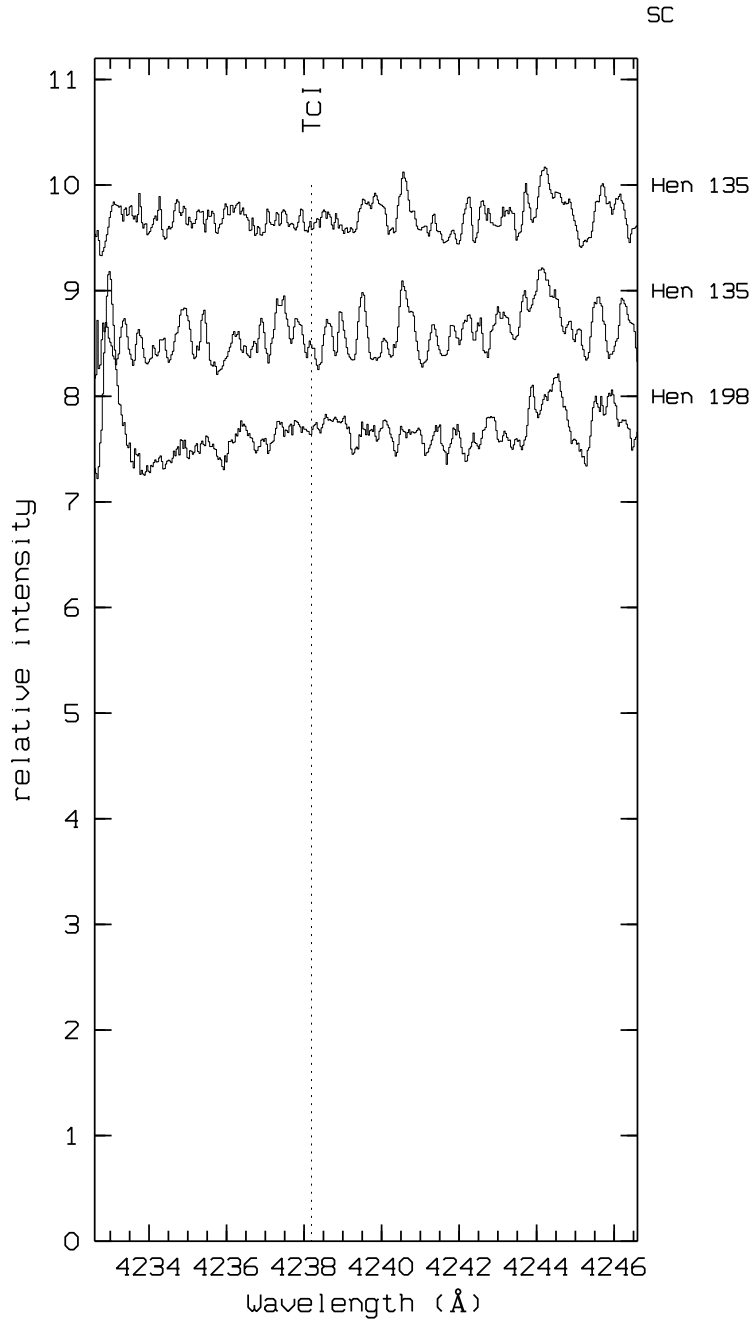


Figure A.21: Spectra of SC stars at 4238.191 Å

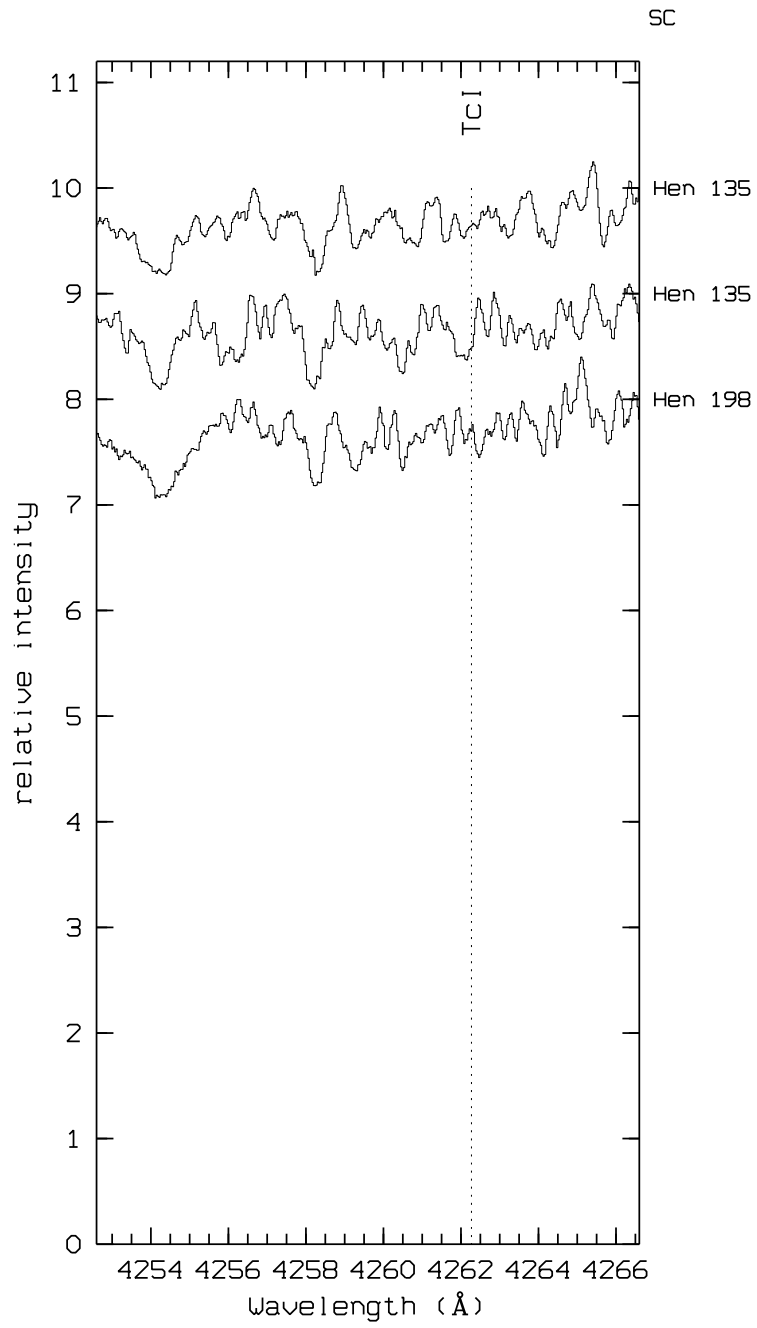


Figure A.22: Spectra of SC stars at 4262.270 Å

Appendix B

The Henize sample of S stars: data

The data used in Chap. 6 and 7 are listed in this Appendix. The tables are organized as follows:

• **Table B.1: CORAVEL data:**

- ▷ Hen is the Henize number as listed in the General Catalogue of Galactic S stars (Stephenson 1984);
- ▷ Tc indicates whether the star is technetium-rich (y) or technetium-poor (n) as derived in Chap. 5;
- ▷ N_C is the number of CORAVEL radial-velocity measurements;
- ▷ ΔT stands for the time span (in days) of the observations;
- ▷ V_r (km s⁻¹) is the mean heliocentric radial velocity and $\sigma(V_r)$ (km s⁻¹) its standard deviation;
- ▷ $\bar{\epsilon}_1$ (km s⁻¹) gives the average error on one measurement;
- ▷ Sb (km s⁻¹) and PR are the reduced width and the depth of the CORAVEL cross-correlation dip, respectively;
- ▷ V_{ran} (km s⁻¹) indicates the range of the radial velocity measurements.

• **Table B.2: Geneva photometric data:**

- ▷ N_p is the number of measurements in the Geneva photometric system;
- ▷ V is the visual apparent magnitude;
- ▷ $U-B$, $B-V$ and $(U-B)_0$, $(B-V)_0$ are the reddened and dereddened colour indices, respectively;
- ▷ m indicates the method chosen for dereddening the photometry, as described in Sect. 6.3.3 [1: E_{B-V} is taken from Burstein & Heiles (1982); 2: $A_V(r)$ is taken from Neckel & Klare (1980); 3: $A_V(r)$ is taken from Arenou et al. (1992)];
- ▷ n_U is the number of measurements fainter than $U = 16.5$; they were all discarded;
- ▷ $\sigma_r(U)$, $\sigma_r(B)$ and $\sigma_r(V)$ stand for the standard deviation of the U , B and V

magnitudes.

• **Table B.3: Infrared photometric data:**

- ▷ the first 4 columns list the $JHKL$ photometry taken at SAAO (Sect. 6.4);
- ▷ $(V-K)_0$ is the dereddened colour index;
- ▷ the $K-[12]$ and $K-[25]$ indices, as described in Sect. 6.5, come next;
- ▷ m_{bol} is the apparent bolometric magnitude obtained by integrating the spectral energy distribution in the $UBVJHKL$ bands (Sect. 7.3.2);
- ▷ $m_{bol,V}$ is a less accurate estimate of the apparent bolometric magnitude derived by applying an appropriate bolometric correction to the V magnitude (see Sect. 7.3.2).

• **Table B.4: Spectroscopic data and clustering results:**

- ▷ I_{ZrO} , I_{TiO} , I_{NaD} and I_{LaO} are the band strength indices as defined in Sect. 6.6.2;
- ▷ S/N stands for the signal-to-noise ratio of the low-resolution spectra used to derive the band strength indices (Sect. 6.6);
- ▷ the weight assigned to each Henize star in order to correct for the unequal galactic longitude coverage at different galactic latitudes is listed in column w ;
- ▷ l and b stand for the galactic longitudes and latitudes, respectively;
- ▷ C_2 and C_6 are the group assignments derived from the clustering algorithm for 2 and 6 resulting clusters (see Sect 7.1.4 and Table 7.1);
- ▷ C_f is the final retained classification, where “e” and “i” stand for “extrinsic” and “intrinsic”, respectively.

Missing data are indicated by a dash.

Table B.1: CORAVEL data

Hen	Tc	N_C	ΔT (d)	V_r km/s	$\sigma(V_r)$ km/s	$\bar{\epsilon}_1$ km/s	Sb km/s	PR	V_{ran} km/s
1	n	6	2338	10.3	0.5	0.2	4.3	0.41	1.4
2	n	8	4931	21.5	3.7	1.3	4.2	0.42	11.0
3	n	5	1826	26.5	2.3	1.0	6.1	0.30	5.3
4	-	4	1826	-6.8	0.2	0.2	4.5	0.43	0.5
5	n	4	1826	77.6	2.2	1.1	5.0	0.36	4.7
6	n	4	1826	49.0	2.4	1.2	6.1	0.30	5.1
7	n	4	1829	53.8	6.0	3.0	4.3	0.40	13.2
8	y	4	1827	47.4	2.1	1.1	6.2	0.28	6.0
9	n	4	1827	-7.2	0.7	0.4	3.8	0.43	1.8
10	-	4	1829	-9.6	5.4	2.7	4.8	0.32	12.9
11	-	-	-	-	-	-	-	-	-
12	-	3	1827	110.5	1.2	0.7	9.3	0.13	1.4
13	-	-	-	-	-	-	-	-	-
14	n	5	1826	31.2	1.2	0.6	4.3	0.42	3.1
15	-	2	1826	49.2	6.7	4.7	2.6	0.11	10.5
16	y	5	1829	38.1	0.8	0.4	6.0	0.34	1.8
17	-	5	1827	76.8	2.9	1.3	4.8	0.34	7.2
18	n	6	1828	67.6	6.6	2.7	5.6	0.22	13.8
19	y	5	1828	71.5	1.3	0.6	6.0	0.34	2.4
20	y	5	1829	-13.5	1.0	0.5	6.2	0.29	2.7
21	-	4	1416	35.5	0.6	0.4	7.2	0.18	2.0
22	-	4	1825	-10.4	3.0	1.5	3.3	0.46	7.4
23	-	3	717	55.6	2.1	1.2	7.8	0.22	4.6
24	-	3	714	35.3	3.5	2.0	9.6	0.25	6.1
25	-	-	-	-	-	-	-	-	-
26	-	-	-	-	-	-	-	-	-
27	-	1	-	4.0	1.4	1.4	18.6	0.25	0.0
28	n	4	1827	25.9	2.0	1.0	4.4	0.39	4.1
29	-	4	1828	49.0	0.8	0.4	5.9	0.39	1.9
30	-	3	1154	26.0	3.0	1.7	9.1	0.33	6.9
31	n	5	1827	-15.5	1.8	0.8	4.1	0.42	4.4
32	-	4	1746	68.8	2.8	1.4	8.5	0.11	6.4
33	-	-	-	-	-	-	-	-	-
34	y	3	763	17.9	1.9	1.1	9.6	0.16	3.4
35	n	5	1828	-13.6	3.3	1.5	3.9	0.46	10.2
36	y	5	1779	39.4	1.9	0.8	7.2	0.18	4.9
37	y	5	1780	12.8	1.4	0.6	7.1	0.27	2.8
38	-	3	1411	34.0	1.9	1.1	6.5	0.33	3.9
39	y	6	1827	12.1	1.1	0.4	6.2	0.31	3.3
40	-	3	740	74.5	1.7	1.0	7.4	0.27	3.4
41	y	3	766	11.8	1.5	0.9	7.0	0.15	3.2
42	-	2	351	56.6	1.8	1.2	5.9	0.34	2.5
43	n	5	1829	37.9	6.3	2.8	5.1	0.35	14.2
44	-	4	1780	32.4	2.1	1.1	6.1	0.30	4.5
45	y	5	1778	16.4	0.8	0.4	4.9	0.38	1.9
46	-	4	1778	29.4	0.8	0.4	5.2	0.35	2.0
47	-	4	1779	8.9	1.6	0.8	7.1	0.32	4.3
48	-	4	1826	81.8	3.1	1.5	6.2	0.29	9.3
49	-	2	715	27.9	0.8	0.6	6.2	0.50	1.5
50	-	3	833	59.9	1.1	0.6	10.0	0.14	2.3
51	-	4	1828	18.8	0.4	0.2	7.8	0.33	0.7

Table B.1: CORAVEL data (continued)

Hen	Tc	N_C	ΔT (d)	V_r km/s	$\sigma(V_r)$ km/s	\bar{v}_1 km/s	Sb km/s	PR	V_{ran} km/s
103	-	-	-	-	-	-	-	-	-
104	y	4	1946	-14.3	1.1	0.6	5.7	0.33	2.0
105	-	4	1183	-30.7	1.4	0.7	5.4	0.33	3.0
106	-	2	1064	-46.0	2.5	1.8	6.7	0.26	3.6
107	-	4	1154	-39.8	2.3	1.2	6.0	0.34	4.5
108	n	10	1826	44.1	10.1	3.2	5.0	0.39	23.6
109	-	-	-	-	-	-	-	-	-
110	-	4	1093	-4.2	2.1	1.1	4.0	0.45	5.1
111	-	3	1092	-16.7	0.4	0.3	7.6	0.38	0.6
112	-	-	-	-	-	-	-	-	-
113	-	6	1535	-11.1	2.1	0.9	6.6	0.26	4.3
114	-	-	-	-	-	-	-	-	-
115	-	-	-	-	-	-	-	-	-
116	-	-	-	-	-	-	-	-	-
117	-	-	-	-	-	-	-	-	-
118	-	3	1412	6.4	3.4	2.0	3.9	0.38	6.8
119	n	6	1781	-22.2	4.3	1.7	4.4	0.41	11.2
120	-	5	1093	-0.4	2.8	1.2	7.3	0.27	10.1
121	n	11	1778	-4.9	6.9	2.1	6.0	0.22	20.0
122	-	3	717	-3.3	7.6	4.4	6.8	0.32	13.7
123	n	5	1764	0.2	2.6	1.2	4.6	0.41	6.1
124	-	7	1414	6.3	3.6	1.4	4.6	0.32	9.4
125	-	3	743	53.7	2.6	1.5	7.1	0.13	4.7
126	n	5	747	-29.8	2.7	1.2	4.6	0.38	6.2
127	-	8	2147	-1.0	0.7	0.2	5.7	0.35	2.2
128	-	-	-	-	-	-	-	-	-
129	n	6	1779	-25.4	3.4	1.4	5.3	0.35	7.9
130	-	6	1781	-5.5	2.2	0.9	6.0	0.35	6.7
131	-	4	1111	-48.3	1.6	0.8	6.6	0.32	3.7
132	n	7	1898	-44.7	0.8	0.3	4.4	0.40	2.5
133	n	7	1764	1.1	0.8	0.3	5.4	0.36	2.1
134	-	9	1705	61.5	2.4	0.8	6.3	0.26	7.3
135	-	7	1882	-22.2	1.5	0.6	7.8	0.40	4.5
136	-	3	328	-56.6	8.8	5.1	25.2	0.26	19.4
137	n	9	1780	-21.1	4.6	1.5	7.2	0.31	11.1
138	n	8	1902	8.3	1.0	0.4	5.7	0.32	2.7
139	-	4	682	-21.1	0.5	0.3	4.9	0.33	1.0
140	y	6	1781	-34.7	1.0	0.4	5.8	0.35	2.9
141	y	4	835	-54.9	1.4	0.7	7.6	0.19	3.0
142	-	2	470	-3.6	2.1	1.5	7.7	0.17	3.0
143	n	6	1106	-26.0	3.5	1.4	4.5	0.41	8.6
144	-	5	1094	-28.7	2.4	1.1	7.9	0.23	5.8
145	-	4	1626	-26.2	2.0	1.0	6.3	0.31	3.9
146	-	7	1572	-12.2	1.3	0.5	7.1	0.25	3.5
147	n	8	1579	-9.9	7.1	2.5	4.2	0.41	16.7
148	-	-	-	-	-	-	-	-	-
149	n	6	1108	25.0	2.9	1.2	4.5	0.40	7.5
150	n	8	1781	23.9	2.1	0.8	4.9	0.37	6.2
151	-	1	-	-22.0	1.9	1.9	21.1	0.21	0.0
152	-	2	466	-56.9	8.7	6.2	16.4	0.32	18.9
153	-	3	955	15.4	2.3	1.3	9.3	0.21	5.6

Table B.2: Geneva photometric data

Hen	N_p	V	$U-B$	$B-V$	n_U	$(U-B)_0$	$(B-V)_0$	m	$\sigma_r(U)$	$\sigma_r(B)$	$\sigma_r(V)$
1	3	7.49	3.22	1.21	0	3.19	1.17	3	0.05	0.03	0.02
2	20	8.48	3.27	1.20	0	3.21	1.12	2	0.02	0.01	0.01
3	4	8.26	2.94	1.03	0	2.92	1.00	2	0.12	0.08	0.08
4	3	9.81	3.37	1.27	0	3.31	1.18	2	0.10	0.04	0.03
5	3	11.01	3.18	1.17	0	3.17	1.16	2	0.00	0.02	0.02
6	5	9.88	3.02	1.07	0	3.01	1.06	2	0.03	0.03	0.04
7	3	8.89	3.18	1.25	0	3.16	1.22	2	0.06	0.02	0.00
8	8	11.03	3.25	1.40	0	3.21	1.34	2	0.23	0.24	0.25
9	4	9.52	3.27	1.22	0	3.26	1.20	2	0.03	0.01	0.00
10	4	9.33	3.11	1.23	0	2.99	1.05	2	0.06	0.06	0.07
11	1	14.37	-	0.85	1	-	0.82	2	-	-	-
12	3	12.38	1.59	0.95	2	2.33	0.89	2	-	1.65	1.86
13	3	13.02	-	1.39	3	-	1.33	2	-	0.25	0.27
14	3	10.32	3.31	1.28	0	3.26	1.19	2	0.06	0.01	0.02
15	2	12.01	2.54	1.21	0	2.46	1.09	2	0.37	0.41	0.31
16	2	11.20	3.37	1.30	0	3.31	1.21	2	0.05	0.13	0.13
17	3	12.37	-	1.21	3	-	1.12	2	-	0.00	0.00
18	13	10.60	1.57	0.99	0	1.44	0.79	2	0.22	0.09	0.06
19	1	10.49	3.84	1.66	0	3.80	1.59	3	-	-	-
20	1	10.29	3.14	1.25	0	3.06	1.14	2	-	-	-
21	2	12.37	-	1.75	2	-	1.65	1	-	0.00	0.01
22	-	-	-	-	-	-	-	-	-	-	-
23	-	-	-	-	-	-	-	-	-	-	-
24	2	11.83	-	2.05	2	-	1.73	1	-	0.35	0.30
25	-	-	-	-	-	-	-	-	-	-	-
26	-	-	-	-	-	-	-	-	-	-	-
27	1	12.65	-	2.23	1	-	2.08	2	-	-	-
28	3	8.87	3.33	1.47	0	3.23	1.31	2	0.01	0.02	0.01
29	2	11.61	-	2.44	2	-	2.24	1	-	0.08	0.06
30	1	13.73	-	2.65	1	-	2.14	1	-	-	-
31	1	7.18	3.34	1.38	0	3.27	1.26	2	-	-	-
32	2	8.69	1.98	0.97	0	1.91	0.85	3	1.43	1.47	1.65
33	-	-	-	-	-	-	-	-	-	-	-
34	2	10.16	2.74	1.22	0	2.64	1.07	2	0.37	0.48	0.62
35	2	9.83	3.32	1.31	0	3.24	1.19	2	0.00	0.00	0.00
36	2	9.01	2.27	0.92	0	2.24	0.88	1	0.02	0.07	0.09
37	5	10.95	3.38	1.49	0	3.30	1.38	3	0.15	0.09	0.10
38	3	11.26	3.37	1.41	0	3.29	1.29	3	0.02	0.05	0.07
39	3	9.31	3.20	1.29	0	3.11	1.15	2	0.05	0.03	0.02
40	3	11.39	2.88	1.29	0	2.60	0.87	1	0.00	0.05	0.06
41	1	9.46	2.32	1.00	0	2.26	0.91	1	-	-	-
42	1	12.43	-	2.68	1	-	2.56	3	-	-	-
43	1	10.59	3.58	1.31	0	3.52	1.22	1	-	-	-
44	2	10.69	3.22	1.40	0	3.16	1.30	1	0.17	0.18	0.19
45	7	9.58	2.80	1.20	0	2.68	1.01	1	0.10	0.04	0.02
46	3	11.42	-	1.64	3	-	1.19	1	-	0.00	0.02
47	-	-	-	-	-	-	-	-	-	-	-
48	-	-	-	-	-	-	-	-	-	-	-
49	3	12.57	-	3.40	3	-	2.82	1	-	0.00	0.13
50	3	10.78	2.37	0.93	0	1.99	0.36	1	0.51	0.56	0.60
51	3	10.68	-	2.58	3	-	2.41	3	-	0.27	0.24

Table B.2: Geneva photometric data (continued)

Hen	N_p	V	$U-B$	$B-V$	n_U	$(U-B)_0$	$(B-V)_0$	m	$\sigma_r(U)$	$\sigma_r(B)$	$\sigma_r(V)$
103	-	-	-	-	-	-	-	-	-	-	-
104	3	10.07	3.24	1.33	0	3.15	1.20	3	0.10	0.02	0.02
105	-	-	-	-	-	-	-	-	-	-	-
106	3	12.10	-	1.61	3	-	1.17	1	-	0.10	0.09
107	3	12.57	-	2.72	3	-	2.40	1	-	0.19	0.10
108	4	8.77	3.19	1.12	0	3.16	1.07	1	0.02	0.04	0.04
109	-	-	-	-	-	-	-	-	-	-	-
110	3	11.26	3.46	1.58	1	3.28	1.29	1	0.00	0.00	0.00
111	3	12.43	-	2.60	3	-	2.21	1	-	0.28	0.23
112	-	-	-	-	-	-	-	-	-	-	-
113	3	12.05	-	1.86	3	-	1.41	1	-	0.03	0.03
114	-	-	-	-	-	-	-	-	-	-	-
115	2	13.42	-	2.08	2	-	1.63	1	-	0.30	0.35
116	-	-	-	-	-	-	-	-	-	-	-
117	-	-	-	-	-	-	-	-	-	-	-
118	4	11.71	3.20	1.35	2	3.15	1.23	2	0.00	0.03	0.03
119	5	8.83	3.17	1.21	0	3.04	1.02	1	0.07	0.00	0.00
120	6	7.48	3.69	3.02	0	3.62	2.91	1	1.50	1.02	0.62
121	30	10.45	1.94	1.07	0	1.89	0.99	2	0.54	0.20	0.10
122	1	13.98	-	3.84	1	-	3.75	2	-	-	-
123	8	9.25	3.37	1.29	0	3.28	1.15	2	0.04	0.02	0.02
124	6	11.50	3.03	1.20	0	2.96	1.09	2	0.14	0.05	0.05
125	3	10.57	2.39	0.95	0	2.34	0.87	2	0.24	0.20	0.23
126	1	10.57	3.31	1.27	0	3.21	1.12	3	-	-	-
127	3	6.88	3.25	1.26	0	3.21	1.19	2	0.05	0.03	0.03
128	-	-	-	-	-	-	-	-	-	-	-
129	31	9.41	3.35	1.44	0	3.25	1.30	2	0.13	0.06	0.06
130	1	11.09	3.27	1.99	0	3.11	1.75	1	-	-	-
131	4	11.79	-	1.97	4	-	1.61	1	-	0.10	0.08
132	4	9.31	3.44	1.59	0	3.33	1.41	2	0.03	0.04	0.04
133	1	9.01	2.98	1.34	0	2.89	1.19	3	-	-	-
134	6	11.58	3.10	1.34	1	3.05	1.28	2	0.19	0.06	0.09
135	9	7.01	5.09	2.78	0	5.04	2.70	2	0.09	0.10	0.08
136	2	11.96	-	2.77	2	-	2.25	1	-	0.60	0.44
137	30	9.09	2.92	1.23	0	2.87	1.15	2	0.16	0.05	0.05
138	4	7.05	3.23	1.39	0	3.09	1.17	3	0.17	0.15	0.14
139	1	11.66	3.07	1.32	0	2.86	0.99	1	-	-	-
140	7	8.41	3.20	1.32	0	3.07	1.13	3	0.02	0.02	0.04
141	4	9.24	2.91	1.61	0	2.69	1.27	1	0.20	0.16	0.14
142	3	11.95	1.24	2.07	2	2.40	1.75	1	-	1.72	1.43
143	10	8.45	3.23	1.13	0	3.19	1.07	2	0.05	0.02	0.02
144	3	11.95	-	2.16	3	-	1.84	1	-	0.03	0.07
145	2	12.25	-	2.20	2	-	1.81	1	-	0.00	0.01
146	5	10.87	3.24	1.81	0	2.98	1.40	1	0.06	0.03	0.01
147	26	10.46	3.29	1.17	0	3.23	1.09	2	0.19	0.03	0.02
148	-	-	-	-	-	-	-	-	-	-	-
149	10	9.40	3.30	1.19	0	3.25	1.12	2	0.03	0.02	0.02
150	6	7.50	3.32	1.28	0	3.18	1.07	1	0.05	0.04	0.04
151	-	-	-	-	-	-	-	-	-	-	-
152	3	13.03	-	2.92	3	-	2.62	3	-	0.47	0.34
153	1	10.53	-	2.64	1	-	2.58	2	-	-	-

Table B.2: Geneva photometric data (continued)

Hen	N_p	V	$U-B$	$B-V$	n_U	$(U-B)_0$	$(B-V)_0$	m	$\sigma_r(U)$	$\sigma_r(B)$	$\sigma_r(V)$
154	-	-	-	-	-	-	-	-	-	-	-
155	-	-	-	-	-	-	-	-	-	-	-
156	3	11.63	1.92	2.04	2	2.10	1.31	1	-	0.70	0.74
157	2	9.40	-	3.06	2	-	2.96	2	-	0.06	0.03
158	1	13.37	-	1.44	1	-	1.14	3	-	-	-
159	1	12.56	-	2.45	1	-	2.27	3	-	-	-
160	2	11.25	2.35	0.64	0	2.24	0.46	3	0.24	0.31	0.30
161	2	11.53	-	2.49	2	-	2.22	2	-	0.11	0.05
162	1	9.53	3.16	1.38	0	2.99	1.12	1	-	-	-
163	2	11.76	-	2.77	2	-	2.34	1	-	0.00	0.03
164	-	-	-	-	-	-	-	-	-	-	-
165	2	9.77	2.80	2.21	1	3.31	1.99	2	-	0.77	0.60
166	1	10.89	-	2.80	1	-	2.54	1	-	-	-
167	3	11.67	-	2.38	3	-	1.94	1	-	0.39	0.33
168	1	10.19	-	2.99	1	-	2.73	2	-	-	-
169	1	10.56	3.38	1.37	0	3.37	1.34	2	-	-	-
170	-	-	-	-	-	-	-	-	-	-	-
171	3	12.65	2.22	0.84	0	1.94	0.40	1	0.50	0.49	0.39
172	1	11.06	1.69	1.36	0	1.28	0.73	1	-	-	-
173	1	10.15	3.27	1.41	0	3.06	1.09	1	-	-	-
174	12	10.90	2.66	1.71	2	2.44	1.38	3	0.40	0.11	0.10
175	1	8.57	3.43	1.66	0	3.24	1.37	1	-	-	-
176	-	-	-	-	-	-	-	-	-	-	-
177	1	10.17	3.38	1.59	0	3.17	1.27	1	-	-	-
178	2	10.55	2.77	1.84	0	2.35	1.19	1	0.00	0.13	0.19
179	3	9.24	3.23	1.27	0	3.15	1.14	2	0.15	0.08	0.09
180	-	-	-	-	-	-	-	-	-	-	-
181	-	-	-	-	-	-	-	-	-	-	-
182	1	8.37	3.01	1.19	0	2.92	1.05	1	-	-	-
183	4	8.45	3.18	1.15	0	3.13	1.07	2	0.04	0.03	0.03
184	2	11.29	-	3.21	2	-	2.71	3	-	0.45	0.26
185	1	11.46	-	1.69	1	-	1.19	3	-	-	-
186	3	8.18	3.19	1.15	0	3.12	1.03	1	0.07	0.05	0.06
187	3	8.42	3.28	1.32	0	3.23	1.24	2	0.04	0.05	0.05
188	2	10.16	-	2.36	2	-	2.11	1	-	0.10	0.08
189	26	11.13	2.72	1.14	0	2.65	1.04	2	0.19	0.07	0.07
190	1	11.34	3.36	1.48	0	3.21	1.25	3	-	-	-
191	3	9.94	3.05	1.36	0	2.98	1.25	2	0.09	0.14	0.16
192	-	-	-	-	-	-	-	-	-	-	-
193	3	10.11	3.68	1.51	0	3.48	1.20	3	0.20	0.02	0.00
194	4	11.32	3.28	1.37	0	3.21	1.27	2	0.10	0.09	0.10
195	3	11.56	0.82	1.71	2	2.21	1.66	2	-	1.54	1.36
196	3	11.38	3.42	1.45	0	3.34	1.32	2	0.00	0.16	0.18
197	4	6.77	3.17	1.22	0	3.15	1.19	2	0.09	0.05	0.05
198	7	8.07	3.35	2.62	2	3.77	2.61	2	1.38	1.34	1.05
199	3	10.20	3.25	1.28	0	3.23	1.25	2	0.07	0.03	0.02
200	5	11.24	-	4.54	5	-	4.53	2	-	0.53	0.22
201	4	10.01	3.20	1.26	0	3.16	1.20	3	0.02	0.00	0.00
202	22	6.60	2.84	1.94	0	2.81	1.89	3	0.19	0.27	0.25
203	3	9.71	3.24	1.43	0	3.20	1.38	3	0.10	0.13	0.14
204	3	9.74	3.20	1.23	0	3.17	1.18	3	0.00	0.02	0.03
205	2	10.55	3.35	1.37	0	3.30	1.29	2	0.00	0.00	0.00

Table B.3: Infrared photometric data

Hen	K	$J-H$	$H-K$	$K-L$	$(V-K)_0$	$K-[12]$	$K-[25]$	m_{bol}	$m_{bol,V}$
1	3.10	0.93	0.19	0.12	4.28	-2.78	-4.26	5.90	5.46
2	4.07	0.92	0.20	0.15	4.18	-	-	6.84	6.32
3	2.67	0.96	0.25	0.18	5.50	-2.66	-4.10	5.63	6.25
4	5.22	0.95	0.20	0.01	4.34	-2.73	-	8.03	7.62
5	5.80	0.81	0.08	0.14	5.18	-	-	8.56	9.07
6	4.18	0.96	0.24	0.22	5.65	-2.51	-4.27	7.14	7.93
7	4.64	0.92	0.18	0.14	4.16	-2.71	-	7.43	7.21
8	5.50	0.94	0.25	0.28	5.36	-1.40	-2.19	8.42	8.09
9	5.30	0.97	0.17	-0.09	4.18	-2.66	-	8.12	7.57
10	-	-	-	-	-	-	-	-	7.19
11	5.73	1.24	0.60	0.39	8.55	-0.97	-2.05	9.09	9.97
12	3.84	1.03	0.33	0.28	8.37	-3.90	-	6.92	7.89
13	-	-	-	-	-	-	-	-	10.92
14	5.82	0.95	0.16	0.09	4.25	-	-	8.58	8.13
15	4.82	0.86	0.14	0.23	6.85	-3.44	-	7.61	7.33
16	6.09	1.02	0.29	0.19	4.86	-	-	9.03	8.17
17	-	-	-	-	-	-	-	-	10.18
18	5.00	0.95	0.27	0.19	5.03	-2.67	-	7.85	7.36
19	5.41	0.96	0.22	0.10	4.91	-2.64	-	8.30	7.55
20	4.31	1.01	0.25	0.11	5.65	-2.41	-3.74	7.25	7.17
21	-	-	-	-	-	-	-	-	7.77
22	7.53	0.83	0.05	-0.12	-	-	-	-	-
23	4.68	1.15	0.32	0.34	-	-2.24	-	-	-
24	-	-	-	-	-	-	-	-	6.53
25	-	-	-	-	-	-	-	-	-
26	-	-	-	-	-	-	-	-	-
27	5.86	0.81	0.54	-	6.37	-0.78	-1.85	-	7.88
28	3.96	0.95	0.24	0.12	4.47	-2.70	-4.23	6.76	6.48
29	5.41	1.17	0.32	0.36	5.64	-2.65	-	8.42	8.23
30	-	-	-	-	-	-	-	-	7.83
31	2.46	0.98	0.22	0.18	4.40	-2.74	-4.22	5.27	4.91
32	-	-	-	-	-	-	-	-	4.03
33	-	-	-	-	-	-	-	-	-
34	3.06	0.98	0.32	0.35	6.68	-2.08	-3.30	6.04	5.40
35	5.59	0.80	0.18	-0.08	3.90	-	-	8.25	7.56
36	2.60	1.02	0.29	0.28	6.27	-2.48	-3.91	5.63	4.94
37	4.17	1.12	0.28	0.27	6.46	-2.55	-3.83	7.19	7.84
38	-	-	-	-	-	-	-	-	8.15
39	3.49	1.01	0.27	0.20	5.42	-2.63	-4.12	6.42	6.12
40	4.88	1.08	0.32	0.36	5.32	-2.50	-3.12	7.70	6.17
41	2.61	1.06	0.32	0.33	6.58	-2.26	-3.50	5.65	5.25
42	-	-	-	-	-	-	-	-	9.29
43	5.50	0.95	0.24	0.36	4.82	-2.73	-	8.36	8.71
44	5.06	1.00	0.31	0.33	5.36	-2.31	-	8.03	7.64
45	4.75	0.97	0.21	0.21	4.29	-2.83	-	7.50	6.23
46	5.41	1.04	0.31	0.20	4.74	-2.62	-	8.16	8.11
47	4.01	1.18	0.36	0.34	-	-	-	-	-
48	5.55	0.96	0.28	0.18	-	-2.51	-	-	-
49	-	-	-	-	-	-	-	-	8.02
50	2.68	0.99	0.38	0.46	6.48	-1.70	-2.96	5.44	5.08
51	3.34	1.20	0.39	0.34	6.86	-1.84	-2.99	6.46	7.40

Table B.3: Infrared photometric data (continued)

Hen	K	$J-H$	$H-K$	$K-L$	$(V-K)_0$	$K-[12]$	$K-[25]$	m_{bot}	$m_{bot,V}$
103	-	-	-	-	-	-	-	-	-
104	4.21	1.08	0.25	0.24	5.51	-	-	7.16	6.92
105	4.75	1.04	0.32	0.32	-	-	-	-	-
106	-	-	-	-	-	-	-	-	7.96
107	4.88	1.17	0.44	-	6.78	-2.40	-	-	8.82
108	4.32	0.90	0.20	0.18	4.31	-2.64	-	7.12	7.03
109	6.25	0.56	0.40	1.51	-	-0.89	-2.27	-	-
110	-	-	-	-	-	-	-	-	8.45
111	-	-	-	-	-	-	-	-	8.47
112	-	-	-	-	-	-	-	-	-
113	5.15	1.29	0.34	0.20	5.63	-2.73	-	8.08	7.90
114	-	-	-	-	-	-	-	-	-
115	-	-	-	-	-	-	-	-	7.72
116	-	-	-	-	-	-	-	-	-
117	-	-	-	-	-	-	-	-	-
118	-	-	-	-	-	-	-	-	9.43
119	4.24	0.90	0.22	0.21	4.04	-2.64	-4.35	6.93	6.64
120	1.56	1.18	0.47	0.33	5.59	-2.12	-3.37	4.72	4.37
121	4.14	0.96	0.27	0.25	6.08	-2.69	-	7.10	7.58
122	5.21	0.96	0.27	-	8.52	-2.17	-	-	9.40
123	4.47	1.00	0.20	0.14	4.39	-2.79	-	7.27	6.92
124	6.06	0.91	0.24	0.01	5.13	-	-	8.93	9.25
125	3.73	0.86	0.42	0.54	6.63	-1.85	-3.20	6.75	6.42
126	5.35	0.99	0.24	0.24	4.80	-2.73	-	8.20	8.20
127	1.47	1.36	0.70	0.70	5.21	-2.55	-4.06	4.80	3.91
128	-	-	-	-	-	-	-	-	-
129	4.11	1.01	0.22	0.14	4.90	-2.67	-	6.97	7.07
130	4.34	1.18	0.32	0.27	6.07	-2.45	-3.67	7.35	7.58
131	4.26	1.19	0.36	0.36	6.53	-2.45	-3.59	7.24	7.93
132	4.14	1.04	0.22	0.22	4.67	-2.63	-4.16	6.98	6.85
133	3.60	0.97	0.27	0.09	5.00	-2.75	-4.11	6.48	6.64
134	6.20	0.84	0.28	0.23	5.21	-	-	9.10	8.64
135	0.58	1.15	0.36	0.37	6.21	-2.05	-3.12	3.69	4.01
136	3.62	1.51	0.66	0.66	6.88	-1.18	-1.52	6.83	6.05
137	3.59	0.97	0.26	0.18	5.29	-2.77	-4.34	6.52	6.95
138	-	-	-	-	-	-	-	-	4.44
139	-	-	-	-	-	-	-	-	7.91
140	2.72	1.03	0.28	0.16	5.15	-2.70	-4.23	5.62	5.06
141	0.44	1.07	0.36	0.30	7.85	-2.37	-3.66	3.40	3.90
142	6.92	0.87	0.00	0.36	4.12	1.29	0.31	9.39	6.65
143	3.89	0.90	0.21	0.17	4.41	-2.84	-4.34	6.70	6.38
144	3.18	1.15	0.37	0.33	7.87	-2.41	-3.59	6.19	6.66
145	-	-	-	-	-	-	-	-	8.29
146	2.51	1.14	0.36	0.30	7.22	-2.55	-3.92	5.45	5.31
147	5.84	0.86	0.17	0.08	4.40	-	-	8.58	8.63
148	-	-	-	-	-	-	-	-	-
149	4.72	0.97	0.17	-	4.48	-2.68	-	-	7.27
150	2.06	1.00	0.26	0.14	4.84	-2.76	-4.23	4.91	4.94
151	-	-	-	-	-	-	-	-	-
152	-	-	-	-	-	-	-	-	7.80
153	2.19	1.24	0.56	0.66	8.17	-1.44	-2.41	5.49	6.04

Table B.3: Infrared photometric data (continued)

Hen	K	$J-H$	$H-K$	$K-L$	$(V-K)_0$	$K-[12]$	$K-[25]$	m_{bol}	$m_{bol,V}$
154	–	–	–	–	–	–	–	–	–
155	3.68	1.00	0.45	0.39	–	-2.49	-3.81	–	–
156	–	–	–	–	–	–	–	–	5.05
157	2.50	1.15	0.32	0.42	6.64	-2.49	-3.77	5.57	6.36
158	5.49	1.16	0.31	0.37	7.03	0.13	-0.84	8.46	8.13
159	4.46	1.16	0.36	0.32	7.59	-2.50	-3.36	7.54	7.70
160	–	–	–	–	–	–	–	–	6.39
161	2.42	1.34	0.46	0.34	8.36	-2.32	-3.05	5.59	6.39
162	2.85	1.05	0.32	0.22	5.95	-2.51	-3.91	5.78	5.97
163	1.53	2.08	0.73	0.83	9.00	-0.83	-1.68	4.97	6.10
164	3.69	1.60	0.63	0.58	–	-1.52	-2.32	–	–
165	0.56	1.23	0.39	0.34	8.58	-2.13	-3.07	3.67	4.78
166	3.80	1.16	0.40	0.33	6.37	-2.48	-3.66	6.85	7.34
167	2.98	1.17	0.35	0.28	7.46	-2.57	-3.91	5.92	6.01
168	2.67	1.19	0.41	0.38	6.78	-2.42	-3.56	5.74	6.62
169	–	–	–	–	–	–	–	–	8.56
170	3.35	1.13	0.45	0.40	–	-2.02	-3.35	–	–
171	2.99	1.19	0.50	0.46	8.44	-1.71	-2.86	6.04	7.38
172	0.26	1.17	0.55	0.63	9.02	-1.21	-2.16	3.21	5.18
173	4.53	1.01	0.23	-0.04	4.71	–	–	7.29	7.24
174	3.81	1.04	0.41	–	6.15	-2.48	–	–	5.95
175	1.43	1.07	0.31	0.24	6.33	-2.62	-3.95	4.36	4.92
176	–	–	–	–	–	–	–	–	–
177	3.12	1.15	0.32	0.28	6.14	-2.43	–	6.07	6.42
178	–	–	–	–	–	–	–	–	4.63
179	3.71	1.00	0.22	0.12	5.17	-2.61	-4.02	6.60	6.93
180	4.62	1.78	0.78	0.68	–	-0.92	–	–	–
181	3.05	1.07	0.55	–	–	-1.88	–	–	–
182	3.04	0.97	0.24	0.19	4.95	-2.84	-4.02	5.90	6.36
183	3.47	1.31	0.23	–	4.77	-2.67	-4.22	–	6.63
184	–	–	–	–	–	–	–	–	6.98
185	4.57	1.09	0.28	0.03	5.48	–	–	7.34	7.16
186	3.28	0.85	0.25	0.18	4.58	-2.82	-4.15	6.08	6.24
187	3.40	0.99	0.22	0.16	4.80	-2.75	-4.27	6.27	6.26
188	3.23	1.15	0.33	0.35	6.22	-2.35	-3.50	6.22	6.62
189	–	–	–	–	–	–	–	–	8.90
190	–	–	–	–	–	–	–	–	8.72
191	2.66	1.04	0.30	0.28	6.97	-2.40	-3.54	5.68	5.29
192	–	–	–	–	–	–	–	–	–
193	4.74	1.03	0.25	0.14	4.52	-2.64	–	7.50	7.26
194	–	–	–	–	–	–	–	–	9.10
195	–	–	–	–	–	–	–	–	7.10
196	5.96	0.75	0.34	0.27	5.06	–	–	8.80	8.23
197	1.66	0.96	0.22	0.17	5.02	-2.77	-4.17	4.57	3.91
198	1.30	1.06	0.39	0.35	6.76	-1.73	-2.19	4.45	3.75
199	–	–	–	–	–	–	–	–	8.20
200	4.02	1.33	0.93	–	7.21	-0.81	-2.05	–	6.92
201	5.76	0.90	0.18	0.10	4.07	–	–	8.50	8.22
202	-2.12	1.14	0.43	0.44	8.57	-1.71	-2.50	1.07	2.13
203	5.01	0.86	0.23	0.21	4.55	-2.54	–	7.83	7.64
204	5.17	0.92	0.21	0.16	4.42	-2.84	–	7.99	7.99
205	4.99	1.00	0.25	0.19	5.35	–	–	7.93	8.41

Table B.4: Spectroscopic data and clustering results

Hen	I_{ZrO}	I_{TiO}	I_{NaD}	I_{LaO}	S/N	w	l	b	C_2	C_6	C_f
1	-	-	-	-	-	4.27	311.9	-53.7	1	2	e
2	-	-	-	-	-	4.59	300.6	-37.7	1	2	e
3	0.14	0.44	0.54	0.04	188	4.52	231.1	-40.9	1	2	e
4	0.08	0.23	0.43	0.06	182	3.37	297.5	-30.3	1	2	e
5	0.18	0.31	0.43	0.03	157	3.47	237.6	-32.3	1	2	e
6	0.17	0.43	0.55	0.05	233	3.61	258.3	-33.9	1	2	e
7	0.16	0.19	0.37	0.03	70	3.22	244.2	-26.5	1	1	e
8	0.28	0.34	0.46	0.03	188	3.15	246.5	-24.2	2	4	i
9	0.16	0.18	0.41	0.05	306	3.27	270.0	-28.2	1	2	e
10	0.22	0.39	0.54	0.06	192	3.27	296.3	-28.2	1	1	e
11	0.28	0.71	0.90	0.20	107	3.01	234.6	-15.8	2	6	i
12	0.20	0.33	0.42	0.03	174	3.10	252.2	-22.0	2	6	i
13	0.19	0.34	0.45	0.04	65	3.12	256.2	-22.6	1	2	e
14	0.18	0.21	0.43	0.05	157	3.03	243.6	-17.7	1	2	e
15	0.28	0.70	0.91	0.17	64	3.00	236.7	-14.8	2	6	i
16	0.15	0.35	0.47	0.04	125	3.05	247.8	-18.9	2	4	i
17	0.24	0.36	0.51	0.04	109	3.02	243.6	-16.7	1	2	e
18	0.27	0.36	0.47	0.02	139	2.96	239.9	-11.2	1	3	e
19	0.31	0.24	0.49	0.04	172	2.95	242.5	-8.7	2	4	i
20	0.17	0.44	0.54	0.04	155	2.99	256.8	-14.1	2	4	i
21	0.30	0.54	0.72	0.10	186	2.94	244.6	-7.3	2	6	i
22	0.06	0.09	0.34	0.06	90	3.01	265.2	-16.5	0		-
23	0.50	0.28	0.66	0.13	123	2.94	244.6	-6.3	2	6	i
24	0.36	0.40	0.73	0.08	201	2.94	247.8	-7.1	2	6	i
25	0.27	0.77	0.90	0.20	81	3.04	271.6	-18.3	2	6	i
26	-	-	-	-	-	2.92	239.0	-1.3	0		-
27	0.49	0.21	0.84	0.18	79	3.19	294.8	-25.7	2	6	i
28	0.27	0.21	0.44	0.06	219	3.10	282.1	-21.6	1	2	e
29	0.37	0.17	0.77	0.05	169	2.92	241.2	-1.6	2	4	i
30	0.51	0.33	0.76	0.20	119	2.93	245.9	-3.0	2	6	i
31	0.16	0.21	0.41	0.04	172	3.01	273.2	-16.3	1	2	e
32	0.28	0.82	0.94	0.13	171	2.95	258.5	-8.3	2	6	i
33	0.57	0.39	0.99	0.56	31	2.92	246.2	-0.5	0		i
34	0.17	0.53	0.62	0.04	215	3.03	277.9	-17.9	2	6	i
35	0.14	0.14	0.44	0.07	243	3.08	283.8	-20.6	1	2	e
36	0.16	0.39	0.48	0.03	210	2.92	248.4	-1.0	2	5	i
37	0.15	0.50	0.59	0.02	218	2.93	257.5	-5.9	2	4	i
38	0.18	0.39	0.50	0.05	194	2.94	258.4	-6.4	2	4	i
39	0.18	0.42	0.52	0.04	95	3.03	278.6	-17.7	2	4	i
40	0.12	0.43	0.59	0.04	211	2.92	248.5	0.9	2	5	i
41	0.21	0.38	0.50	0.03	202	2.93	246.7	2.8	2	5	i
42	0.44	0.21	0.81	0.17	104	2.92	249.2	1.2	2	4	i
43	0.25	0.31	0.51	0.03	237	2.93	245.8	4.5	1	1	e
44	0.24	0.40	0.51	0.03	207	2.93	248.8	3.1	2	4	i
45	0.17	0.24	0.46	0.05	147	2.92	251.2	1.5	2	4	i
46	0.29	0.28	0.50	0.05	126	2.92	255.3	-0.4	2	2	e
47	0.52	0.29	0.88	0.10	118	2.92	254.5	1.0	2	4	i
48	0.24	0.41	0.55	0.02	155	2.93	250.6	5.5	2	4	i
49	0.38	0.18	0.90	0.14	94	2.92	257.8	0.4	2	4	i
50	0.25	0.67	0.79	0.41	49	2.93	256.3	2.3	2	5	i
51	0.42	0.19	0.89	0.30	122	2.93	268.8	-6.0	2	4	i

Table B.4: Spectroscopic data and clustering results (continued)

Hen	I_{ZrO}	I_{TiO}	I_{NaD}	I_{LaO}	S/N	w	l	b	C_2	C_6	C_f
52	0.20	0.30	0.46	0.05	97	2.93	267.2	-4.7	1	2	e
53	0.45	0.39	0.84	0.18	127	2.92	259.1	1.7	2	6	i
54	0.59	0.43	0.78	0.03	147	2.93	254.1	6.0	2	6	i
55	0.36	0.19	0.94	0.16	108	2.92	265.2	-1.7	2	6	i
56	0.29	0.45	0.59	0.04	169	2.95	274.2	-8.3	2	5	i
57	0.23	0.44	0.54	0.03	162	2.93	269.1	-4.2	2	4	i
58	0.09	0.27	0.43	0.05	71	2.92	266.5	-1.0	1	1	e
59	0.20	0.32	0.44	0.04	98	3.01	286.1	-16.5	1	2	e
60	-	-	-	-	-	2.95	277.6	-9.4	0		-
61	0.20	0.18	0.42	0.06	60	2.93	262.8	4.0	1	2	e
62	0.40	0.18	0.87	0.20	78	2.93	263.5	4.3	2	6	i
63	0.12	0.29	0.48	0.04	271	2.95	258.2	9.3	1	2	e
64	0.51	0.30	0.72	0.09	179	2.97	254.8	12.4	2	4	i
65	0.15	0.38	0.53	0.04	227	2.93	264.6	3.8	1	2	e
66	0.16	0.39	0.52	0.03	152	2.95	259.1	9.0	2	4	i
67	0.10	0.41	0.50	0.04	146	3.11	296.1	-22.3	2	2	e
68	0.49	0.22	0.97	0.37	73	2.92	276.3	-1.5	2	6	i
69	0.53	0.30	0.84	0.19	124	2.95	284.5	-10.0	2	6	i
70	0.19	0.38	0.52	0.03	133	2.93	272.3	4.5	1	2	e
71	0.19	0.22	0.45	0.05	110	2.95	284.0	-8.6	1	2	e
72	0.36	0.21	0.93	0.26	128	2.94	283.5	-8.0	2	6	i
73	0.29	0.63	0.75	0.05	86	2.93	273.0	4.9	2	6	i
74	0.16	0.21	0.41	0.05	82	2.93	282.4	-5.9	1	1	e
75	0.51	0.28	0.88	0.17	65	2.94	284.3	-7.7	2	6	i
76	0.18	0.22	0.47	0.06	142	3.02	265.2	16.9	1	2	e
77	0.23	0.36	0.48	0.04	112	2.93	276.4	4.0	2	4	i
78	0.44	0.23	0.93	0.25	159	2.94	275.1	6.9	2	6	i
79	0.16	0.35	0.51	0.08	164	2.96	288.4	-10.7	1	2	e
80	0.33	0.56	0.70	0.05	205	2.97	289.4	-12.0	2	6	i
81	0.41	0.17	0.72	0.25	43	2.93	283.9	-4.4	2	6	i
82	0.27	0.15	0.59	0.07	116	2.93	284.3	-5.0	2	5	i
83	0.23	0.17	0.52	0.07	77	2.93	278.5	3.2	1	1	e
84	0.23	0.15	0.95	0.07	108	2.93	283.4	-3.5	2	6	i
85	0.27	0.49	0.63	0.07	143	2.94	275.3	7.7	2	6	i
86	0.23	0.24	0.48	0.04	144	2.97	271.8	12.4	1	1	e
87	0.32	0.20	0.97	0.23	151	2.93	284.0	-4.1	2	4	i
88	0.17	0.42	0.52	0.04	224	3.08	267.2	21.0	2	4	i
89	0.17	0.37	0.52	0.07	234	2.93	284.8	-3.6	2	4	i
90	0.22	0.28	0.47	0.05	158	2.92	281.5	1.7	1	2	e
91	0.25	0.72	0.92	0.15	115	2.95	277.6	9.3	2	6	i
92	0.24	0.38	0.53	0.04	141	2.93	281.4	4.7	2	4	i
93	0.50	0.29	0.80	0.24	172	2.94	289.9	-7.9	2	6	i
94	0.45	0.22	0.89	0.20	69	2.92	287.0	-1.9	2	6	i
95	0.18	0.46	0.55	0.05	259	2.92	286.9	-1.7	2	4	i
96	0.47	0.23	0.87	0.25	79	2.93	283.5	4.8	2	4	i
97	0.21	0.43	0.55	0.05	185	2.93	283.1	5.9	2	4	i
98	0.26	0.42	0.53	0.04	155	2.92	285.6	2.0	2	4	i
99	0.39	0.29	0.87	0.10	230	2.93	284.9	3.5	2	6	i
100	0.30	0.24	0.93	0.08	157	2.92	287.1	-0.5	2	4	i
101	0.30	0.58	0.77	0.09	102	3.08	275.2	20.9	2	6	i
102	0.14	0.41	0.56	0.04	52	2.92	287.4	-0.6	0		-

Table B.4: Spectroscopic data and clustering results (continued)

Hen	I_{ZrO}	I_{TiO}	I_{NaD}	I_{LaO}	S/N	w	l	b	C_2	C_6	C_f
103	0.39	0.32	0.88	0.16	71	5.85	288.1	0.0	2	6	i
104	0.17	0.41	0.55	0.05	155	2.93	285.8	6.1	2	4	i
105	0.22	0.38	0.52	0.05	92	2.92	289.1	-0.7	2	4	i
106	0.17	0.43	0.56	0.05	96	2.92	290.2	-2.1	2	4	i
107	0.44	0.21	0.88	0.21	75	2.93	287.9	3.3	2	4	i
108	0.14	0.26	0.50	0.06	293	2.93	287.8	3.6	1	1	e
109	0.28	0.55	0.66	0.04	165	2.94	293.3	-7.5	2	6	i
110	0.14	0.19	0.45	0.05	173	2.92	290.6	-1.4	1	2	e
111	0.44	0.19	0.89	0.24	134	2.92	290.2	0.3	2	4	i
112	0.14	0.71	0.88	0.05	108	2.95	286.9	9.7	2	6	i
113	0.24	0.32	0.50	0.04	139	2.93	293.4	-4.8	2	4	i
114	0.60	0.34	0.90	0.12	172	2.92	292.1	-0.7	2	6	i
115	0.47	0.26	0.73	0.13	84	5.85	292.3	0.0	2	6	i
116	-	-	-	-	-	2.93	296.4	-3.3	0	-	-
117	0.28	0.15	0.82	0.07	121	2.93	295.3	2.2	2	4	i
118	0.16	0.22	0.39	0.06	112	3.10	291.7	21.7	1	2	e
119	0.20	0.24	0.49	0.05	267	2.94	295.4	6.3	1	1	e
120	0.25	0.21	0.97	0.09	174	2.94	297.6	6.5	2	4	i
121	0.24	0.42	0.51	0.04	102	3.66	295.0	34.4	1	3	e
122	0.59	0.51	0.86	0.40	64	2.96	298.6	10.5	2	6	i
123	0.13	0.24	0.42	0.04	217	3.00	298.5	15.1	1	2	e
124	0.23	0.39	0.49	0.05	192	3.07	298.9	20.4	1	2	e
125	0.21	0.57	0.72	0.10	198	3.95	299.0	36.4	2	5	i
126	0.19	0.32	0.49	0.04	206	2.95	301.3	9.4	1	2	e
127	0.08	0.38	0.51	0.03	143	3.22	303.0	-26.7	2	4	i
128	0.35	0.15	0.89	0.39	67	3.07	302.0	20.1	2	6	i
129	0.25	0.29	0.46	0.05	260	3.01	302.8	16.0	1	2	e
130	0.49	0.23	0.82	0.18	152	2.93	303.6	-3.8	2	4	i
131	0.26	0.37	0.58	0.04	124	2.93	304.0	2.2	2	4	i
132	0.24	0.23	0.50	0.05	164	2.95	304.1	-10.1	1	2	e
133	0.24	0.31	0.47	0.06	203	2.93	305.4	6.1	1	2	e
134	0.19	0.35	0.43	0.03	105	3.43	308.1	31.5	2	4	i
135	0.24	0.14	0.91	0.06	129	3.04	307.1	18.3	2	4	i
136	0.51	0.27	0.99	0.47	44	2.92	306.4	-0.4	2	6	i
137	0.15	0.38	0.52	0.05	252	2.97	309.6	11.4	1	2	e
138	0.15	0.41	0.52	0.03	172	2.95	306.6	-9.1	1	2	e
139	0.17	0.41	0.54	0.05	88	2.93	308.1	-5.5	2	4	i
140	0.14	0.39	0.55	0.06	171	2.94	310.7	6.9	2	4	i
141	0.29	0.60	0.78	0.07	175	2.92	309.9	2.0	2	6	i
142	0.75	0.60	1.03	0.46	28	2.93	308.7	-4.8	2	6	i
143	0.15	0.28	0.51	0.07	178	3.05	316.4	19.3	1	2	e
144	0.45	0.47	0.76	0.14	148	2.93	312.5	2.4	2	6	i
145	0.21	0.38	0.54	0.06	100	2.92	312.9	1.3	2	4	i
146	0.42	0.46	0.67	0.09	176	2.93	312.6	-2.6	2	6	i
147	0.19	0.27	0.45	0.04	198	3.45	329.1	31.9	1	1	e
148	0.35	0.18	0.87	0.12	154	2.92	315.4	-0.8	2	6	i
149	0.20	0.28	0.46	0.06	159	3.06	327.1	19.5	1	2	e
150	0.16	0.35	0.51	0.03	134	2.92	317.0	-1.3	1	2	e
151	0.57	0.37	0.89	0.22	77	2.93	316.2	-3.6	2	6	i
152	0.43	0.17	0.95	0.32	51	2.93	320.2	3.7	2	6	i
153	0.42	0.18	0.93	0.45	119	3.00	327.9	15.1	2	6	i

Table B.4: Spectroscopic data and clustering results (continued)

Hen	I_{ZrO}	I_{TiO}	I_{NaD}	I_{LaO}	S/N	w	l	b	C_2	C_6	C_f
154	0.05	0.06	0.22	0.07	152	2.97	312.8	-12.0	0		-
155	0.52	0.25	0.76	0.19	144	3.07	335.9	20.3	2	6	i
156	0.46	0.68	0.85	0.09	125	2.92	326.0	0.1	2	6	i
157	0.31	0.14	0.96	0.07	245	3.01	314.5	-15.8	2	4	i
158	0.44	0.22	0.98	0.24	70	2.92	328.3	-1.5	2	6	i
159	-	-	-	-	-	2.94	323.2	-8.2	2	6	i
160	0.22	0.75	0.90	0.23	74	2.94	324.1	-7.5	2	6	i
161	0.51	0.28	0.90	0.14	88	3.00	349.2	15.4	2	6	i
162	0.21	0.42	0.54	0.03	249	2.93	329.5	-4.7	2	4	i
163	-	-	-	-	-	2.92	334.4	-1.5	2	6	i
164	0.77	0.64	1.08	0.25	64	2.92	335.1	-0.9	2	6	i
165	0.48	0.37	0.81	0.22	167	2.96	348.9	11.3	2	6	i
166	-	-	-	-	-	2.94	329.9	-7.0	2	4	i
167	-	-	-	-	-	2.93	331.3	-5.9	2	6	i
168	-	-	-	-	-	2.95	327.9	-10.1	2	4	i
169	-	-	-	-	-	3.02	321.1	-16.7	1	2	e
170	-	-	-	-	-	2.96	329.3	-10.3	2	6	i
171	-	-	-	-	-	2.94	334.4	-6.3	2	5	i
172	-	-	-	-	-	2.93	348.0	3.5	2	5	i
173	-	-	-	-	-	2.93	353.0	4.4	1	2	e
174	-	-	-	-	-	2.95	1.3	8.5	2	5	i
175	-	-	-	-	-	2.93	346.3	-2.4	2	4	i
176	-	-	-	-	-	2.93	356.5	4.8	0		i
177	-	-	-	-	-	2.93	353.7	2.3	2	4	i
178	-	-	-	-	-	2.93	357.4	4.9	2	5	i
179	-	-	-	-	-	2.97	337.8	-11.8	1	2	e
180	-	-	-	-	-	2.92	0.9	-0.1	2	6	i
181	-	-	-	-	-	2.93	355.1	-3.8	2	5	i
182	-	-	-	-	-	2.93	360.0	-2.7	1	1	e
183	-	-	-	-	-	3.05	328.7	-19.4	1	1	e
184	-	-	-	-	-	2.92	4.5	-1.8	2	4	i
185	-	-	-	-	-	2.92	4.7	-1.5	2	4	i
186	-	-	-	-	-	2.94	355.1	-7.7	1	1	e
187	-	-	-	-	-	3.08	326.3	-21.0	1	2	e
188	-	-	-	-	-	2.94	355.9	-7.9	2	4	i
189	-	-	-	-	-	2.99	344.8	-14.4	2	2	e
190	-	-	-	-	-	2.95	0.4	-9.3	1	2	e
191	-	-	-	-	-	2.97	358.6	-11.6	2	6	i
192	-	-	-	-	-	2.97	0.0	-12.0	0		i
193	-	-	-	-	-	2.95	10.7	-8.7	1	2	e
194	-	-	-	-	-	3.09	358.5	-21.2	1	2	e
195	-	-	-	-	-	3.17	347.0	-24.8	2	6	i
196	-	-	-	-	-	3.18	7.9	-25.3	2	4	i
197	-	-	-	-	-	3.53	334.2	-32.9	2	4	i
198	-	-	-	-	-	3.49	355.4	-32.5	2	6	i
199	-	-	-	-	-	3.63	0.3	-34.1	1	2	e
200	-	-	-	-	-	4.47	350.7	-43.8	2	6	i
201	-	-	-	-	-	4.43	22.5	-45.4	1	1	e
202	-	-	-	-	-	4.25	350.2	-54.5	2	6	i
203	-	-	-	-	-	4.32	338.0	-51.3	1	2	e
204	-	-	-	-	-	4.17	349.4	-58.6	1	1	e
205	-	-	-	-	-	3.38	304.8	-30.7	1	2	e

References

- Aaronson M., Mould J., Cook K. H., 1985, *ApJ* 291, L41
Abia C., Boffin H. J. M., Isern J., Rebelo R., 1993, *A&A* 272, 455
Abia C., Wallerstein G., 1998, *MNRAS* 293, 89
Acker A., Chopinet M., Pottasch S. R., Stenholm B., 1987, *A&AS* 71, 163
Ake T. B., 1979, *ApJ* 234, 538
Ake T. B., Johnson H. R., 1988, *ApJ* 327, 214
Ake T. B., Johnson H. R., 1992, American Astronomical Society Meeting 180, 3708
Ake T. B., Johnson H. R., Ameen M. M., 1991, *ApJ* 383, 842
Ake T. B., Jorissen A., Johnson H. R., Mayor M., Bopp B., 1992, *BAAS* 24, 1280
Alksnis A., Balklavs A., Dzervitis U., Eglitis I., 1998, *A&A* 338, 209
Arenou F., Grenon M., Gómez A., 1992, *A&A* 258, 104
Arenou F., Lindegren L., Froeschle M., Gomez A. E., Turon C., Perryman M. A. C., Wielen R., 1995, *A&A* 304, 52
Arhipova V. P., Noskova R. I., 1985, *Sov. Astron. Lett.* 11, 297
Arnould M., 1991, in G. Michaud, A. Tutukov (eds.), *Evolution of stars: the photospheric abundance connection (IAU Symp. 145)*, Kluwer, Dordrecht, 287
Arnould M., Takahashi K., 1999, *Rep. Prog. Phys.* 62, 395
Baranne A., Mayor M., Poncet J. L., 1979, *Vistas in Astronomy* 23, 279
Barbier M., Petit H., Mayor M., Mennessier M. O., 1988, *A&AS* 72, 463
Barblan F., Bartholdi P., North P., Burki G., Olson E., 1998, *A&AS* 132, 367
Barnbaum C., Kastner J. H., Morris M., Likkell L., 1991, *A&A* 251, 79
Barnbaum C., Morris M., 1993, American Astronomical Society Meeting 182, 4617
Battrock B. (ed.), 1997, *Hipparcos - Venice '97*, ESA SP-402, ESA
Beckwith S., Evans, N. J. I., Becklin E. E., Neugebauer G., 1976, *ApJ* 208, 390
Berdyugina S. V., 1994, *Pi'sma Astron. J.* 20, 910
Bergeat J., Knapik A., 1997, *A&A* 321, L9
Bernasconi P. A., 1996, *A&AS* 120, 57
Bessell M. S., Castelli F., Plez B., 1998, *A&A* 333, 231
Bessell M. S., Wood P. R., 1984, *PASP* 96, 247
Bessell M. S., Wood P. R., Evans T. L., 1983, *MNRAS* 202, 59
Bidelman W. P., 1985a, *AJ* 90, 341

- Bidelman W. P., 1985b, in Jaschek & Keenan 1985, 43
Bidelman W. P., Keenan P. C., 1951, *ApJ* 114, 473
Biegging J. H., Latter W. B., 1994, *ApJ* 422, 765
Blanco V. M., Blanco B. M., McCarthy M. F., 1980, *ApJ* 242, 938
Blöcker T., 1995, *A&A* 297, 727
Blöcker T., 1999, in Le Bertre et al. 1999, 21
Boesgaard A. M., 1969, *PASP* 81, 283
Boesgaard A. M., Fesen R. A., 1974, *PASP* 86, 76
Boffin H. M. J., Cerf N., Paulus G., 1993, *A&A* 271, 125
Boffin H. M. J., Jorissen A., 1988, *A&A* 205, 155
Böhm-Vitense E., Johnson H. R., 1985, *ApJ* 293, 288
Böhm-Vitense E., Nemeč J., Proffitt C., 1984, *ApJ* 278, 726
Bolton C. T., 1975, *ApJ* 200, 269
Bond H. E., 1974, *ApJ* 194, 95
Bond H. E., 1984, in J.-M. Mead, R. D. Chapman, Y. Kondo (eds.), *Future of Ultraviolet Astronomy based on six years of IUE Research*, NASA CP 2349, Greenbelt, 289
Bondi H., Hoyle F., 1944, *MNRAS* 104, 273
Boothroyd A. I., Sackmann I. J., 1988, *ApJ* 328, 632
Boothroyd A. I., Sackmann I.-J., Ahern S. C., 1993, *ApJ* 416, 762
Boothroyd A. I., Sackmann I.-J., Wasserburg G. J., 1995, *ApJ* 442, L21
Brewer J. P., Richer H. B., Crabtree D. R., 1996, *AJ* 112, 491
Brown A. G. A., Arenou F., van Leeuwen F., Lindegren L., Luri X., 1997, in Battrick 1997, 63
Brown J. A., Smith V. V., Lambert D. L., Dutchover E. J., Hinkle K. H., Johnson H. R., 1990, *AJ* 99, 1930
Burbidge E. M., Burbidge G. R., 1957, *ApJ* 126, 357
Burbidge E. M., Burbidge G. R., Fowler W. A., Hoyle F., 1957, *Rev. Mod. Phys.* 29, 4
Burns D., Baldwin J. E., Boysen R. C., Haniff C. A., Lawson P. R., Mackay C. D., Rogers J., Scott T. R., St.-Jacques D., Warner P. J., Wilson D. M. A., Young J. S., 1998, *MNRAS* 297, 462
Burstein D., Heiles C., 1982, *AJ* 87, 1165
Busso M., Gallino R., Lambert D. L., Raiteri C. M., Smith V. V., 1992, *ApJ* 399, 218
Busso M., Lambert D. L., Beglio L., Gallino R., Raiteri C. M., Smith V. V., 1995, *ApJ* 446, 775
Cameron A. J. W., Fowler W. A., 1971, *ApJ* 164, 111
Carquillat J. M., Jorissen A., Udry S., Ginestet N., 1998, *A&AS* 131, 49
Catchpole R. M., Feast M. W., 1971, *MNRAS* 154, 197
Catchpole R. M., Feast M. W., 1976, *MNRAS* 175, 501
Catchpole R. M., Robertson B. S. C., Lloyd Evans T. H. H., Feast M. W., Glass I. S., Carter B., 1979, *Circulars of the South African Astronomical Observatory* 1, 61
Catchpole R. M., Robertson B. S. C., Warren P. R., 1977, *MNRAS* 181, 391
Cerf N., Boffin H. M. J., 1994, *Inverse Problems* 10, 533

- Chabrier G., Baraffe I., 1997, *A&A* 327, 1039
- Charbonnel C., Meynet G., Maeder A., Schaerer D., 1996, *A&AS* 115, 339
- Chen P. S., Gao H., A. J., 1995, *A&AS* 113, 51
- Chen P. S., Gao H., Chen Y. K., Dong H. W., 1988, *A&AS* 72, 239
- Chen P. S., Kwok S., 1993, *ApJ* 416, 769
- Chen P. S., Wang X. H., Xiong G. Z., 1998, *A&A* 333, 613
- Claussen M. J., Kleinmann S. G., Joyce R. R., Jura M., 1987, *ApJS* 65, 385
- Clayton D. D., 1988, *MNRAS* 234, 1
- Cohen J. G., Persson S. E., Elias J. H., Frogel J. A., 1981, *ApJ* 249, 481
- Cosner K. R., Despain K. H., Truran J. W., 1984, *ApJ* 283, 313
- Côté P., Hanes D. A., McLaughlin D. E., Bridges T. J., Hesser J. E., Harris G. L. H., 1997, *ApJ* 476, L15
- Cowley A. P., Hartwick F. D. A., 1991, *ApJ* 373, 80
- Cramer N., 1994, Ph.D. thesis, Observatoire de Genève, Sauverny, Switzerland
- Culver R. B., Ianna P. A., 1975, *ApJ* 195, L37
- De Jong T., 1989, *A&A* 223, L23
- De Kool M., 1992, *A&A* 261, 188
- De Kool M., Green P. J., 1995, *ApJ* 449, 236
- Dean C. A., 1976, *AJ* 81, 364
- Dominy J. F., 1984, *ApJS* 55, 27
- Dominy J. F., 1985, *PASP* 97, 1104
- Dominy J. F., Lambert D. L., 1983, *ApJ* 270, 180
- Duquennoy A., Mayor M., 1991, *A&A* 248, 485
- Duquennoy A., Mayor M. (eds.), 1992, *Binaries as tracers of stellar formation*, Cambridge Univ. Press, Cambridge
- Duquennoy A., Mayor M., Halbwachs J.-L., 1991, *A&AS* 88, 281
- Duquennoy A., Mayor M., Mermilliod J.-C., 1992, in *Duquennoy & Mayor 1992*, 52
- Edvardsson B., Andersen J., Gustafsson B., Lambert D. L., Nissen P. E., Tomkin J., 1993, *A&A* 275, 101
- Eggen O. J., 1972a, *ApJ* 177, 489
- Eggen O. J., 1972b, *PASP* 84, 406
- Eggleton P. P., 1983, *ApJ* 268, 368
- ESA, 1997, in *The Hipparcos and Tycho Catalogues*, ESA SP-1200
- Eyer L., Grenon M., 1997, in *Batrick 1997*, 467
- Feast M. W., 1953, *MNRAS* 113, 510
- Feast M. W., Catchpole R. M., Glass I. S., 1976, *MNRAS* 174, 81
- Feast M. W., Robertson B. S. C., Catchpole R. M., Evans T. L., Glass I. S., Carter B. S., 1982, *MNRAS* 201, 439
- Feast M. W., Whitelock P. A., Carter B. S., 1990, *MNRAS* 247, 227
- Fekel F. C., Henry G. W., Busby M. R., Eitter J. J., 1993, *AJ* 106, 2370
- Feltzing S., Gustafsson B., 1998, *A&AS* 129, 237
- Fischer D. A., Marcy G. W., 1992, *ApJ* 396, 178
- Forestini M., 1991, Ph.D. thesis, Université Libre de Bruxelles, Brussels, Belgium

- Fouqué P., Le Bertre T., Epchtein N., Guglielmo F., Kerschbaum F., 1992, *A&AS* 93, 151
- Frogel J. A., Elias J. H., 1988, *ApJ* 324, 823
- Frost C. A., Cannon R. C., Lattanzio J. C., Wood P. R., Forestini M., 1998, *A&A* 332, L17
- Gallino R., Arlandini C., Busso M., Lugaro M., Travaglio C., Straniero O., Chieffi A., Limongi M., 1998, *ApJ* 497, 388
- García-Berro E., Ritossa C., Iben, Jr I., 1997, *ApJ* 485, 765
- Gass H., Wehrse R., Liebert J., 1988, *A&A* 189, 194
- Gillett F. C., Merrill K. M., Stein W. A., 1971, *ApJ* 164, 83
- Gilmore G., Reid N., 1983, *MNRAS* 202, 1025
- Glass I. S., Feast M. W., 1973, *MNRAS* 163, 245
- Golay M., 1980, *Vistas in Astron.* 24, 141
- Goriely S., 1999, in P. Magain, A. Noels (eds.), *The Galactic Halo : from Globular Clusters to Field Stars*, 35th Liege International Astrophysics Colloquium
- Gray R. F., 1988, *Lectures on spectral-line analysis: F, G and K stars*, The Publisher, Arva (Ontario)
- Green P. J., Margon B., 1994, *ApJ* 423, 723
- Green P. J., Margon B., Anderson S. F., Cook K. H., 1994, *ApJ* 434, 319
- Green P. J., Margon B., Anderson S. F., Macconnell D. J., 1992, *ApJ* 400, 659
- Green P. J., Margon B., Macconnell D. J., 1991, *ApJ* 380, L31
- Grenon M., 1978, Ph.D. thesis, Observatoire de Genève
- Griffin R., Griffin R., 1980, *MNRAS* 193, 957
- Griffin R. F., 1984, *The Observatory* 104, 224
- Griffin R. F., 1991, *The Observatory* 111, 29
- Griffin R. F., 1996, *The Observatory* 116, 398
- Griffin R. F., Jorissen A., Mayor M., 1996, *The Observatory* 116, 298
- Griffin R. F., Keenan P., 1992, *The Observatory* 112, 168
- Groenewegen M. A. T., 1993, *A&A* 271, 180
- Groenewegen M. A. T., 1999, in Le Bertre et al. 1999, 535
- Guglielmo F., Le Bertre T., Epchtein N., 1998, *A&A* 334, 609
- Habing H. J., 1987, in I. Appenzeller, C. Jordan (eds.), *Circumstellar Matter*, I.A.U. Symp. 122, D. Reidel Publishing Company, 197
- Habing H. J., 1996, *Ann. Rev. Astron. Astrophys.* 7, 97
- Hacking P., Neugebauer G., Emerson J., Beichman C., Chester T., Gillett F., Habing H., Helou G., Houck J., Olton F., Rowan-Robinson M., Soifer B. T., Walker D., 1985, *PASP* 97, 616
- Hackos W. J., Peery B. F. J., 1968, *AJ* 73, 504
- Hakkila J., McNamara B. J., 1987, *A&A* 186, 255
- Han Z., Eggleton P. P., Podsiadlowski P., Tout C. A., 1995, *MNRAS* 277, 1443
- Hanson R. B., 1979, *MNRAS* 186, 875
- Hartwick F. D. A., Cowley A. P., 1988, *ApJ* 334, 135
- Heber U., Bade N., Jordan S., Voges W., 1993, *A&A* 267, L31
- Henize K., 1960, *AJ* 65, 491
- Henize K. K., 1954, Ph.D. thesis, University of Michigan

- Herbig G. H., 1965, *Kleine Veroff. Reimis-Sternwarte* 4 Nr 40, 164
- Herwig F., Blöcker T., Schönberner D., El Eid M., 1997, *A&A* 324, L81
- Hinkle K., Fekel F., Joyce R., 1999, in Le Bertre et al. 1999
- Hjellming M. S., 1989, Ph.D. thesis, Univ. Illinois, Urbana-Champaign
- Hjellming M. S., Webbink R. F., 1987, *ApJ* 318, 794
- Hoffleit D., Jaschek C., 1991, *The Bright star catalogue*, 5th rev. ed., Yale University Observatory, New Haven
- Horne K., 1986, *PASP* 98, 609
- Houk N., 1978, in *Michigan Spectral Survey*, Ann Arbor, Dep. Astron., Univ. Michigan, 2 (1978), p. 0
- Houk N., 1982, in *Michigan Spectral Survey*, Ann Arbor, Dep. Astron., Univ. Michigan, 3 (1982), p. 0
- Houk N., Cowley A. P., 1975, in *Michigan Spectral Survey*, Ann Arbor, Dep. Astron., Univ. Michigan, 1 (1975), p. 0
- Houk N., Smith-Moore M., 1988, in *Michigan Spectral Survey*, Ann Arbor, Dept. of Astronomy, Univ. Michigan (Vol. 4) (1988), p. 0
- Hrivnak B. J., 1999, in *Wing 1999*, in press
- Hron J., 1993, in R. Weinberger, A. Acker (eds.), *Planetary Nebulae (IAU Symp. 155)*, Kluwer, Dordrecht, p. 327
- Iben, Jr I., 1981, *ApJ* 246, 278
- Iben, Jr I., 1991, *ApJS* 76, 55
- Iben, Jr I., Livio M., 1993, *PASP* 105, 1373
- Iben, Jr I., Renzini A., 1983, *Ann. Rev. Astron. Astrophys.* 21, 271
- Iben, Jr I., Ritossa C., García-Berro E., 1997, *ApJ* 489, 772
- Iben, Jr I., Tutukov A. V., 1993, *ApJ* 418, 343
- IRAS Science Team, 1988, in *IRAS Point Source Catalogue*, prepared by Beichman, C.A., Neugebauer, G., Habing, H.J., Clegg, P.E., NASA-RP 1190
- Jaschek C., Jaschek M., 1987, *The Classification of Stars*, Cambridge Univ. Press, Cambridge
- Jaschek M., 1978, *Bull. Inf. CDS* 15, 121
- Jaschek M., Keenan P. C. (eds.), 1985, *Cool Stars with Excesses of Heavy Elements*, Reidel, Dordrecht
- Jeffries R. D., Burleigh M. R., Robb R. M., 1996, *A&A* 305, L45
- Jeffries R. D., Smalley B., 1996, *A&A* 315, L19
- Jeffries R. D., Stevens I. R., 1996, *MNRAS* 279, 180
- Johnson H. L., 1966, *ARA&A* 4, 193
- Johnson H. R., Ake T. B., Ameen M. M., 1993, *ApJ* 402, 667
- Jorissen A., 1997, in J. Mikolajewska (ed.), *Physical Processes in Symbiotic Binaries and Related Systems*, Publ. Copernicus Foundation for Polish Astron., Warsaw, 135
- Jorissen A., 1999, in Le Bertre et al. 1999, 437
- Jorissen A., Boffin H. M. J., 1992, in Duquennoy & Mayor 1992, 110
- Jorissen A., Frayer D. T., Johnson H. R., Mayor M., Smith V. V., 1993, *A&A* 271, 463
- Jorissen A., Hennen O., Mayor M., Bruch A., Sterken C., 1995, *A&A* 301, 707
- Jorissen A., Knapp G. R., 1998, *A&A* 129, 363

- Jorissen A., Mayor M., 1988, *A&A* 198, 187
Jorissen A., Mayor M., 1992, *A&A* 260, 115
Jorissen A., Mowlavi N., Sterken C., Manfroid J., 1997, *A&A* 324, 578
Jorissen A., Schmitt J. H. M. M., Carquillat J. M., Ginestet N., Bickert K. F., 1996, *A&A* 306, 467
Jorissen A., Van Eck S., 1999, in Wing 1999, in press
Jorissen A., Van Eck S., Mayor M., Udry S., 1998, *A&A* 332, 877
Jura M., 1988, *ApJS* 66, 33
Jura M., 1994, *ApJ* 422, 102
Jura M., Kleinmann S. G., 1992a, *ApJS* 83, 329
Jura M., Kleinmann S. G., 1992b, *ApJS* 79, 105
Kaper L., Pasquini L., 1996, CAT+CES Operating Manual 3p6; CAT-MAN-0633-0001, ESO
Käppeler F., Beer H., Wisshak K., 1989, *Rep. Prog. Phys.* 52, 945
Kastner J. H., Forveille T., Zuckerman B., Omont A., 1993, *A&A* 275, 163
Kaufman L., Rousseeuw P. J., 1990, Finding groups in data: an introduction to cluster analysis, Wiley series in probability and statistics, A Wiley-Interscience publication, John Wiley & Sons, Inc., New York
Keenan P. C., 1942, *ApJ* 96, 101
Keenan P. C., 1950, *AJ* 55, 172
Keenan P. C., 1954, *ApJ* 120, 484
Keenan P. C., 1993, *PASP* 105, 905
Keenan P. C., Boeshaar P. C., 1980, *ApJS* 43, 379
Keenan P. C., McNeil R. C., 1976, *An Atlas of Spectra of the Cooler Stars*, Ohio State University Press, Columbus
Keenan P. C., McNeil R. C., 1989, *ApJS* 71, 245
Keenan P. C., Morgan W. W., 1941, *ApJ* 94, 501
Keenan P. C., Pitts R. E., 1980, *ApJS* 42, 541
Keenan P. C., Wilson O. C., 1977, *ApJ* 214, 399
Kellett B. J., Bromage G. E., Brown A., Jeffries R. D., James D. J., Kilkenny D., Robb R. M., Wonnacott D., Lloyd C., Clayton C., 1995, *ApJ* 438, 364
Kenyon S. J., 1986, *The Symbiotic Stars*, Cambridge Univ. Press, Cambridge
Kerschbaum F., Hron J., 1992, *A&A* 263, 97
Kholopov P. N., Samus N. N., Frolov M. S., Goranskij V. P., Gorynya N. A., Karitskaya E. A., Kazarovets E. V., Kireeva N. N., Kukarkina N. P., Kurochkin N. E., Medvedeva G. I., Pastukhova E. N., Perova N. B., Rastorguev A. S., Shugarov S. Y., 1985, *General Catalogue of Variable Stars (4th edition)*, Nauka, Moscow
Kipper T., Jörgensen U. G., Klochkova V. G., Panchuk V. E., 1996, *A&A* 306, 489
Knapik A., Bergeat J., Rutily B., 1999, *A&A* 344, 263
Kondo Y., McCluskey, G. E. J., Gulden S. L., 1976, in E. Bold, Y. Kondo (eds.), *X-ray Binaries*, NASA-SP 389, Washington D.C., 499
Koornneef J., 1983, *A&A* 128, 84
Kovács N., 1985, *A&A* 150, 232
Kroupa P., 1995, *MNRAS* 277, 1522

- Kukarkin B. V., Kholopov P. N., Artiukhina N. M., Samus N. N., Frolov M. S., Goranskij V. P., Gorynya N. A., Karitskaya E. A., Kazarovets E. V., Kireeva N. N., Kukarkina N. P., Kurochkin N. E., Medvedeva G. I., Pastukhova E. N., Perova N. B., Rastorguev A. S., Shugarov S. Y., 1982, *New General Catalogue of Suspected Variable Stars*, Nauka, Moscow
- Kwok S., Chan S. J., 1993, *AJ* 106, 2140
- Lada E. A., Evans, N. J. I., Depoy D. L., Gatley I., 1991, *ApJ* 371, 171
- Lambert D. L., 1985, in Jaschek & Keenan 1985, 191
- Lambert D. L., Gustafsson B., Eriksson K., Hinkle K. H., 1986, *ApJS* 62, 373
- Lambert D. L., Smith V. V., Busso M., Gallino R., Straniero O., 1995, *ApJ* 450, 302
- Lambert D. L., Smith V. V., Heath J., 1993, *PASP* 105, 568
- Lambert D. L., Smith V. V., Hinkle K. H., 1990, *AJ* 99, 1612
- Landolt, Börnstein, 1982, in K.-H. Hellwege, K. Schaifers, H. H. Voigt (eds.), *Astronomy and Astrophysics*, Vol. 2, subvol b, Springer-Verlag
- Langer N., Heger A., Wellstein S., Herwig F., 1999, *A&A* 346, L37
- Lattanzio, J. C., 1995, in M. Busso, R. Gallino, C. Raiteri (eds.), *Nuclei in the cosmos III*, AIP Conf. Proc. 327, American Institute of Physics, 353
- Lattanzio, J. C., Frost C., Cannon R., Wood P., 1997, in R. Rood, A. Renzini (eds.), *Stellar Ecology, Advances in Stellar Evolution*, Cambridge Univ. Press, Cambridge
- Le Bertre T., Deguchi S., Nakada Y., 1990, *A&A* 235, L5
- Le Bertre T., Lèbre A., Waelkens C. (eds.), 1999, *Asymptotic Giant Branch stars (IAU Symp. 191)*, Astronomical Society of the Pacific
- Liebert J., Dahn C. C., Gresham M., Strittmatter P. A., 1979, *ApJ* 233, 226
- Liebert J., Schmidt G. D., Lesser M., Stepanian J. A., Lipovetsky V. A., Chaffe F. H., Foltz C. B., Bergeron P., 1994, *ApJ* 421, 733
- Lindgren L., 1995, *A&A* 304, 61
- Lindgren H., Gilliotte A., 1989, *The Coudé Echelle Spectrometer, The Coudé Auxiliary Telescope*, ESO Operating Manual No. 8
- Little S. J., Little-Marenin I. R., Bauer W. H., 1987, *AJ* 94, 981
- Little-Marenin I. R., 1986, *ApJ* 307, L15
- Little-Marenin I. R., Benson P. J., Dickinson D. F., 1988, *ApJ* 330, 828
- Little-Marenin I. R., Little S. J., 1979, *AJ* 84, 1374
- Little-Marenin I. R., Little S. J., 1987, *AJ* 93, 1539
- Livio M., Shore S. N., van den Heuvel E. P. J., 1992, *Interacting binaries*, Springer-Verlag
- Lloyd Evans T., 1983a, *MNRAS* 204, 985
- Lloyd Evans T., 1983b, *MNRAS* 204, 975
- Lloyd Evans T., 1984, *MNRAS* 208, 447
- Lloyd Evans T., 1986, *MNRAS* 220, 723
- Lloyd Evans T., 1990, *MNRAS* 243, 336
- Lloyd Evans T., 1991, *MNRAS* 249, 409
- Lloyd Evans T., Catchpole R. M., 1989, *MNRAS* 237, 219
- Lloyd Evans T., Little-Marenin I. R., 1999, *MNRAS* 304, 421
- Lü P. K., 1991, *AJ* 101, 2229

- Lü P. K., Dawson D. W., Upgren A. R., Weis E. W., 1983, *ApJS* 52, 169
- Lubow S. H., Artymowicz P., 1992, in *Duquennoy & Mayor 1992*, 145
- Luck R. E., 1977, *ApJ* 212, 743
- Luck R. E., Bond H. E., 1982, *ApJ* 259, 792
- Luck R. E., Bond H. E., 1991, *ApJS* 77, 515
- Lucy L. B., Sweeney M. A., 1971, *AJ* 76, 544
- Lundgren K., 1988, *A&A* 200, 85
- Lundgren K., 1990, *A&A* 233, 21
- Luri X., Arenou F., 1997, in *Battrick 1997*, 449
- Lutz T. E., 1979, *MNRAS* 189, 273
- Lutz T. E., Kelker D. H., 1973, *PASP* 85, 573
- MacConnell D. J., 1979, *A&AS* 38, 335
- MacConnell D. J., 1982, *A&AS* 48, 355
- MacConnell D. J., 1997, *Baltic Astronomy* 6, 105
- MacConnell D. J., Frye R. L., Upgren A. R., 1972, *AJ* 77, 384
- Maeder A., Meynet G., 1989, *A&A* 210, 155
- Malmquist K. G., 1936, *Stockholms Obs. Medd.* 26
- Mathews G. J., Takahashi K., Ward R. A., Howard W. M., 1986, *ApJ* 302, 410
- Mathieu R. D., 1994, *Ann. Rev. Astron. Astrophys.* 32, 465
- Mavridis L. N., 1960, *PASP* 72, 48
- Mavridis L. N., 1971, in *Proceedings of the NATO Advanced Study Institute*, held in Athens, Greece, September 8-19, 1969, Dordrecht: Reidel, 1971, edited by Mavridis, L.N.
- Maxted P. F. L., Marsh T. R., 1999, *MNRAS* 307, 122
- Mayor M., 1997, in *Planetary systems. The long view*, *Rencontres de Blois*
- Mayor M., Benz W., Imbert M., Martin N., Prevot L., Andersen J., Nordstrom B., Ardeberg A., Lindgren H., Maurice E., 1984, *A&A* 134, 118
- Mayor M., Duquennoy A., Halbwachs J. L., Mermilliod J. C., 1992, in *ASP Conf. Ser. 32: Complementary Approaches to Double and Multiple Star Research*, p. 73
- Mayor M., Duquennoy A., Udry S., Andersen, J. and Nordström B., 1996, in G. Milone, J.-C. Mermilliod (eds.), *ASP Conf. Ser. 90: The Origins, Evolution, and Destinies of Binary Stars in Clusters*, p. 190
- Mazeh T., 1990, *AJ* 99, 675
- Mazeh T., Shaham J., 1979, *A&A* 77, 145
- McClure R. D., 1983, *ApJ* 268, 264
- McClure R. D., 1984a, *PASP* 96, 117
- McClure R. D., 1984b, *ApJ* 280, L31
- McClure R. D., 1997a, *PASP* 109, 536
- McClure R. D., 1997b, *PASP* 109, 256
- McClure R. D., Fletcher J. M., Nemeč J. M., 1980, *ApJ* 238, L35
- McClure R. D., Forrester W. T., Gibson J., 1974, *ApJ* 189, 409
- McClure R. D., Woodsworth A. W., 1990, *ApJ* 352, 709
- McWilliam A., 1990, *ApJS* 74, 1075
- Meadows P. J., Good A. R., Wolstencroft R. D., 1987, *MNRAS* 225, 43P

- Mennessier M. O., Luri X., Figueras F., Gomez A. E., Grenier S., Torra J., North P., 1997, *A&A* 326, 722
- Mermilliod J.-C., 1996, in G. Milone, J.-C. Mermilliod (eds.), *ASP Conf. Ser. 90: The Origins, Evolution, and Destinies of Binary Stars in Clusters*, p. 95
- Mermilliod J.-C., Mayor M., 1996, in R. Pallavicini, K. Dupree (eds.), *Ninth Cambridge Workshop on Cool Stars, Stellar Systems and the Sun*, *ASP Conf. Ser. 109*, 373
- Merrill P. W., 1922, *ApJ* 56, 457
- Merrill P. W., 1952, *ApJ* 116, 21
- Merrill P. W., 1955, *ApJ* 67, 70
- Merrill P. W., 1956a, *PASP* 68, 162
- Merrill P. W., 1956b, Line of chemical elements in astronomical spectra, Papers of the Mount Wilson Observatory, Volume IX, Carnegie Institution of Washington Publication 610
- Meyer F., Meyer-Hofmeister E., 1979, *A&A* 78, 167
- Mihalas D., Binney J., 1987, *Galactic astronomy*, W. H. Freeman, New york, 2nd edition
- Miller G. E., Scalo J. M., 1982, *ApJ* 263, 259
- Morgan W. W., Whitford A. E., Code A. D., 1953, *ApJ* 118, 318
- Mowlavi N., 1999, *A&A* 344, 617
- Mowlavi N., Jorissen A., Arnould M., 1995, *A&A* 311, 803
- Murtagh F., Heck A., 1987, *Multivariate Data Analysis*, Reidel, Dordrecht
- Nakagiri M., Yamashita Y., 1979, *Annals of the Tokyo Astronomical Observatory* 17, 221
- Nassau J. J., 1958, in D. J. K. O'Connell (ed.), *Stellar Populations*, *Ric. Astron. Specola Vaticana*, Vol.5, 183
- Nassau J. J., Blanco V. M., 1954, *ApJ* 120, 464
- Neckel T., Klare G., 1980, *A&AS* 42, 251
- Neugebauer G., Leighton R. B., 1969, in *Two-Micron Sky Survey*, NASA SP-3047 (TMSS)
- Newberry M. V., 1991, *PASP* 103, 122
- Noguchi K., Sun J., Wang G., 1991, *PASJ* 43, 311
- Nomoto K., 1987, *ApJ* 322, 206
- Norris J. E., Green E. M., 1989, *ApJ* 337, 272
- North P., Berthet S., Lanz T., 1994, *A&A* 281, 775
- North P., Duquennoy A., 1991, *A&A* 244, 335
- North P., Jorissen A., Mayor M., 1999, in *Wing 1999*, in press
- North P., Lanz T., 1991, *A&A* 251, 489
- Nussbaumer H., Vogel M., 1987, *A&A* 182, 51
- Pastetter L., Ritter H., 1989, *A&A* 214, 186
- Peery, B. F. J., 1971, *ApJ* 163, L1
- Perraud H., 1959, *J. Observateurs* 42, 142
- Petr M. G., Coude Du Foresto V., Beckwith S. V. W., Richichi A., McCaughrean M. J., 1998, *ApJ* 500, 825
- Piccirillo J., 1977, Ph.D. thesis, Indiana University, Bloomington, Indiana, U.S.A.

- Piccirillo J., 1980, *MNRAS* 190, 441
Pickering E. C., 1908, *Harvard Circ.* 145
Plez B., 1992, *A&AS* 94, 527
Plez B., Brett J. M., Nordlund A., 1992, *A&A* 256, 551
Pollard K. R., Cottrell P. L., Kilmartin P. M., Gilmore A. C., 1996, *MNRAS* 279, 949
Pont F., Mayor M., Turon C., Vandenberg D. A., 1998, *A&A* 329, 87
Press W. H., Teukolsky S. A., Vetterling W. T., Flannery B. P., 1992, *Numerical Recipes in Fortran*, Second Edition, Cambridge Univ. Press, Cambridge
Price S. D., Murdock T. L., 1983, in *The Revised AFGL Infrared Sky Survey Catalog (AFGL-TR-83-0161)*
Proust D., Ochsenbein F., Pettersen B. R., 1981, *A&AS* 44, 179
Rebeirot E., Azzopardi M., Westerlund B. E., 1993, *A&A* 97, 603
Reid I. N., 1996, *AJ* 111, 2000
Reid N., Majewski S. R., 1993, *ApJ* 409, 635
Reid N., Mould J., 1985, *ApJ* 299, 236
Renzini A., 1981, in I. Iben Jr, A. Renzini (eds.), *Physical processes in Red Giants*, D. Reidel Publ. Co., Dordrecht, 431
Richer H. B., 1981, *ApJ* 243, 744
Ridgway S. T., Joyce R. R., White N. M., Wing R. F., 1980, *ApJ* 235, 126
Ritossa C., García-Berro E., Iben, Jr I., 1996, *ApJ* 460, 489
Ritossa C., García-Berro E., Iben, Jr I., 1999, *ApJ* 515, 381
Ritter H., 1996, in R. A. M. J. Wijers, C. A. Davies M. B. and Tout (eds.), *Evolutionary Processes in Binary Stars*, Kluwer, Dordrecht, 223
Rufener F., 1988, *Catalogue of stars measured in the Geneva Observatory Photometric system: A new determination of the Geneva photometric passbands and their absolute calibration, fourth edition*, Geneva Observatory Publication
Rufener F., Nicolet B., 1988, *A&A* 206, 357
Sackmann I.-J., Boothroyd A. I., 1991, in G. Michaud, A. Tutukov (eds.), *Evolution of Stars: The Photospheric Abundance Connection*, I.A.U. Symposium 145, Kluwer, Dordrecht, 275
Sackmann I.-J., Boothroyd A. I., 1992, *ApJ* 392, L71
Saffer R. A., Liebert J., Olszewski E. W., 1988, *ApJ* 334, 947
Saffer R. A., Livio M., Yungelson L. R., 1998, *ApJ* 502, 394
Sahai R., Liechti S., 1995, *A&A* 293, 198
Santer F., 1978, *ApJ* 219, 538
Sauval A. J., 1978, *A&A* 62, 295
Scalo J. M., 1973, *ApJ* 186, 967
Scalo J. M., 1976, *ApJ* 206, 474
Scalo J. M., Miller G. E., 1981, *ApJ* 246, 251
Scalo J. M., Ross J. E., 1976, *A&A* 48, 219
Schaller G., Schaerer D., Meynet G., Maeder A., 1992, *A&AS* 96, 269
Schindler M., Stencel R. E., Linsky J. L., Basri G. S., Helfand D. J., 1982, *ApJ* 263, 269
Schmid H. M., 1994, *A&A* 284, 156

- Schmid H. M., Nussbaumer H., 1993, *A&A* 268, 159
- Schuerman D. W., 1972, *Ap&SS* 19, 351
- Schwarzschild M., Härm R., 1965, *ApJ* 142, 855
- Smith H. J., 1988, *A&A* 198, 365
- Smith V. V., Coleman H., Lambert D. L., 1993, *ApJ* 417, 287
- Smith V. V., Cunha K., Jorissen A., Boffin H. M. J., 1996, *A&A* 315, 179
- Smith V. V., Cunha K., Jorissen A., Boffin H. M. J., 1997, *A&A* 324, 97
- Smith V. V., Lambert D. L., 1985, *ApJ* 294, 326
- Smith V. V., Lambert D. L., 1986, *ApJ* 311, 843
- Smith V. V., Lambert D. L., 1987, *MNRAS* 226, 563
- Smith V. V., Lambert D. L., 1988, *ApJ* 333, 219
- Smith V. V., Lambert D. L., 1990, *ApJS* 72, 387
- Smith V. V., Plez B., Lambert D. L., Lubowich D. A., 1995, *ApJ* 441, 735
- Smith V. V., Wallerstein G., 1983, *ApJ* 273, 742
- Snedden C., 1974, Ph.D. thesis, University of Texas, Austin, U.S.A.
- Snedden C., Pilachowski C. A., Lambert D. L., 1981, *ApJ* 247, 1052
- Stein J. W., 1991, *ApJ* 377, 669
- Stephenson C. B., 1973, *A General Catalogue of Cool Carbon Stars*, Publications of the Warner & Swasey Observatory, 1, 1, Columbus
- Stephenson C. B., 1984, *A General Catalogue of Galactic S stars*, Second Edition, Publications of the Warner and Swasey Observatory, 3, 1, Columbus
- Stephenson C. B., 1986, *PASP* 98, 467
- Stephenson C. B., 1989, *A general catalog of cool galactic carbon stars*, Second edition., Publications of the Warner & Swasey Observatory, 3, 53, Columbus
- Stephenson C. B., 1990, *AJ* 100, 569
- Straniero O., Gallino R., Busso M., Chieffi A., Limongi, M. and Salaris M., 1995, *ApJ* 440, L85
- Suntzeff N. B., Phillips M. M., Elias J. H., Cowley A. P., Hartwick F. D. A., Bouchet P., 1993, *PASP* 105, 350
- Takayanagi W., 1960, *PASJ* 12, 314
- Theuns T., Boffin H. M. J., Jorissen A., 1996, *MNRAS* 280, 1264
- Theuns T., Jorissen A., 1993, *MNRAS* 265, 946
- Tomkin J., Lambert D. L., Edvardsson B., Gustafsson B., Nissen P. E., 1989, *A&A* 219, L15
- Tout C. A., Eggleton P. P., 1988, *MNRAS* 231, 823
- Turon C., al., 1992, in *The HIPPARCOS Input Catalogue*, ESA SP-1136
- Turon C., Creze M., Egret D., Gomez A., Grenon M., Jahreiss H., Requieme Y., Argue A. N., Bec-Borsenberger A., Dommagnet J., Mennessier M. O., Arenou F., Chareton M., Crifo F., Mermilliod J. C., Morin D., Nicolet B., Nys O., Prevot L., Rousseau M., Perryman M. A. C., 1992, *Bull. Inf. CDS* 41, 9
- Turon C., Creze M., Egret D., Gomez A., Grenon M., Jahreiss H., Requieme Y., Argue A. N., Bec-Borsenberger A., Dommagnet J., Mennessier M. O., Arenou F., Chareton M., Crifo F., Mermilliod J. C., Morin D., Nicolet B., Nys O., Prevot L., Rousseau M., Perryman M. A. C., Et Al., 1993, *Bull. Inf. CDS* 43, 5

- Udry S., Jorissen A., Mayor M., Van Eck S., 1998a, *A&AS* 131, 25
- Udry S., Mayor M., Van Eck S., Jorissen A., Prevot L., Grenier S., Lindgren H., 1998b, *A&AS* 131, 43
- Utsumi K., 1985, in Jaschek & Keenan 1985, 243
- Van Belle G. T., Dyck H. M., Benson J. A., Lacasse M. G., 1996, *AJ* 112, 2147
- van der Veen W. E. C. J., Habing H. J., 1988, *A&A* 194, 125
- Van Eck S., Jorissen A., Udry S., Mayor M., Pernier B., 1998, *A&A* 329, 971
- Van Leeuwen F., Feast M. W., Whitelock P. A., Yudin B., 1997, *MNRAS* 287, 955
- van Loon J. T., Zijlstra A. A., Whitelock P. A., te Lintel Hekkert P., Chapman J. M., Loup C., Groenewegen M. A. T., Waters L. B. F. M., Trams N. R., 1998, *A&A* 329, 169
- Van Winckel H., 1999, in Le Bertre et al. 1999, 465
- Van Winckel H., Mathis J. S., Waelkens C., 1992, *Nat* 356, 500
- Van Winckel H., Waelkens C., Fernie J. D., Waters L. B. F. M., 1999, *A&A* 343, 202
- Van Winckel H., Waelkens C., Waters L. B. F. M., 1995, *A&A* 293, L25
- Van Winckel H., Waelkens C., Waters L. B. F. M., Molster F. J., Udry S., Bakker E. J., 1998, *A&A* 336, L17
- Vanture A. D., 1992a, *AJ* 103, 2035
- Vanture A. D., 1992b, *AJ* 104, 1986
- Vanture A. D., 1992c, *AJ* 104, 1997
- Vanture A. D., Wallerstein G., 1999, *PASP* 111, 84
- Vanture A. D., Wallerstein G., Brown J. A., 1994, *PASP* 106, 835
- Vanture A. D., Wallerstein G., Brown J. A., Bazan G., 1991, *ApJ* 381, 278
- VanWinckel H., 1999, in Wing 1999, in press
- Vogt N., Moffat A. F. J., 1975, *A&A* 39, 477
- Vysotsky A. N., Balz A. G. A., 1958, *Publ. McCormick Obs.* 13, pt. 2
- Wagenhuber J., Tuchman Y., 1996, *A&A* 311, 509
- Wallerstein G., 1985, *PASP* 97, 994
- Wallerstein G., Knapp G. R., 1998, *Ann. Rev. Astron. Astrophys.* 36, 369
- Warner B., 1965, *MNRAS* 129, 263
- Warren S. J., Irwin M. J., Evans D. W., Liebert J., Osmer P. S., Hewett P. C., 1993, *MNRAS* 261, 185
- Waters L. B. F. M., Waelkens C., Mayor M., Trams N. R., 1993, *A&A* 269, 242
- Webbink R. F., 1986, in K. C. Leung, D. S. Zhai (eds.), *Critical Observations vs Physical Models for Close Binary Systems*, Gordon and Breach, New York, 403
- Weidemann V., 1990, *A&AR* 28, 103
- Weigert A., 1966, *Zs. Ap.* 64, 395
- Westerlund B., 1964, in F. Kerr, A. Rodgers (eds.), *The Galaxy and the Magellanic Clouds (IAU Symp. 20)*, Australian Academy of Sciences, Canberra, 160
- Westerlund B. E., Azzopardi M., Breysacher J., Rebeiro E., 1995, *A&A* 303, 107

- Westerlund B. E., Azzopardi M., Rebeirot E., Breysacher J., 1991, *A&AS* 91, 425 (with erratum in *A&AS* 92, 683)
- Westerlund B. E., Olander N., 1978, *A&AS* 32, 401
- Westerlund B. E., Olander N., Hedin B., 1981, *A&A* 43, 267
- Whitelock P., 1994, *MNRAS* 270, L15
- Whitelock P., Catchpole R. M., 1985, *MNRAS* 212, 873
- Willems F. J., De Jong T., 1986, *ApJ* 309, L39
- Williams P. M., 1975, *MNRAS* 170, 343
- Winfrey S., Barnbaum C., Morris M., Omont A., 1994, *BAAS* 26, 1382
- Wing R. (ed.), 1999, *The Carbon Star Phenomenon* (IAU Symp. 177), Kluwer, Dordrecht
- Wing R. F., Yorke S. B., 1977, *MNRAS* 178, 383
- Wood P. R., Alcock C., A. A. R., Alves D., Axelrod T. S., 1999, in Le Bertre et al. 1999, 151
- Wood P. R., Bessell M. S., Fox M. W., 1983, *ApJ* 272, 99
- Wray J. D., 1966, Ph.D. thesis, Northwestern University, Evanston, Illinois
- Yamashita Y., Norimoto Y., 1981, *Annales of the Tokyo Astronomical Observatory* 18, 125
- Yorke S. B., Wing R. F., 1979, *AJ* 84, 1010
- Young J. S., Baldwin J. E., Boysen R. C., Haniff C. A., Pearson D., Rogers J., St.-Jacques D., Warner P. J., Wilson D. M. A., 1999, in Le Bertre et al. 1999, 145
- Young K., Phillips T. G., Knapp G. R., 1993, *ApJS* 86, 517
- Začs L., 1994, *A&A* 283, 937
- Začs L., Musaev F. A., Bikmaev I. F., Alksnis O., 1997, *A&AS* 122, 31
- Zijlstra A. A., Loup C., Waters L. B. F. M., De Jong T., 1992, *A&A* 265, L5
- Zijlstra A. A., Pottasch S. R., 1991, *A&A* 243, 478

Bibliography

▷ Refereed papers:

- *The Hipparcos Hertzsprung-Russell diagram of S stars: probing nucleosynthesis and dredge-up*
S. Van Eck, A. Jorissen, S. Udry, M. Mayor, B. Pernier, 1998, A&A 329, 971
- *Insights into the formation of barium and Tc-poor S stars from an extended sample of orbital elements*
A. Jorissen, S. Van Eck, M. Mayor, S. Udry, 1998, A&A 332, 877
- *A CORAVEL radial-velocity monitoring of giant Ba and S stars: spectroscopic orbits and intrinsic variations (I)*
S. Udry, A. Jorissen, M. Mayor, S. Van Eck, 1998, A&AS 131, 25
- *New CORAVEL spectroscopic-binary orbits of giant barium stars (II)*
S. Udry, M. Mayor, S. Van Eck, A. Jorissen, L. Prévot, S. Grenier, H. Lindgren, 1998, A&AS 131, 43
- *The Henize sample of S stars. I. The technetium dichotomy*
S. Van Eck, A. Jorissen, 1999, A&A 345, 127

▷ To be submitted:

- *The Henize sample of S stars. II. Data*
S. Van Eck, A. Jorissen, S. Udry, M. Mayor, G. Burki, M. Burnet, R. Catchpole, M. Feast, A&AS
- *The Henize sample of S stars. III. Properties of extrinsic and intrinsic S stars*
S. Van Eck, A. Jorissen, A&A

▷ Contributions to conferences:

- *The Hipparcos Hertzsprung-Russell diagram of S stars*
S. Van Eck, A. Jorissen, S. Udry, M. Mayor, B. Pernier, in: The Hipparcos and Tycho catalogues, M. Perryman (ed.), ESA-SP 402, 1997
- *Barium and Tc-poor S stars: binary masqueraders among carbon stars*
A. Jorissen, S. Van Eck, in: Proceedings of the IAU Symposium 177 (The carbon star phenomenon), 11pp., R. Wing (ed.), Kluwer, Dordrecht, 1999
- *The link between barium stars and optically bright post-AGB binaries*
H. van Winckel, C. Waelkens, A. Jorissen, S. Van Eck, P. North, R. Waters, in: Proceedings of the IAU Symposium 180 (Planetary Nebulae), 1p., Kluwer, Dordrecht, 1997